Regulation of photosystem II in the context of climate change

Lucas Leverne

To cite this version:

Lucas Leverne. Regulation of photosystem II in the context of climate change. Biological Physics [physics.bio-ph]. Université Paris-Saclay, 2023. English. NNT : 2023UPASB065 . tel-04468772

HAL Id: tel-04468772
https://theses.hal.science/tel-04468772

Submitted on 20 Feb 2024

HAL is a multi-disciplinary open access archive for the deposit and dissemination of scientific research documents, whether they are published or not. The documents may come from teaching and research institutions in France or abroad, or from public or private research centers.

L'archive ouverte pluridisciplinaire **HAL**, est destinée au dépôt et à la diffusion de documents scientifiques de niveau recherche, publiés ou non, émanant des établissements d'enseignement et de recherche français ou étrangers, des laboratoires publics ou privés.

Regulation of photosystem II in the context of climate change

Régulation du photosystème II face au changement climatique

Thèse de doctorat de l'université Paris-Saclay

École doctorale n° 567, Sciences du végétal : du gène à l'écosystème et SEVE
Spécialité de doctorat : Sciences végétales
Graduate School : BioSphERA. Référent : Faculté des sciences d'Orsay

Thèse préparée dans l'unité de recherche **Institute for Integrative Biology of the Cell (I2BC) (Université Paris-Saclay, CEA, CNRS)**,
sous la direction de **Anja KRIEGER-LISZKAY** directrice de recherche,
et la co-encadremente **Fabienne MAIGNAN**, Ingénieur-Chercheur

Thèse soutenue à Paris-Saclay, le 15 novembre 2023, par

Lucas LEVERNE

Composition du Jury

Membres du jury avec voix délibérative

Michael HODGES Directeur de recherche, CNRS, Université Paris-Saclay	Président
Jean ALRIC Directeur de recherche, CNRS, CEA Cadarache	Rapporteur & Examinateur
Gilles CURIEN Chargé de recherche, HDR CNRS, CEA Grenoble	Rapporteur & Examinateur
Valérie LE DANTEC Maître de conférences, Université Paul Sabatier - Toulouse III	Examinatrice

THÈSE DE DOCTORAT

NNT : 2023UPASB065

ÉCOLE DOCTORALE
Agriculture, alimentation, biologie, environnement, santé (ABIES)

Titre : Régulation du photosystème II face au changement climatique

Mots-clés : Photosynthèse**,** mécanismes de régulation, modélisation, fluorescence de la chlorophylle

Résumé : L'absorption du CO_2 atmosphérique via la photosynthèse joue un rôle majeur pour l'atténuation du changement climatique. Néanmoins via des épisodes de canicule et de sécheresse ces dernier induit d'importants stress sur les plantes terrestres. Dans ce contexte des incertitudes considérables persistent dans la prévision des capacités d'absorption du CO_2 par les plantes terrestres pour les décennies futures. C'est pourquoi nous avons étudié la régulation de la photosynthèse dans ces conditions de stress, depuis l'échelle moléculaire au niveau du chloroplaste, jusqu'à l'échelle globale des surfaces continentales. Nous avons utilisé principalement des mesures de fluorescence de la chlorophylle *a*, permettant de faire le lien entre les connaissances de la plus petite échelle à la plus grande. Cette thèse nous a permis de proposer de nouveaux modèles pour la régulation de la photosynthèse à plusieurs échelles : un rôle potentiel pour le glycolate au niveau du PSII (chapitre 2), une voie de signalisation possible entre le chloroplaste et les racines (chapitre 3), l'impact combiné de l'âge et l'espèce de la plante pour les température extrêmes (chapitre 4), la modélisation d'un processus de régulation moléculaire implémenté dans le modèle de surfaces continentales ORCHIDEE pour l'ensemble des forêts boréales à aiguilles persistantes (chapitre 5), et enfin la modélisation d'un processus de régulation pour des arbustes en conditions de sécheresse et hautes températures (chapitre 6). Dans l'ensemble, ce travail a permis une première connexion entre des chercheurs experts de la régulation de la photosynthèse aux échelles moléculaires et globales. Cette connexion a conduit à améliorer la modélisation de l'absorption du CO_2 atmosphérique par les surfaces continentales, ce qui permettra de réduire les incertitudes associées dans les projections climatiques.

Title: Regulation of photosystem II in the context of climate change

Keywords: Photosynthesis, regulatory mechanism, modelling, chlorophyll fluorescence

Abstract: The absorption of atmospheric CO_2 through photosynthesis plays a crucial role in mitigating climate change. However, climate change-induced heatwaves and drought impose significant stresses on terrestrial plants. Despite ongoing efforts, there remain considerable uncertainties in predicting the future of the CO_2 absorption capacities of these plants. Consequently, we conducted a study to investigate the regulation of photosynthesis under such stresses, spanning from the molecular scale at chloroplast level to the global scale of continental surfaces. Using chlorophyll *a* fluorescence measurements as our primary tool, we established connections between knowledge at different scales. This thesis has yielded novel models for photosynthesis regulation across multiple levels: identifying a potential role for glycolate at the PSII level (Chapter 2), exploring a potential signalling pathway between the chloroplast and roots (Chapter 3), examining the combined effects of plant age and species on extreme temperatures (Chapter 4), implementing a molecular regulation process in the ORCHIDEE model for boreal evergreen needleleaf forests (Chapter 5), and modelling regulation processes for poplar trees under drought and high temperature conditions (Chapter 6). Overall, this research establishes a valuable connection between research on photosynthesis regulation at molecular and global scales. This connection has led to improvements in the modelling of atmospheric CO_2 absorption by continental surfaces, which will allow reducing associated uncertainties for climate projections.

Acknowledgements

Thank you to Anja and Fabienne for agreeing to supervise my thesis despite knowing the difficulties I faced with writing (dyslexia, dysorthography). I would like to thank them for the considerable work they have put into proofreading all my work.

This work benefited from the French state aid managed by the ANR under the “Investissements d'avenir” programme with the reference ANR-16-CONV-0003 (CLand), and by the LabEx Saclay Plant Sciences-SPS (grant number ANR-17-EUR-0007).

I thank the members of my jury, listed on the front page, as well as Gabriel Hmimina, researcher at the “Laboratoire de Météorologie Dynamique”, invited member.

Thanks to Édouard, or Doudou, for introducing me to the fighting spirit in rugby, which was greatly needed during this thesis.

Thank you to Alfred, always ready to do anything and especially to try to explain my work.

Thank you, Tanguy, for our conversations, which, although rarely scientific, allowed me to put things into perspective.

Thank you, Zoé, for listening to my complaints and my strange ideas.

Thank you, Elliot, for making the film and our tumultuous debates.

Thank you to Martin, Ferdinand, Antoine, Guilhem, Daphne, Pauline, Hugo and all my other friends whom I have forgotten, for helping me change my ideas.

Thank you to my lab colleagues turned friends: Camille, Julien, Noémie, Mathilde, Adrian, Alice, Marine, Umama.

Thank you, Agathe, for her sowing protocol that saved me a lot of time.

Thank you my family Marguerite, Rosalie, Mahaut, Mathilda, François, Jeanne, Antoine, Balsamie, Guylaine, Christophe, Manou, Mani and to my dear ones Caroline, Zélie, Alessia, Marc for their moral support.

I want to thank my parents for always believing in me and being proud of me. Their support has been a driving force in getting me to where I am today.

Table des matières

1 Chapter 1: General introduction

Anthropogenic activities such as those relying on the burning of fossil fuels and land use have led to massive emissions of carbon dioxide (CO_2), of which the main part has accumulated into the atmosphere (Friedlingstein et al., 2022). The increased level of atmospheric CO_2, which is a greenhouse gas, has caused drastic changes in the global climate (IPCC Sixth Assessment Report, 2021). Climate change (CC) has led to increased frequency and intensity of droughts and high temperatures, which have put significant stresses on plants (Crausbay et al., 2017). These changes in weather patterns have made it increasingly difficult for plants to maintain their physiological functions, which has led to reduced crop yields (Lobell et al., 2011) and loss of forestry vegetation cover (Allen et al., 2010).

This raises the question of how long plants can still mitigate climate change. Through photosynthesis, plants absorb atmospheric CO_2 and convert it into sugars, which they use to sustain their growth and development. This process is critical not only for plant survival but also for global food security. Photosynthesis thus contributes to the regulation of atmospheric CO_2 levels, which makes plants a key player for mitigation of the impacts of climate change (Field et al., 1998).

Drought stress is one of the most significant environmental factors that affect plant growth and productivity (Chaves et al., 2002). Drought-induced stress can damage the photosynthetic apparatus of plants, leading to reduced CO_2 uptake and limited plant growth. In drought conditions, plants close their stomata to reduce transpiration; this leads to reduced CO_2 concentration in leaves, and decreases the electron donor consumption during CO_2 reduction and increases the potential for oxidative stress. Non-photochemical quenching (NPQ) is an ensemble of key regulatory mechanisms used by plants as a protection against drought-induced oxidative stress, which allows to dissipate excess energy as heat.

In order to improve the global modelling of plant productivity, it is crucial to comprehend the regulation of plant responses to drought at a molecular level, and translate it into conceptual leaf-level models. Modelling photosynthetic processes at leaf-level, and up-scaling the corresponding fluxes at the canopy, ecosystem and global scales is critical for predicting the impact of plant responses to climate change. Land surface numerical models represent our understanding of the ability of terrestrial plants to absorb CO_2. They are used to compute the quantity of CO_2 assimilated by plants through photosynthesis over all continental surfaces, called gross primary production (GPP), and to analyse how this ability to absorb CO_2 may alter under various future climatic scenarios.

The main goal of this thesis is to connect the understanding of plant regulation on a molecular level with the processes represented in land surface models, as well as with large-scale observations, to improve global simulations of plant CO_2 uptake. I will study the regulation of photosynthesis at multiple scales including: photosystem (PS) II, linear electron flow of chloroplast, plant model *A. thaliana*, model tree poplar, and boreal evergreen needleleaf forests. By integrating these different levels of understanding, we can develop more accurate representations of how plants respond to climate conditions. This knowledge can help us to

develop better strategies for managing our planet's natural resources and mitigating the impacts of climate change.

1.1 A vegetation increasingly exposed to droughts and elevated temperatures

Figure 1-1 from Chapter 11 of the Sixth Assessment Report (AR6) (“Weather and Climate Extreme Events in a Changing Climate,” 2023) of Working Group I of the Intergovernmental Panel on Climate Change (IPCC) shows the spatial patterns expected in temperature and precipitation under a scenario with a 4°C warming. Predicting drought levels will be quite challenging, as significant modifications are expected between mean and extreme precipitation for different regions of the world.

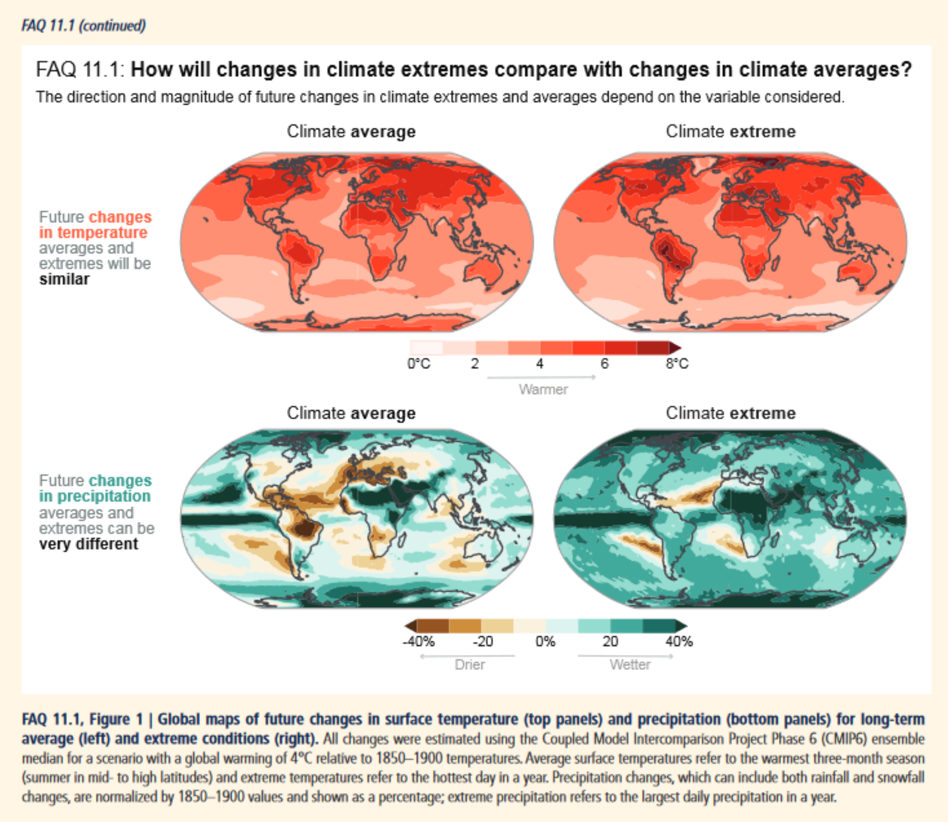

FAQ 11.1 (continued)

FAQ 11.1: **How will changes in climate extremes compare with changes in climate averages?**

The direction and magnitude of future changes in climate extremes and averages depend on the variable considered.

FAQ 11.1, Figure 1 | Global maps of future changes in surface temperature (top panels) and precipitation (bottom panels) for long-term average (left) and extreme conditions (right). All changes were estimated using the Coupled Model Intercomparison Project Phase 6 (CMIP6) ensemble median for a scenario with a global warming of 4°C relative to 1850–1900 temperatures. Average surface temperatures refer to the warmest three-month season (summer in mid- to high latitudes) and extreme temperatures refer to the hottest day in a year. Precipitation changes, which can include both rainfall and snowfall changes, are normalized by 1850–1900 values and shown as a percentage; extreme precipitation refers to the largest daily precipitation in a year.

Figure 1-1: Illustration of the spatial patterns of changes in the warmest three-month season temperature and annual mean precipitation, and extreme temperature and precipitation (projections for a 4°C global warming by 2100), source Chapter 11 of the IPCC AR6 of Working Group I (“Weather and Climate Extreme Events in a Changing Climate,” 2023)(“Weather and Climate Extreme Events in a Changing Climate,” 2023).

Chapter 8 of the IPCC AR6 of Working Group I (“Water Cycle Changes,” 2023) provides a detailed description of the impacts of climate change on the global water cycle. The IPCC foresees an increase in soil evapotranspiration, air humidity, and a global modification of precipitation patterns, with less frequent but more intense rainfalls. An increase in precipitation is expected for the high northern latitudes of the globe, and a corresponding increase in drought for many regions. The IPCC anticipates a decrease in soil moisture over the Mediterranean, southwestern North America, southern Africa, southwestern South America, and southwestern Australia. Aridification is predicted to far exceed the magnitude of change observed during the last millennium in the Mediterranean, southwestern South America, and western North America. Some tropical regions, such as the Amazon basin and Central America, are also expected to experience increased aridity, (Chapter 11 of the IPCC AR6 of Working Group I, "Weather and Climate Extreme Events in a Changing Climate," 2023).

There has already been an increase in drought and high temperatures over the past decades, with a significant interannual variation (Figure 1-2).

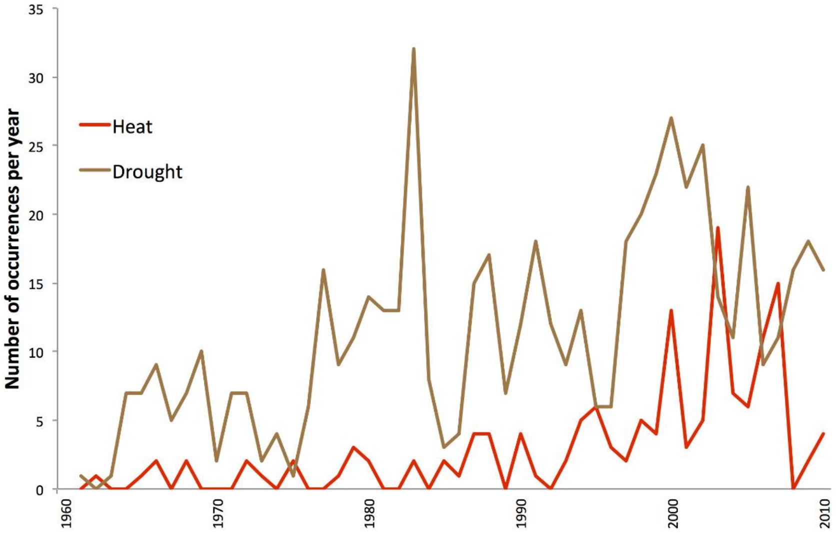

Figure 1-2: Time series of the number of extreme heat and drought disasters per year from the Emergency Events Database (EM-DAT). The EM-DAT database is based on a compilation of disaster reports gathered from various organizations including United Nations agencies, governments and the International Federation of Red Cross and Red Crescent Societies (Lesk et al., 2016).

These changes have greatly disrupted agricultural yields and food security. By analysing the yield losses reported by the Food and Agriculture Organization of the United Nations and the reports of extreme hydro-meteorological disasters collected by the Emergency Events Database (EM-DAT) between 1964 and 2007, (Lesk et al., 2016) show a significant effect of heatwaves on yields, with a global decrease in cereal yields of 9.1%. However, droughts alone have an even greater effect on yields, with a decrease of 10.1% (Lesk et al., 2016). Analysing the response of plants to water stress can allow us to understand their behaviour in such conditions, bring out processes mitigating stress, and maybe find leads to improve crop resistance.

Forests represent a large proportion of vegetative cover on terrestrial land, and serve as a significant carbon sink (Harris et al., 2021). They represent 40 millions of km^2 against 16 millions of km^2 for crops and 32 millions of km^2 for grazing (Ritchie and Roser, 2013). However, forests are increasingly suffering from climate change too, being windthrow, droughts, and associated increased risks of cavitation, fires, pest attacks, leading to mortality (Allen et al., 2010; Forzieri et al., 2022).

In order to improve both crops and forest modelling, **it is necessary to study the fundamental behaviour of photosynthesis under conditions of drought or/and high temperatures**. The following sections will describe the basis of photosynthesis in a plant cell, first the light reactions, and then the dark reactions.

1.2 Photosynthetic processes

1.2.1 The light reactions

Photosynthesis occurs in the chloroplast, a specific organelle of the plant cell. This process can be divided into two main parts called light and dark reactions. The light reactions take place in an electron transport chain in the thylakoid membrane of the chloroplast, and produce adenosine triphosphate (ATP) and nicotinamide adenine dinucleotide phosphate (NADPH). These are subsequently used during the dark reactions, also called the Calvin-Benson cycle and described in section 1.2.2, which produces sugar from CO_2. The electron transport reactions go through four main protein complexes: PSII, cyt b_6f, PSI, ATP synthase, which are embedded in the thylakoid membrane. I will first describe these four protein complexes, and then how they interact in the linear electron flow (source: Krieger-Liszkay & Kirilovsky (2022) in Photosynthesis in Action (eds Ruban, Foyer, Murchie, Elsevier)).

1.2.1.1 Photosystem II (PSII)

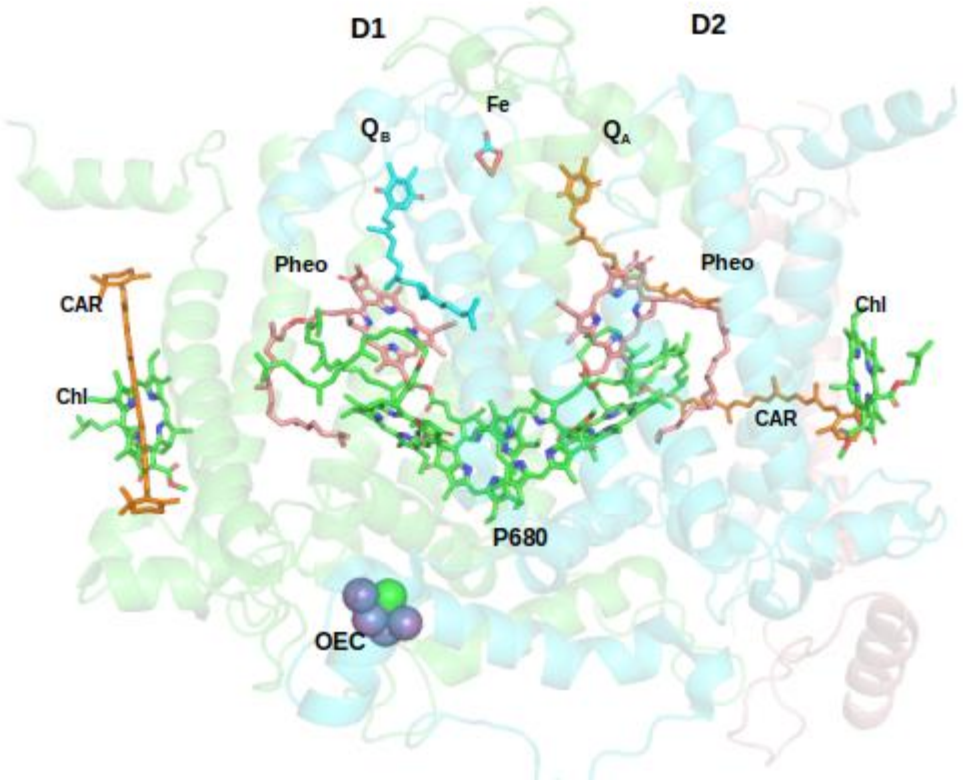

Figure 1-3: Photosystem II structure and cofactors and pigments attached to the heterodimer D1/D2. Chl: chlorophyll; CAR: β-carotene; Pheo: pheophytin; Q_a and Q_b: primary and secondary quinone acceptors; OEC: Oxygen Evolving Complex, P680 photosystem II primary donor. The electron transport takes place between the cofactors of the D1 protein, only Q_a is located on the D2 protein (source: Krieger-Liszkay & Kirilovsky (2022) in Photosynthesis in Action (eds Ruban, Foyer, Murchie, Elsevier)).

PSII is mostly located in the grana region of the thylakoid membrane. It uses light energy to drive two reactions: oxidation of water and reduction of plastoquinone. PSII is a dimer composed of two identical complexes that function independently. The photochemical reaction centre of each PSII is formed by two homologous proteins, D1 and D2, forming a symmetric heterodimer which binds all the cofactors needed for charge separation and stabilization. Only one site of the heterodimer is active in electron transport. An inorganic complex, Mn_4CaO_5, called Oxygen Evolving Complex (OEC), responsible for the oxidation of water and production of oxygen, is attached to the lumenal side of D1. When the chlorophylls of the photosystem II primary donor, noted P680, are excited, charge separation takes place producing $P680^+/Pheo^-$. Then the electron is transferred to Q_a and later to Q_b non-heme iron. The Q_b site differs from the Q_a one in that it works as a two-electron acceptor, and becomes fully reduced after two successive excitations of P680. The double-reduced Q_b exchanges with an oxidized plastoquinone (PQ) from the PQ pool. On the PSII donor side, the charge separation event permits the oxidation of redox active amino acid tyrosine Z by $P680^+$. The tyrosine Z reduces $P680^+$. TyrZ+ in turn is reduced by the OEC. The water splitting requires four successive oxidations of Mn by tyrosine Z. The four oxidation steps of Mn ions permit water splitting that produces one molecule of oxygen and four protons from two molecules of water.

Figure 1-3 also shows that two β-carotenes are present in PSII. They act as scavengers of $^1O_2$ (see presentation of singlet oxygen in section 1.3.1) and the one located at the D2 protein can also be an alternative electron donor to $P680^+$.

1.2.1.2 Cytochrome b_6f

Between PSII and PSI, the cytochrome b_6f (cyt b_6f) complex plays a central role in the linear electron flow. It acts as a plastoquinol-plastocyanin oxidoreductase. The cyt b_6f complex receives electrons from the reduced plastoquinone pool, generated by PSII, and transfers them to PSI through plastocyanin. Additionally, this process involves the translocation of protons across the membrane from the stroma to the lumen. In most environmental conditions, the rate of the electron transport and reoxidation of the PQH_2 pool are controlled by cyt b_6f.

1.2.1.3 Photosystem I (PSI)

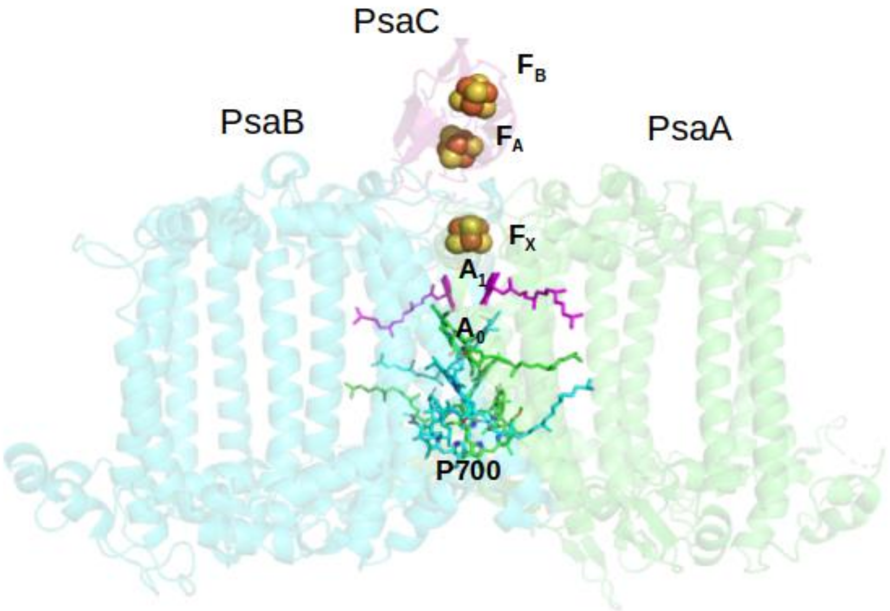

Figure 1-4: Photosystem I structure and cofactors involved in the electron transport. PSI is shown from the side, with the luminal side of the membrane at the bottom and the stromal side at the top of the figure. The following subunits

are visible in this figure: PsaA (green), PsaB (cyan), PcaC (magenta), chlorophyll dimer P700, primary electron acceptor A_0, chlorophyll monomer A_1 single acceptor donor, cluster 4Fe-4S noted Fx and two other 4Fe-4S clusters F_A and F_B located in PsaC (source: Krieger-Liszkay & Kirilovsky (2022) in Photosynthesis in Action (eds Ruban, Foyer, Murchie, Elsevier)).

In PSI, presented in Figure 1-1, there are two symmetric and active branches participating in electron transport from P700 to the Fe-S cluster Fx. When light excites P700, charge separation takes place and it gives the electron to the primary electron acceptor, A0, then to A1, creating the more stable $P^{+}700A^{-}_{1A}$ state. Then Fx is reduced, and the electron is transferred to F_A or F_B Fe-S clusters in PsaC. Ferredoxin (Fd) with its very negative reduction potential (-430 mV) is easily reduced by F_A or F_B clusters (-550 mV). The ultimate stage of linear electron transport involves the reduction of NADP+ to NADPH through the activity of ferredoxin-NADP reductase (FNR). FNR accepts electrons in a sequential manner, one at a time, from ferredoxin (Fd). These electrons are temporarily stored at the Flavin adenine dinucleotide (FAD) cofactor, which can exist in three distinct states: fully oxidized, semi-reduced, and fully reduced, transitioning from FAD to FADH to $FADH_2$. Subsequently, FNR catalyses the two-electron reduction of NADP+ to NADPH.

1.2.1.4 ATP synthase

The acid pH in lumen, linked to protons produced during water splitting in the OEC of PSII and protons pumping from the stroma to the lumen by cyt b_6f, permits ATP synthase activity. The ATP synthase catalyses the addition of inorganic phosphate (noted Pi) to ADP, to produce ATP using the proton gradient as energy source.

1.2.1.5 The linear electron flow

All these complexes (PSII, cyt b_6f, PSI, ATP synthase) interact together to produce ATP and NADPH in what we call the **linear electron flow** (Figure 1-5). First, photons excite the chlorophylls in the antenna, which transfer the energy to the chlorophyll molecules of the primary donor P680 in PSII. On the lumen side of the thylakoid membrane H_2O molecules are oxidized by the water splitting complex of PSII, which produces oxygen molecules, protons and electrons (**step 1**). Electrons reduce quinones A then B (**step 2**) of PSII, and a second charge separation occurs and reduces the plastoquinone pool, converting PQ into PQH_2 (**step 3**). PQH_2 reduces cyt b_6f (**step 4**) and the reduction is further transferred to PSI through plastocyanin (**step 5**). PSI reduces Ferredoxin (Fd). Reduced Fd is used by the Ferredoxin-NADP+-Reductase (FNR) to generate reducing power NADPH from NADP+ (**step 6**). Finally, the proton gradient produced during the water splitting by PSII and the plastoquinol oxidation by the cyt b_6f enable the production of ATP by the ATP synthase (**step 7**) (Nelson & Ben-Shem, 2004).

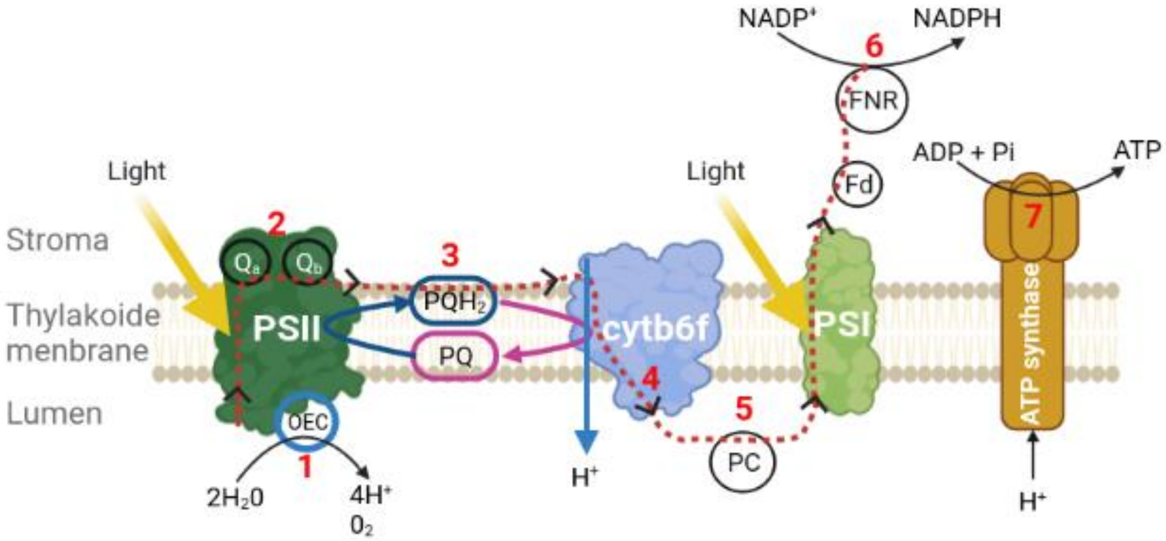

Figure 1-5: Schematic representation of the linear electron transport in the thylakoid membrane of the chloroplast. The red dotted line represents the linear electron flow, and the numbers represent each step described in the core text.

Beside the linear electron transport there exist alternative electron transport pathways that are not detailed here. We just briefly mention the cyclic electron flow. Two pathways of cyclic electron flow exist: one via the NDH complex and one via a still unidentified ferredoxin/plastoquinone oxidoreductase. In both pathways, electrons from the acceptor side of PSI cycle via the PQ pool, cyt b_6f and plastocyanin back to PSI, generating a proton gradient and thereby allowing the producing ATP. The exact pathway is still under debate (Nawrocki et al., 2019).

1.2.2 The dark reactions

The energy stored in the form of reducing power and ATP produced during the light reactions is used to power the Calvin-Benson cycle. This cycle reduces atmospheric CO_2 into sugar. First Ribulose-1,5-bisphosphate carboxylase/oxygenase (RuBisCo) with ribulose-1,5-bisphosphate (RuBP) as substrate reduces CO_2 and produces 3-phosphoglycerate (3-PG). The different steps of the Calvin-Benson cycle will not be described here. For every reduced CO_2, the consumption of 3 ATP and 2 NADPH is required. RuBisCo can also reduce oxygen instead of CO_2. This photorespiratory pathway is detailed in section 2.1.

The localization and activity of RuBisCo varies depending on the type of plant: C3, C4 and CAM. CAM plants will not be discussed in this thesis. In C3 plants, the light reactions and the Calvin-Benson cycle occur in the mesophyll cells, and the dissolved CO_2 reaction with RuBP is directly catalysed by the RuBisCo enzyme.

In contrast, C4 plants (in which the first carbon compound produced contains four carbon atoms) are characterized by the kranz anatomy, i.e., specialized cells around the bundle sheath. This special anatomy isolates RuBisCo from oxygen. Furthermore, in these chloroplasts no or very little PSII activity is present, minimizing photosynthetic O_2 production. Thanks to the prefixation of CO_2 by phosphoenolpyruvate carboxylase, the CO_2 concentration in the bundle sheath cell is higher than in the mesophyll cells allowing more efficient carboxylation reaction by RuBisCo. This particular morphology gives higher photosynthesis and thereby higher fitness of C4 plants in high temperature or aridity conditions by avoiding losses by photorespiration.

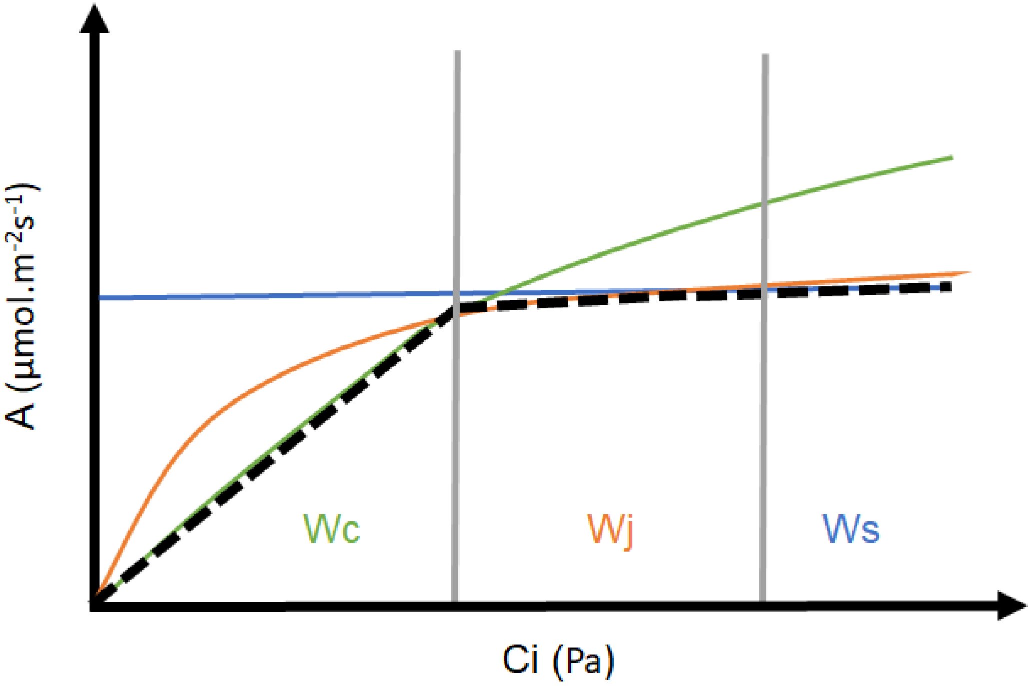

Figure 1-6: Idealized A/Ci response with its limitations defined by the Farquhar model. The Wc limitation associated with the maximum rate of ribulose-1,5-bisphosphate carboxylase/oxygenase (Rubisco) carboxylation is in green. The Wj limitation associated with the electron transport rate for the regeneration of RuBP is in orange, and the Ws limitation associated with the triose-phosphate utilization is in blue. The black dotted line represents the photosynthetic rate derived from these three limitations. Figure inspired from (Long, 2003).

The internal concentration of CO_2, noted Ci (µmol.mol^{-1}), in plants plays a major role in the rate of CO_2 assimilation. The rate of CO_2 fixation via the Calvin-Benson cycle is limited by three parameters, as represented in the Farquhar model (Farquhar et al., 1980), that will be further described here, with equations given for the C3 case. These limitations appear successively as Ci increases under conditions of constant temperature and light (Figure 1-6). First, there is Wc, which is the assimilation associated with the maximum rate of RuBisCo carboxylation ($Vcmax$, eq. (1.1)), second, Wj , which represents a limitation in ATP and NADPH produced during the light phase of photosynthesis (eq. (1.2)), and third, Ws, which is rarely observed at normal CO_2 concentrations and results from triose-phosphate export limitation (eq. (1-3)). The CO_2 assimilation is formulated as the minimum of these three limitations:

$$Wc = \frac{Vcmax\,(Ci - \Gamma *)}{Ci + Kc(1 + \frac{Oi}{Ko})} \qquad \text{eq. (1-1)}$$

$$Wj = \frac{J(Ci - \Gamma *)}{4(Ci + 2\Gamma *)} \qquad \text{eq. (1-2)}$$

$$Ws = Vcmax/2 \qquad \text{eq. (1-3)}$$

Ci is the intercellular CO_2 partial pressure (Pa), $\Gamma *$ is the CO_2 compensation point (Pa), Oi is the partial pressure of oxygen and Kc and Ko are the Michaelis-Menten coefficients, respectively for the carboxylation and oxidation reactions catalysed by Rubisco. J (µmol.electron.m^{-2}.s^{-1}) is computed following an empirical law, it depends on the maximum electron transport rate, $Jmax$, (µmol.electron.m^{-2}.s^{-1}) and the number of photons absorbed by a leaf, noted ϕ (µmol.photon.m^{-2}.s^{-1}), as the smaller of the two roots of the equation:

$$0.7J^2 - (Jmax + 0.385\phi)J + 0.385\,Jmax\phi = 0 \qquad \text{eq. 1-4)}$$

Kc, Ko, $Vcmax$ and $Jmax$ are all temperature dependent.

1.3 Regulation of photosynthesis

1.3.1 The different ROS species and their production sites in the photosynthetic chain

Under natural conditions, it is typical for plants to receive an excessive amount of photons, leading to the saturation of the linear electron transfer chain. As a result, the reduced electron acceptors may react with oxygen and generate ROS (reactive oxygen species). These species can react with, and cause damage to, proteins, lipids, DNA and RNA (Gill & Tuteja, 2010). At high concentrations, ROS can cause irreversible damage and induce cell death. However, there are many different ROS scavengers in plants to control this oxidative stress, and ROS are also used as a signal for cells, and are thus not just a harmful waste (Waszczak et al., 2018). One distinguishes between reduced forms of oxygen (superoxide anion radical, hydrogen peroxide, hydroxyl radicals, etc.) and singlet oxygen ($^1O_2$). Oxygen is in a triplet state ($^3O_2$) in its fundamental state and, therefore, its reactivity is kinetically limited. When the spins are reversed and $^1O_2$ is generated from $^3O_2$, it becomes extremely reactive. In photosynthetic organisms, $^1O_2$ is produced either by excited chlorophylls in their triplet state when the antenna is altered, or in the PSII reaction centre by the recombination of the primary charge pair ($P680^+Phe^-$). This yields the formation of $^3P680$ that reacts with $^3O_2$ to $^1O_2$. The production site in the reaction centre is the main site of $^1O_2$ production in photosynthesis (Krieger-Liszkay, 2004). The singlet of oxygen is more reactive and has a shorter life time and can travel less in the cell, compared to other ROS like H_2O_2. Superoxide anion radicals are generated through the transfer of an electron to molecular oxygen for example during electron transport in the plant's mitochondria. In addition, superoxide anions are also produced during photosynthetic electron transport. This process is known as the Mehler reaction, which involves the transfer of electrons from an electron donor such as F_A^-, F_B^-, PQ^-, Q_b^- to molecular oxygen. F_A and F_B are the terminal electron acceptors in PSI. Superoxide is dismutated to H_2O_2, either catalyzed by superoxide dismutase or spontaneously.

Hydroxyl radicals are highly reactive ROS that are generated by the Fenton reaction. This reaction occurs when iron or copper (Fe(II), Cu(I)) ions and hydrogen peroxide (H_2O_2) interact, resulting in the production of hydroxyl radicals.

Plants have evolved various defence mechanisms to counter the negative effects of ROS, including the production of antioxidant enzymes such as superoxide dismutase, catalase, ascorbate, glutathione, and peroxidase. These enzymes catalyse the conversion of ROS into less reactive molecules, thereby minimizing their damaging effects on the plant's cells (Foyer, 2005). In addition, carotenoids and tocopherols are important antioxidant substances (Sekher Pannala et al., 1998).

1.3.2 Mains NPQ mechanisms in plants

When a plant is exposed to too much light or stressful conditions such as drought or high temperatures, it can dissipate excess energy in the form of heat to protect itself against ROS production. This process is called non-photochemical quenching (NPQ). It is present in all photosynthetic organisms and consists of several mechanisms (Goss and Lepetit, 2015). NPQ mechanisms regulate the linear electron flow and the ROS production. There are three different types of NPQ: 1. **qE**, that is pH-dependent (Ruban, 2018), 2.**qT**, also called state transitions, that involve movement of a part of light harvesting complexes II, noted LHCII (Tikkanen and Aro, 2012), and 3. **qI**, photoinhibition, that involves the damage and turnover of the D1 protein (Nath et al., 2013). These different types of NPQ are classified according to their relaxation time in darkness.

Regarding **qE,** the pH of the thylakoid lumen plays a key role in dissipating received light energy as heat via carotenoids. The decrease in pH in the lumen induces a chain of regulation that leads to the successive and reversible de-epoxidation of violaxanthin to antheraxanthin and then zeaxanthin. This mechanism dissipates the received excess energy at the antenna level as heat, see Figure 1-7 part A. In addition to zeaxanthin, the PSBS protein is also involved in NPQ. Its activity is triggered by low pH in the lumen and it quenches energy and dissipates it as heat. The NPQ type qE has the shortest relaxation time, on the order of a minute. Regarding **qT**, state transitions occur when the transfer of chlorophyll antennas between PSII and PSI balances their level of excitation, see Figure 1-7 part B. qT relaxation in darkness takes around 20 minutes. Regarding **qI**, it is mainly observed during exposure to high light intensities, and induces the degradation of the D1 protein in PSII, rendering the complex non-functional. The synthesis of D1 protein and subsequent assembly of PSII takes several hours.

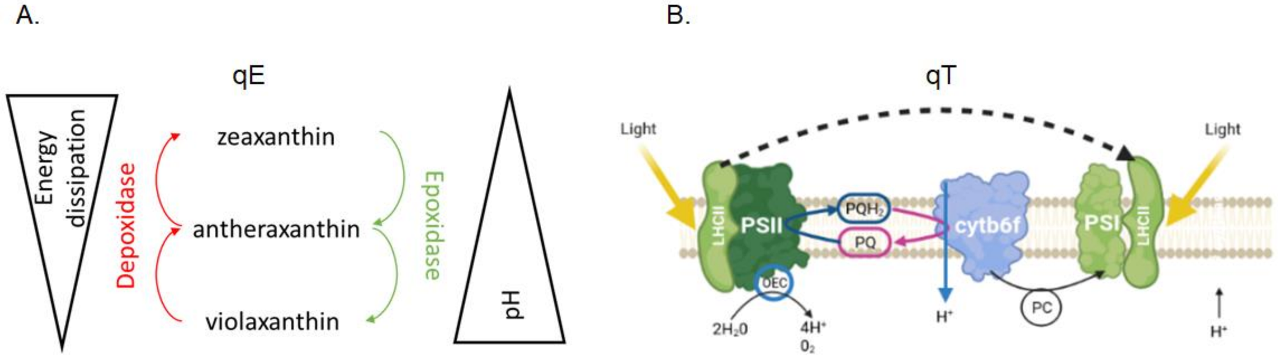

Figure 1-7: Schematic representation of two NPQ mechanisms. A. qE NPQ type, with triangles representing energy and pH gradients, and the transition of violaxanthin to zeaxanthin. B. qT NPQ type, the dotted arrow shows the movement of the loosely bound part of LHCII from PSII to PSI. This takes place after phosphorylation and acetylation of LHCII.

Finally, for gymnosperm needleleaf trees, a specific type of NPQ is observed (e.g., in *Pinus sylvestris*) over the cold season, during which almost all photosynthetic yield is nullified. This one is called sustained NPQ because it lasts several months. In this case, a rearrangement of chlorophyll antennas and PSII prevents the photosystems from receiving light energy and performing the necessary charge separation for photosynthetic activity (Bag et al., 2020). In standard conditions, PSII is preferentially localised in grana stacks and PSI in lamellas of chloroplasts. In this type of NPQ, the thylakoid membrane is disorganised, and there is a direct energy transfer from PSII to PSI, the so-called spillover, see Figure 1-8.

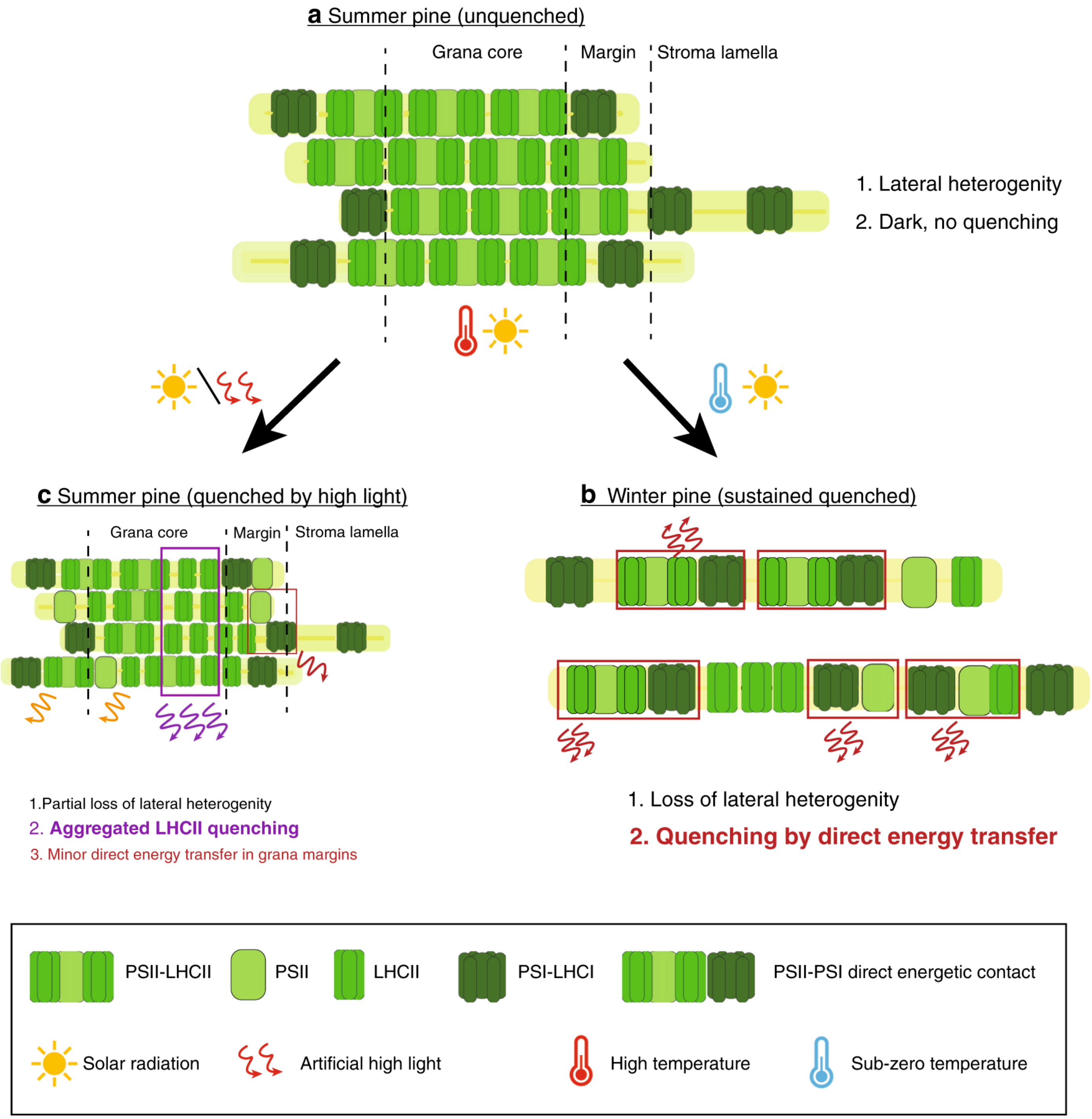

Figure 1-8: Different seasonal quenchings: Summer unquenched (a); Winter quenched (b); Summer quenched (c) in Scots pine. From (Bag et al., 2020).

1.4 Chlorophyll fluorescence measurements

In this part, I present how measurements of chlorophyll *a* fluorescence can be used to get information on photosynthetic activity from the leaf to the global scale.

Fluorescence of chlorophyll *a* is one of the three modes of energy dissipation when a photosynthetic organism is illuminated. The organism can also dissipate energy as heat (NPQ) or use it during photosynthesis to convert atmospheric carbon into sugar. A small part of chlorophyll relaxation generates fluorescence emission, representing at maximum 1-2% of the total energy received. The fluorescence emission spectrum from chlorophyll *a* covers the spectral range from 650 nm to 780 nm with two peaks centred around 685 nm and 740 nm (Franck et al., 2002.).

At room temperature, while the fluorescence emission wavelengths of the two photosystems overlap, the emission intensity from PSII is stronger compared to PSI, as shown in Figure 1-9. In contrast, at 77 K, the emission from the two photosystems can be distinctly separated with PSII emitting at 685 and 695 nm and PSI antenna emitting at 730 nm (Krause and Weis, 1991).

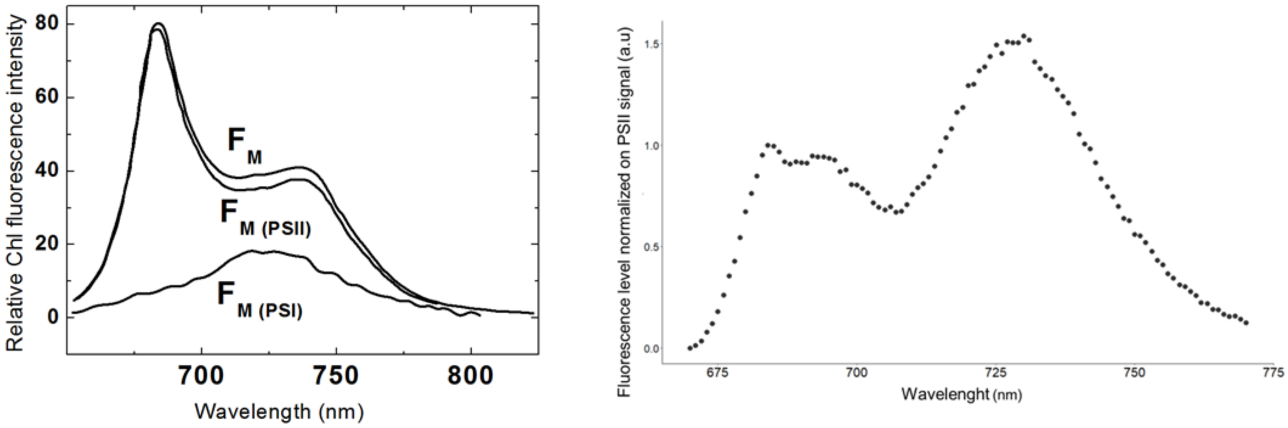

Figure 1-9: Left panel: relative maximal fluorescence emission (Fm) of PSII and PSI at room temperature; modified after (Franck et al., 2002.). Right panel: fluorescence emission at 77K normalised on PSII signal, personal data.

Due to the close link between energy dissipation by heat, photosynthesis, and chlorophyll fluorescence (Baker, 2008), we can calculate the level of photosynthesis and NPQ by measuring the fluorescence of chlorophyll excited with saturating flashes. This method of fluorescence measurement is called the active one. Another method is called passive, both are presented below.

1.4.1 Active measurements

For active measurements, we use a technique called PAM (pulse amplitude modulation). This technique uses a modulated measuring light with a high frequency. The approach relies on the saturation of the photosynthetic system, using short high-intensity light flashes. Using a series of minimum and maximum fluorescence values obtained in dark-adapted and high-light conditions, as detailed in the following section, it becomes possible to calculate the photochemical and non-photochemical yields of the plant (Baker, 2008). The main limitation of this technique is that it is only doable at small spatial scales, from a leaf to a small plant.

1.4.1.1 Procedure for active measurements and yield calculations

The principle of fluorescence active measurement is presented in Figure 1-10. The fluorescence level measured is denoted by **F**. First, the sample is kept in the dark for 5 minutes to fully oxidise the Q_a of PSII. Then, we turn on the measuring light, first at a level, which is too weak to induce photosynthetic activity. At this stage, we measure the dark-adapted fluorescence level **F_0**. Next, we saturate the photosynthetic system with a high-energy flash, which reduces the plastoquinone pool,

Q_a and Q_b. Because the flash excitation is very fast (300 ms), the full photosynthetic electron chain is not operating, resulting in the measurement of the maximal fluorescence level **Fm**. Then, we turn on the actinic light, this one induces photosynthetic activity. Initially, energy is dissipated through fluorescence, which explains the rise in fluorescence, as seen in Figure 1-10. Then, the fluorescence level decreases due to energy dissipation through both photochemical and non-photochemical quenchings. When the fluorescence level becomes stable with the light turned on, we add flashes that fully reduce Q_a, resulting in a new fluorescence level called **Fm'**. There is a last fluorescence level noted on the graph, called **F_0'**; to reach this particular level after illuminating the sample under the previously described conditions, we use a far-red light to specifically excite PSI and pull out the electron flow of PSII to completely oxidise the plastoquinone pool and Q_a.

Because the PAM machine I used during this work did not provide far-red light, we used the following formula to estimate F_0': $F_0' = F_0/ (F/Fm + F_0/Fm')$ (Oxborough & Baker, 1997).

There are various fluorescence parameters that can be computed based on these fluorescence levels, among which the effective PSII quantum yield Y(II), the quantum yield of regulated energy dissipation Y(NPQ), and the quantum yield of non-regulated energy dissipation Y(NO). The sum of the tree previous quantum yields is 1. There are also: the photochemical quenching coefficient, qL, which quantifies the proportion of active PSII reaction centres (meaning the PSII fraction where Q_a is oxidized), and is usually computed based on the "lake model" of PSII antenna organization; qN, the non-photochemical quenching coefficient, taking a value of 0 for the dark-adapted state and of 1 when all variable fluorescence is quenched; and qP, the photochemical quenching, also varying between 0 and 1.

These parameters are calculated as follows: $Y(II) = (Fm'-F)/Fm'$; $Y(NPQ) = 1-Y(II)-1/(NPQ+1+qL(Fm/F_0-1))$; $Y(NO) = 1/(NPQ+1+qL(Fm/F_0-1))$; $qL = (Fm'-F)/(Fm'-F_0') \times F_0'/F$; $qN = (Fm-Fm')/(Fm-F_0')$.

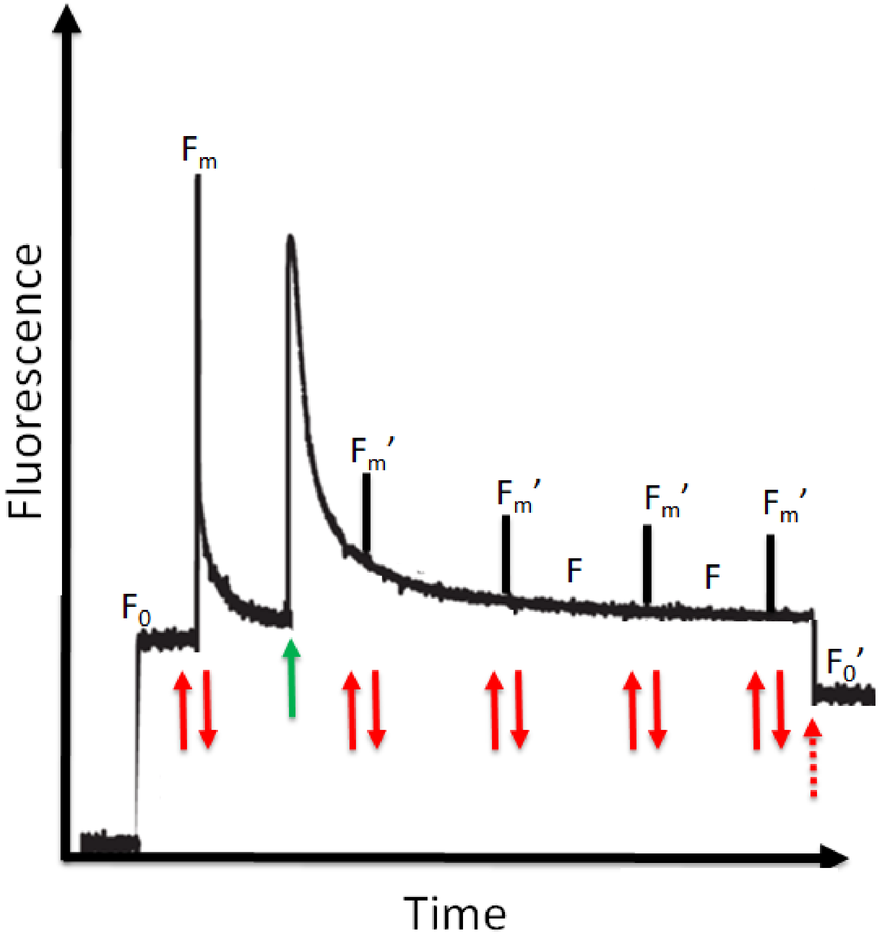

Figure 1-10: Fluorescence levels during a classical photosynthetic PAM measurement starting on fully dark-adapted photosynthetic systems. The green arrow represents the moment when an actinic light is turned on; the double red arrows represent moments of saturating flashes, and the dotted red arrow represents the moment when far-red light is activated. F_0: minimal fluorescence for a dark-adapted sample; Fm: maximal fluorescence for a dark-adapted sample; Fm': maximal fluorescence for an illuminated sample. The total time of the experience is around 5 to 10 min with classically 1 min in between saturating flashes.

1.4.2 Passive measurements

The passive measurements of chlorophyll fluorescence usually rely on the sun as the light source, in which case they estimate the so-called sun-induced fluorescence (SIF). This method allows to estimate the fluorescence at larger scales under sunlight excitation, from an entire canopy at the site scale, to the global scale using space-borne satellite instruments. At scales larger than the leaf, the estimated SIF depends not only on the physiological state of the plant and on the solar radiation, but also on the vegetation structure (Leaf Area Index, Leaf Angle Distribution), and on the acquisition geometry (solar zenith angle, view zenith angle, relative azimuth angle), as conceptually represented in Figure 1-11.

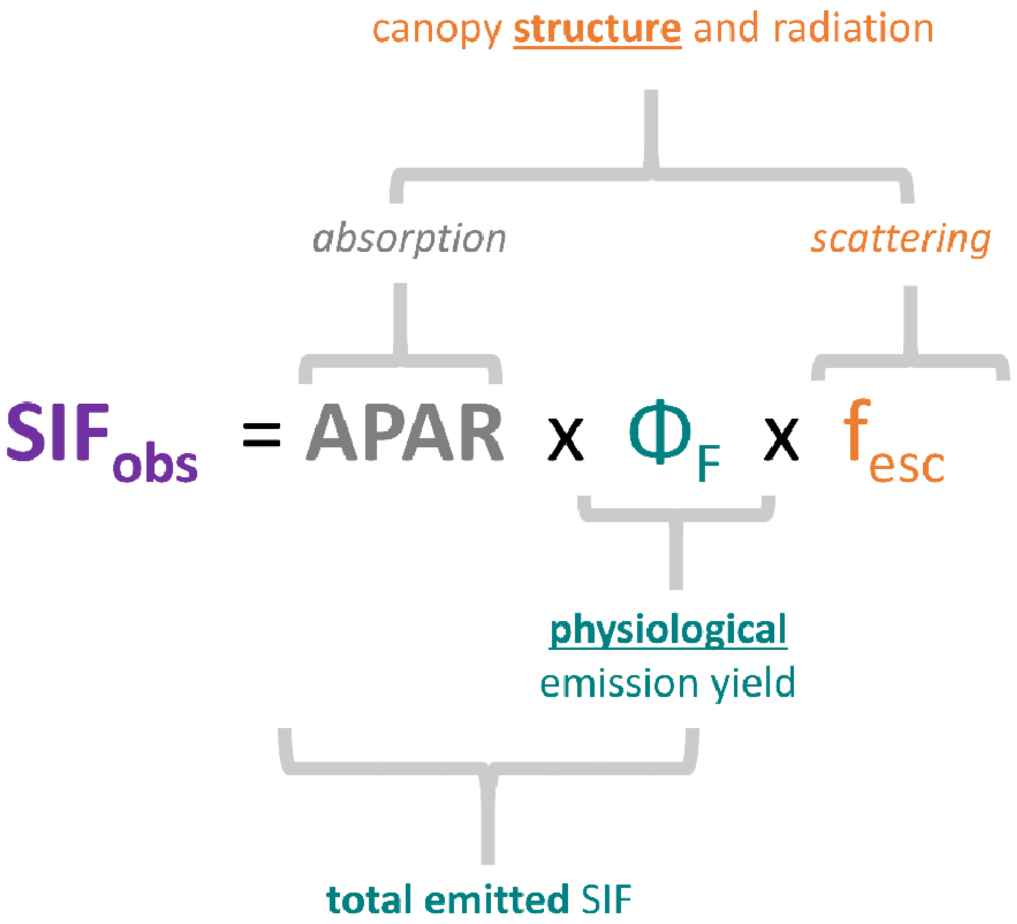

Figure 1-11: Representation of the various drivers impacting the observed SIF. All terms are given at the canopy scale. APAR is the absorbed photosynthetically active radiation. ΦF is the physiological SIF emission yield from all leaves in the canopy, and fesc is the fraction of emitted SIF that escapes from the canopy in the viewing direction. Both APAR and fesc depend on the canopy structure. Figure from (Dechant et al., 2020).

Satellite SIF has gained increasing attention in the last decade due to its potential to provide a GPP proxy, with a spatial coverage much larger than traditional *in situ* methods (Mohammed et al., 2019). Traditional methods for estimating GPP typically rely on gas exchange measurements from individual leaves or chambers, which can be time-consuming, and they are limited in their spatial coverage. In contrast, SIF can be estimated remotely from space, providing information on GPP over large areas, with frequent revisit. This makes it possible to monitor GPP at a global scale, providing insights into the functioning of the Earth's ecosystems and the role of vegetation in the carbon cycle.

Several studies have shown that SIF can provide GPP estimates that are consistent with direct measurements of GPP from eddy covariance towers, which are considered the gold standard for GPP estimation. Eddy covariance flux towers continuously measure gas exchanges between the land surface (soil and vegetation) and the atmosphere (e.g., Baldocchi et al. (2001)). AFor example, a study by (Li et al., 2017) compared SIF-based GPP estimates with GPP estimates from eddy covariance towers across 18 forest sites in the United States, Europe, and China. The study found that SIF-based estimates were highly correlated with eddy covariance GPP estimates, with a determination coefficient $R^2 = 0.72$.

1.5 Modelling and optimisation

1.5.1 Importance of land surface models

Terrestrial plants play a key role in the capture of atmospheric CO_2 via photosynthesis. They represent a major carbon sink, absorbing 33% of the anthropogenic CO_2 emissions, with oceans also absorbing 29% (Friedlingstein et al., 2022). The remaining emissions accumulate in the atmosphere, increasing the greenhouse effect at the origin of climate change.

As opposed to the oceanic sink, the terrestrial sink presents a large spatial and temporal variability, driven both by the gross primary production (GPP), which is the raw uptake of CO_2 assimilated by the continental vegetation through photosynthesis, and by the total ecosystem respiration. The terrestrial sink benefits from the CO_2 fertilisation effect associated with its increased atmospheric concentration (Walker et al., 2021) . However, photosynthesis is negatively affected by extreme events such as droughts and heatwaves (Gampe et al., 2022), whose frequency is increasing (Lesk et al., 2016). In (Duffy et al., 2021), the authors investigated the temperature dependency of photosynthesis in C3 and C4 plants, as well as the respiration, of the terrestrial biosphere. They observed that photosynthesis increases up to a certain temperature threshold, 18°C for C3 plants and 28°C for C4 plants, and beyond these temperatures, photosynthesis starts to decrease. In contrast, respiration exhibits a linear increase between 10°C and 38°C, and, due to this difference in behaviour, respiration surpasses photosynthesis around 32°C. Hence, the land surface sink may turn into a land surface source, depending on future climate scenarios (Friedlingstein et al., 2014).

Land surface models (LSMs) simulate the biogeochemical and physical processes occurring in terrestrial ecosystems, which allows computing the exchanges of energy, water, carbon and other nutrients at the interface between land surfaces and the atmosphere (Bonan, 2008). They are essential tools to study the present and the future response of terrestrial ecosystems to climate change (Fisher & Koven, 2020)

1.5.2 The ORCHIDEE LSM

The ORCHIDEE (Organising Carbon and Hydrology In Dynamic Ecosystems) LSM (Boucher et al., 2020; Krinner et al., 2005) is a state-of-the-art model developed at Institut Pierre Simon Laplace (IPSL). The model can be run from the site to the global scale, coupled to an atmospheric model or forced by prescribed meteorological fields from local observations, or larger-scale reanalyses (offline mode).

Fast processes related to the energy budget and the water balance (e.g., evaporation, transpiration), as well as photosynthesis, are computed at a half-hourly time step, while other carbon-related processes (e.g., phenology, allocation, litter and soil decomposition) are computed at a daily time step. Heat dissipation and water fluxes are distributed vertically within the soil, and runoff is collected in rivers and lakes. Plants are gathered into large Plant Functional Types (PFTs); within a PFT, plants share the same photosynthetic pathway, have similar structure and phenology, and live under the same climate. Leaf area index (LAI) is a dimensionless quantity that characterizes plant canopies; it is defined as the one-sided green leaf area per unit ground surface area ($m^2.m^{-2}$). LAI is a prognostic variable of the model. The canopy is discretized, with LAI layers of increasing thickness from top to bottom. The photosynthesis is computed at leaf level following (Yin & Struik, 2009), using the classical Farquhar et al. (1980) model for C3 species and the (Collatz et al., 1992) model for C4 species. The quantity of absorbed CO_2 is then up-scaled at canopy level, summing over LAI layers, to compute GPP.

To be able to use SIF estimates to constrain GPP, the model needs to simulate SIF. Such an observation operator was implemented in (Bacour et al., 2019). The authors first developed a parametric model for the relative rate constant of NPQ ($kNPQ$), depending on temperature, photosynthetic active radiation and the relative light saturation of photosynthesis, as defined in (van der Tol et al., 2014). The fluorescence yield is computed at the leaf level, as a function of the photosynthetic yield and $kNPQ$, following the lake model (Kramer et al., 2004). The authors then used a parametric representation of the SCOPE (Soil Canopy Observation Photosynthesis Energy) model (van der Tol et al., 2009), to upscale at canopy level, and compute the SIF observed at nadir. (Bacour et al., 2019) then assimilated OCO-2 (Orbiting Carbon Observatory-2) SIF estimates to optimize parameters of the ORCHIDEE LSM related to the photosynthesis, fluorescence and phenology processes. They demonstrated that the posterior simulation was improved, when evaluated against global GPP reference products. However, the improvement was very variable, depending on the considered PFT. In Chapter 5, we will focus on boreal needleleaf evergreen forests, revisiting the NPQ model, and applying a new strategy for data assimilation. In Chapter 6, we will this time focus on improving the NPQ model in drought-stress conditions.

1.5.3 Specific NPQ mechanism observed in evergreen needleleaf species

It is now well established that evergreens of different genera, such as the Norway spruce (*Picea abies*), the Scots pine (*Pinus sylvestris*), the ponderosa pine (*Pinus ponderosa*), and the Douglas fir (*Pseudotsuga menziesii*), show seasonal fluctuations in their photosynthetic capacity, as reviewed in (Öquist & Huner, 2003) These fluctuations range from high photosynthetic efficiencies during the summer to low efficiencies in winter, when freezing temperatures may completely inhibit photosynthesis.

It has been shown in *Pinus sylvestris* that molecular modifications within the chloroplast induce an almost complete inhibition of photosynthesis during winter; these modifications induce the built up of a particular NPQ (Bag et al., 2020). Instead of being associated with a quenching process in the antenna, PSII and PSI approach each other, allowing a direct energy transfer in between PSII and PSI in the thylakoid membrane that induces a high NPQ level during winter. This type of NPQ is called sustained NPQ, and it is based on a spillover mechanism (Steffen Grebe, 2004). A model for representing sustained NPQ will be presented in Chapter 5.

1.5.4 ORCHIDAS

ORCHIDAS (ORCHIDEE Data Assimilation System; https://orchidas.lsce.ipsl.fr/, last access: 3 July 2023) is a software tool developed to optimize the parameters of the ORCHIDEE LSM through data assimilation techniques. ORCHIDAS allows for the assimilation of various data streams, such as remote sensing or *in situ* estimates. Parameters are optimized through the minimization of a cost function, and the tool offers several minimization algorithms such as a gradient-descent approach or a genetic algorithm (Bastrikov et al., 2018).

1.6 The different model species

During my thesis I focused on C3 plants, using model species from the two major groups of vascular seed plants: angiosperms and gymnosperms. For the angiosperms family, I used three plant models: *A. thaliana*, the sunflower and the poplar tree. *A. thaliana* was chosen because it presents several advantages, such as requiring little space and maintenance, having a short life cycle (4 weeks for developing large rosettes under a 16-hour illumination), being self-fertilizing, and producing numerous seeds. Additionally, *A. thaliana* is currently a valuable tool as its genome has been fully sequenced, and there is at least one mutant for each gene. Sunflower (*Helianthus annuus*) is used because it is a crop plant, unlike *A. thaliana,* and it is also adapted to higher temperatures. This can be interesting when studying the photosynthetic efficiency at high temperatures (see Chapter 4). Poplar has been selected as a model tree, because of its rapid growth for a tree, and the specific variety of poplar used in this study (Chapter 6) has also been fully sequenced (Tuskan et al., 2023).

For Gymnosperms, *Pinus sylvestris* has been used as a model due to its abundant presence in boreal evergreen needleleaf forests. This species has been extensively studied, and we have access to one year of continuous active fluorescence measurements (Porcar-Castell, 2011). Additionally, a unique non-photochemical quenching (NPQ) mechanism has been observed during the winter in Scots pine (Bag et al., 2020), which is of interest for modelling in the ORCHIDEE land surface model.

In this introduction we have described the key role of photosynthesis in mitigating climate change. However, due to this same climate change, plants are increasingly subjected to stress, particularly drought and heatwaves. We then examined the various protein complexes involved in the light reactions of photosynthesis, which permit conversion of light energy to chemical energy. Then, we discussed the significance of NPQ in protecting plants against oxidative stress and adapting photosynthesis levels to environmental conditions. To measure the levels of photosynthesis and NPQ, we employ fluorescence measurements. These measurements can be categorized into two main groups: active and passive. Passive measurements provide more limited information about plant physiology but offer a signal available at global scale. The global SIF estimates enable us to constrain the quantity of CO_2 absorbed by the continental vegetation, as simulated by the ORCHIDEE land surface model.

In the subsequent chapters, we will study the regulation of PSII and, more generally, photosynthesis under environmental stress conditions. We will begin with a molecular-scale investigation and gradually progress towards a global understanding.

2 Chapter 2: Study of a photoprotective mechanism under moderate drought: the effect of glycolate on PSII

2.1 Introduction of the scientific question: can glycolate play a role in drought conditions by slowing down the photosynthetic electron transport in between Q_a and Q_b?

Ribulose-1,5-bisphosphate carboxylase/oxidase RuBisCo (RuBisCo) is the key enzyme in the reduction of atmospheric CO_2 into organic carbon. One particularity of RuBisCo is that it can use both CO_2 and oxygen (O_2) as substrates. Its affinity for CO_2 is 40 % higher than that for O_2 (Van Lun et al., 2014). RuBisCo first evolved in an anoxic environment and did not need to discriminate between O_2 and CO_2. When it uses CO_2 as substrate, the reaction is called carboxylation, and in photosynthesis solar energy is transformed into chemical energy stored in sugars. In the second case when RuBisCo reacts with O_2 as substrate, the process is called oxygenation, which leads to the production of 2-phosphoglycolate (2PG), the first metabolite of the photorespiratory pathway. 2PG is a toxic compound (Flügel et al., 2017) (that is detoxified during photorespiration (PR)). This effect is limited in C4 plants, in which CO_2 is prefixed by the Phosphoenolpyruvate carboxylase and subsequently concentrated in the bundle sheath cell, increasinging RuBisCo's carboxylation activity. In C3 plants, PR becomes more important under stress conditions. The stomata close upon high temperatures or drought to limit transpiration. This leads to a decrease in the CO_2 concentration inside the mesophyll cells and the chloroplast, and an increased leaf temperature. In these conditions, oxygenation is promoted compared to carboxylation (Dusenge et al., 2019; Sage & Khoshravesh, 2016). This leads to an increase in 2PG production and PR activity to detoxify 2PG. **PR is mostly considered as a wasteful process, and identified as a target to be removed or decreased in crop improvement**. PR uses one ribulose-1,5-bisphosphate (RuBP) and consumes 3.5 ATP and 2 NADPH per O_2 and produces no additional organic carbon. In comparison, carboxylation consumes 3 ATP and 2 NADPH for one RuBP and produces sugar in hexose (Shi & Bloom, 2021).

Figure 2-1 from (Hodges et al., 2016) shows the main steps and subcellular localizations of the photorespiratory pathway, involving three organelles. Glycolate is produced inside the chloroplast and transported to the peroxisome through the plastidic glycolate/glycerate transporter PLGG1. This transporter exchanges one glycolate out of the chloroplast for one glycerate in the chloroplast (Pick et al., 2013). The glycolate conversion into glyoxylate produces H_2O_2 in the peroxisome. Recycling of carbon nitrogen occurs in the mitochondrion through the glycine decarboxylase (GDC) complex, producing CO_2 and NH_4^+. PR consumes ATP in the last step of glycerate conversion into 3-phosphoglycerate.

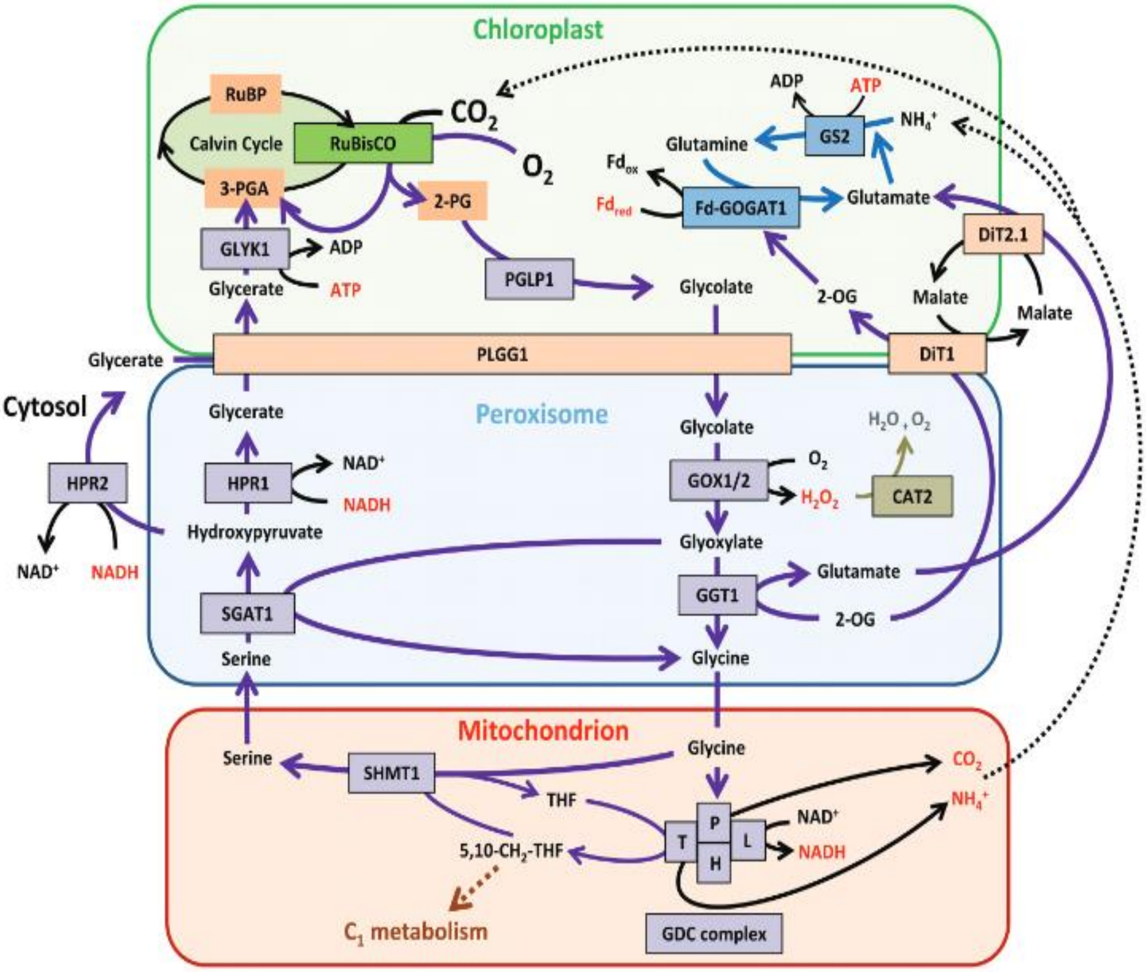

Figure 2-1: The photorespiratory cycle and its interaction with the Calvin cycle, ammonium assimilation, and C1 metabolism. Abbreviations: CAT2, catalase 2; DiT1, plastidial 2-OG/malate transporter 1; DiT2, plastidial glutamate-malate transporter 1; Fd-GOGAT1, ferredoxin-dependent glutamate synthase 1; GGT1, glutamate:glyoxylate aminotransferase 1; GDC complex, glycine decarboxylase complex (composed of the P, T, L, H proteins); GLYK1, glycerate kinase 1; GOX1/2, glycolate oxidase 1/2; GS2, plastidial glutamine synthetase; HPR1/2, hydroxypyruvate reductase 1/2; PGLP1, 2-PG phosphatase 1; PLGG1, plastidial glycolate/glycerate transporter 1; RuBisCO, RuBP carboxylase/oxygenase; RuBP, ribulose-1,5-bisphosphate; SGAT1, serine:glyoxylate aminotransferase 1; SHMT1, serine hydroxymethyl transferase 1; THF, tetrahydrofolate; 2-OG, 2-oxoglutarate; 2-PG, 2-phosphoglycolate; 3-PGA, 3-phosphoglycerate. Figure from (Hodges et al., 2016).

It is known that PR plays a critical role in nitrate assimilation (Rachmilevitch et al., 2004), for sulfate metabolism (Abadie & Tcherkez, 2019), and as an electron sink for the photosynthetic electron transport chain to reduce oxidative stress in excess of light (Eisenhut et al., 2017) or under drought, salinity, low CO_2 and chilling (Voss et al., 2013).

We hypothesized that glycolate can play a more specific role under stress conditions such as drought, by regulating the photosynthetic electron transport in between Q_a and Q_b.

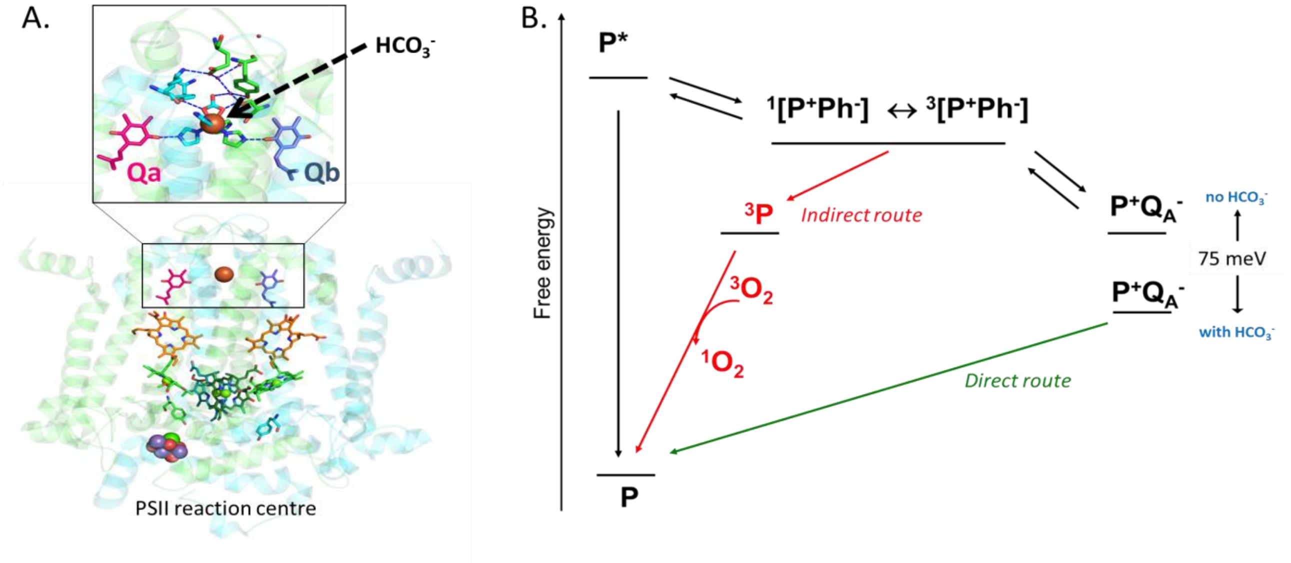

Figure 2-2: PSII reaction centre, bicarbonate (HCO3-) localisation and effect on PSII. Part A shows the HCO3- localisation on non-heme iron (red ball) in between Q_a and Q_b. B. Charge recombination pathways and singlet O_2 generation in PSII. Abbreviations: P, P680; P*, P680 excited; 3P, chlorophyll triplet state; Q_a, quinone A. Figure inspired by (Brinkert et al., 2016).

Brinkert and coworkers (Brinkert et al., 2016b) previously demonstrated in isolated PSII that bicarbonate depletion has the potential to protect PSII through the modulation of the midpoint potential of the primary quinone acceptor. **This led to the hypothesis that the replacement of bicarbonate with other small carboxylic acids, such as glycolate, in a location between quinone A and B (Q_a, Q_b)** presented in Figure 2-2A**, could also modify the midpoint potential of the redox couple Q_a/Q_a^-, thereby lowering the yield of $^1O_2$ generated by charge recombination reactions within PSII and potentially provide a protective effect on PSII**, as shown in Figure 2-2B.

(Messant et al., 2018) have characterized a photorespiratory mutant of Arabidopsis that over-accumulates glycolate, and they showed a slow down of the electron transfer between Q_a and Q_b. The alteration of the PSII acceptor side allowed the production of less singlet oxygen. **These results suggest that, during stress, PR is induced and produces glycolate which may replace bicarbonate at the non-heme iron at the acceptor side of PSII, thereby limiting the linear electron transfer chain and protecting plants from oxidative stress**. More broadly, this work supports the hypothesis of a protective role of PR through glycolate production and a rise of the glycolate concentration inside the chloroplast.

2.2 First publication: "Moderate drought stress stabilizes the primary quinone acceptor Q_a and the secondary quinone acceptor Q_b in photosystem II" (Leverne and Krieger-Liszkay, 2020).

Please refer to appendix in section 13.1 for access to this first publication.

To investigate if a slow down of the electron transfer can be observed in wild-type plants through PR during stress conditions, we used wild-type *A. thaliana* submitted to moderate drought stress by withholding water for 4-6 days. We performed measurements on intact leaves and determined PSII activity in drought and control conditions. Electron flow in between Q_a and Q_b was followed by measuring chlorophyll fluorescence induction and decay to determine electron transport to the plastoquinone pool. In addition, stabilization of Q_a/Q_a^- or destabilization of Q_b/Q_b^- upon drought stress was observed by thermoluminescence measurements. Immunoblots of proteins involved in alternative electron transport pathways were done to show whether drought conditions induced proteins that participate in cyclic electron flow. Indeed a higer amount of the NDH complex was observed, which isinvolved in one pathway of cyclic electron flow. **Taken together, the results of these experiences support the hypothesis of an alteration of Q_a Q_b electron transfer in PSII upon drought, and we suspect glycolate to be responsible for this effect.**

2.3 Subsequent work on the effect of glycolate on PSII

In the article Leverne & Krieger-Liszkay (2020), we highlighted that the electron transfer from Q_a to Q_b in PSII is slowed down in plants in drought conditions. We suspected glycolate to be at the origin of this effect. However, we did neither measure photorespiratory activity upon mild drought stress, nor studied the effect of glycolate on isolated PSII and potential protective effects of glycolate against photoinhibition. The following work addresses the effect of glycolate on PSII in more detail.

First, I investigated the effect of glycolate on the activity of isolated PSII. In the second part, I measured the midpoint potential of Q_a in the presence and absence of glycolate. In the third part, I studied the protective effect of glycolate against photoinhibition. Finally, I exposed leaves to different gas compositions to induce photorespiration and measured changes in the amount of photorespiratory metabolites.

2.3.1 Materials and Methods

2.3.1.1 PSII enriched membrane fraction

Spinach leaves were mixed in a solution of 0.4 M sorbitol, 10 mM NaCl, 5 mM $MgCl_2$, 20 mM HEPES, pH=7.5, buffer 1, to permit disruption of the cells. The supernatant was filtered through 4 layers of cheesecloth and centrifuged at 8000 rpm, 4°C, 10 min for thylakoid isolation. The pellet was resuspended using a brush with a 5 mM $MgCl_2$ solution, buffer 2, to stack the thylakoid membranes well and centrifuged at 7800 *g*, 4°C, 10 min. The pellet was further resuspended in a buffer 3, 5 mM NaCl, 5 mM $MgCl_2$, 25 mM MES, pH=6.5. Absorption was measured in 80% acetone by spectrophotometry and the chlorophyll content was calculated using the following equation (Porra & Scheer, 2019):

$$[\text{Chls a + b}]\ (\mu g/ml) = 17.76 \times \cdot A^{646.6} + 7.34 \times \cdot A^{663.6} \qquad \text{eq. (2-1)}$$

Then a given volume of buffer (15 mM NaCl, 5 mM $MgCl_2$, 25 mM MES, pH=6.5) was added to reach a concentration of 3 mg Chl.mL^{-1}. 33% of buffer 4 (buffer 3 with 100 mg.mL^{-1} triton X-100, pH=6.5) was added to the volume previously determined. The suspension was covered with foil and incubated in the dark in ice water for 30 min under very gentle agitation, then centrifuged at 1100 *g* for 5 min at 4°C to remove non-solubilised thylakoid membranes and starch. The supernatant was kept and centrifuged at 40,500 *g* for 20 min at 4°C. The pellet was resuspended in buffer 5 (0.3 M Sucrose, 10 mM NaCl, 25 mM MES, pH=6.5) and centrifuged at 40,000 *g* for 20 min at 4°C. This centrifugation step was repeated until the supernatant was pale green and chlorophyll concentration was measured again. PSII enriched membranes were conserved at -80°C until their use.

2.3.1.2 Measurement of oxygen evolution

Oxygen evolution of isolated PSII was measured using a Clark electrode (Hansatech Instruments Ltd, Norfolk United Kingdom) at 20°C and saturating light intensity (white light; 2,000 µmol.quanta $m^{-2}.s^{-1}$, using a halogen lamp; Osram XENOPHOT 15V 150W). Two buffers were used: for the first one we used 0.4 M sorbitol, 10 mM NaCl 5 mM $MgCl_2$, 20 mM HEPES , and for the second one 0.3 M sucrose, 10 mM NaCl, 5 mM $MgCl_2$, 20 mM MES. pH were adjusted to 7.5 and 6.5, respectively, adding saturated NaOH. PSII activity was measured in 1 ml of solution containing 20 µg.chlorophyll and 10 µM DCBQ used as the final electron acceptor.

In Figure 2-3, oxygen evolution has been normalised on maximum PSII activity measured in control conditions before inhibition, with no glycolate and no light incubation. We observed an activity of 208.64 and 271.36 oxygen µmol.mg.$Chl^{-1}.h^{-1}$ for the 6.5 and 7.5 pH buffers, respectively.

2.3.1.3 Titration of the midpoint potential of the redox couple Q_a/Q_a^-

Electrochemical redox titrations of Q_a in isolated PSII were performed at 15°C in an optically transparent quartz thin-layer (013511 SEC-C Thin Layer Quartz Glass Spectroelectrochemical cell Kit (Allum Corp)) with a SEC-C Gold (Allum Corp) gauze working electrode, and a SEC-C Pt counter electrode. The solutions were maintained under anaerobic conditions with an argon stream, cuvettes were closed and electrodes maintained by a teflon cap. The redox state of Q_a was monitored by measuring chlorophyll a fluorescence. Photosystem II was diluted to a [Chl] = 150 µg mL^{-1} in a buffer containing 50 mM MES-NaOH (pH 6.5), 0.2 M KCl, 0.1 % dodecyl-β-D-maltoside, 1 M glycine-betaine and 1% taurine.

A combination of redox mediators was added: 100 µM anthraquinone-2-sulfonate, 100 µM 2-hydroxy-1,4-naphthoquinone and 200 µM N,N,N',N'-tetramethyl- p-phenylenediamine. The sample was kept in the electrochemical cell in complete darkness. The fluorescence measurement was carried out with a PAM (pulse amplitude modulation) 101 Chlorophyll Fluorescence Measuring System (Heinz WALZ GmbH) using the measuring light at an intensity low enough not to reduce Q_a. The electrode potential was controlled by a potentiostat (CH Instruments CHI660D Electrochemical Workstation).

2.3.1.4 Metabolites measured in low and high photorespiratory conditions

To create specific gas compositions to induce or inhibit PR in plants, I increased or decreased each gas percentage compared to the control. The control gas composition is: 21 % oxygen and 400 ppm CO_2, the composition inducing PR is 40% oxygen and 400 ppm CO_2, or 21% oxygen and 100 ppm CO_2, and the composition inhibiting PR is 21% oxygen and 2000 ppm CO_2, or 2% oxygen and 400 ppm CO_2. Intact leaves of *A. thaliana* of the wild-type genotype Columbia 0, Col-0, grown in short days (8h light and 16h night) were exposed during 15 min to different gas compositions using a Licor-6400 gas-exchange system. Then a circular sample, centred on the leaf but not on the vein, with a diameter of 1 cm was exposed on the leaf and rapidly frozen in liquid nitrogen prior to the measurement of metabolites.

2.3.1.5 Plants growth conditions

Plants were grown in controlled-environment chambers (Percival; 10/14-h day/night cycle, 20°C/18°C, 120 µmol m^{-2} s^{-1} irradiance, 390 µL L^{-1} CO_2) on a 4:1 mixture of soil (Type Mini Tray; Einheitserdewerk) and vermiculite and regularly watered with 0.2% Wuxal liquid fertilizer (Aglukon).

2.3.1.6 Liquid chromatography–mass spectrometry (LC-MS) measurements

For LC-MS/MS analysis, leaf material was harvested from fully expanded rosette leaves of Col-0, at stage 3.90 as defined in (Boyes et al., 2001). Briefly, approximately 50 mg leaf-tissue was ground to a fine powder and extracted in 500 mL of ice-cold LC MS/MS buffer [150 mL chloroform, 350 mL methanol, 1 mL of MES as internal standard (1 mg/mL)]. Following addition of 400 mL ice-cold water, samples were vortexed thoroughly and incubated for at least 2 h at 220°C. After centrifugation (10 min, 20,000 *g*, 4°C), the aqueous phase was transferred to a new tube and 400 mL of ice-cold water again added to the ex-traction tube. Following stirring and centrifugation (5 min, 20,000 *g*, 4°C), supernatants were combined and lyophilized. Next, the dried extracts were dissolved in 400 mL water and filtrated through 0.2 mm filters (Omnifix-F, Braun, Germany). The cleared supernatants were analysed using the high performance liquid chromatograph mass spectrometer LCMS-8050 system (Shimadzu) and the incorporated LC-MS/MS method package for primary metabolites (version 2, Shimadzu). In brief, 1 mL of each extract was separated on a pentafluorophenylpropyl column (Supelco Discovery HS FS, 3 mm, 150 3 2.1 mm) with a mobile phase containing 0.1% (v/v) formic acid. The compounds were eluted at 0.25 mL min^{-1} using the following gradient: 1 min 0.1% (v/v) formic acid, 95% Aqua destillata (A. dest.), 5% acetonitrile, within 15 min linear gradient to 0.1% (v/v) formic acid, 5% A. dest., 95% acetonitrile, 10 min 0.1% (v/v) formic acid, 5% A. dest., 95% acetonitrile. The compounds were identified and quantified using the multiple reaction monitoring values given in the LC-MS/MS method package and the LabSolutions software package (Shimadzu). Authentic standard substances (Merck) at varying concentrations were used for calibration and peak areas normalized to signals of the internal standard. Glyoxylate and glycerate were determined in the negative ion mode using selective ion monitoring for m/z 73, and 105 corresponding to the deprotonated glyoxylate, and glycerate ions [M-H]-. Retention time acquisition window (2 min) was verified with coelution experiments using purchased glyxoylate and glycerate (Sigma Aldrich). Varying concentrations of the two metabolites were also used for calibration curves. Data were interpreted using the Lab solution software package (Shimadzu).

2.3.1.7 Fluorescence decay

Chlorophyll fluorescence was measured on leaves attached to the plants at room temperature using a Dual-PAM-100 (Walz). Fluorescence decay was measured after excitation with a saturating single turnover flash, with a sampling rate of 2.5 µs.

In this experiment, we used three *A. thaliana* genotypes: Col-0 and mutants with Col-0 background of genes PGLP (phosphoglycolate phosphatase) (Schwarte & Bauwe, 2007) and GOX (glycolate oxidaxe) (Dellero et al., 2016) (mutants respectively noted *pglp* and *gox*). We measured the fluorescence decay of the three genotypes immediately after removing them from the high CO_2

growth chamber (1000 ppm CO_2). Measurements were also taken after 15 minutes of adaptation to normal air. The measurements were repeated on at least four mature leaves per genotype. Then, for each condition and genotype, fluorescence decay was analysed by fitting with a second order exponential decay.

2.3.2 Results

2.3.2.1 Determination of the inhibitory glycolate concentration for PSII oxygen evolution in a buffer adapted either to the donor or to the acceptor side

To distinguish between effects of glycolate on the donor and acceptor sides of PSII, we first investigated the inhibitory effect of glycolate on PSII activity, by measuring the activity of isolated PSII, through oxygen production, with various glycolate concentrations.

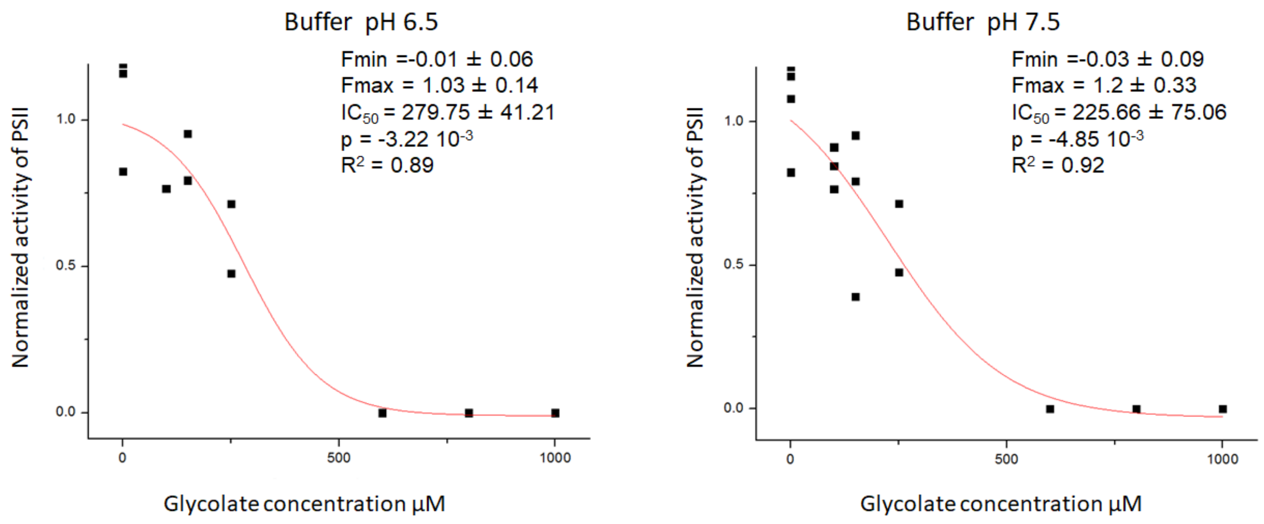

Figure 2-3: Activity of isolated PSII at pH 6.5 and 7.5, measured by oxygen production in the presence of 10 µM 1,5-DCBQ, normalized on maximum value, for increasing glycolate concentrations. Black squares represent measured values and the red curve is a sigmoidal fit described below with parameter values presented on the graph.

Figure 2-3 shows the inhibitory effect of glycolate on the activity of isolated PSII. We observed 50% of inhibition (IC50) around 250 µM glycolate at pH = 6.5, compared to 225 µM at pH = 7.5. Due to lack of data, the standard deviation errors of fitting parameters remain high and we cannot conclude on the significance of the difference in IC50 between pH 6.5 or 7.5.

I used a sigmoidal fitting with a Cheng-Prusoff equation to analyse the effect of glycolate concentrations as follows:

$$\text{Normalized activity} = \text{Fmin} + \frac{\text{Fmax} - \text{Fmin}}{1 + 10^{(\log[\text{Glycolate}]_0 - [\text{Glycolate}])\text{p}}} \qquad \text{eq. (2-2)}$$

An IC 50 value of 168 µM glycolate was first determined, without fitting against eq (2.2). However, due to the absence of data between 250 and 500 µM of glycolate concentrations, this previous IC50 estimation remains within the range authorized by the standard deviation range of the IC50 determined by the sigmoidal fitting: 225.66 ± 75.06 µM. The concentrations of glycolate used seem to be relatively high. However, considering the very small volume of the chloroplast stroma, it is still feasible to achieve such concentrations inside the chloroplast. To assess the impact of glycolate on the acceptor side, we selected the optimal pH for this side: pH 7.5 (Homann and Homann, 1988).

2.3.2.2 Redox titration of isolated PSII with glycolate

In this section, I will explain how to determine the midpoint potential of Q_a using chlorophyll fluorescence and electrical current.

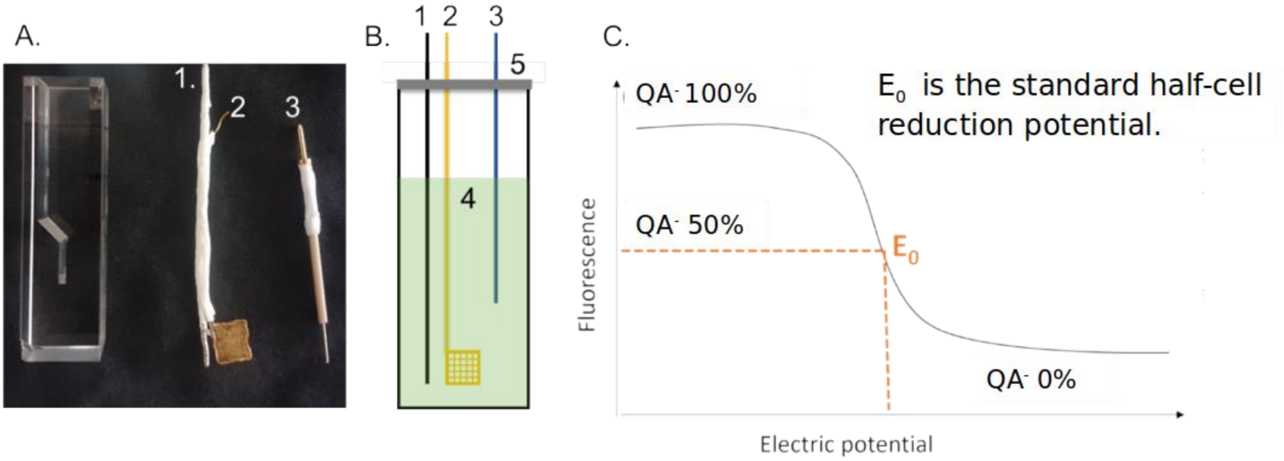

Figure 2-4: Redox titration setup: A) photography of the actual setup for PSII titration; B) schematic representation of the setup, with numbers corresponding to 1: counter electrode, platinum, 2: working electrode, gold, 3: reference electrode, silver, 4: buffer containing isolated PSII, 5: teflon cap; C) represents the Q_a redox states, as measured by fluorescence as a function of the electric potential.

In most cases in photosynthesis research, light-induced changes of chlorophyll *a* fluorescence are used to follow the reduction of Q_a in PSII (Baker, 2008). In case of redox titrations, we reduce Q_a not by light but chemically. We impose an increasing electric potential to PSII to reduce thereby Q_a as it was already performed in (Brinkert et al., 2016a). We can determine E_0, the midpoint potential of the redox couple Q_a/Q_a^- according to the Nernst equation:

$$E = E_0 + \frac{(RT/Far)}{n} \log \frac{[ox]}{[red]} \qquad \text{eq. (2-3)}$$

with E the redox potential of the ox./red. couple in volts, E_0 the standard potential of the ox./red. couple, R the constant of perfect gases, T the absolute temperature in kelvin, n the number of electrons transferred in the half-reaction, Far the Faraday constant, $[ox]$ and $[red]$ the chemical activity of the oxidant and reductant, respectively. We used the following equation for fitting:

$$\text{Fraction oxidized } (E) = Fmin + \frac{(Fmax - Fmin)}{1 + e^{-\left(\frac{Em - E_0}{KT}\right)}} \qquad \text{eq. (2-4)}$$

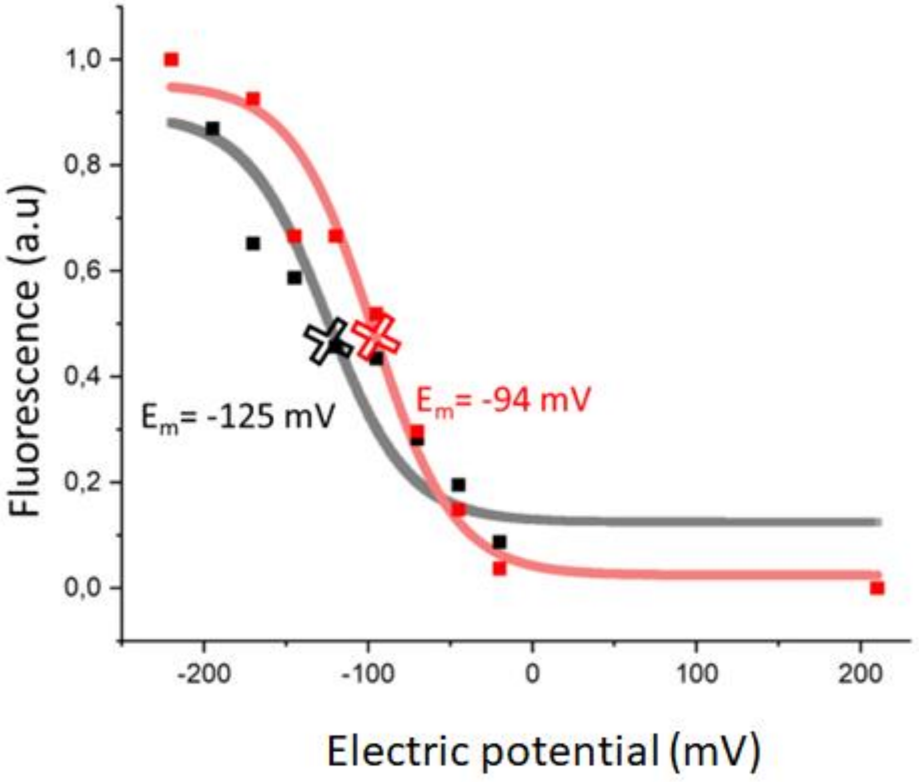

Figure 2-5: Redox titration of isolated PSII in control conditions (black squares/curve) and with a 168 µM glycolate concentration (red squares/curve). The midpoint potential (Em) is measured at pH 7.5.

Parameters	Control	With glycolate
E_m (Q_a/Q_a^-) (mV)	-125.07± 13.36	-94.16± 8.60
Fmax (a.u)	0.90± 0.08	0.93± 0.06
Fmin (a.u)	0.12 ± 0.06	0.02 ± 0.05
Adjusted R^2	0.89	0.95

Table 2-1: Parameter values and standard-deviation, for E_m, Fmin, Fmax, and determination coefficient of the Nernst fitting for PSII redox titration in control conditions (middle column) and in the presence of glycolate (last column).

In Figure 2-5 and Table 2-1, we see that the Nernst equation correctly fits our data with high R^2 for both conditions. E_m is more positive with glycolate compared to control, being -94.16 mV and -125.07 mV, respectively, which means that Q_a^- is more stable in the presence of glycolate. This shift to a more positive value of Em in the presence of glycolate is significant. This result supports the hypothesis that glycolate alters both the probability of charge recombination via the formation of the primary radical pair, thereby triplet chlorophyll and $^1O_2$, and the electron transfer between Q_a and Q_b in PSII. In (Brinkert et al., 2016a), authors find an analogue result by exchanging bicarbonate with formate in isolated PSII, inducing a shift of E_m values to −95 mV. In (Sedoud et al., 2011), authors also replaced bicarbonate by formate and observed the formation of the $Q_a^{\bullet -}Fe^{2+}Q_bH_2$ complex inhibiting PSII activity.

2.3.2.3 Potential role of glycolate in protection against photoinhibition

Next, I studied if glycolate plays a protective role on PSII. I measured isolated PSII activity by following oxygen production, using a light intensity of 350 µmol.m^{-2}.s^{-1} and DCBQ as the final electron acceptor.

To mimic stress conditions, I induced ROS production by exposing isolated PSII to a high light of 500 µmol.m^{-2}.s^{-1}; during the exposition there is no final acceptor of electrons in the solution of extracted PSII, and electron transfer induces ROS production. I chose 500 µmol.m^{-2}.s^{-1} as a light intensity to avoid a too strong oxidative stress. To quantify the glycolate effect, I measured the oxygen production by PSII with and without glycolate at increasing incubation times in the photoinhibiting light, from 0 to 40 min. PSII were incubated with or without 254 µM glycolate (at pH 6.5) during the photoinhibition treatment. To compare the data, I normalized all observations to the value of oxygen production obtained for the same time of incubation in the dark.

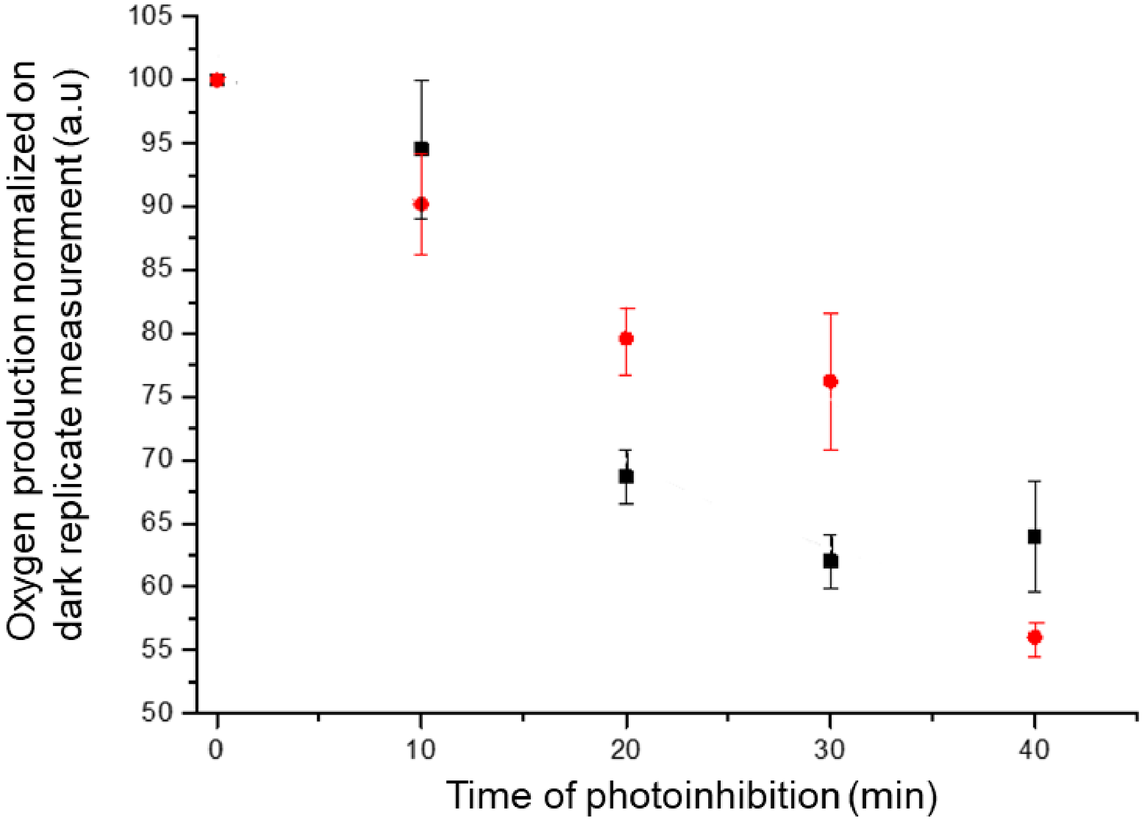

Figure 2-6: Photoinhibition effect on PSII activity without (black) or with the glycolate treatment (red), normalised with the oxygen production with no photoinhibition (axis y 100% = oxygen production of 65.2 µmol.mg.Chl.h^{-1}); DCBQ 1 mM as final electron acceptor for each condition.

Figure 2-6 shows a significantly higher activity for PSII with glycolate compared to the control experiment without glycolate for durations of the photoinhibition treatment of 20 and 30 min. However, the effect was no longer observed after a longer incubation time. For 40 min, the control sample shows a higher activity than the glycolate sample. One has to keep in mind that glycolate itself inhibits PSII activity (Figure 2-3). At such a long incubation time, the inhibitory effect of glycolate on the donor side of PSII seems to overrun its protective effect at the acceptor side. Looking at time durations of 20 and 30 min, **the results may support the hypothesis that glycolate can play a protective role against ROS production occurring during stress conditions**.

2.3.2.4 Measurement of PR metabolites

Next, I wanted to know if we could measure glycolate accumulation in chloroplasts in photorespiratory conditions to support the idea that it is glycolate which directly interacts with PSII in chloroplasts. Unfortunately, I did not succeed in extracting chloroplasts in a fast enough way to conserve metabolites, and I thus switched to working at leaf level. I measured metabolites of photorespiration (PR) and of the Calvin-Benson cycle on total leaf extracts, after 15 minutes exposure to different gas conditions that induce or suppress PR. To modify the activity ratio of photosynthesis and PR we can play on oxygen or CO_2 concentrations as it is explained in the method section 2.3.1.4.

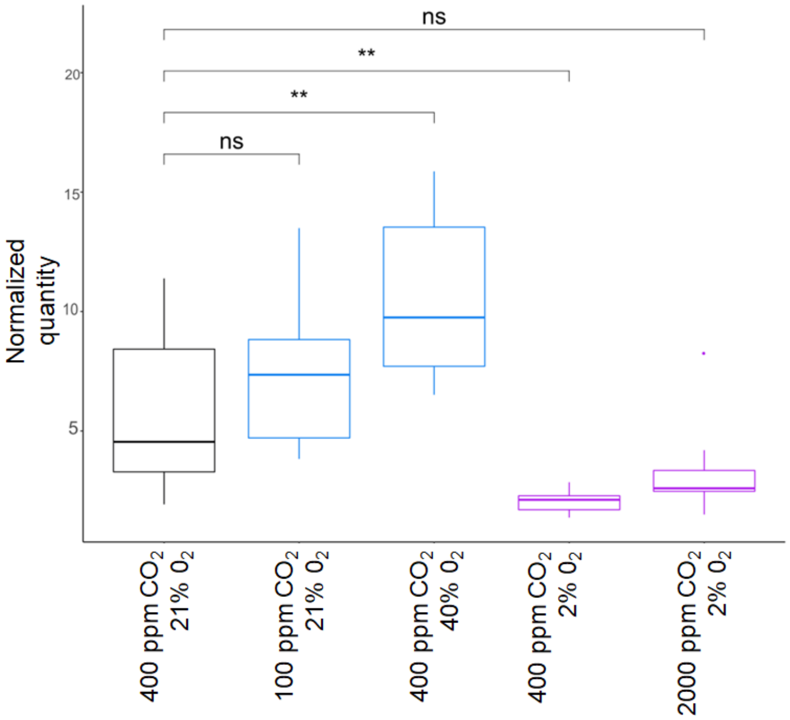

Figure 2-7: Glycine content, normalized by chlorophyll content, of total leaf extracts submitted to 15 min of different gas conditions that induce or suppress photorespiration; n=8 leaves for each gas condition.

Figure 2-7 focuses on the change in glycine content between the different gas mixture treatments. We used two different gas mixtures for both induction and inhibition of PR. For glycine, a significant change occurred only when we changed the oxygen concentration in the gas mixture. The glycine content decreased when O_2 increased and vice versa. These results support the idea that photorespiratory metabolites accumulate in leaves rapidly, in 15 min or less.

In Figure 2-8, I present the results for the three types of gas composition (control in black, inducing PR in blue or inhibiting PR in purple) and for various metabolites (one per sub-plot). Stars identify gas composition types that exhibit a significantly different content of a given metabolite as compared to control conditions.

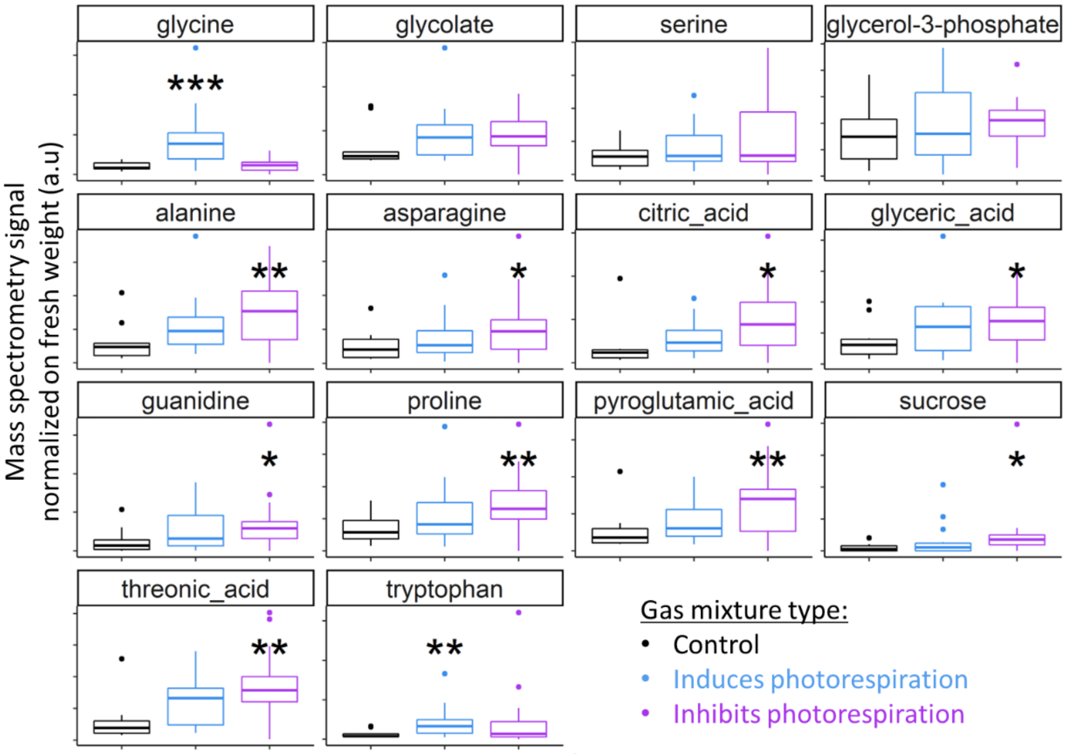

Figure 2-8: Metabolite quantity normalized by leaf fresh weight measured by mass spectrometry, for *A. thaliana* mature leaves exposed to a gas mixture during 15 min that induces, in blue, or decreases, in purple, photorespiration. Black is for the control gas mix. n=8 for control and n=16 leaves for special conditions; distributions are represented through boxplots; stars are shown when the mean value is significantly different from the one of the control case (*: p-value<=0.1, **: p-value<=0.05). Each subplot represents a specific metabolite.

Among the four metabolites involved in **PR**, three of them: glycerol-3-phosphate, glycolate and serine, have no significant modifications of content in the various specific gas conditions. However, the fourth one, glycine, is significantly induced in conditions favouring photorespiration. Glycine synthesis in the peroxisome occurs downstream of glycolate during photorespiration (Figure 2-1). Hence, variations, be it an increase or decrease, in glycine concentration can potentially indicate a corresponding variation in glycolate concentration within the chloroplast.

When we induce more **carboxylation**, we observe the rise of various metabolites that can play different roles. Asparagine is known for his role in nitrogen assimilation, recycling, transport and storage in plants (Sieciechowicz et al., 1989). There are also metabolites involved in abiotic stress response: alanine (Parthasarathy et al., 2019), citric acid (Tahjib-Ul-Arif et al., 2021), proline (Marsden et al., 2015), pyroglutamic acid (Jiménez-Arias et al., 2019) and sucrose (Shulaev et al., 2008). The glyceric acid (Khan et al., 2019; Radwanski & Last', 1995) plays a role in the regulatory pathway of plant growth. Tryptophan is also known to be involved in plant growth regulation (Radwanski & Last', 1995) but, contrary to the glyceric acid, it is induced in photorespiratory conditions.

We also observed a significant increase for both gas composition types for isoleucine, leucine, malic acid, myo-inositol, ornithine, phenylalanine, rhamnose, threonine, tyrosine and valine. It is difficult to determine the role of these metabolites in these conditions due to their non-specific response.

We also measured metabolites, not presented on this graph, with no significant modifications of concentration for both gas composition types: 2oxo-glutaric-acide, aspartic acid, fructose, fumaric acid, galactinol, glucose, glutamine, glycerol, glycerol 3 phosphate, glycolic acid, hydroxylamine, putrescine, pyruvic acid, raffinose, succinic acid, and urea.

The results indicate that, under photorespiratory conditions, there is a significant alteration in the glycine concentration within the entire leaf. This observation potentially suggests an increase in glycolate levels within the chloroplast. However, we still need measurements of the glycolate content in isolated chloroplasts, in order to better understand the potential protective role of glycolate for PSII in photorespiratory conditions induced by abiotic stress. To confirm this protective role of glycolate for PSII in vivo, we measured the PSII activity in a mutated plant line over-accumulating glycolate, as presented in the following section.

2.3.2.5 Effect of glycolate tested on mutated lines of A. thaliana

In order to quantify the potential effect of glycolate on electron transfer between Q_a, Q_b, and the plastoquinone pool, we measured fluorescence decay, which allows us to quantify the rate of PQH_2 reoxidation. We used *A. thaliana* photorespiratory mutants for the glycolate oxidase (GOX) and photorespiratory 2-phosphoglycolate phosphatase (PGLP) genes. These mutants over-accumulate glycolate (Dellero et al., 2016; Flügel et al., 2017) and require growth in an elevated CO_2 chamber (1000 ppm CO_2) to survive.

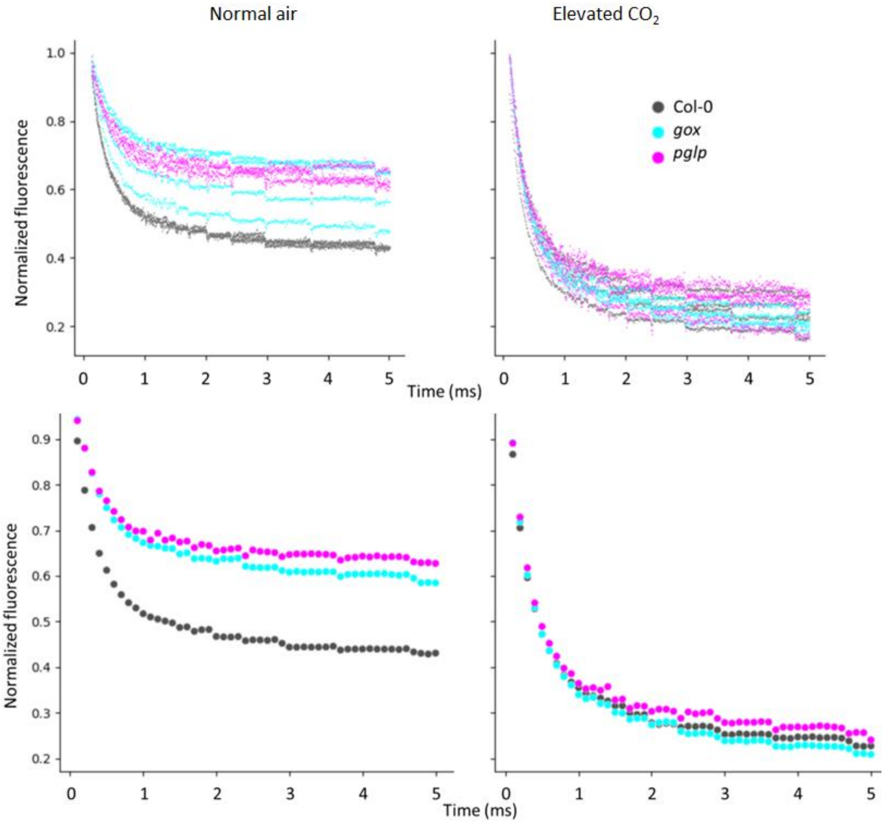

Figure 2-9: Normalised signal of fluorescence decay in different PR mutants and air conditions. The top row presents fluorescence measurements over four replicates, the bottom row shows means for each genotype. The left column is for a 15-minute normal air adaptation, and the right column is for the measurements performed directly when plants were extracted from the elevated CO_2 growth chamber. The colour code for Col-0, *gox* and *pglp* genotypes is black, cyan and magenta, respectively.

The top row of Figure 2-9 shows results of experiments that we replicated at least four times, plus we repeated these measurements on at least four mature leaves per genotype. On the bottom row of Figure 2-9, we see the mean for each genotype in the two air conditions. We observed a faster decay for the Col-0 genotype in normal air conditions, compared to the mutant plants. In elevated CO_2 conditions, nearly the same decay is observed for all genotypes, but faster than Col-0 in normal air conditions. Then, for each condition and genotype, the fluorescence decay was analysed by fitting the measurements with a second order exponential decay, expressed as follows:

$$\mathrm{y} = \mathrm{A1} \times \exp^{\frac{-\mathrm{x}}{\mathrm{t1}}} + \mathrm{A2} \times \exp^{\frac{-\mathrm{x}}{\mathrm{t2}}} + \mathrm{y0} \qquad \text{eq. (2-5)}$$

Higher values of $\mathrm{t1}$ and $\mathrm{t2}$ indicate a slower decrease in the y function.

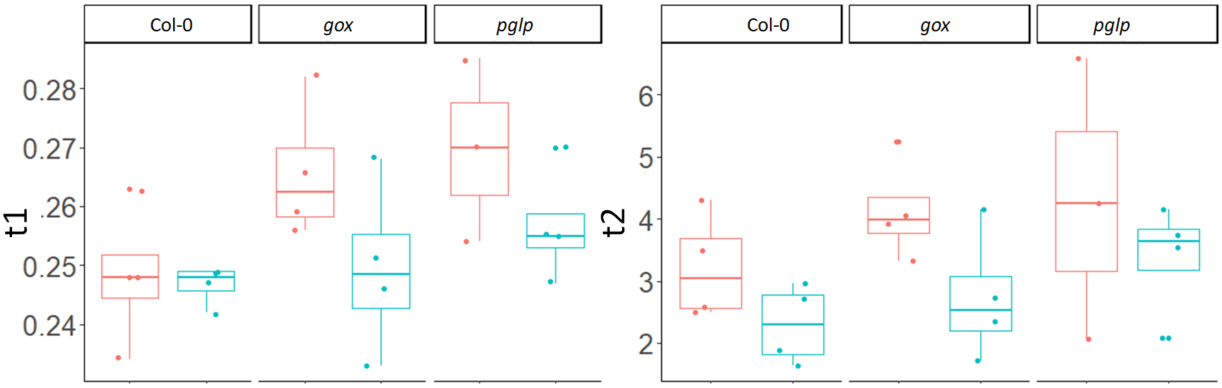

Figure 2-10: Comparison of $\mathrm{t1}$ and $\mathrm{t2}$ fitting parameters for the different air compositions and genotypes. In pink, measurements are performed after 15 min under normal air conditions, and in blue, directly when plants are extracted from the elevated CO_2 growth chamber.

In Figure 2-10, we present the values of parameters $\mathrm{t1}$ and $\mathrm{t2}$. Although the differences are not significant, there is a trend of increasing $\mathrm{t1}$ for the mutants or under high CO_2 conditions.

Under high CO_2 concentration conditions, photorespiration is inhibited , but in normal air conditions PR mutants, *gox* and *pglp*, over-accumulated glycolate. The fluorescence decay measures the re-oxidation kinetics of PQH_2, Q_b^-, Q_a-. There is no significant difference in between wild-type plants and mutants for each condition, but there are some trends.

For all genotypes, we observed higher $\mathrm{t1}$ and $\mathrm{t2}$ values under normal conditions indicating a slower decay compared to high CO_2 conditions (Figure 2-10). This reflects a slower re-oxidation of Q_a- due to a slower electron flow in between Q_a, Q_b and PQ. This is likely due to the presence of glycolate, which is produced during photorespiration under normal air conditions. The effect is even more pronounced in the glycolate over-accumulating mutants, *pglp* and *gox*.

These results support the idea that the accumulation of glycolate induced by photorespiration leads to a decrease in the electron transport rate between Q_a, Q_b, and PQ.

2.4 Discussion

A main limitation of the results on the glycolate effect on isolated PSII is that we need to choose one value of pH for measurements. In chloroplasts, the PSII is located inside the thylakoid membrane, in the presence of a proton gradient between the donor and acceptor sides of PSII. The donor side is localized on the lumen side. Here, the water splitting occurs and produces oxygen and protons, preferentially at low pH (lower than 7). As has been shown in Homann (1988), the donor side activity is controlled by two ions with antagonist effects: the chloride (Cl^-) and calcium ions (Ca^{2+}). Both ions are obligatory cofactors for the water-splitting activity at the PSII donor side. At low pH, the Cl^- is favourably binding on PSII while Ca^{2+} is released; at higher pH (higher than 7), PSII is depleted of Cl^- . Therefore, water-splitting activity is optimal only at a slightly acidic pH and a too low or too alkaline pH induces a decline of the activity at the PSII donor side. Despite this complicated pH dependency at the PSII donor side, **the results obtained on isolated PSII treated with glycolate and incubated in high light support the hypothesis of its protective role through inhibition of PSII activity**.

In bicarbonate-depleted PSII, the E_m (Q_a/Q_a^-) was shifted by 75 mV towards a more positive value, while in the presence of formate it was shifted only by 50 mV (Brinkert et al., 2016a).

(Messant et al., 2018) also showed a probable protection of PSII by glycolate, by measuring less singlet oxygen in a glycolate over-accumulating mutant of *A. thaliana.* I also saw the same effect as (Messant et al., 2018) on the electron transfer at the PSII acceptor side using glycolate over-accumulating mutants (Figure 2-9), for which the electron flux in between Q_a and Q_b of PSII is slower.

Our results are coherent with these previous findings (Brinkert et al., 2016a; Messant et al., 2018), and we suspected a replacement of bicarbonate with glycolate to permit the PSII protection (see Figure 2-6). Under photorespiratory conditions, an increase in glycine concentration is observed (Figure 2-7), which could be linked to an increase in glycolate concentration in the chloroplast. This supports the hypothesis that the protection of PSII under photorespiration conditions is permitted through an elevation of glycolate concentration at the chloroplast level.

More generally, photorespiration is less and less considered as a wasteful process. In this work we showed its potential importance to protect PSII in drought conditions. It is also known that PR has a role in other abiotic stress conditions, such as salinity, chilling, and low CO_2 (Voss et al., 2013).

PR may have a negative impact on plant growth since we can enhance productivity by short-circuiting PR as in (Cavanagh et al., 2022; South et al., 2019). In these two papers PR is not totally removed but modified. Export of glycolate to peroxisome is downregulated, and a new pathway is introduced to directly metabolise glycolate in the chloroplast. It will be interesting to explore the glycolate homeostasis of this plant, to determine if the chloroplastic glycolate content changes and if it affects the redox potential of Q_a and its potential protective effect on PSII in stress conditions. PR modification and the productivity gain is impressive, but it needs to be considered in various extreme conditions like is expected with climate change. **Crop improvement cannot be focused only on productivity but needs a fine balance in between yield and stress resistance to ensure food security in our actual and future climate conditions**.

In the upcoming chapter, we will examine the response of photosynthesis at a broader scale than the regulation of photosystem II. We will study *A. thaliana* mutant plants disrupted in one specific

NPQ type (state transition). We will investigate its potential role in the overall plant response to water stress.

3 Chapter 3: Why are *A. thaliana* qT mutants less sensitive to drought stress?

3.1 Key points of Leverne et al. (2023), and implications

In the following study, we observed mutants of *A.thaliana,* altered in their NPQ regulation, in drought stress conditions. We studied different mutants affected in different genes, which led to the same phenotype. The *stn7* mutant that has been characterized for a long time, and *nsi1* and *nsi2* mutants, which were more recently discovered, are characterized by the absence of qT. qT is the NPQ mechanism in which some proteins of the chlorophyll antennas (LCHII) migrate between PSII and PSI in the linear electron chain. Due to the absence of phosphorylation in *stn7* and acetylation in *nsi*, the antennas always remain on PSII. This induces a modification of the redox state of the plastoquinone pool. Surprisingly, these mutants exhibited a root development faster than the wild type, conferring them a greater tolerance to drought through an easier access to soil moisture, whereas they were not altered in genes directly involved in root regulation. We hypothesized that the redox state of the plastoquinone pool can play a role in root development thought signalling from leaf to root. However, we could not identify the signalling pathway allowing this communication, even if we suspected the role of carotenoid products oxidized by ROS, such as β-cyclocitral.

We thus have uncovered a potential new pathway for regulating root development, that could render plants more tolerant to drought. This finding could have implications in the context of food security, where crop types may be modified to mitigate the effects of climate change.

3.2 Personal contribution to the study

In this research article, I discussed the strategy with my supervisors, performed all experiments and data analyses (related to the relative water content, the stomata opening, chlorophyll fluorescence at room temperature, 77K chlorophyll fluorescence, spin-trapping electron paramagnetic resonance (EPR) spectroscopy, and pigment analyses), produced all figures and contributed to the writing of the manuscript.

3.3 Second publication: ”Increased drought resistance in state transition mutants is linked to modified plastoquinone pool redox state” (Leverne et al., under review)

Please refer to appendix in section 13.2 for access to this second publication.

After studying the effect of drought, we will address another abiotic stress also becoming increasingly important with climate change: heat stress. The next chapter will focus on the stress induced by high temperatures in two C3 model plants, *A. thaliana* and the sunflower, *Helianthus annuus*.

4 Chapter 4: The effect of high temperatures on photosynthesis in two C3 plant models

4.1 Introduction

In this chapter, we will focus on the effect of high temperatures associated with climate change (CC) on photosynthesis. CC comprises a warmer global climate, (Gulev et al., 2021) assessed an increase of the mean global surface temperature of 0.85°C from 1880 to 2012, associated with more extreme events, including heatwaves (Chapter 2 of the IPCC AR6 of Working Group I, (Intergovernmental Panel on Climate Change, 2023). Plants are drastically impacted by these changes, photosynthesis being very sensitive to temperature for carboxylation and the quantum efficiency of light, as reviewed in (Zhao et al., 2020). Plants also suffer from several inhibitions of physiological responses such as transpiration, and membrane thermostability (Zhao et al., 2020).

In this chapter, we will focus on the impacts of heat stress on the quantum efficiencies of PSI and PSII, and discuss which photosystem causes the major limitation. I performed experiments on *A. thaliana* as it is a plant model for angiosperms, and also on sunflower as this is a crop, growing from June to August, being particularly subject to heatwaves. I measured the various quantum yields (including for photosynthesis and heat dissipation) of PSII and PSI by chlorophyll fluorescence and P700 absorbance on both plants. I followed the efficiency of PSII and PSI in parallel for ranges of temperature and light from 15 to 40°C and 0 to 1000 µmol.m^{-2}.s^{-1}, respectively. I used sunflowers of different ages from 2 to 5 weeks to specifically look at the ageing effect on the plant response, and I will mainly focus my analysis on how the high temperature effect varies with the age of sunflower.

4.2 Material and Methods

4.2.1 Plant material and measurements conditions

Sunflowers (*Helianthus annuus),* variety soleil Géante simple jaune VILMORIN, were grown for different durations at different periods, as presented in Table 4-1. The plants were situated on the roof of a building at the Paris-Saclay CEA centre. None of the plants had yet flowered. The medians of air temperature were calculated using measurements from the ICOS Saclay site (https://meta.icos-cp.eu/resources/stations/AS_SAC, last access: 3 July 2023) during each growth period from 6 AM to 10 PM.

Table 4-1: Growth period and air temperature, and age of each sunflower culture batch.

Plant age (days)	Growth period (day/month/year)	Median of air temperature during the day (°C)
14	01/09/2022 to 14/09/2022	19.02
21	01/09/2022 to 21/09/2022	17.07
28	25/06/2021 to 23/07/2022	17.34
35	15/08/2021 to 20/09/2021	18.28

I selected fully mature leaves, using the second one from the top of each plant. During sunflower growth, new leaves emerge at the top of the plant, resulting in the upper leaves being younger than the lower leaves. To avoid measuring the effects of the ageing of only one leaf, and instead monitor the effects of overall plant senescence, we consistently measured leaves at the same level within the plant. Additionally, there is heterogeneity in the photosynthetic response of the leaf, which is why we always measured at the same position on the leaf.

For *A. thaliana*, plants were grown in a chamber at 20°C, in long days (16h of light, 8h of dark) with a light intensity of 100 $\mu mol.m^{-2}.s^{-1}$ during 4 weeks. Fully mature rosette leaves were selected and measured in the middle of the leaf near, but not on, the midrib.

The same procedure of measurement was used for Col-0 (wild type) *A. thaliana* and sunflower: plants were adapted 3 min in the dark, then illuminated during 3 min at each light intensity before measuring quantum efficiencies. The same leaves were used for each temperature used in the given experiment.

4.2.2 Principle of P700 measurements

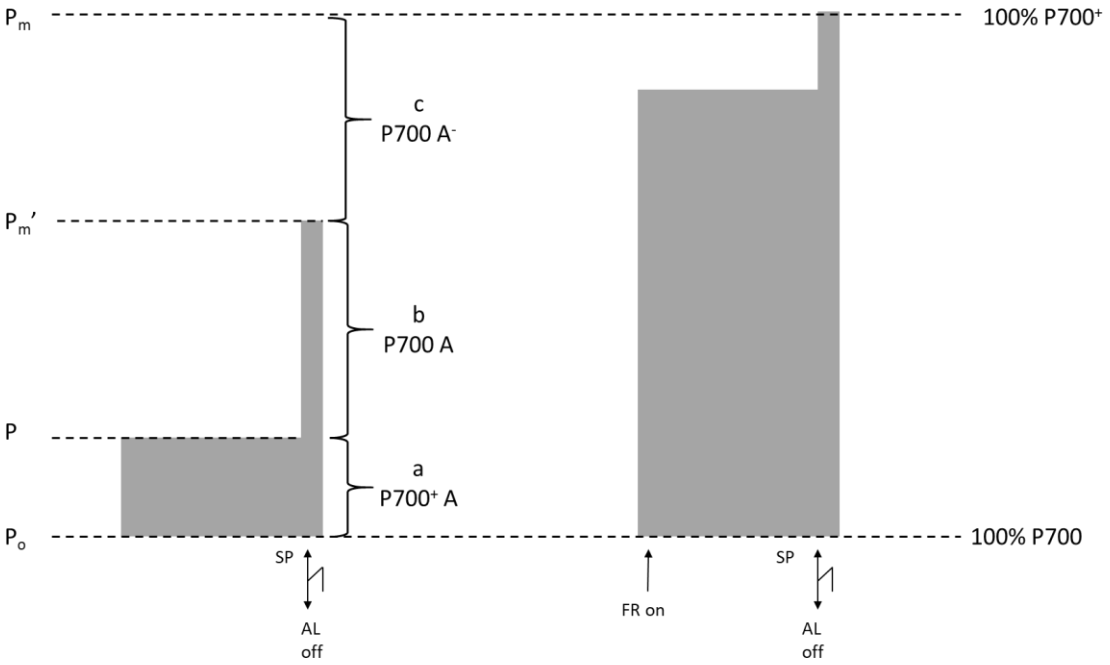

Figure 4-1: Principle of the Saturation Pulse method for the determination of the efficiency of energy conversion in PSI. P700 is measured in the dual-wavelength mode (difference of intensities between 875 nm and 830 nm of the pulse-modulated measuring light reaching the detector). P700 oxidation is characterized by a positive signal change. Complete P700 oxidation is induced by a Saturation Pulse (SP) in the presence of Far-Red (FR) light, with the maximal P700 signal denoted by Pm. Complete reduction is induced after the SP and cessation of FR-illumination, with the zero P700 signal denoted by Po. In the presence of Actinic Light (AL) a fraction ‘a’ (donor-side limited closed centres $P700^+A$) is oxidized by the AL resulting in an intermediate P700 signal denoted by P. In this state the SP-induced signal change corresponds to the oxidation of the active fraction ‘b’ (open centres, P700 A), with the maximal P700 signal being denoted by Pm'. The fraction ‘c’ (acceptor-side limited closed centres, P700 A^-) that cannot be oxidized, corresponds to the difference between Pm and Pm'. Inspired by Klughammer & Schreiber PAM Application Notes (2008, source: https://www.walz.com/files/downloads/pan/PAN07002.pdf, last access: 11 July 2023).

The experiment presented in Figure 4-1 allowed us to calculate the photosynthetic yield of PSI: Y(I), the quantum yield of non-photochemical energy dissipation due to the donor-side limitation: Y(ND), or to the acceptor-side limitation: Y(NA). Figure 4-1 shows how we measured the various fluorescence levels and determined the fractions a, b, c defined as:

$$Y(I) = b/(a+b+c) \quad \text{eq. (4-1)}$$

$$Y(ND) = a/(a+b+c) \quad \text{eq. (4-2)}$$

$$Y(NA) = c/(a+b+c) \quad \text{eq. (4-3)}$$

Y(I) is the fraction of overall P700 that for a given light is reduced and not limited by the acceptor side. Y(ND) corresponds to the fraction of the overall P700 that is oxidized for a given light, and Y(NA) corresponds to the fraction of the overall P700 that cannot be oxidized by a saturating flash.

4.3 Results: Effect of light, heat, and ageing on photosynthetic parameters

4.3.1 For PSII

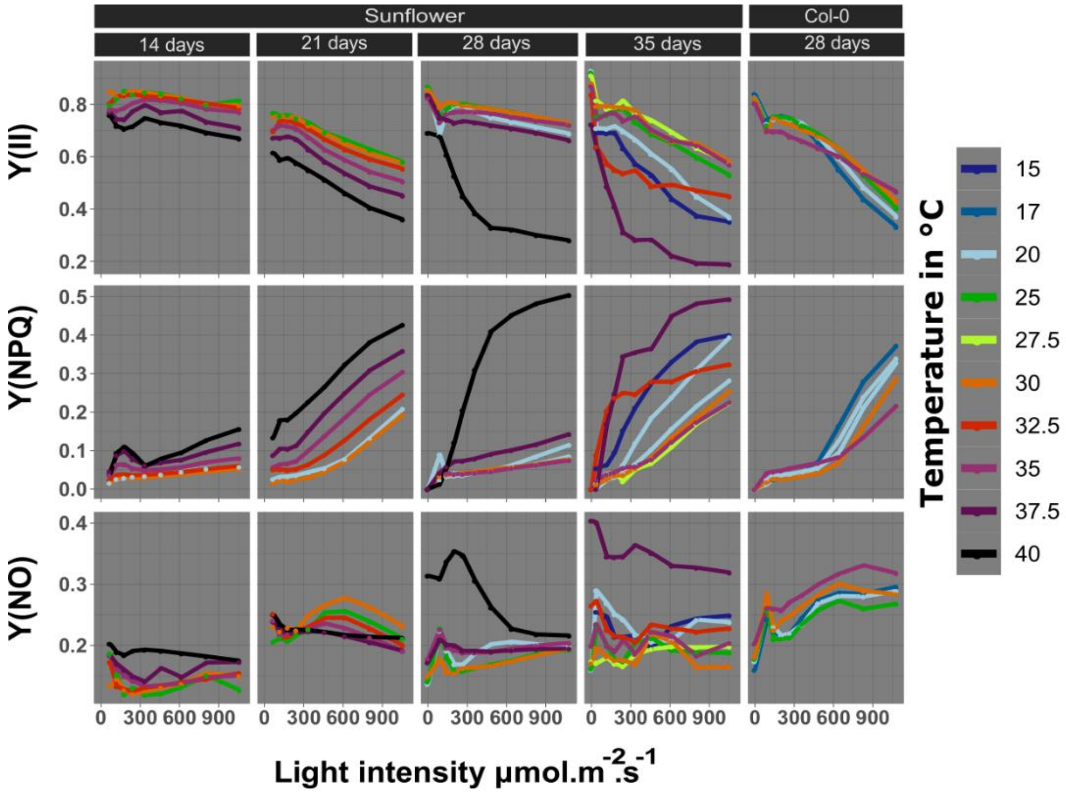

Figure 4-2: Quantum efficiencies of PSII (Y(II)), NPQ (Y(NPQ)) and non-regulated energy dissipation (Y(NO)) for sunflowers *Helianthus annuus* of various ages, and for the *A. thaliana* Columbia-0 ecotype (Col-0). Each coloured curve represents a different temperature.

Figure 4-2 presents the effects of temperature and ageing on yields estimated with chlorophyll fluorescence measurements, for sunflower and *A. thaliana* Col-0. We show here 3 parameters classically measured: the yield of photosystem II Y(PSII), the yield of regulated and basal energy dissipation through heat, Y(NPQ) and Y(NO), respectively, The details for the calculations are provided in 1.4.1.1.

4.3.1.1 Sunflowers

For all measured ages, Y(II) decreases with the increase of the light intensity and of the temperature used for the measurement, as seen on Figure 4-2. This decrease is even more significant as the plant gets older. The effect of elevated temperature on 35-day old plants is the most pronounced.

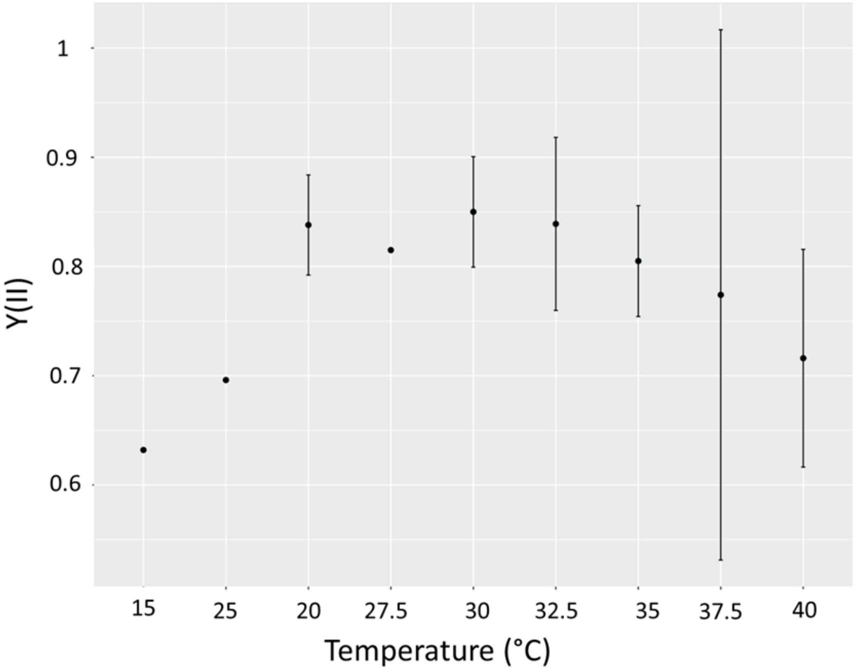

Figure 4-3: PSII yield of sunflowers *Helianthus annuus*, for different temperatures and a light of 240 µmol.m^{-2}.s^{-1}. For each temperature, the dot represents the mean over the leaf ages, and the error bar represents the standard deviation, n=3.

In Figure 4-3, our focus is on the measurement of Y(II) using a light intensity equivalent to the one used during the growth period, specifically at an intensity of 240 µmol.m^{-2}.s^{-1}. This allows us to capture the quantum yield equivalent to that present during the growth period. Furthermore, the differences between the temperatures are more pronounced at this specific light intensity level.

We observe that the Y(II) increases with the increase of the temperature between 15 and 30°C, and we measure the maximum of the photosynthetic capacity at 30 °C, which can be considered as the optimal temperature for PSII activity for sunflower grown in summer. Then, if we increase the temperature above 30°C, the PSII yield decreases. After reaching a temperature of 35°C, we observe a high standard deviation due to the increased sensitivity of older plants to high temperatures.

In Figure 4-2, we observe an abrupt fall of Y(II) at 40°C, even for weak light intensities. Comparing Y(II) and Y(NPQ), we see that the two curves are relatively symmetrical, the energy that is not used by photosystem II is dissipated as heat. The variations of Y(NO) generally remain weak with the temperature increase in comparison with the variations of Y(II) and Y(NPQ), and are difficult to link to physiological effects. At 37.5°C and above, we however observe a different behaviour of Y(NO) with a brutal increase. It is interesting to note that this increase of Y(NO) is mainly observed for the 28 and 35-day old sunflowers. In summary, the optimal temperature for sunflower photosynthesis is around 30°C. Temperature variations have an even stronger effect on older leaves, especially above 37.5°C, where we observed a drastic increase of Y(NO) and decrease of Y(II).

4.3.1.2 A. thaliana

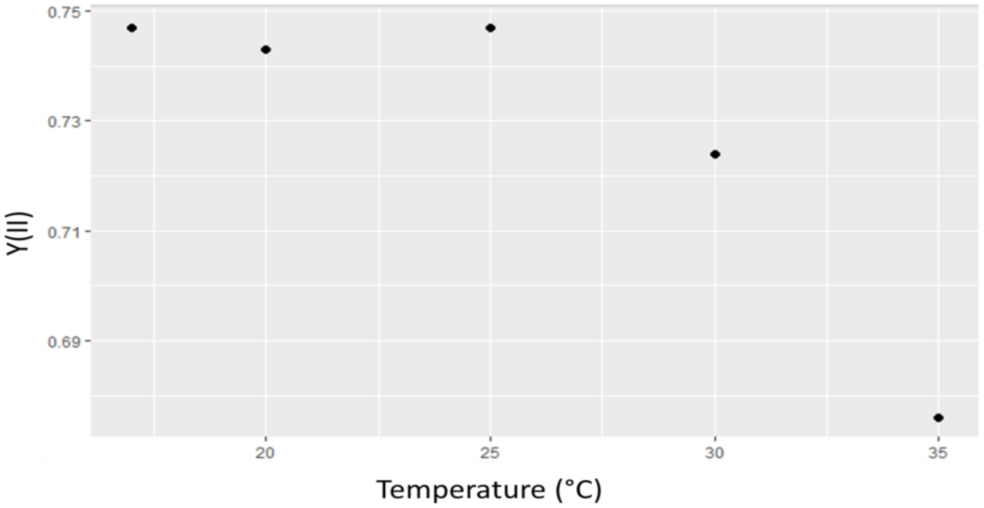

Figure 4-4: PSII yield of *A. thaliana* Col-0, 28-day old, for a light of 260 µmol .m^{-2}.s^{-1}

We observe a lower optimum temperature at 25°C in Figure 4-4, as compared to sunflowers.

4.3.2 Sunflower PSI yields

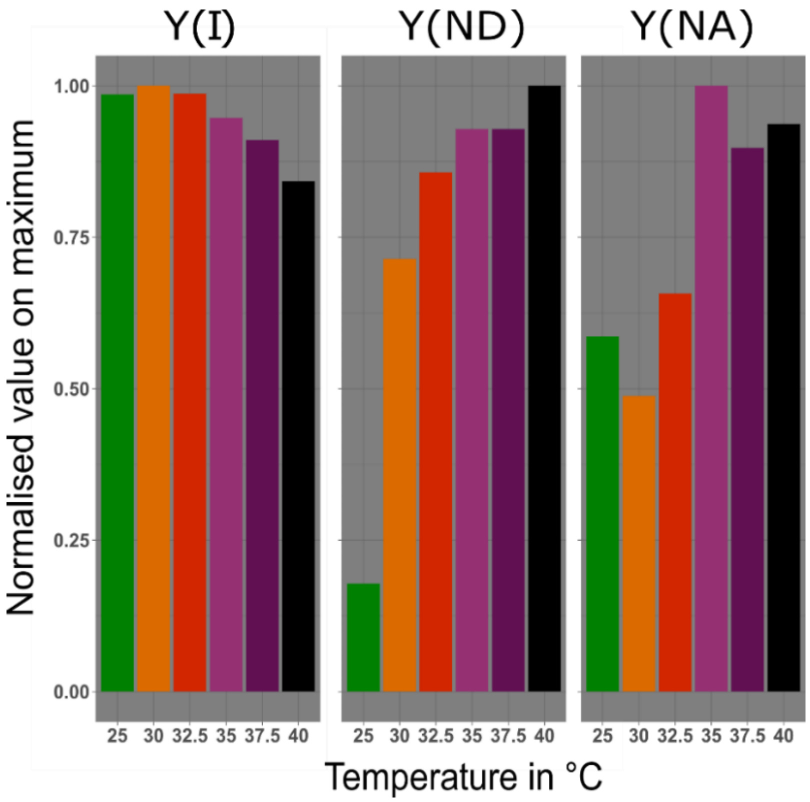

Figure 4-5: Quantum efficiencies for PSI, donor side limitation (Y(ND)) and acceptor side limitation (Y(NA)) of sunflower, *Helianthus annuus*, for a range of temperatures, at a light intensity of 245 µmol.m^{-2}.s^{-1}.

Figure 4-5 shows the quantum yields at a light of 245 µmol.m^{-2}.s^{-1}, each normalised by its maximum value, to illustrate the temperature response over the 25°C to 40°C range. For both Y(I) and Y(NA), important modifications occur above 32.5°C, whereas Y(ND) is more than tripled between 25°C and 30°C. The Y(ND) parameter reflects a limitation upstream of PSI, likely on the PSII side, while Y(NA) reflects a limitation downstream of PSI towards ferredoxin NADP$^+$ reduction. The results clearly show that it is first Y(ND) that is affected by temperature changes, probably due to a decrease of

Y(II). Then, Y(I) and Y(NA) are affected at higher temperatures, signalling downstream limitations of the linear electron flow.

4.4 Discussion

4.4.1 Combined effects of elevated temperature and leaf age on photosynthesis

4.4.1.1 Effects on PSII

The objective of this study was to highlight photosynthetic behaviour in elevated temperature conditions. The Y(II) parameter is related to Vcmax and Jmax, which are known to follow a peaked function in response to temperature (Medlyn et al., 2002). Our experiments showed that PSII reaches its optimal state at 25°C in *A. thaliana* (Figure 4-4) and 30°C in sunflowers (Figure 4-3). Table 4-1 indicates that the median growth temperature of sunflowers is similar to *A. thaliana*. We can thus attribute this difference in optimal temperature to different temperature-dependencies between the species, as it was previously documented, e.g., in (Medlyn et al., 2002).

Figure 4-2 shows that Y(II) is dependent on leaf age, and older leaves are more sensitive to hotter temperatures. Fluorescence measurements alone cannot explain the physiological causes of this age effect. (Zhou et al., 2015) also found a lower temperature optimum and a lower electron transport rate in older plants; their study was performed on another C3 plant, the *Quercus aquifolioides*, a typical evergreen alpine oak species. In Figure 4-2 we observe an important increase of Y(NO) at 40°C in plants of 28 days, and 37.5°C in plants of 35 days. It was previously shown in (Chen et al., 2014) that some heat tolerant *Festuca arundinacea Schreb* varieties can dissipate more energy through Y(NO) in heat stress conditions compared to accessions sensitive to heat stress. The induction of an important Y(NO) thus seems to be associated with heat stress, but we need more measurements to build a comprehensive view of the response of Y(NO) to heat stress. (Agüera et al., 2010) showed that, in sunflowers, antioxidant activity, as measured by catalase and ascorbate peroxidase, increased after 28 days but subsequently decreased, leading to the accumulation of reactive oxygen species (ROS) and damage to the photosynthetic apparatus. A reduction in antioxidant enzyme levels may increase temperature stress sensitivity in 35-day old plants, which could explain the more significant differences in yields observed between temperatures in this case. This increased temperature sensitivity associated to ageing needs further research to be elucidated.

4.4.1.2 Effects on PSI

It is already well established that RuBisCo is more sensitive to heat compared to light reactions (Weis, 1982). Then, in between the two photosystems, it has been shown that PSII is firstly affected by heat stress compared to PSI, with an inhibition of the donor-side of PSII (Yan et al., 2013). In the review by (Ivanov et al., 2017a)), the authors propose that heat stress induces a modification of the organization of the thylakoid membrane: LHCII detaches from PSII to associate with PSI. Measurements over a temperature gradient (Figure 4-5) show first an increase in Y(ND) followed by an increase in Y(NA). It is consistent with the model proposed in (Ivanov et al., 2017b) and the relocation of LCHII from PSII to PSI, but may also indicate a higher activity of cyclic electron flow around PSI. (Rath et al., 2022) performed analogous measurements in *Pisum sativum* at different temperatures, and they found similar results: first, inhibition of the donor side, and then inhibition of the acceptor side during the temperature increase. The authors also observed modifications in the organization of the thylakoid membrane, as proposed in the (Ivanov et al., 2017b) review. This review point outs that the regulation of different electron flows, including linear electron flow, and cyclic electron flow, and of PTOX activity remain however ambiguous, due to the complexity of each pathway and their interaction. In (Krieger-Liszkay et al., 2019) authors also proposed that, with leaf ageing, alternative electron pathways become increasingly important. That is coherent with our observations of Y(II) depending of leaf age (Figure 4-2), leading to a loss of the capacity of linear electron transport.

4.4.2 General conclusion on the effect of high temperatures on C3 species

(Yamori et al., 2014) showed that the optimum of photosynthetic activity depends on the type of C3 or C4 plant, and that the ability to adapt to higher temperatures is greater in C3 plants. The limiting factors of photosynthesis at moderately high temperatures are still debated. The authors put forward two important limiting factors of the Rubisco carboxylation activity: i) the stability of Rubisco activase, which decreases with increasing temperatures, and ii) the decrease in PSII activity, which decreases the ratio ATP/ADP, leading to a decrease in the activity of Rubisco controlled by the redox state of the chloroplast.

Regarding our experiments, we can imagine that the temperature increase induces a decrease of the linear electron flow, leading to the modification of the ATP/ADP ratio, decreasing the activity of the Rubisco. This would explain the progressive decrease of the Y(II) observed between 25°C and 35°C. However, once a certain temperature limit is reached, the Rubisco activase is significantly destabilized, resulting in a sudden change in photosynthetic activity, which was observed at 40°C in our measurements.

More generally, these results show that the effects of high temperatures on photosynthesis depend on species, and leaf age. In this chapter, we induced abrupt temperature stress. We cannot observe the effects of acclimation to temperature that would occur over longer time scales. Acclimation to temperature was previously shown for various plant species (Kattge & Knorr, 2007); Vcmax and Jmax can shift under higher temperatures, expressing an adaptation to the changing climate conditions, allowing the plant to reach higher optimum temperatures for photosynthesis. However, this acclimation varies with species and is not infinite (Sánchez et al., 2014). As it was concluded in (Sánchez et al., 2014) , lethal temperatures are similar in the three major crops: wheat, rice (C3 plants), and maize (C4 plant) and range from 43 °C to 48 °C. This is a major problem regarding food security. In the 2019 IPCC special report on climate change and land, the authors assert in the executive summary of Chapter 5: “Food Security”, that: “Food security will be increasingly affected by projected future climate (*high confidence*)”. To conclude, we can say that heatwaves with their effect on photosynthesis will endanger carbon fixation capacity, and thus food security.

In the next chapter, I will switch to a first large scale study, using active fluorescence measurements to constrain a NPQ model specific to boreal evergreen needleleaf forests, and passive fluorescence measurements to constrain the NPQ, SIF and GPP simulated by a land surface model.

5 Chapter 5: Simulating NPQ, SIF and GPP over boreal evergreen needleleaf forests with a land surface model

5.1 Gross primary production (GPP)

It is a challenge to accurately represent the highly variable dynamics of GPP (Anav et al., 2015; Seiler et al., 2022). The associated uncertainty is thus large, which is one of the primary causes of the large spread in predicting the future land sink/source based on coupled carbon-climate projections (Friedlingstein et al., 2014). The temporal variability of GPP is mainly driven by the weather, including sunlight, precipitation, and temperature, at diurnal to seasonal scales, and by the increasing trend of atmospheric CO_2 concentrations at a longer time scale (CO_2 fertilisation effect). The spatial variability is driven by the species distribution, the soil types, and the climate (Li & Xiao, 2020).

Unfortunately, GPP cannot be measured at scales larger than the leaf. It can be estimated at the ecosystem scale using eddy-covariance flux measurements. The eddy covariance technique is a crucial method for measuring and calculating vertical turbulent fluxes in atmospheric boundary layers. This statistical approach utilizes high-frequency data series of wind and scalar atmospheric variables, such as gas, energy, and momentum, to determine the flux values of these properties. It quantifies gas emission rates from land and water areas, and is commonly used for estimating fluxes of momentum, heat, water vapor, carbon dioxide, and methane.

At larger scales, we can use proxies derived from space-borne satellite measurements. The most promising one, that has emerged in the 2010's, is the sun-induced fluorescence (Frankenberg et al., 2011; Mohammed et al., 2019; Parazoo et al., 2019; Porcar-Castell et al., 2014).

5.2 Boreal evergreen needleleaf forests

Boreal forests account for around 20% of the global forest sink (Harris et al., 2021; Hayes et al., 2022). In this study, we focused on boreal evergreen needleleaf forests. This forest type is a major ecosystem covering a total area of nearly 7 Mkm^2 (https://orchidas.lsce.ipsl.fr/dev/lccci/orchidee_pfts.php, last access: 3 July 2023). From the photosynthetic point of view, they present the unique interest of keeping needles during the cold winter times, posing quite a challenge for photoprotection mechanisms. Species developed a sustained NPQ, as presented in (Bag et al., 2020). Active fluorescence measurements are available for *Pinus sylvestris*, at the forest site of Hyytiälä in Finland, allowing for the computation of NPQ parameters (Porcar-Castell, 2011). Satellite and *in situ* SIF measurements have also been used to study the seasonal cycle of the photosynthetic activity in boreal evergreen needleleaf forests (Pierrat et al., 2021, 2022; Walther et al., 2016).

5.3 Summary of data, tools and methodology

5.3.1 Satellite SIF estimates

There are several space-borne platforms and instruments capable of estimating SIF, with various resolutions (spatial, temporal, and spectral). The spatial resolution refers to the minimum Earth surface that can be sampled by the instrument. An instrument with a high spatial resolution can capture more detailed information, and is useful to study homogeneous patches of a specific biome. The temporal resolution refers to the shortest time between measurements of the same target. An instrument with a high temporal resolution can provide more frequent SIF measurements, cloud-cover permitting, which is particularly useful for studying short-term variations in vegetation productivity and physiology. The revisit time is the period between two consecutive observations in the exact same geometry. Finally, the spectral resolution plays a key role in the choice of the associated retrieval SIF method. Table 5-1 provides these features for the main sensors for which SIF estimates are available (Guanter et al., 2021; Parazoo et al., 2019).

Table 5-1: Resolutions of main instruments for which a SIF product is available.

Satellite name	**Resolution**		
	spectral (nm)	spatial (km^2)	revisit time (day)
SCIAMACHY	0.5	30 × 120	6
GOME-2	0.5	40 × 40	3
GOSAT	0.025	10 in diameter	3
OCO-2	0.05	1.3 x 2.25	16
TROPOMI	0.38	3.5 x 5.5	1

In this work, we used the ESA TROPOSIF product, derived from the TROPOMI instrument on-board the Copernicus Sentinel-5P platform (Guanter et al., 2021). The TROPOMI SIF estimates were chosen for data assimilation into the ORCHIDEE model because they provide a daily global coverage, at a moderate spatial resolution, still suitable for land surface models, which usually run at global scale using a 0.5° spatial resolution (~50km at the equator). The methodologies developed for the SIF retrieval usually rely on the in-filling of a strongly absorbing band, O_2 bands in the terrestrial atmosphere or Fraunhofer lines in the solar atmosphere. These latter are specific wavelengths of the solar radiation where the signal is absorbed by the heliosphere, so that all the luminance received by the Earth observing satellite is being emitted by the Earth only (Mohamed et al., 2020). Using the method with oxygen absorption bands requires some knowledge of the state of the terrestrial atmosphere; this is not the case for data-driven methods using Fraunhofer lines. This latest method was used for TROPOMI. The retrieved SIF is highly uncertain (Guanter et al., 2021), however, by aggregating a large amount of data, the random uncertainty can be significantly reduced. The SIF potential to improve the GPP simulated by the ORCHIDEE land surface model was already demonstrated, using data assimilation of GOME-2 (MacBean et al., 2018) and OCO-2 SIF estimates (Bacour et al., 2019). However, as several PFTs showed a GPP degradation (Bacour et al., 2019), we explored in the study the benefits of co-assimilating satellite SIF estimates and *in situ* GPP estimates.

5.3.2 *In situ* GPP estimates

The FLUXNET network is composed of 206 flux towers around the world, mainly in the northern hemisphere, with complete seasonal cycles spanning 20 years for the oldest sites. The FLUXNET network produces a peer-reviewed dataset containing meteorological data such as temperature, radiation, precipitation, relative humidity, as well as estimates of carbon, water and energy fluxes (Pastorello et al., 2020). A tower footprint is roughly on the order of 1 km^2.

5.3.3 Data assimilation

5.3.3.1 Sensitivity analysis

First, we had to select a restricted number of parameters to limit the computational time and to avoid overfitting. Overfitting may occur when we optimize too many parameters; it makes the model very accurate, but only for the dataset on which it was trained, and it does not allow to derive parameters that are generic enough to also get good performances on the independent evaluation dataset. For this selection, we performed a sensitivity analysis using the Morris method (Morris, 1991). The Morris method is a global sensitivity analysis technique used to identify the most influential parameters in a model by quantifying their impact on the considered model output. This method involves varying one parameter at a time while keeping all other parameters fixed and computing the change in the model output in response to the parameter change.

We defined a prior value and a range of variation for each parameter. We tested 126 parameters and used ten random values for each one, leading to a total of 1270 simulations. In the end, we selected the 9 most important parameters for GPP and the 9 most important for SIF. Among these parameters, 5 were common, resulting in a total of 13 parameters to optimize during the simultaneous assimilation of SIF and GPP data.

5.3.3.2 Optimization with a genetic algorithm

To optimize these parameters, we minimized a cost function within a Bayesian framework (Tarantola, 1987). The cost function is typically formulated as the negative log-likelihood of the observed data given the model parameters. In this work we used a genetic algorithm method to minimize the cost function; this method is able to find the global minimum, as opposed to gradient-descent techniques that can be trapped in local minima (Bastrikov et al., 2018).

The genetic algorithm is a stochastic approach that is inspired by natural selection and uses concepts of cross-over, mutation, and selection. This algorithm is efficient in exploring the parameter space but may change insensitive parameters. During the optimization using the genetic algorithm, we took the same prior, minimum and maximum values for each parameter as used in the sensitivity analysis. During optimization, the parameter values are first randomly chosen within the authorized range, and then further modified based on the cost function and the genetic algorithm criteria. The model converges after numerous iterations (approximately 800) to deliver a set of optimized parameters.

5.3.4 Methodology

We first updated the modelling of the NPQ relative rate constant by splitting it into a reversible and a sustained component. Sustained NPQ is mostly active during winter, and it is modelled based on a moving average of the air temperature (Makela et al., 2004). Reversible NPQ is mostly active during the growing season, it is very sensitive to the photosynthesis yield and, as such, exhibits a strong diurnal cycle. We derived prior values of the parameters for the NPQ reversible and sustained components, by fitting their respective model using one year of active measurements performed on *Pinus sylvestris* at the Hyytiälä (Finland) site (Porcar-Castell, 2011).

We then used TROPOMI SIF estimates and *in situ* FLUXNET GPP estimates to optimize various parameters of the ORCHIDEE model. We took data from 9 boreal forest evergreen needleleaf forest sites. Three years of *in situ* GPP estimates and two years of co-located SIF satellite estimates were used to optimize parameters, and one other year to evaluate the posterior SIF and GPP. Significant improvements in the accuracy were observed following data assimilation. The optimized parameters obtained were then applied to perform regional simulations over the boreal evergreen needleleaf forests. At this larger scale, there was also an enhancement in the simulation of SIF and GPP after optimization, as shown when comparing with large-scale reference products.

5.4 Third publication: “Improving the SIF constraint on GPP for boreal evergreen needleleaf forests in a land surface model using a physiologically-based representation of non-photochemical quenching and data assimilation” (Leverne et al., submitted)

Please refer to appendix in section 13.3 for access to this third publication.

The objective of this thesis was to reinforce connections between two relatively distant scientific communities, building a bridge between the molecular understanding of photosynthesis and large-scale modelling, to improve the latter. The modelling work developed in this chapter is a first step towards this objective.

In this article, we modified the NPQ model for boreal evergreen needleleaf forests through two successive strategies. Firstly, we modelled a new type of NPQ, based on molecular observations of evergreen plants in this specific biome. We referred to this NPQ as "sustained NPQ", which is induced and remains during the cold winter of boreal latitudes. Next, we constrained the parameters of this model, as well as others related to the photosynthesis and fluorescence models, through the coupled assimilation of satellite-derived SIF estimates and *in situ* GPP estimates at the canopy scale. This allowed us to improve the GPP and SIF simulated by the ORCHIDEE model for this biome. This methodology could now be extended to all plant functional types.

In this research article, I discussed the strategy with my supervisors, performed all simulations, data assimilation experiments and data analyses. I produced most figures and contributed to the writing of the manuscript.

Now, we would like to have in this same LSM a better modelling of plant behaviour specifically under stress conditions induced by climate change. In the following chapter, we will use fluorescence active measurements performed at the leaf level on poplar, under drought conditions. Our objective is to develop a NPQ model that enables to improve the plant's response to drought stress, and will be further implemented within the ORCHIDEE LSM.

6 Chapter 6: Modelling the drought response of NPQ

6.1 Introduction

(Wohlfahrt et al., 2018) reported a decoupling between SIF and GPP using canopy-scale measurements in a Mediterranean pine forest. Other studies documented the same behaviour, using additional PAM monitoring, e.g., in (Helm et al., 2020) for poplars, in (Marrs et al., 2020)) for oaks and tulip poplars, in (Martini et al., 2022) for a Mediterranean open woodland. This allowed them to simultaneously look at the NPQ at leaf-level, and see that: "The highly nonlinear [GPP-SIF] relationship was strongly shaped by non-photochemical quenching (NPQ)", as stated in (Martini et al., 2022) .

This stresses the need of having a NPQ model valid in drought conditions, to correctly exploit the SIF signal in land surface models. In this chapter, I will study the impact of the recent heatwave conditions during summer in France on poplar, our selected model tree. I will first present the experiment during which I acquired the data, and then I will develop a model for the relative rate constant of Non-Photochemical Quenching (kNPQ), depending on environmental variables and valid in drought conditions.

6.2 Material and methods

6.2.1 Environmental conditions

This study was made possible thanks to the IPSL BIOTECA (Biogéochimie terrestre, écosystème et agriculture) working group (https://www.ipsl.fr/recherche/les-thematiques-scientifiques/biogeochimie-terrestre-ecosysteme-et-agriculture/, last access: 3 July 2023). It was performed at the CEREEP-Ecotron Ile-de-France (https://www.cereep.bio.ens.psl.eu/, last access: 3 July 2023). We used two Ecolab systems (https://www.cereep.bio.ens.psl.eu/spip.php?article9, last access: 3 July 2023), labelled as "control" and "stress". In these chambers, temperature, light, and relative humidity were controlled and measured. The poplar trees *(Populus trichocarpa*) were grown in a greenhouse with 16 hours of illumination (at 110 µmol.m^{-2}.s^{-1}) at 20°C for five months before starting the experiment. Then, three plants were planted in soil columns within PVC tubes measuring 60 cm with a 20 cm diameter, in both chambers. First, we put plants for two weeks at 20°C, with a 50% air relative humidity (RH), and 12 hours of light at 300 µmol.m^{-2}.s^{-1}, to acclimate to the measurement conditions. Then, we started the experiment, on day noted 0 in the next figures. The stress chamber simulated the weather conditions from June 7th to 28th, averaging over seven years from 2016 to 2022, while the control chamber simulated the average weather of the previous 20 years during the same period.

6.2.2 Measured variables

To monitor fluorescence, we used a MICRO-PAM Walz device (https://www.walz.com/products/chl_p700/micro-pam/introduction.html, last access: 3 July 2023), placed on one leaf from the upper part of the plant in each chamber. This device emitted saturating light pulses (4,000 µmol.m^{-2}.s^{-1}, with a pulse duration of 0.8 s) every 10 minutes; the fluorescence measurements allowed to calculate yields and rate constants for the processes of interest (photosynthesis, NPQ, fluorescence), in particular the NPQ relative rate constant (Baker, 2008; Porcar-Castell, 2011):

$$\mathrm{kNPQ} = \left(\frac{\mathrm{Fm}}{\mathrm{Fm}'} - 1\right) \qquad \text{eq. (6-1)}$$

Additionally, we measured the chlorophyll content in five leaves for each of the three poplar trees in each chamber on a weekly basis. Soil water content and conductivity were continuously measured using METER TEROS 12 probes.

Thus, we directly measured or derived the following parameters: air temperature (AT, °C), air relative humidity (RH), leaf temperature (LT, °C), vapour pressure deficit (VPD, kPa), soil temperature (ST, °C), soil water content (SWC, m^3 m^{-3}), soil electro-conductivity (SEC, $mS.cm^{-1}$), photosynthetic active radiation (PAR, $\mu mol.m^2.s^{-1}$), chlorophyll content (Chl_content, $mg.m^{-2}$), kNPQ, the photosynthetic yield (phi_P) and the degree of photosynthetic saturation, x, as defined in (Tol et al., 2014) .

6.2.3 Modelling approaches

6.2.3.1 Evaluating potential relations between VPD and NPQ

The increase in VPD is accelerating under climate change, with adverse effects on the vegetation, going from stomatal closure and reduced photosynthesis and transpiration, till possibly hydraulic failure and cavitation (Lesk et al., 2016). VPD strongly correlates with NPQ, especially in stress conditions (Martini et al., 2022). In a first approach, we will use test a simple model expressing kNPQ in drought conditions as a linear function of VPD.

6.2.3.2 Ranking the importance of potential factors using a Random Forest model

A random forest (RF) model is a machine learning method, whose output is based on an ensemble of many decision trees (Breiman, 2001). We used it here as a regression algorithm to compute kNPQ, based on environmental and physiological factors.

I coded the RF computations with the Python 3 language and the scikit-learn library. I used 75% of the samples for the training dataset, and 25% for the evaluation dataset.

I tested RF models with all possible combinations of a selected set of input factors (n=255) in order to determine how many factors were needed to predict kNPQ with an accuracy larger than 90%, and to identify the best combinations. Accuracy is calculated as the median absolute error percentage minus 100.

6.2.3.3 Fitting model parameters to link environmental and physiological factors to NPQ

We tested several empirical parametric models to compute kNPQ from environmental ad physiological conditions, in drought stress conditions. These fitting experiments were performed with the Model function from the lmfit library (Newville et al., 2016) .

6.2.3.4 Calculation of scores for fitting performance

To rank and choose among tested empirical equations, we used different scores evaluating their performance. The Root Mean Square Deviation (RMSD) quantifies the average difference between the predicted values of a model and the corresponding observed values. To calculate RMSD, we first compute the squared differences between each predicted value and its corresponding observed value. These squared differences are then averaged, and the square root of the average is taken to obtain the RMSD. For a model that perfectly fits the observed data, the RMSD value would be equal to 0. The Akaike Information Criterion (AIC) quantifies the balance between the fit quality and the complexity of a model. It penalizes models that employ a larger number of parameters to fit the data. The AIC is calculated as the sum of the negative logarithm of the likelihood of the model and twice the number of parameters utilized. Models with lower AIC values are considered more favourable, as they achieve a superior equilibrium between precision and simplicity. The reduced chi2 score, noted RedChi2, provides a normalized measure of the discrepancy between the model predictions and the observed data, taking into account the complexity of the model, by dividing the discrepancy by the degree of freedom defined as the number of data points minus the number of parameters. It allows for fair comparison between models with different numbers of parameters. For a model that perfectly fits the observed data, the RedChi2 value would be equal to 1.

6.3 Results

6.3.1 Monitoring of environmental and physiological conditions

6.3.1.1 Daily means

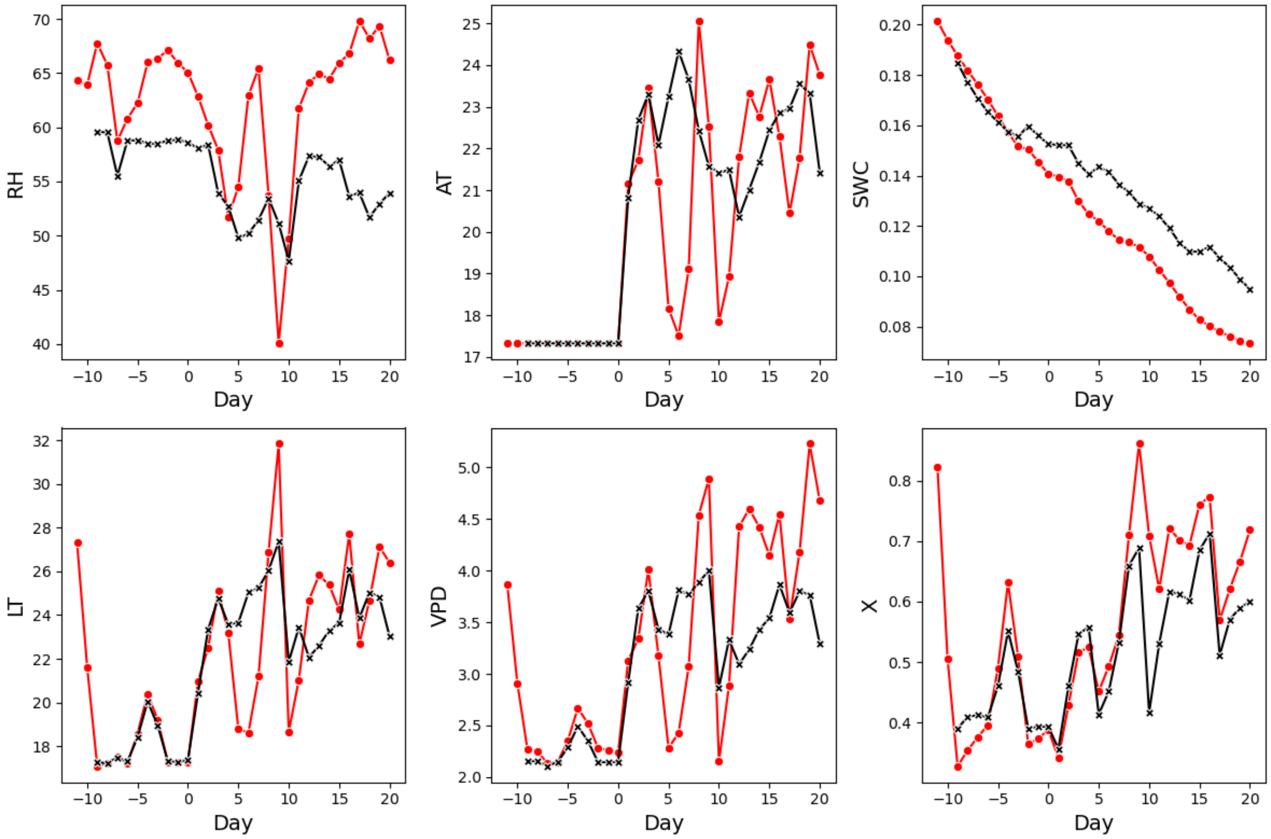

Figure 6-1: Evolution of the daily mean of weather and physiological variables: air relative humidity (RH), air temperature (AT, °C), soil water content (SWC, $m^3.m^{-3}$), leaf temperature (LT, °C), vapour pressure deficit (VPD, kPa) and the degree of photosynthetic saturation (x, a.u). Day 0 is defined as the beginning of the experiment, the days before represent chamber acclimation. The black symbols and lines represent the control chamber, and the red ones represent the stress chamber.

It can be observed that the humidity and temperature were more variable in the stress chamber, reflecting the mean 2016-2022 conditions, compared to the control chamber, representing a mean climatology over 20 years. The soil water decreases more rapidly in the stress chamber.

Under low SWC conditions, plants tend to close their stomata to limit water loss through excessive transpiration, thereby reducing their assimilation. The SWC in both the stress and control chambers are comparable at the beginning of the experiment, but in the last week the difference of SWC has increased up to around 0.03 $m^3.m^{-3}$.

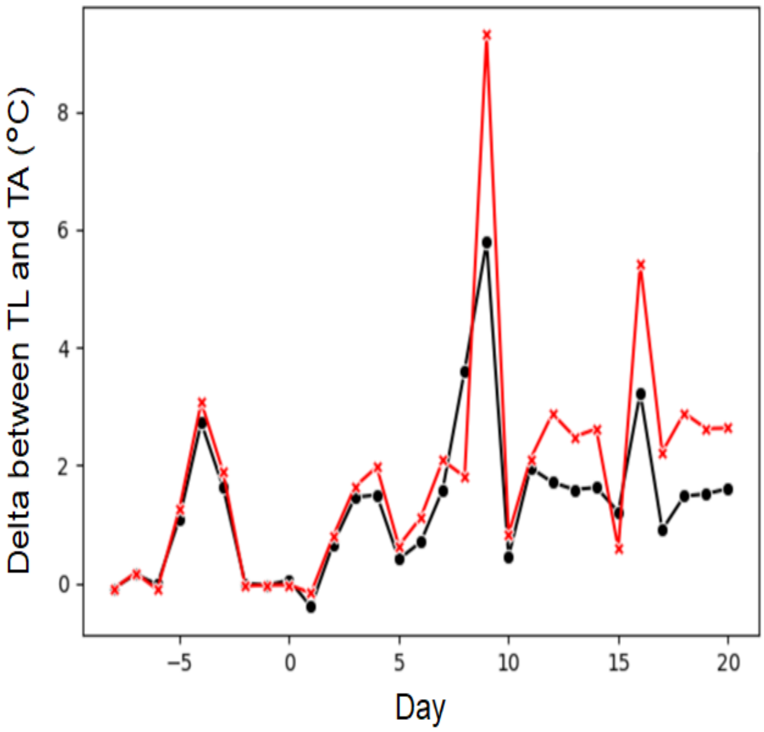

Figure 6-2: Evolution of the daily mean of the difference between leaf (TL) and air temperatures (TA) (°C), in the control (black) and stress (red) chambers.

In addition to the larger decrease in SWC, we observed that the difference between leaf and air temperatures was more pronounced in stressed plants compared to the control group, especially after day 9 when the difference becomes larger (Figure 6-2). The plant under stress conditions has more difficulty regulating its leaf temperature, likely due to stomatal closure and reduced transpiration.

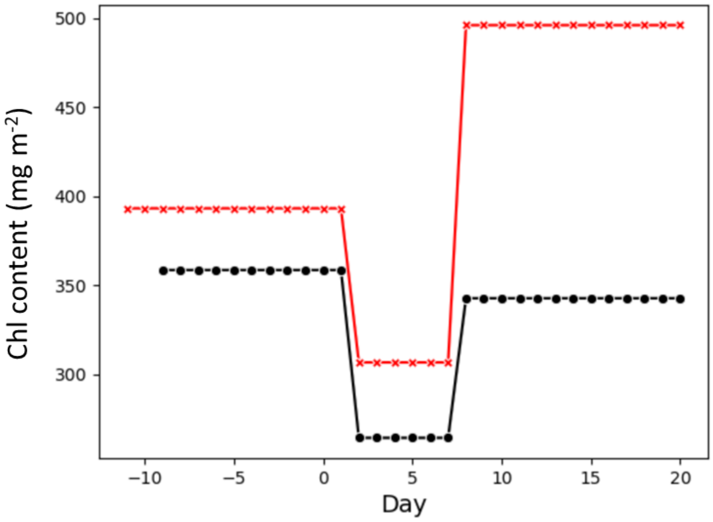

Figure 6-3: Evolution of the leaf chlorophyll content (mg.m^{-2}), mean of weekly measured were used input factors in models, in the control (black) and stress (red) chambers.

In Figure 6-3, we observed important variations of the leaf chlorophyll contents in between week, with an important decrease between the last two weeks of experiment in stress conditions.

6.3.1.2 *Diurnal cycles*

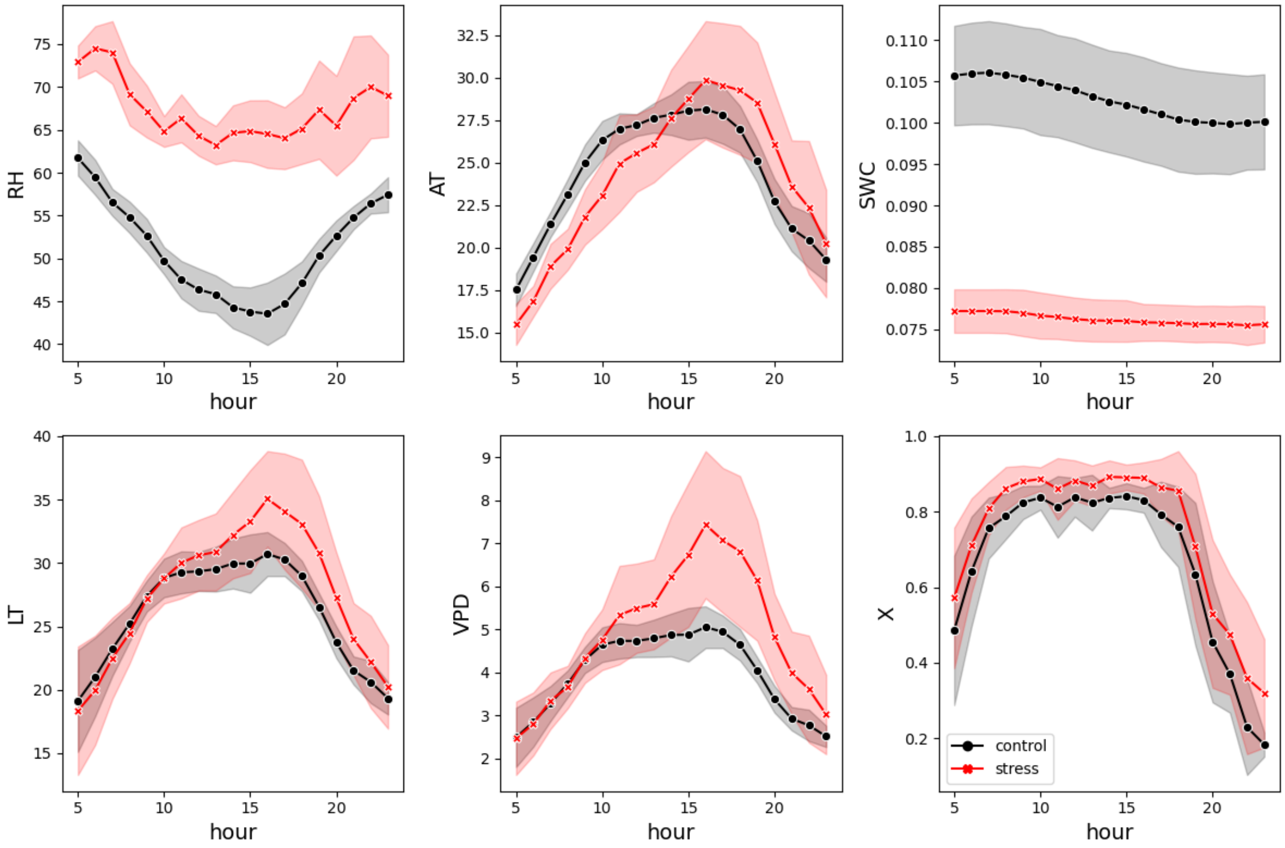

Figure 6-4: Mean diurnal cycles computed over the last 5 days of the experiment for air relative humidity (RH), air temperature (AT, °C), soil water content (SWC, $m^3.m^{-3}$), leaf temperature (LT, °C), vapour pressure deficit (VPD, kPa), and the degree of photosynthetic saturation (x, a.u) for the control (black) and stress (red) chambers. Shaded areas represent the corresponding standard deviations.

Figure 6-4 represents the mean diurnal cycles computed at an hourly frequency over the last 5 days of the experiment for the previously studied parameters. We observed the same trend as for the daily means, with lower air and soil humidity in stress conditions. A highest leaf temperature is also observed in stress conditions starting mid-morning, indicating that the stressed plants have more difficulties regulating their temperature through transpiration.

Thanks to these continuous measurements performed over three weeks at a high temporal resolution under contrasting conditions, we were able to attempt to model the behaviour of NPQ under high temperature and drought conditions.

6.3.2 Modelling

The objective here is to define a parametric model for NPQ in drought stress conditions, which will be implemented within the ORCHIDEE land surface model. Such a NPQ model should relate to plant physiology, and allows ORCHIDEE to represent the decoupling observed between SIF and GPP in drought conditions (Wohlfahrt et al., 2018; Martini et al., 2022). We will select the most economical expression in terms of variables and parameters, in order to ensure its generality for a large-scale use through ORCHIDEE.

6.3.2.1 Linear relationship between of NPQ and VPD

We started with the idea of first linking NPQ to VPD.

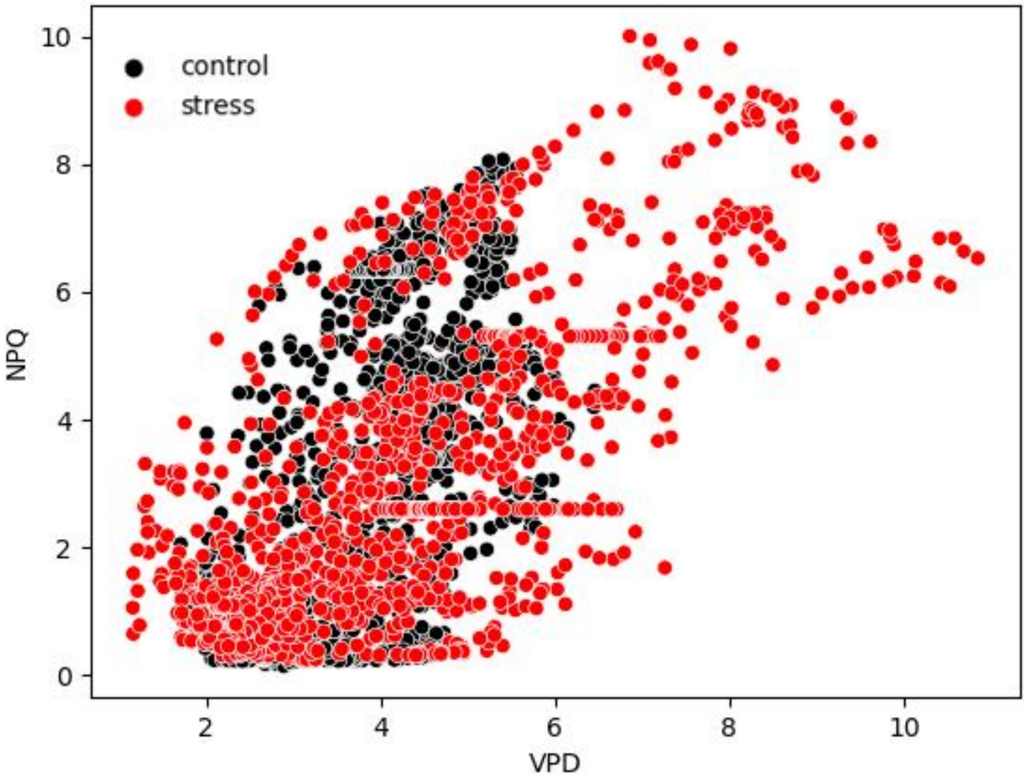

Figure 6-5: Scatter plot of NPQ against VPD using all measured data points, for the control (black) and stress (red) chambers.

Figure 6-5 shows the relationship between VPD and NPQ measured in the two chambers. There appears to be a linear relationship between VPD and NPQ, with a correlation of 0.66. The relationship seems to be consistent between the two chambers, with a correlation of 0.59 and 0.73 in the control chamber and in the stress chamber, respectively. The correlation between VPD and NPQ is more pronounced in the stress chamber, probably because VPD modulates the NPQ response even more in stress conditions. Based on these initial results, we examined the capacity of the current kNPQ model implemented in ORCHIDEE to represent the kNPQ estimated using the active fluorescence measurements performed in the two chambers. We used eq. (7) of Chapter 5 representing the reversible component to express kNPQ, because we are measuring fluorescence on poplar trees in summer weather, and no sustained NPQ is activated in these conditions.

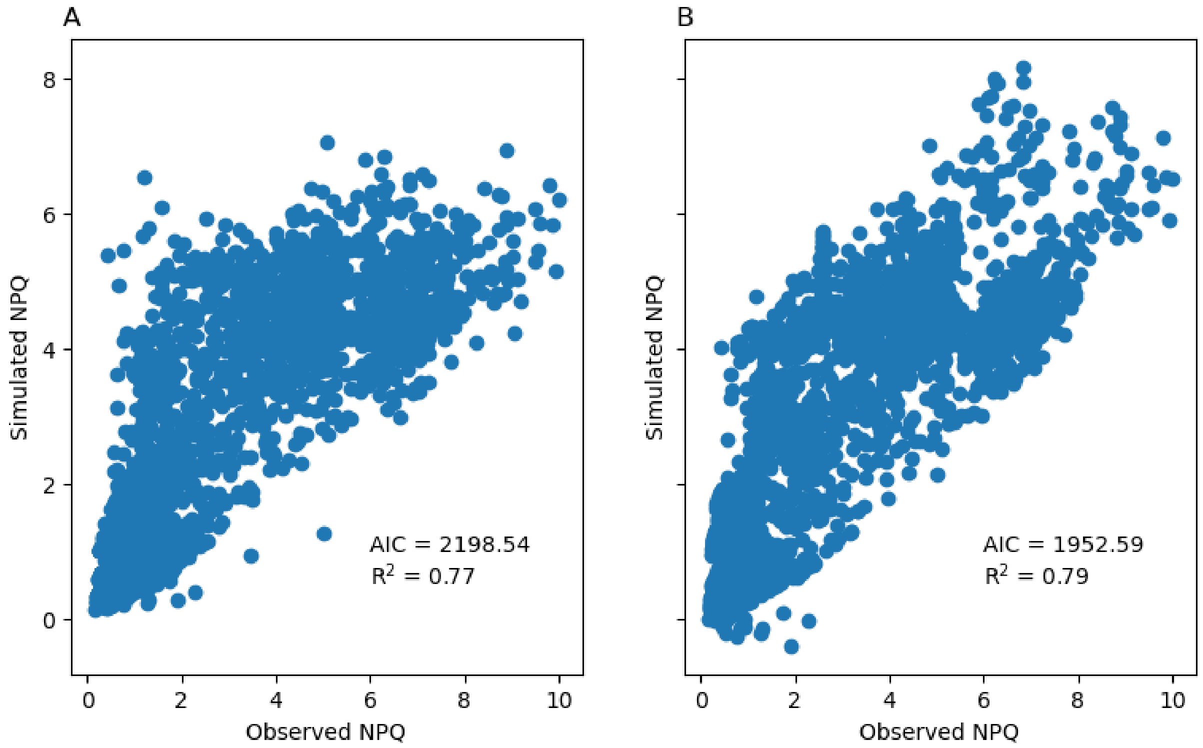

Figure 6-6: Scatter plots of simulated versus observations-derived kNPQ; A) using the current ORCHIDEE model; B) using the updated kNPQ model developed in this study.

Eq. (6-2) used for panel A in Figure 6-6 is currently used in ORCHIDEE. We added a simple linear dependency on VPD in eq. (6-3), used for panel B.

$$\mathrm{kNPQ} = \mathrm{A1} \times \mathrm{x} + \mathrm{A2} \times \mathrm{x}^3 \qquad \text{eq. (6-2)}$$

$$\mathrm{kNPQ} = \mathrm{A1} \times \mathrm{x} + \mathrm{A2} \times \mathrm{x}^3 + (\mathrm{A3} \times \mathrm{VPD} + \mathrm{A4}) \qquad \text{eq. (6-3)}$$

with x the degree of light (van der Tol et al., 2014). A1, A2, A3 and A4 are parameters adjustable during fitting.

If the model was perfect, points should be aligned on the 1:1 line and the coefficient of correlation (R) should be equal to one. The lower AIC score observed in Figure 6-6 B, as well as the larger coefficient of determination (R^2), support the use of VPD as a proxy of drought intensity in NPQ modelling.

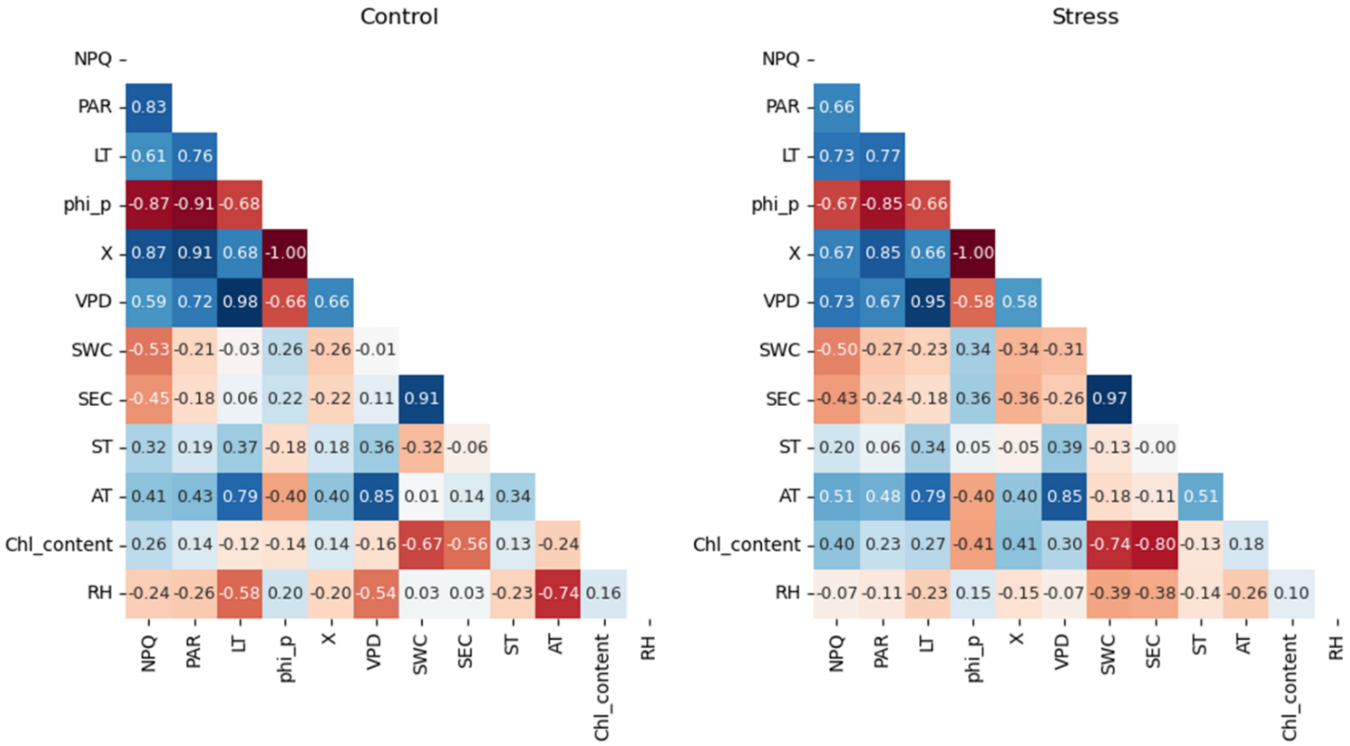

Control

	NPQ	PAR	LT	phi_p	X	VPD	SWC	SEC	ST	AT	Chl_content	RH
NPQ												
PAR	0.83											
LT	0.61	0.76										
phi_p	-0.87	-0.91	-0.68									
X	0.87	0.91	0.68	-1.00								
VPD	0.59	0.72	0.98	-0.66	0.66							
SWC	-0.53	-0.21	-0.03	0.26	-0.26	-0.01						
SEC	-0.45	-0.18	0.06	0.22	-0.22	0.11	0.91					
ST	0.32	0.19	0.37	-0.18	0.18	0.36	-0.32	-0.06				
AT	0.41	0.43	0.79	-0.40	0.40	0.85	0.01	0.14	0.34			
Chl_content	0.26	0.14	-0.12	-0.14	0.14	-0.16	-0.67	-0.56	0.13	-0.24		
RH	-0.24	-0.26	-0.58	0.20	-0.20	-0.54	0.03	0.03	-0.23	-0.74	0.16	

Stress

	NPQ	PAR	LT	phi_p	X	VPD	SWC	SEC	ST	AT	Chl_content	RH
NPQ												
PAR	0.66											
LT	0.73	0.77										
phi_p	-0.67	-0.85	-0.66									
X	0.67	0.85	0.66	-1.00								
VPD	0.73	0.67	0.95	-0.58	0.58							
SWC	-0.50	-0.27	-0.23	0.34	-0.34	-0.31						
SEC	-0.43	-0.24	-0.18	0.36	-0.36	-0.26	0.97					
ST	0.20	0.06	0.34	0.05	-0.05	0.39	-0.13	-0.00				
AT	0.51	0.48	0.79	-0.40	0.40	0.85	-0.18	-0.11	0.51			
Chl_content	0.40	0.23	0.27	-0.41	0.41	0.30	-0.74	-0.80	-0.13	0.18		
RH	-0.07	-0.11	-0.23	0.15	-0.15	-0.07	-0.39	-0.38	-0.14	-0.26	0.10	

Figure 6-7: Correlation matrices for all pairs of the measured or derived variables. Colour and value indicate the correlation coefficients (darkest blue=1, darkest red=-1).

The correlation matrices represented in Figure 6-7 enable the identification of relationships between variables. Regarding kNPQ in both chambers, the absolute value of the correlation coefficient is larger than 0.5 for VPD, x, phi_P, LT, and PAR, meaning that kNPQ is positively or negatively correlated with these variables. We observe higher correlations between kNPQ and variables that are mainly driven by light conditions, such as x and phi_P for the control chamber. On the contrary, the correlation with VPD is larger in the stress chamber.

However, it is still challenging to determine which combinations of variables best represent the variability of kNPQ. To identify these combinations, we used a machine learning model, the Random Forest. I first needed to select input variables based on their paired correlations. Indeed, when variables are strongly correlated, they provide redundant information to the RF model. This redundancy can lead to incorrect importance scores being assigned to these correlated variables, making it difficult to evaluate their individual contribution to the prediction. I also privileged variables available in the ORCHIDEE model, for a further implementation. For the RF models, I thus considered combinations of the eight input factors: AT, RH, VPD, ST, SWC, PAR, Chl_content, and x.

6.3.2.2 Random Forest models

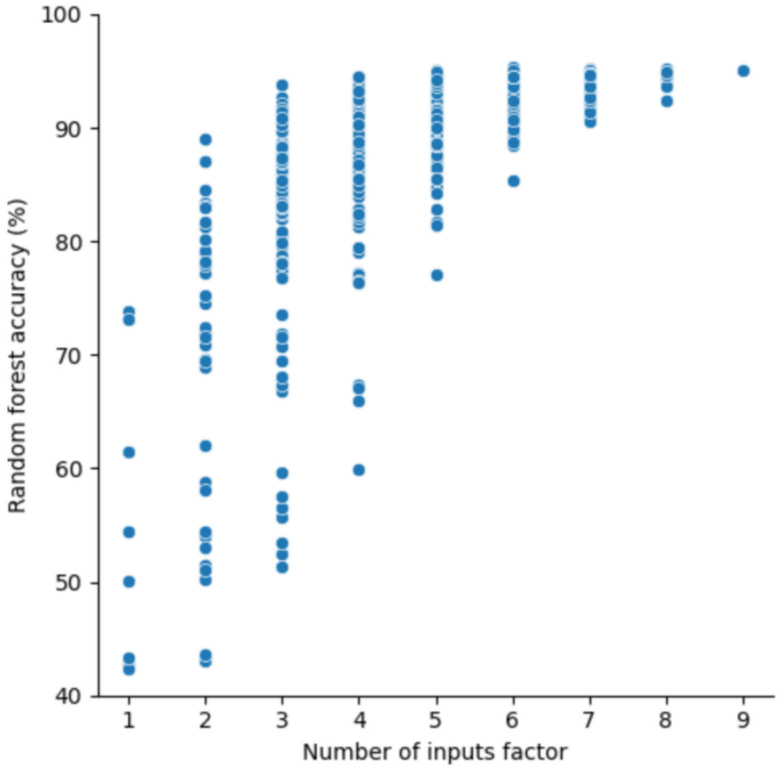

Figure 6-8: Accuracy of random forest models depending of the number of input factors. Each point represents the accuracy of a RF model for a possible combination of the corresponding number of input factors read on the x-axis, yielding a total number of 255 RF models.

In Figure 6-8, I observed that the maximum accuracy of RF models increases rapidly when using one to three factors, then it reaches a plateau with more input factors. With one to three factors, we note a large variation in accuracy among the combinations, these small numbers of factors do not sufficiently explain the variability of NPQ, evidencing the presence of primary factors.

Table 6-1: Best combination and related accuracy and determination coefficient (R^2) for combinations of one to five input factors.

Numbers of parameters	Combination	Result for the best combination	
		Accuracy (%)	R^2
1	PAR	73.9	0.61
2	PAR, SWC	89.1	0.84
3	x, SWC, Chl_content	93.8	0.93
4	x, SWC, ST, Chl_content	94.6	0.95
5	x, SWC, ST, Chl_content, VPD	95.1	0.96

In Table 6-1, we see that we can achieve accuracies around 90% with two to three parameters, using the combinations (PAR, SWC), or (x, SWC, Chl_content), respectively.

6.3.2.3 *Empirical expressions of NPQ in drought conditions*

RF models are powerful for prediction, but their results are typically based on statistical relationships and do not provide explicit equations that can be easily implemented into ORCHIDEE. We prefer to avoid this kind of "black box", and build instead an empirical model, based on the main factors previously identified, thanks to the RF models.

I have fitted the parameters of the 19 empirical models listed in Table 6-2 against my dataset, relating kNPQ to the main factors. Models 1 to 9 and 10 to 19, respectively, use the best combinations of two or three input factors identified during the RF analysis. To evaluate the models we used AIC, RedChi2 and RMSD scores, their calculation and meaning were explained 6.2.3.4.

Table 6-2: Expression and performance of the 19 empirical equations tested for kNPQ. ' *' stands for the multiplication operation, '**' stands for the power operation, and 'exp' stands for the exponential function. A1, A2, A3 and A4 are parameters adjustable through the fitting. The reduced Chi2 score is noted RedChi2, the Akaike Information Criterion is noted AIC, the root mean square difference is noted RMSD. Scores are noted 'high' when the model performs too poorly and the related scores are too high to be computed.

Model number	Model	RedChi2	AIC	RMSD
1	kNPQ = (A1*PAR*SWC)	3.55	3430.27	1.88
2	kNPQ = (PAR*A1)+(SWC*A2)	2.67	2660.4	1.63
3	kNPQ = (PAR*A1)*(SWC*A2)	3.55	3432.27	1.88
4	kNPQ = (PAR*A1)+(A2*exp(SWC*A3))	2.43	2411.89	1.56
5	kNPQ = (PAR*A1)*((A2*exp(SWC*A3)))	2.59	2579.62	1.61
6	kNPQ = ((A2*exp(PAR*A1))+SWC*A3)	high	high	16.92
7	kNPQ = ((A2*exp((PAR*A1)))*SWC*A3)	high	high	16.92
8	kNPQ = exp(PAR*A1*SWC)	4.08	3810.88	2.02
9	kNPQ = exp((PAR*A1)+(A2*SWC))	high	high	16.92
10	kNPQ = (Chl_content*X*A1)+(SWC*A2)	3.68	3527.03	1.92
11	kNPQ = (Chl_content*X*A1)*(SWC*A2)	4.01	3766.02	2
12	kNPQ = (Chl_content*X*A1)+(A2*exp(SWC*A3))	3.67	3527.13	1.92
13	kNPQ = (Chl_content*X*A1)*(A2*exp(SWC*A3))	3.67	3525.55	1.92
14	kNPQ = (Chl_content*A1)+(SWC*A2)	5.42	4580.67	2.33
15	kNPQ = (Chl_content*A1)+(A2*exp(SWC*A3))	4.55	4104.85	2.13
16	kNPQ = (Chl_content*A1**2)+(A2*SWC+A3)+X*A4	2.3	2261.43	1.52
17	kNPQ = (A1*exp(Chl_content))+(A2*SWC+A3)+X*A4	2.17	2097.46	1.47
18	kNPQ = (A1*exp(Chl_content))*(A2*SWC+A3)*X*A4	2.37	2340.08	1.54
19	kNPQ = (A1*Chl_content)+(A2*exp(SWC)+A3)+X*A4	2.3	2261.25	1.52

The best model using two input factors is Model 4, with the following fitted parameter values:

A1 = 0.004 +/- 7.18 x 10^5, A2=12.98 +/- 2.69 A3=-27.04 +/- 2.50

The best model using three input factors is Model 17, with the following fitted parameter values:

A1 = 14.02+/- 1.08 , A2 = 14.57+/- 1.44, A3 = -11.33 +/- 0.84, A4 = -18.02 +/- 2.05

Even though Model 17 has more explanatory factors and is more complex, its lower AIC score compared to all others justifies its use.

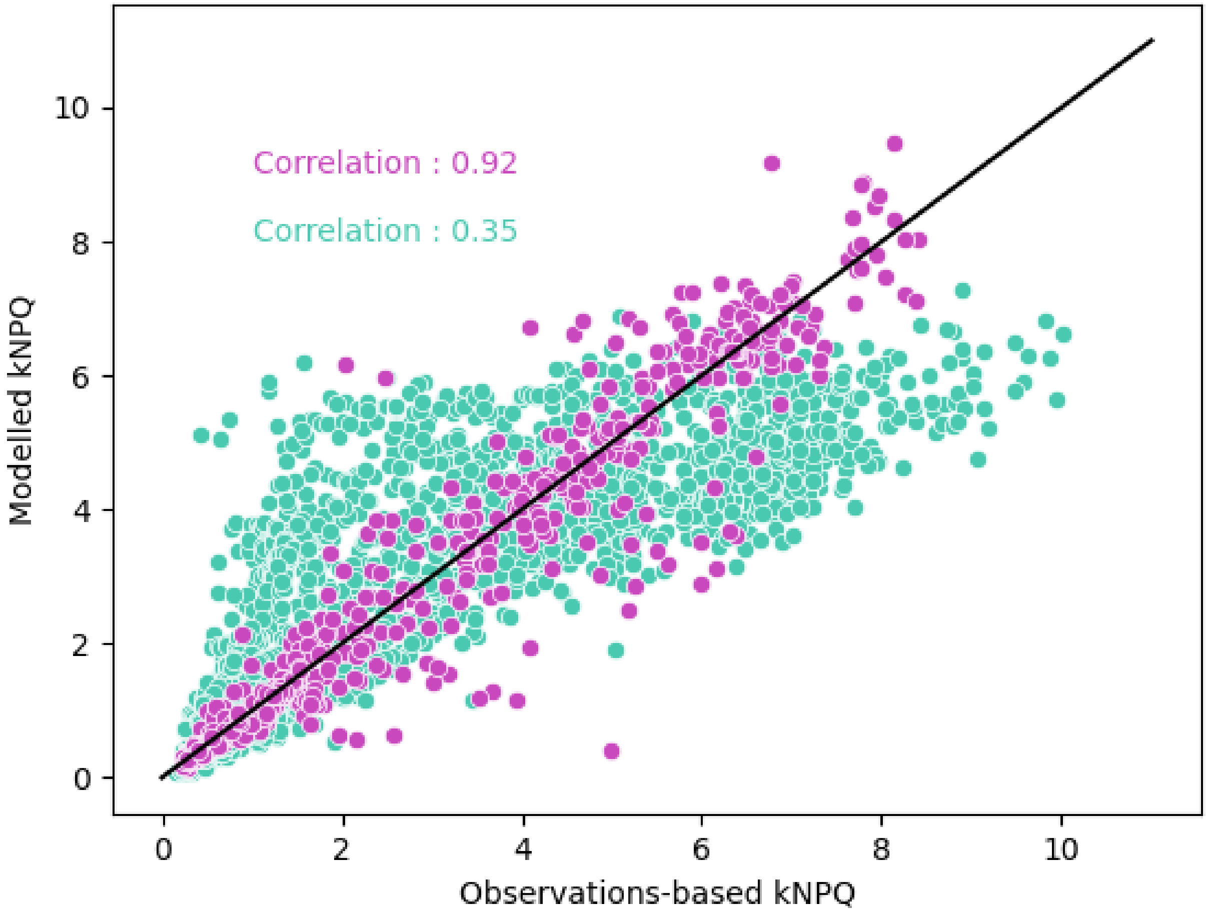

Figure 6-9: Modelled versus observations-based kNPQ for the RF model (magenta) and Model 17 (green). The black 1:1 line represents a perfect fitting.

As shown in Figure 6-9, the RF model outperforms the empirical model, as expected. As a perspective, we could consider using another machine learning approach, the Shapley values. Shapley values are used to assess the importance of input features in making predictions, when using RF or XGBoost models. They provide insights into how each feature contributes to the statistical model, allowing for a better understanding of the model's behaviour and the relative importance of input factors. It could provide a better insight on the relations between kNPQ and the considered factors, as shown for example for GPP (Wang et al., 2022).

6.4 Discussion

In (Wang et al., 2018) the authors showed, in apple tree leaves, that the relationship between leaf water potential and assimilation is not linear. The authors identified two phases. In the first phase, the decline in photosynthetic CO_2 assimilation is linked to stomatal closure, which induce a decline in Jmax and NADPH production. In the second phase, the reduction of CO_2 assimilation is due to non-stomatal limitation. This is caused by an over-reduction of the electron transport chain, leading to increased production of ROS. The accumulation of ROS inhibits the turnover of the D1 protein of PSII, which limits electron transport from Q_a to Q_b. Additionally, NADP+ declines, further limiting ATP synthesis and the regeneration of RuBP.

In this study, our best empirical model for kNPQ expresses the sum of three reactions. These three reactions evolve at different rates, x, which depends on photosynthetic efficiency and stomatal conductance, is fast. The SWC changes more slowly over time, and the chlorophyll content varies at an even slower pace. Additionally, their relationship to NPQ, as represented in Model 17, is also different. x and SWC are linearly related to NPQ, while NPQ shows an exponential relationship with Chl_content.

7 Chapter 7: Conclusions and outlooks

The main objective of this thesis was to establish connections between the understanding of plant regulation at the molecular level and the processes represented in land surface models, in order to improve global simulations of plant CO_2 uptake under stress conditions. Throughout the thesis, we were able to explore multiple scales of comprehension. In Chapter 1, we investigated how PR metabolites could potentially play a role in isolated PSII regulation. In Chapter 2, we examined how the electron linear flux and the redox state of PQ pool could contribute to the communication between the chloroplast and the rest of the plant in drought stress conditions. In Chapter 3, we focused on the response of the linear electron transfer chain and its rapid reaction to temperature variations, with a particular emphasis on the sensitivity of PSII and PSI to high temperatures. In Chapter 4, we updated the NPQ model implemented in the ORCHIDEE land surface model in the case of boreal evergreen needleleaf forests, favouring a process-based representation of the sustained mechanism resulting from modifications in the organization of the antenna systems at the chloroplast level. Additionally, we highlighted the importance of co-assimilating SIF and GPP to avoid overfitting and simulate both variables in a consistent way. Finally, in the last chapter, we studied poplar as a model tree species in drought conditions, and developed a stress-extended NPQ model, that could be further implemented in the ORCHIDEE LSM, to improve the drought-stress response of the simulated GPP and SIF.

For each chapter, we can propose perspectives for improvement. In Chapter 2, it would be necessary to quantify glycolate in vivo at the chloroplast level to validate its potential role in PSII protection under stress conditions. In Chapter 3, quantifying apocarotenoids in roots and leaves separately would be crucial to validate the significance of beta-cyclocitral or other apocarotenoids in the chloroplast to root communication system. Conducting grafting experiments could confirm the existence of communication between chloroplasts and roots. Additionally, studying the response of root systems by manipulating the redox state of the PQ pool for wild-type plants by other means such as modifying the light quality could provide valuable insights. Chapter 4 would benefit from more comprehensive measurements encompassing a wider range of temperatures and plant ages to thoroughly examine the combined effect of leaf senescence and temperature sensitivity on photosynthesis. Chapters 5 and 6 advocate the need for a better representation of NPQ in LSMs, which is required for a correct interpretation and use of SIF estimates. The improvements concern both potential PFT specificities, and stress conditions. On top of the molecular-level studies, LSMs would also benefit from a global FLUXNET-like network of standardized high-frequency active and passive fluorescence measurements, to validate and constrain the next-generation NPQ models.

The seminal publications inserted in this thesis formed the basis for an ANR proposal entitled FACET (“Multiscale use of fluorescence for an enhanced understanding of the vegetation carbon uptake during drought”) that just got accepted (https://anr.fr/fileadmin/aap/2023/selection/aapg-2023-selection-vague-3.pdf, last access: 10 July 2023), opening the way for even deeper collaborations.

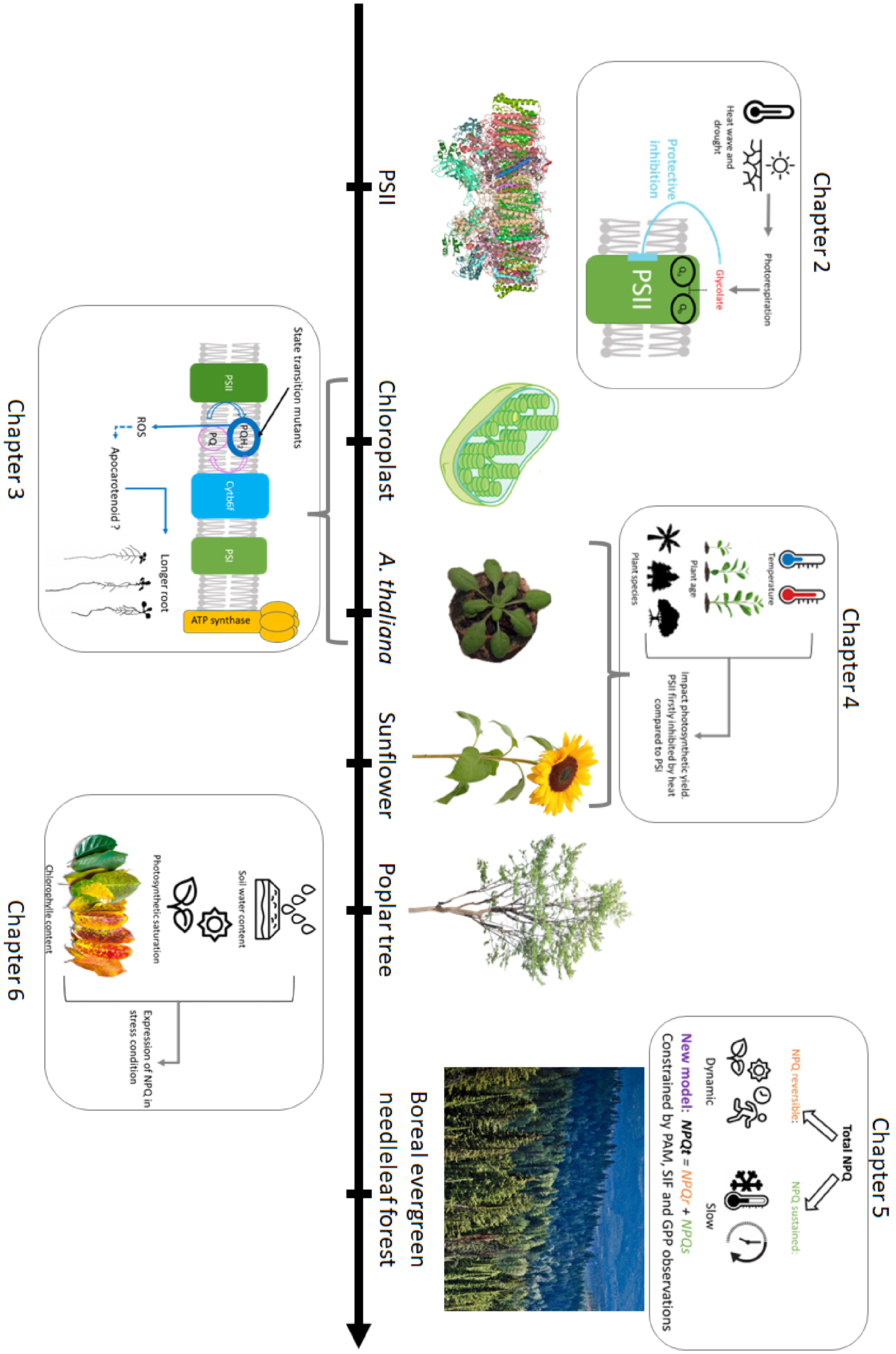

Figure 7-1: Summary diagram, regulation of photosynthesis from PSII to global scale. Each box summarises a chapter along the axis indicating the scale at which photosynthesis is studied.

8 Abbreviations

ADP: Adenosine diphosphate
AIC : Akaike Information Criterion
APAR: absorbed photosynthetically active radiation
ATP: Adenosine triphosphate
CAM: crassulacean acid metabolism
CC: climate change
Cyt b_6f: Cytochrome b_6f complex
DCBQ: 2,6-dichloro-1,4-benzo-quinone
DNA: Deoxyribonucleic acid
EPR: Electron paramagnetic resonance
ESA: European spatial agency
FAD: Flavin adenine dinucleotide
FADH: semiquinone flavin adenine dinucleotide
Fd: Ferredoxin
FNR: ferredoxin-NADP$^+$ reductase
GOX: glycolate oxidase
GPP: gross primary production
H_2O: water
HEPES:(4-(2-hydroxyethyl)-1-piperazineethanesulfonic acid
IC50 value: concentration at which 50% of the inhibitory effect is observed.
IPCC: Intergovernmental Panel on Climate Change
IPSL: Institut Pierre-Simon Laplace
LAI: leaf area index
LC: Liquid chromatography
LCHII: Light-harvesting complex II
LHCII: light harvesting complex
LSM: land surface model
LT: leaf temperature
MES: 2-(N-Morpholino)ethanesulfonic acid
MS: mass spectrometry
NADH: Nicotinamide adenine dinucleotide
NADP: Nicotinamide adenine dinucleotide phosphate
NPQ: non photochemical quenching
OEC: oxygen evolving complex
ORCHIDAS: ORCHIDEE Data Assimilation System
ORCHIDEE: Organising Carbon and Hydrology In Dynamic Ecosystems
PAM: pulse amplitude modulation
PAR: photosynthetic active radiation
PC: plastocyanin
PFT: plant functional type

PGA: phosphoglycerate
PGLP: 2-phosphoglycolate phosphatase
PQ: plastoquinone
PQH$_2$: reduced plastoquinone
PR: photorespiration
PSI: photosystem I
PSII: photosystem II
PTOX: plastid terminal oxidase
Q$_a$: quinone A
Q$_b$: quinone B
RF: random forest
RH: relative humidity
RMSD: root mean square deviation.
RNA: ribonucleic acid
ROS: reactive oxygen species
SEC: soil electroconductivity
SIF: sun-induced fluorescence
ST: soil temperature
SWC: soil water content
TA: air temperature
TL: leaf temperature
TROPOMI: tropospheric monitoring instrument
VPD: vapor pressure deficit

9 List of Figures

10 List of Tables

11 References

Abadie, C., & Tcherkez, G. (2019). Plant sulphur metabolism is stimulated by photorespiration. *Communications Biology*, *2*(1). https://doi.org/10.1038/s42003-019-0616-y

Agüera, E., Cabello, P., & de la Haba, P. (2010). Induction of leaf senescence by low nitrogen nutrition in sunflower (Helianthus annuus) plants. *Physiologia Plantarum*, *138*(3), 256–267. https://doi.org/10.1111/j.1399-3054.2009.01336.x

Allen, C. D., Macalady, A. K., Chenchouni, H., Bachelet, D., McDowell, N., Vennetier, M., Kitzberger, T., Rigling, A., Breshears, D. D., Hogg, E. H. (Ted), Gonzalez, P., Fensham, R., Zhang, Z., Castro, J., Demidova, N., Lim, J. H., Allard, G., Running, S. W., Semerci, A., & Cobb, N. (2010). A global overview of drought and heat-induced tree mortality reveals emerging climate change risks for forests. *Forest Ecology and Management*, *259*(4), 660–684. https://doi.org/10.1016/j.foreco.2009.09.001

Anav, A., Friedlingstein, P., Beer, C., Ciais, P., Harper, A., Jones, C., Murray-Tortarolo, G., Papale, D., Parazoo, N. C., Peylin, P., Piao, S., Sitch, S., Viovy, N., Wiltshire, A., & Zhao, M. (2015). Spatiotemporal patterns of terrestrial gross primary production: A review: GPP Spatiotemporal Patterns. *Reviews of Geophysics*, *53*(3), 785–818. https://doi.org/10.1002/2015RG000483

Bacour, C., Maignan, F., MacBean, N., Porcar-Castell, A., Flexas, J., Frankenberg, C., Peylin, P., Chevallier, F., Vuichard, N., & Bastrikov, V. (2019). Improving Estimates of Gross Primary Productivity by Assimilating Solar-Induced Fluorescence Satellite Retrievals in a Terrestrial Biosphere Model Using a Process-Based SIF Model. *Journal of Geophysical Research: Biogeosciences*, *124*(11), 3281–3306. https://doi.org/10.1029/2019JG005040

Bag, P., Chukhutsina, V., Zhang, Z., Paul, S., Ivanov, A. G., Shutova, T., Croce, R., Holzwarth, A. R., & Jansson, S. (2020). Direct energy transfer from photosystem II to photosystem I confers winter sustainability in Scots Pine. *Nature Communications*, *11*(1). https://doi.org/10.1038/s41467-020-20137-9

Baker, N. R. (2008). Chlorophyll Fluorescence: A Probe of Photosynthesis In Vivo. *Annual Review of Plant Biology*, *59*(1), 89–113. https://doi.org/10.1146/annurev.arplant.59.032607.092759

Bastrikov, V., MacBean, N., Bacour, C., Santaren, D., Kuppel, S., & Peylin, P. (2018). Land surface model parameter optimisation using in situ flux data: comparison of gradient-based versus random search algorithms (a case study using ORCHIDEE v1.9.5.2). *Geoscientific Model Development*, *11*(12), 4739–4754. https://doi.org/10.5194/gmd-11-4739-2018

Boucher, O., Servonnat, J., Albright, A. L., Aumont, O., Balkanski, Y., Bastrikov, V., Bekki, S., Bonnet, R., Bony, S., Bopp, L., Braconnot, P., Brockmann, P., Cadule, P., Caubel, A., Cheruy, F., Codron, F., Cozic, A., Cugnet, D., D'Andrea, F., … Vuichard, N. (2020). Presentation and Evaluation of the IPSL-CM6A-LR Climate Model. *Journal of Advances in Modeling Earth Systems*, *12*(7). https://doi.org/10.1029/2019MS002010

Boyes, D. C., Zayed, A. M., Ascenzi, R., Mccaskill, A. J., Hoffman, N. E., Davis, K. R., & Görlach, J. (2001). Growth Stage-Based Phenotypic Analysis of Arabidopsis: A Model for High Throughput Functional Genomics in Plants. In *The Plant Cell* (Vol. 13). www.plantcell.org

Brinkert, K., De Causmaecker, S., Krieger-Liszkay, A., Fantuzzi, A., & Rutherford, A. W. (2016a). Bicarbonate-induced redox tuning in PhoQtosystem II for regulation and protection. *Proceedings of the National Academy of Sciences*, *113*(43), 12144–12149. https://doi.org/10.1073/pnas.1608862113

Brinkert, K., De Causmaecker, S., Krieger-Liszkay, A., Fantuzzi, A., & Rutherford, A. W. (2016b). Bicarbonate-induced redox tuning in Photosystem II for regulation and protection. *Proceedings of the National Academy of Sciences*, *113*(43), 12144–12149. https://doi.org/10.1073/pnas.1608862113

Chaves, M. M., Pereira, J. S., Maroco, J., Rodrigues, M. L., Ricardo, C. P. P., Osório, M. L., Carvalho, I., Faria, T., & Pinheiro, C. (2002). How plants cope with water stress in the field. Photosynthesis and growth. *Annals of Botany*, *89*(SPEC. ISS.), 907–916. https://doi.org/10.1093/aob/mcf105

Collatz, Ribas-Carbo Miquel, & Berry Joseph. (1992). Coupled Photosynthesis-Stomata1 Conductance Model for Leaves of C4 Plants*. In *Aust. J. Plant Physiol* (Vol. 19).

Crausbay, S. D., Higuera, P. E., Sprugel, D. G., & Brubaker, L. B. (2017). Fire catalyzed rapid ecological change in lowland coniferous forests of the Pacific Northwest over the past 14,000 years. *Ecology*, *98*(9), 2356–2369. https://doi.org/10.1002/ecy.1897

Dechant, B., Ryu, Y., Badgley, G., Zeng, Y., Berry, J. A., Zhang, Y., Goulas, Y., Li, Z., Zhang, Q., Kang, M., Li, J., & Moya, I. (2020). Canopy structure explains the relationship between photosynthesis and sun-induced chlorophyll fluorescence in crops. *Remote Sensing of Environment*, *241*. https://doi.org/10.1016/j.rse.2020.111733

Dellero, Y., Jossier, M., Glab, N., Oury, C., Tcherkez, G., & Hodges, M. (2016). Decreased glycolate oxidase activity leads to altered carbon allocation and leaf senescence after a transfer from high CO2 to ambient air in Arabidopsis thaliana. *Journal of Experimental Botany*, *67*(10), 3149–3163. https://doi.org/10.1093/jxb/erw054

Duffy, K. A., Schwalm, C. R., Arcus, V. L., Koch, G. W., Liang, L. L., & Schipper, L. A. (2021). *How close are we to the temperature tipping point of the terrestrial biosphere?*

Dusenge, M. E., Duarte, A. G., & Way, D. A. (2019). Plant carbon metabolism and climate change: elevated CO2 and temperature impacts on photosynthesis, photorespiration and respiration. *New Phytologist*, *221*(1), 32–49. https://doi.org/10.1111/nph.15283

Eisenhut, M., Bräutigam, A., Timm, S., Florian, A., Tohge, T., Fernie, A. R., Bauwe, H., & Weber, A. P. M. (2017). Photorespiration Is Crucial for Dynamic Response of Photosynthetic Metabolism and Stomatal Movement to Altered CO2 Availability. *Molecular Plant*, *10*(1), 47–61. https://doi.org/10.1016/j.molp.2016.09.011

Farquhar, G. D., Von Caemmerer, S., & Berry, J. A. (1980). A biochemical model of photosynthetic CO2 assimilation in leaves of C3 species. *Planta*, *149*(1), 78–90. https://doi.org/10.1007/BF00386231

Field, C. B., Behrenfeld, M. J., Randerson, J. T., & Falkowski, P. (1998). *Primary Production of the Biosphere: Integrating Terrestrial and Oceanic Components*. http://www.sciencemag.org

Fisher, R. A., & Koven, C. D. (2020). Perspectives on the Future of Land Surface Models and the Challenges of Representing Complex Terrestrial Systems. *Journal of Advances in Modeling Earth Systems*, *12*(4). https://doi.org/10.1029/2018MS001453

Flügel, F., Timm, S., Arrivault, S., Florian, A., Stitt, M., Fernie, A. R., & Bauwe, H. (2017). The photorespiratory metabolite 2-phosphoglycolate regulates photosynthesis and starch accumulation in Arabidopsis. *Plant Cell*, *29*(10), 2537–2551. https://doi.org/10.1105/tpc.17.00256

Forzieri, G., Dakos, V., McDowell, N. G., Ramdane, A., & Cescatti, A. (2022). Emerging signals of declining forest resilience under climate change. *Nature*, *608*(7923), 534–539. https://doi.org/10.1038/s41586-022-04959-9

Franck, F., Juneau, P., & Popovic, R. (2002). *Resolution of the Photosystem I and Photosystem II contributions to chlorophyll fluorescence of intact leaves at room temperature*. www.bba-direct.com

Frankenberg, C., Fisher, J. B., Worden, J., Badgley, G., Saatchi, S. S., Lee, J. E., Toon, G. C., Butz, A., Jung, M., Kuze, A., & Yokota, T. (2011). New global observations of the terrestrial carbon cycle from GOSAT: Patterns of plant fluorescence with gross primary productivity. *Geophysical Research Letters*, *38*(17). https://doi.org/10.1029/2011GL048738

Friedlingstein, P., Meinshausen, M., Arora, V. K., Jones, C. D., Anav, A., Liddicoat, S. K., & Knutti, R. (2014). Uncertainties in CMIP5 climate projections due to carbon cycle feedbacks. *Journal of Climate*, *27*(2), 511–526. https://doi.org/10.1175/JCLI-D-12-00579.1

Friedlingstein, P., O'Sullivan, M., Jones, M. W., Andrew, R. M., Gregor, L., Hauck, J., Le Quéré, C., Luijkx, I. T., Olsen, A., Peters, G. P., Peters, W., Pongratz, J., Schwingshackl, C., Sitch, S., Canadell, J. G., Ciais, P., Jackson, R. B., Alin, S. R., Alkama, R., … Zheng, B. (2022). Global Carbon Budget 2022. *Earth System Science Data*, *14*(11), 4811–4900. https://doi.org/10.5194/essd-14-4811-2022

Gampe, A., Zscheischler, D. ;, & Reichstein, J. ; (2022). *ORE Open Research Exeter TITLE Increasing impact of warm droughts on northern ecosystem productivity over recent decades A NOTE ON VERSIONS*. http://hdl.handle.net/10871/129361

Gill, S. S., & Tuteja, N. (2010). Reactive oxygen species and antioxidant machinery in abiotic stress tolerance in crop plants. In *Plant Physiology and Biochemistry* (Vol. 48, Issue 12, pp. 909–930). https://doi.org/10.1016/j.plaphy.2010.08.016

Guanter, L., Aben, I., Tol, P., Krijger, J. M., Hollstein, A., Köhler, P., Damm, A., Joiner, J., Frankenberg, C., & Landgraf, J. (2015). Potential of the TROPOspheric Monitoring Instrument (TROPOMI) onboard the Sentinel-5 Precursor for the monitoring of terrestrial chlorophyll fluorescence. *Atmospheric Measurement Techniques*, *8*(3), 1337–1352. https://doi.org/10.5194/amt-8-1337-2015

Guanter, L., Bacour, C., Schneider, A., Aben, I., Van Kempen, T. A., Maignan, F., Retscher, C., Köhler, P., Frankenberg, C., Joiner, J., & Zhang, Y. (2021). The TROPOSIF global sun-induced fluorescence dataset from the Sentinel-5P TROPOMI mission. *Earth System Science Data*, *13*(11), 5423–5440. https://doi.org/10.5194/essd-13-5423-2021

Hannah Ritchie and Max Roser. (2013). Land Use. *Our World in Data*.

Harris, N. L., Gibbs, D. A., Baccini, A., Birdsey, R. A., De Bruin, S., Farina, M., Fatoyinbo, L., Hansen, M. C., Herold, M., Houghton, R. A., Potapov, P. V, Suarez, D. R., Roman-Cuesta, R. M., Saatchi, S. S., Slay, C. M., Turubanova, S. A., & Tyukavina, A. (2021). Global maps of twenty-first century forest carbon fluxes. *Nature Climate Change*, *11*(3), 234–240. https://doi.org/10.1038/s41558-020-00976-6

Hayes, D. J., Butman, D. E., Domke, G. M., Fisher, J. B., Neigh, C. S. R., & Welp, L. R. (2022). Boreal forests. In *Balancing Greenhouse Gas Budgets* (pp. 203–236). Elsevier. https://linkinghub.elsevier.com/retrieve/pii/B9780128149522000253

Helm, L. T., Shi, H., Lerdau, M. T., & Yang, X. (2020). Solar-induced chlorophyll fluorescence and short-term photosynthetic response to drought. *Ecological Applications*, *30*(5). https://doi.org/10.1002/eap.2101

Hodges, M., Dellero, Y., Keech, O., Betti, M., Raghavendra, A. S., Sage, R., Zhu, X. G., Allen, D. K., & Weber, A. P. M. (2016). Perspectives for a better understanding of the metabolic integration of photorespiration within a complex plant primary metabolism network. In *Journal of Experimental Botany* (Vol. 67, Issue 10, pp. 3015–3026). Oxford University Press. https://doi.org/10.1093/jxb/erw145

Intergovernmental Panel on Climate Change. (2023). Changing State of the Climate System. In *Climate Change 2021 – The Physical Science Basis* (pp. 287–422). Cambridge University Press. https://doi.org/10.1017/9781009157896.004

Ivanov, A. G., Velitchkova, M. Y., Allakhverdiev, S. I., & Huner, N. P. A. (2017a). Heat stress-induced effects of photosystem I: an overview of structural and functional responses. *Photosynthesis Research*, *133*(1–3), 17–30. https://doi.org/10.1007/s11120-017-0383-x

Ivanov, A. G., Velitchkova, M. Y., Allakhverdiev, S. I., & Huner, N. P. A. (2017b). Heat stress-induced effects of photosystem I: an overview of structural and functional responses. In *Photosynthesis Research* (Vol. 133, Issues 1–3, pp. 17–30). Springer Netherlands. https://doi.org/10.1007/s11120-017-0383-x

Jiménez-Arias, D., García-Machado, F. J., Morales-Sierra, S., Luis, J. C., Suarez, E., Hernández, M., Valdés, F., & Borges, A. A. (2019). Lettuce plants treated with L-pyroglutamic acid increase yield under water deficit stress. *Environmental and Experimental Botany*, *158*, 215–222. https://doi.org/10.1016/j.envexpbot.2018.10.034

Kattge, J., & Knorr, W. (2007). Temperature acclimation in a biochemical model of photosynthesis: a reanalysis of data from 36 species. *Plant, Cell & Environment*, *30*(9), 1176–1190. https://doi.org/10.1111/j.1365-3040.2007.01690.x

Khan, N., Bano, A., & Babar, M. A. (2019). Metabolic and physiological changes induced by plant growth regulators and plant growth promoting rhizobacteria and their impact on drought tolerance in Cicer arietinum L. *PLOS ONE*, *14*(3), e0213040. https://doi.org/10.1371/journal.pone.0213040

Krieger-Liszkay, A. (2004). Singlet oxygen production in photosynthesis. *Journal of Experimental Botany*, *56*(411), 337–346. https://doi.org/10.1093/jxb/erh237

Krieger-Liszkay, A., Krupinska, K., & Shimakawa, G. (2019). The impact of photosynthesis on initiation of leaf senescence. *Physiologia Plantarum*, *166*(1), 148–164. https://doi.org/10.1111/ppl.12921

Krinner, G., Viovy, N., de Noblet-Ducoudré, N., Ogée, J., Polcher, J., Friedlingstein, P., Ciais, P., Sitch, S., & Prentice, I. C. (2005). A dynamic global vegetation model for studies of the coupled atmosphere-biosphere system. *Global Biogeochemical Cycles*, *19*(1), 1–33. https://doi.org/10.1029/2003GB002199

Lesk, C., Rowhani, P., & Ramankutty, N. (2016). Influence of extreme weather disasters on global crop production. *Nature*, *529*(7584), 84–87. https://doi.org/10.1038/nature16467

Li, X., Cai, W., Liu, Y., Li, H., Fu, L., Liu, Z., Xu, L., Liu, H., Xu, T., & Xiong, Y. (2017). Differential TOR activation and cell proliferation in Arabidopsis root and shoot apexes. *Proceedings of the National Academy of Sciences of the United States of America*, *114*(10), 2765–2770. https://doi.org/10.1073/pnas.1618782114

Li, X., & Xiao, J. (2020). Global climatic controls on interannual variability of ecosystem productivity: Similarities and differences inferred from solar-induced chlorophyll fluorescence and enhanced vegetation index. *Agricultural and Forest Meteorology*, *288–289*. https://doi.org/10.1016/j.agrformet.2020.108018

Long, S. P. (2003). Gas exchange measurements, what can they tell us about the underlying limitations to photosynthesis? Procedures and sources of error. *Journal of Experimental Botany*, *54*(392), 2393–2401. https://doi.org/10.1093/jxb/erg262

MacBean, N., Maignan, F., Bacour, C., Lewis, P., Peylin, P., Guanter, L., Köhler, P., Gómez-Dans, J., & Disney, M. (2018). Strong constraint on modelled global carbon uptake using solar-induced chlorophyll fluorescence data. *Scientific Reports*, *8*(1). https://doi.org/10.1038/s41598-018-20024-w

Makela, A., Hari, P., Berninger, F., Hanninen, H., & Nikinmaa, E. (2004). Acclimation of photosynthetic capacity in Scots pine to the annual cycle of temperature. *Tree Physiology*, *24*(4), 369–376. https://doi.org/10.1093/treephys/24.4.369

Marrs, J. K., Reblin, J. S., Logan, B. A., Allen, D. W., Reinmann, A. B., Bombard, D. M., Tabachnik, D., & Hutyra, L. R. (2020). Solar-Induced Fluorescence Does Not Track Photosynthetic Carbon Assimilation Following Induced Stomatal Closure. *Geophysical Research Letters*, *47*(15). https://doi.org/10.1029/2020GL087956

Martini, D., Sakowska, K., Wohlfahrt, G., Pacheco-Labrador, J., van der Tol, C., Porcar-Castell, A., Magney, T. S., Carrara, A., Colombo, R., El-Madany, T. S., Gonzalez-Cascon, R., Martín, M. P., Julitta, T., Moreno, G., Rascher, U., Reichstein, M., Rossini, M., & Migliavacca, M. (2022). Heatwave breaks down the linearity between sun-induced fluorescence and gross primary production. *New Phytologist*, *233*(6), 2415–2428. https://doi.org/10.1111/nph.17920

Medlyn, B. E., Dreyer, E., Ellsworth, D., Forstreuter, M., Harley, P. C., Kirschbaum, M. U. F., Le Roux, X., Montpied, P., Strassemeyer, J., Walcroft, A., Wang, K., & Loustau, D. (2002). Temperature response of parameters of a biochemically based model of photosynthesis. II. A review of experimental data: Temperature response of photosynthetic parameters - review. *Plant, Cell & Environment*, *25*(9), 1167–1179. https://doi.org/10.1046/j.1365-3040.2002.00891.x

Messant, M., Timm, S., Fantuzzi, A., Weckwerth, W., Bauwe, H., Rutherford, A. W., & Krieger-Liszkay, A. (2018). Glycolate Induces Redox Tuning Of Photosystem II in Vivo: Study of a Photorespiration Mutant. *Plant Physiology*, *177*(3), 1277–1285. https://doi.org/10.1104/pp.18.00341

Mohamed, H. S., Li, X., Dong, S., & Hassanein, M. F. (2020). Parametric equation to predict the SIF of cracked tubular T/Y-joints. *Journal of Constructional Steel Research*, *164*. https://doi.org/10.1016/j.jcsr.2019.105773

Mohammed, G. H., Colombo, R., Middleton, E. M., Rascher, U., van der Tol, C., Nedbal, L., Goulas, Y., Pérez-Priego, O., Damm, A., Meroni, M., Joiner, J., Cogliati, S., Verhoef, W., Malenovský, Z., Gastellu-Etchegorry, J. P., Miller, J. R., Guanter, L., Moreno, J., Moya, I., … Zarco-Tejada, P. J. (2019). Remote sensing of solar-induced chlorophyll fluorescence (SIF) in vegetation: 50 years of progress. *Remote Sensing of Environment*, *231*. https://doi.org/10.1016/j.rse.2019.04.030

Nath, K., Jajoo, A., Poudyal, R. S., Timilsina, R., Park, Y. S., Aro, E.-M., Nam, H. G., & Lee, C.-H. (2013). Towards a critical understanding of the photosystem II repair mechanism and its regulation during stress conditions. *FEBS Letters*, *587*(21), 3372–3381. https://doi.org/10.1016/j.febslet.2013.09.015

Nawrocki, W. J., Bailleul, B., Picot, D., Cardol, P., Rappaport, F., Wollman, F. A., & Joliot, P. (2019). The mechanism of cyclic electron flow. In Biochimica et Biophysica Acta - Bioenergetics (Vol. 1860, Issue 5, pp. 433–438). Elsevier B.V. https://doi.org/10.1016/j.bbabio.2018.12.005

Newville, M., Stensitzki, T., Allen, D. B., Rawlik, M., Ingargiola, A., & Nelson, A. (2016). *Lmfit: Non-Linear Least-Square Minimization and Curve-Fitting for Python* (p. ascl:1606.014).

Öquist, G., & Huner, N. P. A. (2003). Photosynthesis of Overwintering Evergreen Plants. In *Annual Review of Plant Biology* (Vol. 54, pp. 329–355). Annual Reviews Inc. https://doi.org/10.1146/annurev.arplant.54.072402.115741

Parazoo, N. C., Frankenberg, C., Köhler, P., Joiner, J., Yoshida, Y., Magney, T., Sun, Y., & Yadav, V. (2019). Towards a Harmonized Long-Term Spaceborne Record of Far-Red Solar-Induced Fluorescence. *Journal of Geophysical Research: Biogeosciences*, *124*(8), 2518–2539. https://doi.org/10.1029/2019JG005289

Parthasarathy, A., Savka, M. A., & Hudson, A. O. (2019). The synthesis and role of β-alanine in plants. *Frontiers in Plant Science*, *10*. https://doi.org/10.3389/fpls.2019.00921

Pastorello, G., Trotta, C., Canfora, E., Chu, H., Christianson, D., Cheah, Y. W., Poindexter, C., Chen, J., Elbashandy, A., Humphrey, M., Isaac, P., Polidori, D., Ribeca, A., van Ingen, C., Zhang, L., Amiro, B., Ammann, C., Arain, M. A., Ardö, J., … Papale, D. (2020). The FLUXNET2015 dataset and the ONEFlux processing pipeline for eddy covariance data. *Scientific Data*, *7*(1), 225. https://doi.org/10.1038/s41597-020-0534-3

Pick, T. R., Bräutigam, A., Schulz, M. A., Obata, T., Fernie, A. R., & Weber, A. P. M. (2013). PLGG1, a plastidic glycolate glycerate transporter, is required for photorespiration and defines a unique class of metabolite transporters. *Proceedings of the National Academy of Sciences of the United States of America*, *110*(8), 3185–3190. https://doi.org/10.1073/pnas.1215142110

Pierrat, Z., Magney, T., Parazoo, N. C., Grossmann, K., Bowling, D. R., Seibt, U., Johnson, B., Helgason, W., Barr, A., Bortnik, J., Norton, A., Maguire, A., Frankenberg, C., & Stutz, J. (2022). Diurnal and Seasonal Dynamics of Solar-Induced Chlorophyll Fluorescence, Vegetation Indices, and Gross Primary Productivity in the Boreal Forest. *Journal of Geophysical Research: Biogeosciences*, *127*(2). https://doi.org/10.1029/2021JG006588

Pierrat, Z., Nehemy, M. F., Roy, A., Magney, T., Parazoo, N. C., Laroque, C., Pappas, C., Sonnentag, O., Grossmann, K., Bowling, D. R., Seibt, U., Ramirez, A., Johnson, B., Helgason, W., Barr, A., & Stutz, J. (2021). Tower-Based Remote Sensing Reveals Mechanisms Behind a Two-phased Spring Transition in a Mixed-Species Boreal Forest. *Journal of Geophysical Research: Biogeosciences*, *126*(5). https://doi.org/10.1029/2020JG006191

Porcar-Castell, A. (2011). A high-resolution portrait of the annual dynamics of photochemical and non-photochemical quenching in needles of Pinus sylvestris. *Physiologia Plantarum*, *143*(2), 139–153. https://doi.org/10.1111/j.1399-3054.2011.01488.x

Porcar-Castell, A., Tyystjärvi, E., Atherton, J., Van Der Tol, C., Flexas, J., Pfündel, E. E., Moreno, J., Frankenberg, C., & Berry, J. A. (2014). Linking chlorophyll a fluorescence to photosynthesis for remote sensing applications: Mechanisms and challenges. *Journal of Experimental Botany*, *65*(15), 4065–4095. https://doi.org/10.1093/jxb/eru191

Rachmilevitch, S., Cousins, A. B., & Bloom, A. J. (2004). *Nitrate assimilation in plant shoots depends on photorespiration*. http://www.pnas.orgcgidoi10.1073pnas.0404388101

Radwanski, E. R., & Last', R. L. (1995). Tryptophan Biosynthesis and Molecular Genetics Biochemical and. In *The Plant Cell* (Vol. 7).

Rath, J. R., Pandey, J., Yadav, R. M., Zamal, M. Y., Ramachandran, P., Mekala, N. R., Allakhverdiev, S. I., & Subramanyam, R. (2022). Temperature-induced reversible changes in photosynthesis efficiency and organization of thylakoid membranes from pea (Pisum sativum). *Plant Physiology and Biochemistry*, *185*, 144–154. https://doi.org/10.1016/j.plaphy.2022.05.036

Sage, R. F., & Khoshravesh, R. (2016). Passive CO2 concentration in higher plants. *Current Opinion in Plant Biology*, *31*, 58–65. https://doi.org/10.1016/j.pbi.2016.03.016

Sánchez, B., Rasmussen, A., & Porter, J. R. (2014). Temperatures and the growth and development of maize and rice: A review. *Global Change Biology*, *20*(2), 408–417. https://doi.org/10.1111/gcb.12389

Schwarte, S., & Bauwe, H. (2007). Identification of the photorespiratory 2-phosphoglycolate phosphatase, PGLP1, in arabidopsis. *Plant Physiology*, *144*(3), 1580–1586. https://doi.org/10.1104/pp.107.099192

Sedoud, A., Kastner, L., Cox, N., El-Alaoui, S., Kirilovsky, D., & Rutherford, A. W. (2011). Effects of formate binding on the quinone-iron electron acceptor complex of photosystem II. *Biochimica et Biophysica Acta - Bioenergetics*, *1807*(2), 216–226. https://doi.org/10.1016/j.bbabio.2010.10.019

Seiler, C., Melton, J. R., Arora, V. K., Sitch, S., Friedlingstein, P., Anthoni, P., Goll, D., Jain, A. K., Joetzjer, E., Lienert, S., Lombardozzi, D., Luyssaert, S., Nabel, J. E. M. S., Tian, H., Vuichard, N., Walker, A. P., Yuan, W., & Zaehle, S. (2022). Are Terrestrial Biosphere Models Fit for Simulating the Global Land Carbon Sink? *Journal of Advances in Modeling Earth Systems*, *14*(5). https://doi.org/10.1029/2021MS002946

Sekher Pannala, A., Rice-Evans, C., Sampson, J., & Singh, S. (1998). *Interaction of peroxynitrite with carotenoids and tocopherols within low density lipoprotein*.

Shi, X., & Bloom, A. (2021). Photorespiration: The futile cycle? *Plants*, *10*(5). https://doi.org/10.3390/plants10050908

Sieciechowicz, K. A., Joy, K. W., & Ireland, R. J. (1989). Effect of Methionine Sulfoximine on Asparaginase Activity and Ammonium Levels in Pea Leaves1. In *Plant Physiol* (Vol. 89).

Steffen Grebe, A. T. , A. A. B. , I. M. , P. B. , S. J. , M. T. , E.-M. A. (2004). Specific thylakoid protein phosphorylations are prerequisites for overwintering of Norway spruce (Picea abies) photosynthesis. *PNAS*, *117*. https://doi.org/10.6019/PXD018941

Tahjib-Ul-Arif, Md., Zahan, Mst. I., Karim, Md. M., Imran, S., Hunter, C. T., Islam, Md. S., Mia, Md. A., Hannan, Md. A., Rhaman, M. S., Hossain, Md. A., Brestic, M., Skalicky, M., & Murata, Y. (2021). Citric Acid-Mediated Abiotic Stress Tolerance in Plants. *International Journal of Molecular Sciences*, *22*(13), 7235. https://doi.org/10.3390/ijms22137235

Tol, C., Berry, J. A., Campbell, P. K. E., & Rascher, U. (2014). Models of fluorescence and photosynthesis for interpreting measurements of solar-induced chlorophyll fluorescence. *Journal of Geophysical Research: Biogeosciences*, *119*(12), 2312–2327. https://doi.org/10.1002/2014JG002713

Tuskan, G. A., Difazio, S., Jansson, † S, Bohlmann, † J, Grigoriev, † I, Hellsten, † U, Putnam, † N, Ralph, † S, Rombauts, † S, Salamov, † A, Schein, † J, Sterck, † L, Aerts, † A, Bhalerao, R. R., Bhalerao, R. P., Blaudez, D., Boerjan, W., Brun, A., Brunner, A., … Rokhsar, ‡ D. (2023). *The Genome of Black Cottonwood, Populus trichocarpa (Torr. & Gray)*. http://files/737/science.1128691.pdf

Van Lun, M., Hub, J. S., Van Der Spoel, D., & Andersson, I. (2014). CO2 and O2 distribution in rubisco suggests the small subunit functions as a CO2 reservoir. *Journal of the American Chemical Society*, *136*(8), 3165–3171. https://doi.org/10.1021/ja411579b

Voss, I., Sunil, B., Scheibe, R., & Raghavendra, A. S. (2013). Emerging concept for the role of photorespiration as an important part of abiotic stress response. *Plant Biology*, *15*(4), 713–722. https://doi.org/10.1111/j.1438-8677.2012.00710.x

Walker, A. P., De Kauwe, M. G., Bastos, A., Belmecheri, S., Georgiou, K., Keeling, R. F., McMahon, S. M., Medlyn, B. E., Moore, D. J. P., Norby, R. J., Zaehle, S., Anderson-Teixeira, K. J., Battipaglia, G., Brienen, R. J. W., Cabugao, K. G., Cailleret, M., Campbell, E., Canadell, J. G., Ciais, P., … Zuidema, P. A. (2021). Integrating the evidence for a terrestrial carbon sink caused by increasing atmospheric CO $_2$. *New Phytologist*, *229*(5), 2413–2445. https://doi.org/10.1111/nph.16866

Walther, S., Voigt, M., Thum, T., Gonsamo, A., Zhang, Y., Köhler, P., Jung, M., Varlagin, A., & Guanter, L. (2016). Satellite chlorophyll fluorescence measurements reveal large-scale decoupling of photosynthesis and greenness dynamics in boreal evergreen forests. *Global Change Biology*, *22*(9), 2979–2996. https://doi.org/10.1111/gcb.13200

Wang, H., Yan, S., Ciais, P., Wigneron, J. P., Liu, L., Li, Y., Fu, Z., Ma, H., Liang, Z., Wei, F., Wang, Y., & Li, S. (2022). Exploring complex water stress–gross primary production relationships: Impact of climatic drivers, main effects, and interactive effects. *Global Change Biology*, *28*(13), 4110–4123. https://doi.org/10.1111/gcb.16201

Wang, Z., Li, G., Sun, H., Ma, L., Guo, Y., Zhao, Z., Gao, H., & Mei, L. (2018). Effects of drought stress on photosynthesis and photosynthetic electron transport chain in young apple tree leaves. *Biology Open*, *7*(11). https://doi.org/10.1242/bio.035279

Waszczak, C., Carmody, M., & Kangasjärvi, J. (2018). *Annual Review of Plant Biology Reactive Oxygen Species in Plant Signaling*. https://doi.org/10.1146/annurev-arplant-042817

Water Cycle Changes. (2023). In *Climate Change 2021 – The Physical Science Basis* (pp. 1055–1210). Cambridge University Press. https://doi.org/10.1017/9781009157896.010

Weather and Climate Extreme Events in a Changing Climate. (2023). In *Climate Change 2021 – The Physical Science Basis* (pp. 1513–1766). Cambridge University Press. https://doi.org/10.1017/9781009157896.013

Wohlfahrt, G., Gerdel, K., Migliavacca, M., Rotenberg, E., Tatarinov, F., Müller, J., Hammerle, A., Julitta, T., Spielmann, F. M., & Yakir, D. (2018). Sun-induced fluorescence and gross primary productivity during a heat wave. *Scientific Reports*, *8*(1). https://doi.org/10.1038/s41598-018-32602-z

Yamori, W., Hikosaka, K., & Way, D. A. (2014). Temperature response of photosynthesis in C3, C4, and CAM plants: Temperature acclimation and temperature adaptation. *Photosynthesis Research*, *119*(1–2), 101–117. https://doi.org/10.1007/s11120-013-9874-6

Yan, K., Chen, P., Shao, H., Shao, C., Zhao, S., & Brestic, M. (2013). Dissection of Photosynthetic Electron Transport Process in Sweet Sorghum under Heat Stress. *PLoS ONE*, *8*(5). https://doi.org/10.1371/journal.pone.0062100

Yin, X., & Struik, P. C. (2009). C3 and C4 photosynthesis models: An overview from the perspective of crop modelling. *NJAS - Wageningen Journal of Life Sciences*, *57*(1), 27–38. https://doi.org/10.1016/j.njas.2009.07.001

Zhao, J., Lu, Z., Wang, L., & Jin, B. (2020). Plant Responses to Heat Stress: Physiology, Transcription, Noncoding RNAs, and Epigenetics. *International Journal of Molecular Sciences*, *22*(1), 117. https://doi.org/10.3390/ijms22010117

12 Résumé détaillé

L'absorption du CO_2 atmosphérique par la biosphère via la photosynthèse joue un rôle essentiel dans l'atténuation du changement climatique. La photosynthèse permet de transformer le carbone inorganique présent dans l'atmosphère (CO_2) en carbone organique contenu dans des sucres produits. Les émissions massives de CO_2 dans l'atmosphère, causées par les activités humaines telles que la combustion d'énergies fossiles et les changements d'utilisation des sols, ont entraîné le changement climatique que nous connaissons. Les plantes terrestres, par le biais de la photosynthèse, peuvent contribuer à atténuer les émissions de gaz à effet de serre en capturant le CO_2 produit.

Cependant, le changement climatique induit des contraintes importantes sur les plantes terrestres, telles que les températures élevées et la sécheresse. Ces conditions tendent à limiter la croissance et la survie des plantes, réduisant ainsi la captation du CO_2. Les modèles climatiques actuels présentent d'importantes incertitudes quant à la capacité des plantes terrestres à absorber le CO_2 dans les décennies à venir.

Dans cette thèse, nous étudions la régulation de la photosynthèse dans des conditions de stress induites par le changement climatique, en allant de l'échelle moléculaire au niveau des chloroplastes jusqu'à l'échelle globale des surfaces continentales. Nous utilisons prinicpalement des mesures de la fluorescence de la chlorophylle *a*, qui nous informent sur le processus photosynthétique. Lorsqu'un organisme photosynthétique reçoit de la lumière, il dissipe cette énergie sous trois formes : une partie de l'énergie est utilisée dans le processus photosynthétique pour produire des sucres, une partie est dissipée sous forme de chaleur (via des mécanismes appelés NPQ, de l’anglais Non-Photochemical Quenching), et enfin une partie est rayonnée sous forme de fluorescence. Ainsi, nous pouvons suivre le niveau de photosynthèse d'une plante grâce à la fluorescence de la chlorophylle. Ces mesures nous permettent de faire le lien entre les connaissances à petite et grande échelle.

J'ai étudié la régulation de la photosynthèse à cinq échelles différentes, allant des chloroplastes aux forêts boréales à aiguilles persistantes. Chaque chapitre, du 2 au 6, étudie la photosynthèse à une échelle différente. Le chapitre 1 propose une introduction générale à la photosynthèse, présente les concepts utilisés pour la mesurer et la modéliser.

Dans le chapitre 2, nous examinons les métabolites de la photorespiration, en particulier le glycolate, qui peut protéger le photosystème II contre le stress oxydatif. Le chapitre 3 tend à montrer que l'état redox du pool de plastoquinones peut jouer un rôle dans la régulation du développement racinaire et conférer une résistance au stress hydrique. Le chapitre 4 aborde l'impact de l'âge et de l'espèce des plantes sur l'inhibition de la photosynthèse due aux températures élevées. De plus, nous observons que le photosystème II semble être plus affecté par les hautes températures que le photosystème I.

Dans le chapitre 5, nous nous concentrons sur les forêts boréales à aiguilles persistantes. Nous modifions le modèle de NPQ dans le modèle de surfaces continentales ORCHIDEE en tenant compte des observations faites sur ce type de plante pendant l'hiver. Nous définissons un NPQ spécifique à l'hiver qui se met en place pendant plusieurs jours et interrompt pratiquement la photosynthèse pendant cette période, ainsi qu'un NPQ qui régule dynamiquement la photosynthèse à l'échelle de la demi-heure pendant la saison de croissance. Ensuite, nous assimilons des données satellitaires de fluorescence induite par le soleil (SIF) et des estimations *in situ* de la production primaire brute (GPP), afin d'améliorer la modélisation de la GPP pour les forêts boréales à aiguilles persistantes. Enfin, dans le chapitre 6, nous étudions la réponse des peupliers à trois semaines de fortes températures et de sécheresse afin de formuler un modèle de NPQ adapté à ces conditions. Nous proposons un modèle empirique du NPQ en conditions de stress en utilisant trois variables environnementales et physiologiques.

Dans l'ensemble, ce travail a permis de faire dialoguer des recherches sur des mécanismes moléculaires de la régulation de la photosynthèse avec des applications à l’échelle du globe, ce qui contribue à améliorer la modélisation de l'absorption du CO_2 atmosphérique par les surfaces continentales, et in fine à réduire les incertitudes liées au cycle du carbone continental dans les projections climatiques.

13 Appendix

13.1 “Moderate drought stress stabilizes the primary quinone acceptor Q_a and the secondary quinone acceptor Q_b in photosystem II” (Leverne and Krieger-Liszkay, 2020).

Check for updates

Received: 11 September 2020 | Revised: 26 October 2020 | Accepted: 16 November 2020

DOI: 10.1111/ppl.13286

SPECIAL ISSUE ARTICLE

Physiologia Plantarum

Moderate drought stress stabilizes the primary quinone acceptor Q_A and the secondary quinone acceptor Q_B in photosystem II

Lucas Leverne | **Anja Krieger-Liszkay**

Université Paris-Saclay, Institute for Integrative Cell Biology (I2BC), CEA, CNRS, Gif-sur-Yvette, France

Correspondence
Anja Krieger-Liszkay, Université Paris-Saclay, Institute for Integrative Cell Biology (I2BC), CEA, CNRS, 91198 Gif-sur-Yvette, France.
Email: anja.krieger-liszkay@cea.fr

Funding information
French Infrastructure for Integrated Structural Biology; LabEx Saclay Plant Sciences-SPS

Edited by: V. Hurry

Abstract

Drought induces stomata closure and lowers the CO_2 concentration in the mesophyll, limiting CO_2 assimilation and favoring photorespiration. The photosynthetic apparatus is protected under drought conditions by a number of downregulation mechanisms like photosynthetic control and activation of cyclic electron transport leading to the generation of a high proton gradient across the thylakoid membrane. Here, we studied photosynthetic electron transport by chlorophyll fluorescence, thermoluminescence (TL), and P_{700} absorption measurements in spinach exposed to moderate drought stress. Chlorophyll fluorescence induction and decay kinetics were slowed down. Under drought conditions, an increase of the TL AG-band and a downshift of the maximum temperatures of both, the B-band and the AG-band, were observed when leaves were illuminated under conditions that maintained the proton gradient. When leaves were frozen prior to the TL measurements, the maximum temperature of the B-band was upshifted in drought-stressed leaves. This shows a stabilization of the $Q_B/Q_B^{\bullet-}$ redox couple in accordance with the slower fluorescence decay kinetics. We propose that during drought stress, photorespiration exerts a feedback control on photosystem II via the binding of a photorespiratory metabolite at the non-heme iron at the acceptor side of photosystem II. According to our hypothesis, an exchange of bicarbonate at the non-heme iron by a photorespiratory metabolite such as glycolate would not only affect the midpoint potential of the $Q_A/Q_A^{\bullet-}$ couple, as shown previously, but also that of the $Q_B/Q_B^{\bullet-}$ couple.

1 | INTRODUCTION

Drought is one of the most important abiotic stress conditions leading to a loss of crop production. Upon drought, stomata keep closed, CO_2 concentration in the mesophyll decreases, and CO_2 assimilation declines. When the CO_2 concentration at the ribulose-1,5-bisphosphate carboxylase/oxygenase (RuBisCO) is low, the oxygenase reaction becomes more important compared to the carboxylase reaction and photorespiration is enhanced.

Photosynthetic electron transport is not considered as primary damage site under water deficit (Cornic & Fresneau, 2002; Kaiser, 1987). The photosynthetic apparatus has been demonstrated to be highly resistant to drought as shown by an unaltered quantum yield of photosystem II (ΦPSII) under moderate drought stress and a reversible decrease in ΦPSII upon increasing drought stress (Cornic & Briantais, 1991; Genty et al., 1987). It has been described that photosynthetic electron flow is downregulated under drought stress protecting the photosynthetic apparatus against oxidative stress. A number of regulation mechanisms such as nonphotochemical

---

Abbreviations: FQR, ferredoxin quinone reductase; NPQ, nonphotochemical quenching; PS, photosystem; TL, thermoluminescence.

This work is dedicated to Jean-Marc Ducruet, who introduced me to the afterglow band and constructed two thermoluminescence machines for us.

© 2020 Scandinavian Plant Physiology Society

13993054, 2021, 2, Downloaded from https://onlinelibrary.wiley.com/doi/10.1111/ppl.13286 by Portail BibCNRS INSU, Wiley Online Library on [23/11/2023]. See the Terms and Conditions (https://onlinelibrary.wiley.com/terms-and-conditions) on Wiley Online Library for rules of use; OA articles are governed by the applicable Creative Commons License

quenching (NPQ), photosynthetic control, and cyclic electron transport are operating under drought. Ott et al. (1999) reported under drought conditions a slowing down of the reduction of oxidized P_{700}, the primary electron donor of photosystem I (PSI), and interpreted this effect as a pH-dependent regulation of electron transport, most likely at the level of the cytochrome *b6f* complex (photosynthetic control). Cyclic electron flow was proposed to be responsible for this higher proton gradient leading to higher nonphotochemical quenching and protecting thereby the photosynthetic apparatus (Golding & Johnson, 2003). Chlororespiration employs the same pathways like cyclic electron flow leading to a reduction of the plastoquinone pool and a generation of a proton gradient in the dark (Peltier et al., 2016). Induction of cyclic/chlororespiratory pathways can be seen by thermoluminescence (TL) upon slow dehydration of leaves (Bürling et al., 2014).

TL can be used as a probe of the behavior of PSII reaction centers, both in isolated systems and in whole leaves (for review, see Ducruet & Vass, 2009). Using this method, samples are first cooled down and then illuminated with a given number of single turnover flashes at the lower temperature. Subsequent warming reveals several peaks of luminescence emission. These emission bands originate from recombination of different types of trapped charge pairs, which can be identified by their maximum emission temperature, T_m. For example, recombination of the semiquinone, $Q_B^{\bullet-}$ with the S_2- or S_3-state of the water-splitting complex yields a TL band centered around 30°C, the so-called B-band (Rutherford et al. 1984). In whole leaves, at higher temperatures (40–46°C at a 0.5°C s^{-1} heating rate) an additional TL band, the afterglow band, has been reported and ascribed to the afterglow luminescence emission (AG-band) induced by reverse electron flow (Bürling et al., 2014; Peeva et al., 2012). This AG-band is suppressed by an uncoupler or by freezing the sample.

Physiological conditions like drought that activate cyclic/chlororespiratory pathways cause a downshift in the maximum temperature of the AG-band (Bürling et al., 2014; Ducruet et al., 2005). The intensity of the AG band depends on the illumination protocol and on the concentration of NADPH and ATP in the stroma, dependent on the dihydroxyacetone phosphate/3-phosphoglycerate ratio (Krieger et al., 1998).

The aim of this study was to show the different regulation mechanisms set in place upon drought stress using chlorophyll fluorescence, TL, and P_{700} absorption changes. We investigated whether, in addition to the regulation mechanisms described in the literature, another regulation mechanism is activated at PSII under drought. According to our hypothesis, photorespiration protects the photosynthetic apparatus not only by evacuating excess electrons, thereby keeping the electron transport chain oxidized and protecting against PSI acceptor side limitation (Eisenhut et al., 2017), but also by acting directly on PSII. It has been recently shown in a photorespiratory mutant accumulating the photorespiratory metabolite glycolate that PSII electron transport is altered, thereby protecting PSII against $^1O_2$ production and photooxidative damage (Messant et al., 2018). Glycolate was supposed to exchange the bicarbonate ligated to the non-heme iron at the acceptor side of PSII and to shift the midpoint potential of the redox couple $Q_A/Q_A^{\bullet-}$ (Messant et al., 2018). Release of the bicarbonate ligated to the non-heme iron shifts the midpoint potential of the redox couple $Q_A/Q_A^{\bullet-}$ to a more positive potential (Brinkert et al., 2016). Until now, it remains an open question whether drought stress inducing photorespiratory conditions evokes a similar modification of the acceptor side of PSII in a wild-type plant as has been observed in the photorespiratory mutant. To show alterations of the photosynthetic electron transport and especially of PSII under drought stress, we measured chlorophyll fluorescence induction, decay, TL, and performed P_{700} absorption measurements.

2 | MATERIALS AND METHODS

2.1 | Plant material

Spinach (*Spinacia oleracea* L.) was used for this study. Individual plants were grown in pots with a diameter of 13 cm in a greenhouse for 6 weeks and then moved for 1 week to controlled light condition (8 h light, I = 450 μmol quanta m^{-2} s^{-1}, 22°C, 16 h dark, 18°C; light source, fluorescent light tubes; Osram Dulux L 55 W/840). Plants in control condition were watered every day, while stressed plants were unwatered to attend 35% of total weight pot loss (3–4 days) in stress condition and kept afterwards at the same stress level during the following days by adding the lost water once a day.

2.2 | Chlorophyll fluorescence

Chlorophyll fluorescence was measured on leaves attached to the plants at room temperature with a Dual-PAM-100 (Walz). Fluorescence induction was measured during excitation with a multiple turnover flash (duration 300 ms). Fluorescence decay was measured after excitation with a saturating single turnover flash with a sampling rate of 2.5 μs.

2.3 | Thermoluminescence

TL was measured using a homebuilt apparatus. Leaf discs were dark-adapted for 5 min at 20°C. TL was charged by two single turnover flashes with a xenon flash lamp at 1°C or at −7°C when leaf disks frozen at 77 K were used. The flashes were spaced with a 1 s dark interval. The TL signal was recorded during the warming of the sample to 70°C at a heating rate of 0.4°C s^{-1}.

2.4 | P_{700} absorption

The redox state of the primary donor of photosystem I (PSI), P_{700}, was monitored by following the changes in absorbance of 2 min dark-adapted leaves at 830 versus 875 nm using the Dual-PAM-100. Attached leaves were used. To probe the maximum extent of P_{700}

oxidation, leaves were illuminated with far-red light superimposed on the saturating pulse of red light. Oxidation of P_{700} was measured in leaves as a function of the intensity of the actinic light. Y(NA) = $(P_m - P_{m'})/P_m$ is a measure of the limitation of electron transport at the PSI acceptor side. P_m represents the maximum oxidation of P_{700} and $P_{m'}$ the maximum oxidation at a given light intensity after application of a saturating light pulse. Y(ND) is a measure of the donor side limitation representing the fraction of centers in the state ($P_{700}{}^{+}A$) at a given state (Klughammer and Schreiber, 2008).

2.5 | Immunoblots

Thylakoid membranes were prepared as in Shimakawa et al. (2020) and used for analysis by SDS-PAGE (12% acrylamide) and immunoblotting. Proteins were blotted onto nitrocellulose membrane. Labeling of the membranes with antibodies was carried out at room temperature in 1 x TBS (50 mM Tris–HCl pH 7.6, 150 mM NaCl), 0.1% Tween 20, and 1% non-fat powder milk. Primary antibodies were purchased from Agrisera except for the antibodies raised against PTOX, kindly provided by M. Kuntz (CEA Grenoble). After washing, bound antibodies were revealed with a peroxidase-linked secondary anti-rabbit antibody (Agrisera) and visualized by enhanced chemiluminescence.

3 | RESULTS

Since we are interested in studying a regulation mechanism and not an irreversible damage of the photosynthetic apparatus upon drought stress, mature leaves of moderately stressed plants (about 35% of loss of initial pot weight) were used. Drought stress in spinach plants was achieved by withholding water for 3–4 days until 35% of the initial weight of the pots was lost. This moderate drought stress did not induce a decrease in the absolute quantum yield of PSII (Fv/Fm). Well-watered plants had an Fv/Fm value of 0.81 ± 0.02 and stressed plants of 0.80 ± 0.01. Also, the water content of the stressed leaves remained unchanged. Prolonged drought stress induced a decrease in Fv/Fm.

Alterations of the PSII acceptor side in the drought-stressed plants compared to the control were followed by chlorophyll fluorescence measurements. As shown in Figure 1, in a leaf from a stressed plant, the different phases of the induction curve were flattened, and the area above the induction curve reflecting the number of available electron acceptors was smaller. Similar effects have been observed earlier under drought stress for other species and have been interpreted as reduced electron demand by PSI under these conditions (Oukarroum et al., 2009).

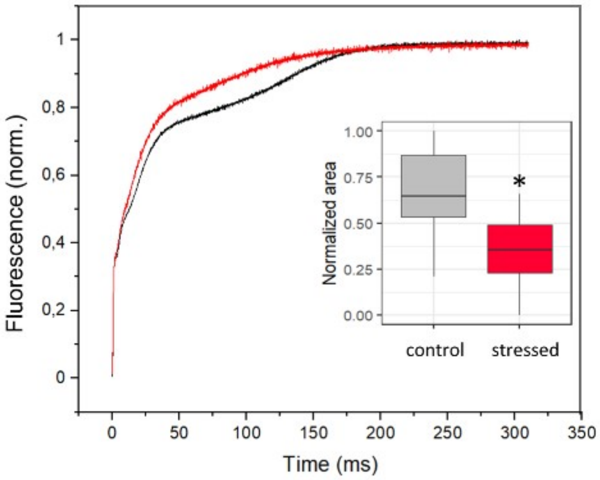

FIGURE 1 Chlorophyll fluorescence induction curves in control and drought-stressed leaves. Representative curves (black: control, red: stressed). Inset: Area above the induction curves. Average values with standard deviation are shown. Statistically significant differences between the area above the induction curves of leaves of control and stressed plants were determined by Student's *t*-test (*$P < 0.01$; $n = 11$)

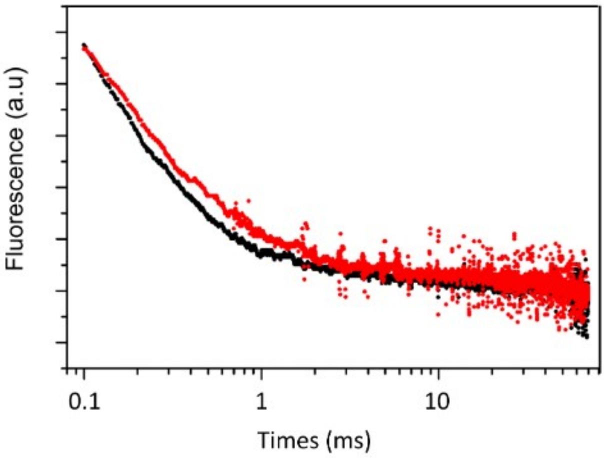

FIGURE 2 Chlorophyll fluorescence decay in control and drought-stressed leaves. Variable fluorescence was induced by a saturating single turnover flash. (A) Representative traces (black: control, red: stressed). (B) Half-times of the fast, middle, and slow phase. Decays were fitted by the sum of two exponential decay functions (fast and middle phase) and a linear function (slow phase)

The kinetics of $Q_A{}^{\bullet -}$ reoxidation can be followed by analyzing the fluorescence decay (Figure 2). According to De Wijn and Van Gorkom (2001), different phases of $Q_A{}^{\bullet -}$ reoxidation are assigned to the electron transfer to Q_B (or $Q_B{}^{\bullet -}$), which is bound to the Q_B site at the time of the flash (fast and slower phases) and to the electron transfer to Q_B but rate-limited by the exchange of a reduced quinone (Q_BH_2) in the Q_B-site for a PQ from the pool (slow phase). We fitted here the decay curves by a sum of two exponential functions (time zero to 20 ms). The slow phase was not analyzed since there was no longer a difference observed between the two conditions. As shown in Figure 2 and Table 1, moderate drought stress led to an increase in

13993054, 2021, 2, Downloaded from https://onlinelibrary.wiley.com/doi/10.1111/ppl.13286 by Portail BibCNRS INSU, Wiley Online Library on [23/11/2023]. See the Terms and Conditions (https://onlinelibrary.wiley.com/terms-and-conditions) on Wiley Online Library for rules of use; OA articles are governed by the applicable Creative Commons License

TABLE 1 Fitted parameters for fluorescence decay of control and drought-stressed plants (Figure 2)

	Fluorescence decay ($t_{1/2}$ in ms)	
	t1	t2
Control	0.303 ± 0.019	4.17 ± 0.50
Drought stress	0.565 ± 0.051*	6.57 ± 0.94*

Note: Life-times (t) were obtained after fitting the fluorescence decay curves by a sum of two exponential functions (*n* = 9). The difference between the life-times of control and drought-stressed plants is statistically different (*) according to Student's *t*-test ($P < 0.05$).

the life-times of the fast phase (t1) and the slower phase (t2). The increase in the life-times indicates a slowdown of the electron transport between Q_A and $Q_B/Q_B^{\bullet -}$ supporting the hypothesis that photorespiratory activity affects the PSII acceptor side shifting the midpoint potential of both quinone acceptors, Q_A and Q_B, to a more positive value.

Drought stress has been described to affect TL emission in barley and wheat leaves favoring the appearance of the AG-band compared to well-watered leaves (Bürling et al., 2014; Peeva et al., 2012). This is indeed the case also for spinach. Figure 3 shows representative TL curves after excitation of the samples by two flashes at 1°C. The well-watered plant showed only a very small AG-band, while a strong increase of the AG-band was observed in the stressed plant. A decrease in both the maximum temperature of the B-band and the AG-band was found in stressed samples similarly to previous reports (Bürling et al., 2014; Peeva et al., 2012). The downshift of the maximum temperature of the TL-bands under drought conditions is attributed to a larger proton gradient across the thylakoid membrane and a stimulation of cyclic electron transport according to Ducruet (Bürling et al., 2014; Miranda & Ducruet, 1995; Peeva et al., 2012). An increase in cyclic electron transport activity may depend on a biochemical activation of this pathway by, for example, redox regulation (Courteille et al., 2013) or by an increase in the amount of the proteins implicated in cyclic electron transport. Western Blot analysis (Figure 4) showed, in thylakoids from stressed leaves, a higher amount of proteins involved in the two pathways of the cyclic electron flow via the NDH complex and the FERREDOXIN QUINONE REDUCTASE (FQR) pathway mediated by the proteins called PROTON GRADIENT REGULATION and PROTON GRADIENT REGULATION-Like PGR5/PGRL1. In addition, higher levels of the PLASTID TERMINAL OXIDASE, PTOX, involved in chlororespiration, and of EARLY LIGHT-INDUCED PROTEINS, ELIP, a stress-related protein (Heddad et al., 2006), were found.

As detailed in the introduction, glycolate, a photorespiratory metabolite, may affect the acceptor side of PSII under drought. A large ΔpH may overlay the effect of glycolate accumulating under drought on the midpoint potentials of the quinone acceptors Q_A and Q_B. To destroy the ΔpH, leaves were frozen in liquid nitrogen prior to the TL measurement. Frozen leaves showed a B-band at a higher temperature in stressed leaves than in control leaves (Figure 5). A temperature difference of 3°C was found between the samples (Table 2), indicating

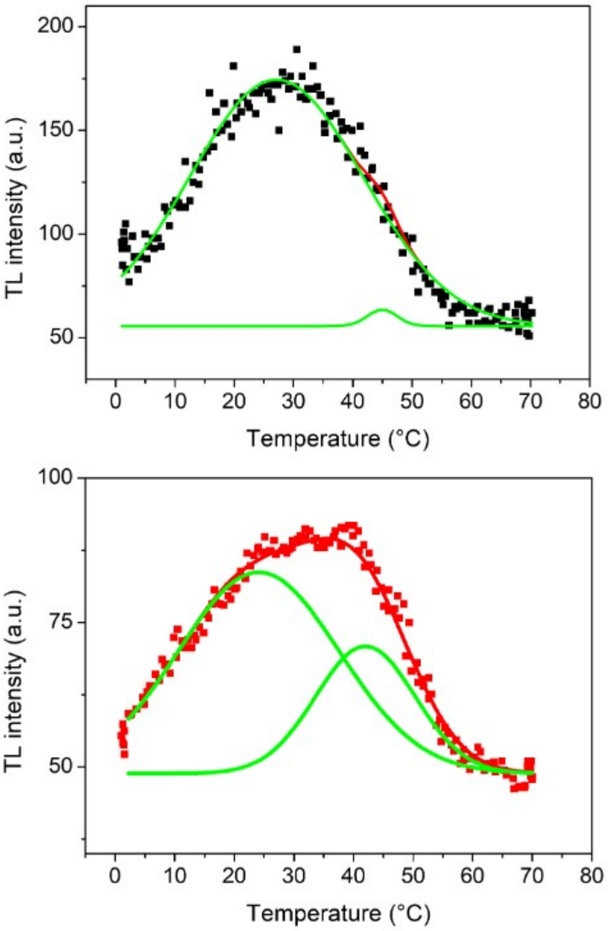

FIGURE 3 Thermoluminescence bands in control and drought-stressed leaves. Samples were excited at 1°C by two single turnover flashes. Black: control, red: stressed leaf. Red line: fit of the experimental curves by two Gaussian functions. The B-band and AG-band intensities are indicated by the green curves, respectively

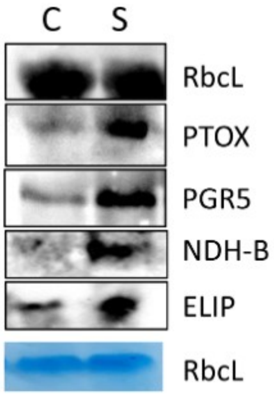

FIGURE 4 Immunoblots of proteins involved in alternative electron transport in membrane fractions isolated from control and drought-stressed leaves. Immunoblots were conducted with antibodies directed against the PLASTID TERMINAL OXIDASE (PTOX), PGR5, the subunit B of the NDH complex (NDH-B), EARLY LIGHT-INDUCED PROTEINS (ELIP). RuBisCo large subunit (RbcL) was used as loading control. In addition, the Coomassie stained gel is shown. 2.5 μg chlorophyll was loaded for both samples

13993054, 2021, 2, Downloaded from https://onlinelibrary.wiley.com/doi/10.1111/ppl.13286 by Portail BibCNRS INSU, Wiley Online Library on [23/11/2023]. See the Terms and Conditions (https://onlinelibrary.wiley.com/terms-and-conditions) on Wiley Online Library for rules of use; OA articles are governed by the applicable Creative Commons License

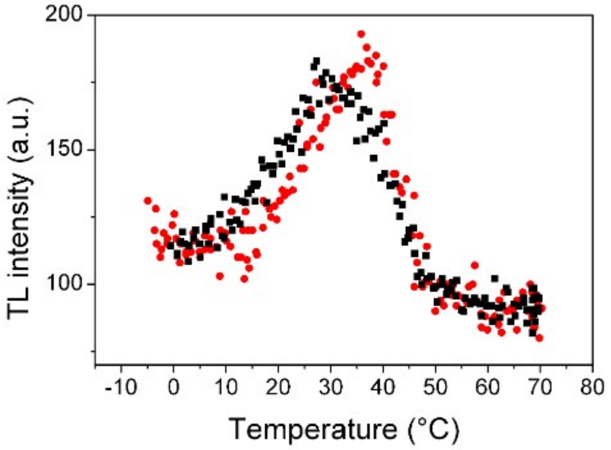

FIGURE 5 Thermoluminescence bands in control and drought-stressed leaves frozen at 77 K. Leave disks were frozen at 77 K prior to the insertion into the thermoluminescence cuvette. Samples were excited at −7°C by two single turnover flashes. Black: control, red: stressed leaf

TABLE 2 Thermoluminescence measurements performed on leaf discs of control and drought-stressed plants

	TL Tmax B-band (°C)
Control	31.2 ± 1.9
Drought stress	34.8 ± 2.0*

Note: Leaf disks were frozen at 77 K, excited at −7°C with two single turnover flashes. The maximum temperature of the B-band was determined ($n = 6$). The difference between the T_m of control and drought-stressed plants is statistically different (*) according to Student's *t*-test ($P < 0.05$).

that the $S_{2,3}Q_B^{\bullet -}$ couple was stabilized in stressed leaves. It would have been interesting to study a possible shift of T_m of the Q-band ($S_2Q_A^{\bullet -}$ recombination) upon drought stress. This would give access to modifications of the midpoint potential of the redox couple $Q_A/Q_A^{\bullet -}$. However, to obtain a Q-band, the addition of DCMU is required that binds to the Q_B-binding site and inhibits electron transfer between Q_A and Q_B. We did not infiltrate leaves with DCMU because such an infiltration procedure could remove photorespiratory metabolites like glycolate from the non-heme iron at the acceptor side of PSII.

It has been reported previously that drought stress affects the redox state of P700 (Ott et al., 1999). As seen in Figure 6, we observed a stronger donor-side limitation of PSI in stressed leaves compared to the control. A clear trend is shown in Figure 6, although the differences are statistically not significant. No sign of acceptor side limitation was observed in the stressed plants showing that photorespiration activity was sufficient to keep the PSI acceptor side open.

4 | DISCUSSION

Photosynthetic electron transport is regulated at different sites during moderate drought stress according to the data shown here and previously published work (Ott et al., 1999; Golding & Johnson, 2003; Peeva et al., 2012; Bürling et al. 2014). In Figure 7, we present a model showing four sites of regulation of photosynthetic electron transport: PSII, PTOX, cyclic flow, and electron donation to PSI. As shown in Figure 6, P_{700} is in a slightly higher oxidation state under steady-state conditions in stressed leaves, although this difference is statistically not significant. A higher oxidation state of P_{700} has been reported previously in different species (Ott et al., 1999; Wada et al., 2019). Accumulation of P_{700}^+ protects PSI against photo-oxidative damage (Shimakawa & Miyake, 2018; Wada et al., 2019). Ott et al. (1999) reported a slowing down of the reduction of P_{700}^+ that can be explained either by a slower electron donation by plastocyanin or by a limitation of electron transport at the cytochrome b_6f complex, the so-called photosynthetic control. Plastocyanin diffusion may become limited under severe drought conditions since the thylakoid lumen may shrink. This has been shown to be the case in desiccated cyanobacteria from a dessert crust (Bar-Eyal et al., 2015). In these cyanobacteria, P_{700}^+ accumulates and acts as a quencher of excess energy, protecting the photosynthetic apparatus against oxidative stress. However, under moderate drought conditions, limitation of plastocyanin seems to be very unlikely and instead photosynthetic control (i. e. electron transport limitation at the cyt b_6f complex when the pH in the lumen drops below a certain threshold value) is the likely reason for slowing down the electron transport towards PSI.

An increase in the proton gradient can be achieved by the cyclic electron transport shown to be enhanced under drought stress (Golding & Johnson, 2003). Cyclic electron flow takes place via two different pathways: the ferredoxin quinone reductase (FQR) pathway that likely involves the proteins PGRL1 and PGR5 and via the NDH

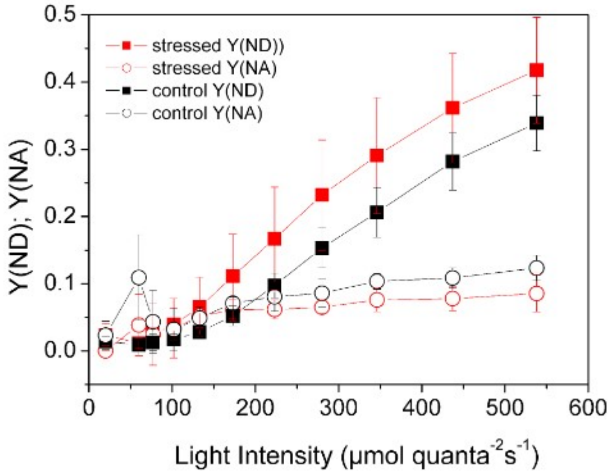

FIGURE 6 The redox state of the PSI primary donor P_{700} was monitored through the changes in absorbance at 830 versus 875 nm. Following the initial determination of maximal oxidation of P_{700}, actinic light of the indicated intensities was given for 60 s. PSI donor-side limitation Y(ND) and acceptor-side limitation Y(NA) are based on saturating pulse analyses. Black symbols: control, red symbols stressed leaves, squares: Y(ND), circles Y(NA); (mean ± SD, $n = 6$; three biological replicates)

13993054, 2021, 2, Downloaded from https://onlinelibrary.wiley.com/doi/10.1111/ppl.13286 by Portail BibCNRS INSU, Wiley Online Library on [23/11/2023]. See the Terms and Conditions (https://onlinelibrary.wiley.com/terms-and-conditions) on Wiley Online Library for rules of use; OA articles are governed by the applicable Creative Commons License

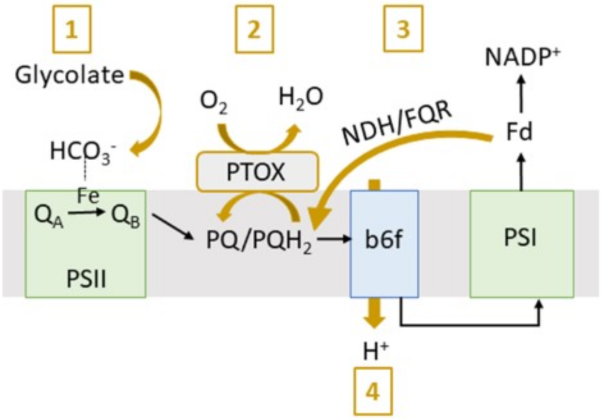

FIGURE 7 Model of the regulation of electron transport under stress conditions. Four different sites slow down electron transport and protect the photosynthetic electron transport. (1) the acceptor side of PSII is modified, most likely by binding of a photorespiratory metabolite at the non-heme iron between Q_A and Q_B. Dashed line shows the ligation of bicarbonate or glycolate to the non-heme iron. According to our model, this induces a stabilization of the midpoint potentials of the redox couples $Q_A/Q_A^{\bullet-}$ and $Q_B/Q_B^{\bullet-}$ and slows down forward electron transport as well as protects PSII against photooxidative damage by $^1O_2$. (2) PTOX activity acting as a safety valve to keep the redox poise of the plastoquinone pool. (3) The cyclic electron transport via the NDH complex or via the FQR pathway involving PGR5/PGRL1 is stimulated under drought leading to an increase in the ΔpH. (4) A high ΔpH slows down the turnover of the cytochrome *b₆f* complex and the electron donation to PSI. Accumulation of P_{700}^+ protects PSI against photooxidative damage

complex (for a recent review see Nawrocki et al., 2019). During slow dehydration, Lehtimäki et al. (2010) reported an increased amount of PGR5 and PGRL1 proteins but not of NDH-H. Ibanez et al. (2010) observed that PTOX and both, the FQR and NDH-dependent pathway of cyclic flow, were activated under a combination of drought, heat and high illumination stress. Under the moderate drought stress applied here, both PGR5 and NDH-B protein levels were increased (Figure 4) supporting the upregulation of cyclic electron transport pathways upon drought stress. The amount of PTOX is also clearly increased, indicating activation not only of the cyclic electron transport but also of chlororespiration. In stressed plants, PTOX may also play a role as a safety valve during illumination. Under drought stress, TL measurements revealed an increase in the AG-band (Figure 3) that has been attributed to an activation of cyclic/chlororespiratory flow (Bürling et al., 2014; Peeva et al., 2012). The lumen acidification leads to a downshift of both the B-band and the AG-band (Figure 3; see also Bürling et al., 2014). The peak temperature of a TL-band is indicative of the energy stored in the charge-separated state and is determined by redox potentials of both the recombination partners, in this case, S_2/S_3 and $Q_B/Q_B^{\bullet-}$. The $Q_B/Q_B^{\bullet-}$ couple involves proton release when $Q_B^{\bullet-}$ is reoxidized and is expected to follow Nernst behavior, with the redox potential changing by −59 mV per pH unit (De Causmaecker et al., 2019; Rutherford et al., 1984; Vass & Inoue, 1986).

In addition to these previously described regulation mechanisms activated upon drought stress and described above, we show here that the electron transport between Q_A and Q_B is slowed down (Figures 1 and 2). We propose that this modification is caused by a photorespiratory metabolite accumulating under drought stress, most likely glycolate that replaces the bicarbonate ligated to the non-heme iron situated between Q_A and Q_B at the acceptor side of PSII. As shown by Messant et al. (2018), the accumulation of glycolate affects the electron transport between Q_A and Q_B and protects PSII against $^1O_2$ generation. $^1O_2$ is highly toxic and able to damage PSII. Brinkert et al. (2016) have shown that the midpoint potential of the redox couple $Q_A/Q_A^{\bullet-}$ is shifted toward a more positive value in the absence of bicarbonate, allowing for a direct charge recombination pathway in PSII that does not lead to chlorophyll triplet formation and subsequent $^1O_2$ production. A protection mechanism at PSII avoiding triplet chlorophyll and $^1O_2$ generation is important to protect PSII against photoinhibition under conditions when the electron transport chain is highly reduced as it is the case under drought stress. In addition to Q_A, the midpoint potential of the $Q_B/Q_B^{\bullet-}$ couple seems to be stabilized under drought stress. As seen in the fluorescence decay, all phases are slowed down, including the slow phase that reflects the exchange of Q_BH_2 in the Q_B-site for a PQ molecule from the PQ pool (De Wijn & Van Gorkom, 2001). The binding efficiency of PQ to the QB site might be affected by the ligand change at the non-heme iron, but is also influenced by the concentration of oxidized PQ. If enhanced cyclic electron flow reduces the PQ pool, the concentration of oxidized PQ is lowered, which limits its availability for binding to the Q_B site and contributes to the decreased rate of fluorescence decay in the ms phase. The rate of forward electron transfer between Q_A^- and Q_B is determined by free energy difference between the $Q_A/Q_A^{\bullet-}$ and $Q_B/Q_B^{\bullet-}$ states. Upon drought stress, the fast phase of the fluorescence decay is also slower, showing that the free energy difference between the quinone acceptors is decreased. This can arise either from stabilization of $Q_A/Q_A^{\bullet-}$ or destabilization of $Q_B/Q_B^{\bullet-}$. Since $Q_B/Q_B^{\bullet-}$ is stabilized according to the TL data (Figure 5), we assume that $Q_A/Q_A^{\bullet-}$ is even more stabilized compared to $Q_B/Q_B^{\bullet-}$. Stabilization of the $Q_B/Q_B^{\bullet-}$ couple has been described previously in *Synechocystis* PCC 6803 mutants, mutated in the D-de loop of the D2 protein, which showed an upshift of the B-band (Kless et al., 2008; Mäenpää et al., 1995) and in the *Synechocystis* PCC 6803 ΔPsbT strain. Stabilization of $S_2Q_B^-$ has been correlated with increased light sensitivity (Fagerlund et al., 2020). Further studies are required to show whether mild drought stress protects higher plants against photoinhibition or increases the susceptibility to photoinhibition.

ACKNOWLEDGMENTS

The authors thank J. M. Ducruet for constructing the TL apparatus at the CEA Saclay; M. Messant (I2BC) and Ginga Shimakawa (Osaka University) for critical reading of the manuscript. This work was supported by the LabEx Saclay Plant Sciences-SPS (grant number

13993054, 2021, 2, Downloaded from https://onlinelibrary.wiley.com/doi/10.1111/ppl.13286 by Portail BibCNRS INSU, Wiley Online Library on [23/11/2023]. See the Terms and Conditions (https://onlinelibrary.wiley.com/terms-and-conditions) on Wiley Online Library for rules of use; OA articles are governed by the applicable Creative Commons License

ANR-17-EUR-0007) and the French Infrastructure for Integrated Structural Biology (FRISBI; grant number ANR-10-INSB-05).

AUTHOR CONTRIBUTIONS

Anja Krieger-Liszkay conceived the work. Lucas Leverne and Anja Krieger-Liszkay performed the measurements and wrote the manuscript.

DATA AVAILABILITY STATEMENT

The data that support the findings of this study are available from the corresponding author upon reasonable request.

ORCID

Anja Krieger-Liszkay https://orcid.org/0000-0001-7141-4129

REFERENCES

Bar-Eyal, L., Eisenberg, I., Faust, A., Raanan, H., Nevo, R., Rappaport, F., *et al.* (2015) An easily reversible structural change underlies mechanisms enabling desert crust cyanobacteria to survive desiccation. *Biochimica et Biophysica Acta*, 1847, 1267–1273.

Brinkert, K., De Causmaecker, S., Krieger-Liszkay, A., Fantuzzi, A. & Rutherford, A.W. (2016) Bicarbonate-induced redox tuning in photosystem II for regulation and protection. *Proceedings of the National Academy of Sciences of the United States of America*, 113, 12144–12149.

Bürling, K., Ducruet, J.M., Cornic, G., Hunsche, M. & Cerovic, Z.G. (2014) Assessment of photosystem II thermoluminescence as a tool to investigate the effects of dehydration and rehydration on the cyclic/chlororespiratory electron pathways in wheat and barley leaves. *Plant Science*, 223, 116–123.

Cornic, G. & Briantais, J.M. (1991) Partitioning of photosynthetic electron flow between CO_2 and O_2 reduction in a C_3 leaf (*Phaseolus vulgaris* L.) at different CO_2 concentrations and during drought stress. *Planta*, 183, 178–184.

Cornic, G. & Fresneau, C. (2002) Photosynthetic carbon reduction and carbon oxidation cycles are the main electron sinks for photosystem II activity during a mild drought. *Annals of Botany*, 89, 887–894.

Courteille, A., Vesa, S., Sanz-Barrio, R., Cazalé, A.C., Becuwe-Linka, N., Farran, I., *et al.* (2013) Thioredoxin m4 controls photosynthetic alternative electron pathways in Arabidopsis. *Plant Physiology*, 161, 508–520.

De Causmaecker, S., Douglass, J.S., Fantuzzi, A., Nitschke, W. & Rutherford, A.W. (2019) Energetics of the exchangeable quinone, Q_B, in photosystem II. *Proceedings of the National Academy of Sciences of the United States of America*, 116, 19458–19463.

De Wijn, R. & Van Gorkom, H.J. (2001) Kinetics of electron transfer from Q_A to Q_B in photosystem II. *Biochemistry*, 40, 11912–11922.

Ducruet, J.M., Roman, M., Havaux, M., Janda, T. & Gallais, A. (2005) Cyclic electron flow around PSI monitored by afterglow luminescence in leaves of maize inbred lines (*Zea mays* L.): correlation with chilling tolerance. *Planta*, 221, 567–579.

Ducruet, J.M. & Vass, I. (2009) Thermoluminescence: experimental. *Photosynthesis Research*, 101, 195–204.

Eisenhut, M., Bräutigam, A., Timm, S., Florian, A., Tohge, T., Fernie, A.R., *et al.* (2017) Photorespiration is crucial for dynamic response of photosynthetic metabolism and stomatal movement to altered CO_2 availability. *Molecular Plant*, 10, 47–61.

Fagerlund, R.D., Forsman, J.A., Biswas, S., Vass, I., Davies, F.K., Summerfield, T.C., *et al.* (2020) Stabilization of photosystem II by the PbsT protein impacts photodamage, repair and biogenesis. *Biochimica et Biophysica Acta*, 1861, 148234. https://doi.org/10.1016/j.bbabio.2020.148234.

Genty, B., Briantais, J.M. & Viera da Silva, J.B. (1987) Partitioning of photosynthetic electron flow between CO_2 and O_2 reduction in a C_3 leaf (*Phaseolus vulgaris* L.) at different CO_2 concentrations and during drought stress. *Plant Physiology*, 83, 360–364.

Golding, A.J. & Johnson, G.N. (2003) Down-regulation of linear and activation of cyclic electron transport during drought. *Planta*, 218, 107–114.

Heddad, M., Norén, H., Reiser, V., Dunaeva, M., Andersson, B. & Adamska, I. (2006) Differential expression and localization of early light-induced proteins in Arabidopsis. *Plant Physiology*, 142, 75–87.

Ibanez, A., Ballester, R. & Munoz, M.J.Q. (2010) Chlororespiration and tolerance to drought, heat and high illumination. *Journal of Plant Physiology*, 167, 732–738.

Kaiser, W.M. (1987) Effects of water deficit on photosynthetic capacity. *Physiologia Plantarum*, 71, 142–149.

Klughammer, C. & Schreiber, U. (2008) Saturation pulse method for assessment of energy conversion in PSI. *PAM Application Notes*, 1, 11–14.

Krieger, A., Bolte, S., Dietz, K.J. & Ducruet, J.M. (1998) Thermoluminescence studies on the facultative crassulacean-acid-metabolism plant *Mesembryanthenum crystallinum* L. *Planta*, 205, 587–594.

Lehtimäki, N., Lintala, M., Allahverdiyeva, Y., Aro, E.M. & Mulo, P. (2010) Drought stress-induced upregulation of components involved in ferredoxin-dependent cyclic electron transfer. *Journal of Plant Physiology*, 167, 1018–1022.

Mäenpää, P., Miranda, T., Tyystjärvi, E., Tyystjärvi, T., Govindjee, D.J.M., Etienne, A.L., *et al.* (1995) A mutation in the D-de loop modifies the stability of the S2QA- and the S2QB- states in photosystem II. *Plant Physiology*, 107, 187–197.

Messant, M., Timm, S., Fantuzzi, A., Weckwerth, W., Bauwe, H., Rutherford, A.W., *et al.* (2018) Glycolate induces redox tuning of photosystem II in vivo: study of a photorespiration mutant. *Plant Physiology*, 177, 1277–1285.

Miranda, T. & Ducruet, J.M. (1995) Effects of dark- and light-induced proton gradients in thylakoids on the Q and B thermoluminescence bands. *Photosynthesis Research*, 43, 251–262.

Nawrocki, W.J., Bailleul, B., Picot, D., Cardol, P., Rappaport, F., Wollman, F. A., *et al.* (2019) The mechanism of cyclic electron flow. *Biochimica et Biophysica Acta*, 1860, 433–438.

Ott, T., Clarke, J., Birks, K. & Johnson, G. (1999) Regulation of the photosynthetic electron transport chain. *Planta*, 209, 250–258.

Oukarroum, A., Schansker, G. & Strasser, R.J. (2009) Drought stress effects on photosystem I content and photosystem II thermotolerance analyzed using Chl *a* fluorescence kinetics in barley varieties differing in their drought tolerance. *Physiologia Plantarum*, 137, 188–199.

Peeva, V.N., Tóth, S.Z., Cornic, G. & Ducruet, J.M. (2012) Thermoluminescence and P700 redox kinetics as complementary tools to investigate the cyclic/chlororespiratory electron pathways in stress conditions in barley leaves. *Physiologia Plantarum*, 144, 83–97.

Peltier, G., Aro, E.M. & Shikanai, T. (2016) NDH-1 and NDH-2 plastoquinone reductases in oxygenic photosynthesis. *Annual Review of Plant Biology*, 67, 55–80.

Rutherford, A.W., Renger, G., Koike, H. & Inoue, Y. (1984) Thermoluminescence as a probe of photosystem II. The redox and protonation states of the secondary acceptor quinone and the O_2-evolving enzyme. *Biochimica et Biophysica Acta*, 767, 548–556.

Shimakawa, G. & Miyake, C. (2018) Oxidation of P700 ensures robust photosynthesis. *Frontiers in Plant Science*, 9, 1617.

Shimakawa, G., Sétif, P. & Krieger-Liszkay, A. (2020) Near-infrared in vivo measurements of photosystem I and its luminal electron donors with a recently developed spectrophotometer. *Photosynthesis Research*, 144, 63–72.

13993054, 2021, 2, Downloaded from https://onlinelibrary.wiley.com/doi/10.1111/ppl.13286 by Portail BibCNRS INSU, Wiley Online Library on [23/11/2023]. See the Terms and Conditions (https://onlinelibrary.wiley.com/terms-and-conditions) on Wiley Online Library for rules of use; OA articles are governed by the applicable Creative Commons License

Vass, I. & Inoue, Y. (1986) pH dependent stabilization of $S_2Q_A^-$ and $S_2Q_B^-$ charge pairs studied by thermoluminescence. *Photosynthesis Research*, 10, 431–436.

Wada, S., Takagi, D., Miyake, C., Makino, A. & Suzuki, Y. (2019) Responses of the photosynthetic electron transport reactions stimulate the oxidation of the reaction center chlorophyll of photosystem I, P700, under drought and high temperatures in rice. *International Journal of Molecular Sciences*, 20, 2068.

How to cite this article: Leverne L, Krieger-Liszkay A. Moderate drought stress stabilizes the primary quinone acceptor Q_A and the secondary quinone acceptor Q_B in photosystem II. *Physiologia Plantarum*. 2021;171:260–267. https://doi.org/10.1111/ppl.13286

13993054, 2021, 2, Downloaded from https://onlinelibrary.wiley.com/doi/10.1111/ppl.13286 by Portail BibCNRS INSU, Wiley Online Library on [23/11/2023]. See the Terms and Conditions (https://onlinelibrary.wiley.com/terms-and-conditions) on Wiley Online Library for rules of use; OA articles are governed by the applicable Creative Commons License

13.2 “Increased drought resistance in state transition mutants is linked to modified plastoquinone pool redox state” (Leverne et al., 2023)

Check for updates

Received: 17 March 2023 | Revised: 1 August 2023 | Accepted: 7 August 2023

DOI: 10.1111/pce.14695

ORIGINAL ARTICLE

Plant, Cell & Environment | PC&E | WILEY

Increased drought resistance in state transition mutants is linked to modified plastoquinone pool redox state

Lucas Leverne[1] | Thomas Roach[2] | François Perreau[3] | Fabienne Maignan[4] | Anja Krieger-Liszkay[1]

[1]Institute for Integrative Biology of the Cell (I2BC), CEA, CNRS, Université Paris-Saclay, Gif-sur-Yvette, France

[2]Department of Botany, University of Innsbruck, Innsbruck, Austria

[3]INRAE, AgroParisTech, Institut Jean-Pierre Bourgin (IJPB), Université Paris-Saclay, Versailles, France

[4]Laboratoire des Sciences du Climat et de l'Environnement, LSCE/IPSL, CEA-CNRS-UVSQ, Université Paris-Saclay, Gif-sur-Yvette, France

Correspondence

Anja Krieger-Liszkay, Institute for Integrative Biology of the Cell (I2BC), CEA, CNRS, Université Paris-Saclay, 91198 Gif-sur-Yvette cedex, France.
Email: anja.liszkay@i2bc.paris-saclay.fr

Funding information

Agence Nationale de la Recherche; CLand ANR-16-CONV-0003; Saclay Plant Science; Labex Saclay Plant Sciences-SPS, Grant/Award Number: ANR-17-EUR-0007; French Infrastructure for Integrated Structural Biology, Grant/Award Number: ANR-10-INSB-05

Abstract

Identifying traits that exhibit improved drought resistance is highly important to cope with the challenges of predicted climate change. We investigated the response of state transition mutants to drought. Compared with the wild type, state transition mutants were less affected by drought. Photosynthetic parameters in leaves probed by chlorophyll fluorescence confirmed that mutants possess a more reduced plastoquinone (PQ) pool, as expected due to the absence of state transitions. Seedlings of the mutants showed an enhanced growth of the primary root and more lateral root formation. The photosystem II inhibitor 3-(3,4-dichlorophenyl)−1, 1-dimethylurea, leading to an oxidised PQ pool, inhibited primary root growth in wild type and mutants, while the cytochrome b_6f complex inhibitor 2,5-dibromo-3-methyl-6-isopropylbenzoquinone, leading to a reduced PQ pool, stimulated root growth. A more reduced state of the PQ pool was associated with a slight but significant increase in singlet oxygen production. Singlet oxygen may trigger a, yet unknown, signalling cascade promoting root growth. We propose that photosynthetic mutants with a deregulated ratio of photosystem II to photosystem I activity can provide a novel path for improving crop drought resistance.

KEYWORDS

photosynthesis, plastoquinone redox state, root growth, singlet oxygen, state transitions

1 | INTRODUCTION

Drought-resistant plants are required to cope with the increase in world population and the challenges of predicted climate change. New traits need to be identified and methods have to be developed to maintain and improve crop productivity under harsh environmental conditions. Water and nutrients are absorbed by plant roots and specific root traits, such as growth and architecture, are important under unfavourable conditions, e.g. drought. Previously it has been shown that inhibition of the carotenoid biosynthesis pathway reduces root growth and the emergence of lateral roots in *Arabidopsis thaliana*, demonstrating the importance of carotenoids for root growth (Van Norman et al., 2014). It has been shown that strigolactones and abscisic acid, both being phytohormones derived from carotenoids, regulate root growth and branching of lateral roots (Gomez-Roldan et al., 2008; Ruyter-Spira et al., 2011). Furthermore, the volatile β-cyclocitral that is either enzymatically produced by carotenoid cleavage dioxygenases or by the non-enzymatic

This is an open access article under the terms of the Creative Commons Attribution License, which permits use, distribution and reproduction in any medium, provided the original work is properly cited.
© 2023 The Authors. *Plant, Cell & Environment* published by John Wiley & Sons Ltd.

$^1O_2$-dependent oxidation of β-carotene has been found to be a root growth regulator (Dickinson et al., 2019). Beside β-cyclocitral, other carotenoid cleavage products (apocarotenoids) and reactive electrophile species (RES) may be capable of promoting root growth and development (Biswas et al., 2019).

Apocarotenoids are generated either by non-enzymatic or enzymatic carotenoid oxidation. Singlet oxygen ($^1O_2$) oxidises β-carotene to, amongst others, β-cyclocitral or β-ionone, both of which can influence plant growth and development. β-cyclocitral has been shown to induce drought resistance in *Arabidopsis thaliana* (D'Alessandro et al., 2019). In photosystem II (PSII) chlorophyll in its triplet state (^{3}Chl) reacts with oxygen, a triplet in its ground state, producing $^1O_2$. ^{3}Chl is generated by charge recombination reactions of the primary radical pair in PSII (Krieger-Liszkay, 2005; Rutherford and Krieger-Liszkay, 2001). Charge recombination leads to the formation of the primary radical pair P^+Ph^-, with pheophytin (Ph) being the primary electron acceptor in PSII, and subsequently to the repopulation of the excited state of P680. The excited state formed can be either a singlet or a triplet state (^{3}P680), depending on the charge recombination route. The probability of charge recombination within PSII increases when the plastoquinone (PQ) pool and the acceptor side of PSII are reduced, for example, when there is a lack of stromal electron acceptors under CO_2 limitation from drought-induced stomatal closure.

The redox state of the PQ pool is also influenced by movements of the light-harvesting antenna trimer (L-LHCII), which changes the absorption cross-sections of PSII and PSI in a process called state transition. Both phosphorylation (Bellafiore et al., 2005; Depège et al., 2003) and N-terminal acetylation (Koskela et al., 2018) are posttranslational modifications of proteins involved in this process. Phosphorylation and acetylation of L-LHCII are required to allow the detachment of L-LHCII from PSII to adjust the amount of excitation energy received by the two photosystems (Koskela et al., 2018). These posttranslational modifications are highly dynamic and are often regulated by changes in the environment and stress (e.g., Linster & Wirtz, 2018; Stone & Walker, 1995). When more light is absorbed by PSII than by PSI, L-LHCII attached to PSII becomes phosphorylated and acetylated. The modified L-LHCII detaches from PSII and migrates to PSI, thereby increasing the cross-section and excitation of PSI. Lysine acetylation of L-LHCII is achieved by the chloroplast acetyltransferase enzyme *NSI* (NUCLEAR SHUTTLE INTERACTING; At1G32070) (Koskela et al., 2018). The reduction of the PQ pool regulates the activity of the serine/threonine-protein kinase STN7 (Bellafiore et al., 2005; Depège et al., 2003), while an oxidised PQ pool leads to dephosphorylation of LHCII by the phosphatase PPH1/TAP38 (Pribil et al., 2010; Shapiguzov et al., 2010). N-terminal acetylation has been shown to decrease significantly after drought stress, and transgenic downregulation of this activity induced drought tolerance (Linster et al., 2015). How state transitions are linked to drought tolerance remains unclear.

We hypothesise that a higher reduction state of the PQ pool and concomitant $^1O_2$ generation leads to a signalling event that induces drought stress tolerance. To test this, we investigated drought resistance in *Arabidopsis thaliana*, using the well-characterised state transition mutant *stn7*, and the less well-characterised mutants, *nsi1* and *nsi2*, two knockout lines lacking the chloroplast acetyltransferase *NSI*.

2 | MATERIALS AND METHODS

2.1 | Plant material and plant growth conditions

Arabidopsis thaliana (ecotype Columbia-0) wild type (WT) *stn7*, *nsi1*, and *nsi2* were grown in Jiffy-7®—Peat Pellets in plastic pots (5 cm high, 5.5 cm diameter) in ambient air for 4 weeks in a growth cabinet in long-day conditions: 16 h of light (22°C), 8 h of dark (18°C), and at a light intensity of 110 µmol quanta $m^{-2} s^{-1}$ (light source, fluorescent light tubes; OSRAM fluora 58 Watt/77). To achieve mild drought stress, watering was stopped for 4–6 days. For each replicate, plants in control and stress conditions of the same age were used.

2.2 | Seedling growth conditions

WT, *stn7*, *nsi1*, and *nsi2* seeds were sterilised in a solution of ethanol 70% (vol/vol) and sodium dodecyl sulfate 0.05% (wt/vol) under gentle agitation for 12 min, washed three times with ethanol 96%, and then dried on a sterile filter paper. Seeds were grown in one-half-strength Gamborg's B5 agar medium (Gamborg et al., 1968). Seeds were stratified in the dark at 4°C for 48 h. Then plates were placed in a growth cabinet 16/8 h day/night, at 22°C/18°C, fluorescent light 110 µmol quanta $m^{-2} s^{-1}$. Supplements including 3-(3,4-dichlorophenyl)−1,1-dimethylurea (DCMU, 2 µM), 2,5-dibromo-3-methyl-6-isopropylbenzoquinone (DBMIB, 30 µM), and mannitol (200 mM) were added directly to the agar medium. The stability of DBMIB in the light was tested by measuring the inhibitory effect of the DBMIB solution after 10 days of storage in the growth cabinet under the same photoperiod and temperature as above. Photosynthetic electron transport activity of thylakoids was still inhibited by 80% in the presence of 3 µM DBMIB. In seedlings, when grown in the presence of 2 µM DCMU, Fv/Fm was low (0.355 ± 0.015) and Y(II) close to zero at low light intensity (21 µmol quanta $m^{-2} s^{-1}$). When grown in the presence of DBMIB, Fv/Fm was lower than without herbicide (0.59 ± 0.09), Y(II) was 0.277 at low light (21 µmol quanta $m^{-2} s^{-1}$). Without addition, Fv/Fm was 0.751 ± 0.01 and Y(II) 0.501 ± 0.005 (21 µmol quanta $m^{-2} s^{-1}$).

2.3 | Rosette size and relative water content (RWC)

Rosette size of the different genotypes was determined using pixel numbers of stationary fluorescence levels of fluorescence images taken by the Imaging-PAM. For the determination of RWC, total rosettes were sampled and weighed. Saturated weight was determined by weighing the rosettes after a 12 h immersion in water at 4°C in the dark. Dry weight was determined by weighing rosettes after drying for 48 h at 70°C. RWC was calculated using:

13653040, 2023, 12, Downloaded from https://onlinelibrary.wiley.com/doi/10.1111/pce.14695 by Portail BibCNRS INSU, Wiley Online Library on [23/11/2023]. See the Terms and Conditions (https://onlinelibrary.wiley.com/terms-and-conditions) on Wiley Online Library for rules of use; OA articles are governed by the applicable Creative Commons License

RWC = (FW − DW)/(SW − DW) where FW, SW, and DW are the rosette fresh, water-saturated, and dry weights, respectively.

2.4 | Stomata opening

To observe the stomata under the microscope, transparent tape was applied to the abaxial part of the leaf, and it was quickly torn off so that a thin layer of the lower epidermis could be removed and fixed to be observed under the microscope. The ratio of width/length was determined with an optical microscope ×40 (Zeiss Axio Imager M1), measured manually using the Fiji software, at least for 100 stomata for each condition and each genotype.

2.5 | Chlorophyll fluorescence

Chlorophyll fluorescence was measured on whole plants at room temperature with an Imaging-PAM Maxi-Version (Walz). Plants were adapted for 15 min in the dark before measuring the minimum fluorescence level Fo. A saturating flash (300 ms, 10 000 µmol quanta $m^{-2} s^{-1}$) was given to determine the maximum fluorescence Fm. To measure the maximum fluorescence level in the light, Fm′, plants were illuminated for 3 min with different intensities of actinic light (55, 80, 110, 145, 185, 230, 335, 425, 610 µmol quanta $m^{-2} s^{-1}$), and a saturating flash was given at the end of each light intensity step.

Parameters are defined as follows: F: fluorescence yield; F_0': dark fluorescence level after illumination; Fm′: maximal fluorescence yield in the light; NPQ: nonphotochemical fluorescence quenching; Y(II): effective PSII quantum yield; Y(NPQ): quantum yield of regulated energy dissipation in PSII; Y(NO): quantum yield of nonregulated energy dissipation in PSII; qP: photochemical quenching; qL: fraction of open PSII reaction centres. The different fluorescence parameters are calculated as follows: Y(II) = (Fm′ − F)/Fm′; NPQ = (Fm − Fm′)/Fm′; Y(NPQ) = 1 − Y(II) − 1/(NPQ + 1 + qL(Fm/Fo-1)); Y(NO) = 1/(NPQ + 1+ qL(Fm/Fo − 1)); qP = (Fm′ − F)/(Fm′ − Fo′); qL = qP × Fo′/F.

2.6 | 77K chlorophyll fluorescence measurements

Fluorescence emission spectra of isolated thylakoids were measured with a Carry Eclipse fluorimeter; excitation wavelength: 430 nm; monochromator slits: 5 nm; scanning speed: 120 nm min^{-1}; averaging time: 0.5 s; average of 6 scans. The intensities were normalised to the intensity of the PSII emission.

2.7 | Spin-trapping electron paramagnetic resonance (EPR) spectroscopy

$^1O_2$ was trapped using the water-soluble spin probe 2,2,6,6-tetramethyl-4-piperidone hydrochloride (TEMPD-HCl) (Hideg et al., 2011). Thylakoids from Arabidopsis were prepared using a standard protocol (e.g., Messant et al., 2018). Thylakoids (20 µg chlorophyll mL^{-1}) were illuminated for 2 min with red light (Schott filter RG 630) at 670 µmol quanta $m^{-2} s^{-1}$ in 100 mM TEMPD-HCl, 0.3 M sorbitol, 50 mM KCl, 1 mM $MgCl_2$ and 25 mM HEPES (pH 7.6). Spin-trapping assays for detecting $^{\bullet}OH$ derived from $O_2^{\bullet -}/H_2O_2$ were carried out using the spin trap 4-pyridyl1-oxide-N-tert-butylnitrone (4-POBN). Leaves were vacuum-infiltrated with a buffer (25 mM HEPES, pH 7.5, 5 mM $MgCl_2$, 0.3 M sorbitol) containing the spin trap reagents (50 mM 4-POBN, 4% ethanol, 50 µM Fe-EDTA). Infiltrated leaves were placed into the buffer containing the spin trap reagents and illuminated for 30 min with white light (100 µmol quanta $m^{-2} s^{-1}$). At the end of the illumination time, the leaves were removed and the EPR signal of the solution was monitored. EPR spectra were recorded at room temperature in a standard quartz flat cell using an ESP-300 X-band spectrometer (Bruker). The following parameters were used: microwave frequency 9.73 GHz, modulation frequency 100 kHz, modulation amplitude: 1 G.

2.8 | Analysis of aldehydes, including RES and β-cyclocitral, with LC-MS/MS

Aldehydes were measured according to Roach et al. (2017). Briefly, leaves frozen in liquid nitrogen were ground for 1 min inside 2 mL reaction tubes using 2 × 5 mm quartz beads in 1 mL of pre-cooled (−20°C) acetonitrile, containing 0.5 µM 2-ethylhexanal (as internal standard) and 0.05% (wt:vol) of butylated hydroxytoluene. The resulting extract was centrifuged for 10 min, 4°C, at 26 000*g*, and the supernatant was split with 600 µL used for the analysis of aldehydes and 200 µL for the measurement of chlorophyll. Aldehydes were derivatized with 2,4-Dinitrophenylhydrazine (2,4-DNPH) in the presence of formic acid and diluted 50:50 with LC-MS-grade H_2O before injection of 3 µL sample. Separation was carried out using a reversed-phase column (NUCLEODUR C18 Pyramid, EC 50/2, 50 × 2 mm, 1.8 µm, Macherey-Nagel), using an ekspert ultraLC 100 UHPLC system coupled to a QTRAP 4500 mass spectrometer (AB SCIEX). Peak areas of selected ions were normalised to 2-ethylhexanal and chlorophyll content of the sample. Chlorophyll was quantified by absorbance in 80% acetone using the extinction coefficients of Porra et al. (1989).

2.9 | Pigment analysis

Mature leaves were frozen in liquid nitrogen, lyophilised and ground. Powder (2 mg dry weight) was dissolved in 500 µL acetone, 0.01% ammoniac, then centrifugation at 12 000*g* 5 min, supernatants were collected and pellet washed twice in acetone. Solvent was evaporated and the precipitates were resuspended in 100 µL acetone. Liquid chromatography-UV-absorption (HPLC-UV) analysis was performed using a HPLC column (Uptisphere Strategy C18-HQ 250 × 3 mm, 3 µm granulometry, Interchim) with a HPLC/UV chain (Shimadzu) including two pumps (LC-20AD), a sample manager

13653040, 2023, 12, Downloaded from https://onlinelibrary.wiley.com/doi/10.1111/pce.14695 by Portail BibCNRS INSU, Wiley Online Library on [23/11/2023]. See the Terms and Conditions (https://onlinelibrary.wiley.com/terms-and-conditions) on Wiley Online Library for rules of use; OA articles are governed by the applicable Creative Commons License

(SIL-20AC HT), a column oven (CTO-20A) and an UV diode array detector (UVSPD-M20A) with a flow of 0.5 mL min^{-1}. The mobile phase A was composed of 10% water and 89.5% acetonitrile with 0.5% acetic acid and the mobile phase B was ethyl acetate with 0.5% acetic acid. The elution gradient was as follows: initially 10% B, 1 min 10% B; then a linear increase up to 95% B for 24 min. At the end, the column was returned to initial conditions for a 15 min equilibration. Absorbance was monitored at 450 nm. Signals were calculated by normalisation of peak areas to chlorophyll *a*.

2.10 | Enzyme activities

Crude protein extracts were prepared by grinding leaves in liquid nitrogen before adding a buffer containing 0.3 M sorbitol, 50 mM KCl, 5 mM $MgCl_2$, 20 mM HEPES pH 7.2. The supernatant after centrifugation (13 000*g*, 5 min, 4°C) was used for the measurements. Protein content was determined using Amioblack. Superoxide dismutase (SOD) activity was measured spectrophotometrically using xanthine/xanthine oxidase as superoxide generating system and XTT (Na,3′-(1-(phenylaminocarbonyl)−3,4-tetrazolium)-bis-(4-methoxy-6-nitro) benzene sulfonic acid hydrate) for the detection of superoxide. A stock solution of xanthine (500 µM) was freshly prepared in water, adding 1 M NaOH until it dissolved. The final assay contained 50 µM xanthine, 100 µM XTT and 0.2 U mL^{-1} xanthine oxidase in 20 mM HEPES pH 7.0. The kinetics of superoxide production were measured as an increase in absorbance at 470 nm, and the SOD activity was determined by following the inhibition of the superoxide production after addition of 10 µg protein mL^{-1} of crude extract. Superoxide production was calculated using the molar extinction coefficient $\varepsilon_{470} = 24.2\ \mathrm{mMl^{-1}\,cm^{-1}}$ for XTT. Catalase activity was measured polarographically at 20°C with a Clark-type electrode in 50 mM HEPES (pH 8) in the presence of 1 mM H_2O_2 as substrate using a final protein concentration of 20 µg mL^{-1}. Guaiacol peroxidase activity was determined spectrophotometrically by measuring the oxidation of guaiacol to tetraguaiacol at 470 nm. At this wavelength, the molar extinction coefficient of tetraguaiacol is 26.6 mM^{-1} cm^{-1}. The reaction mixture contained 50 mM NaH_2PO_4/Na_2HPO_4 pH 7.5, 3 mM H_2O_2 and 0.01% (vol/vol) guaiacol, and 10 µg mL^{-1} protein.

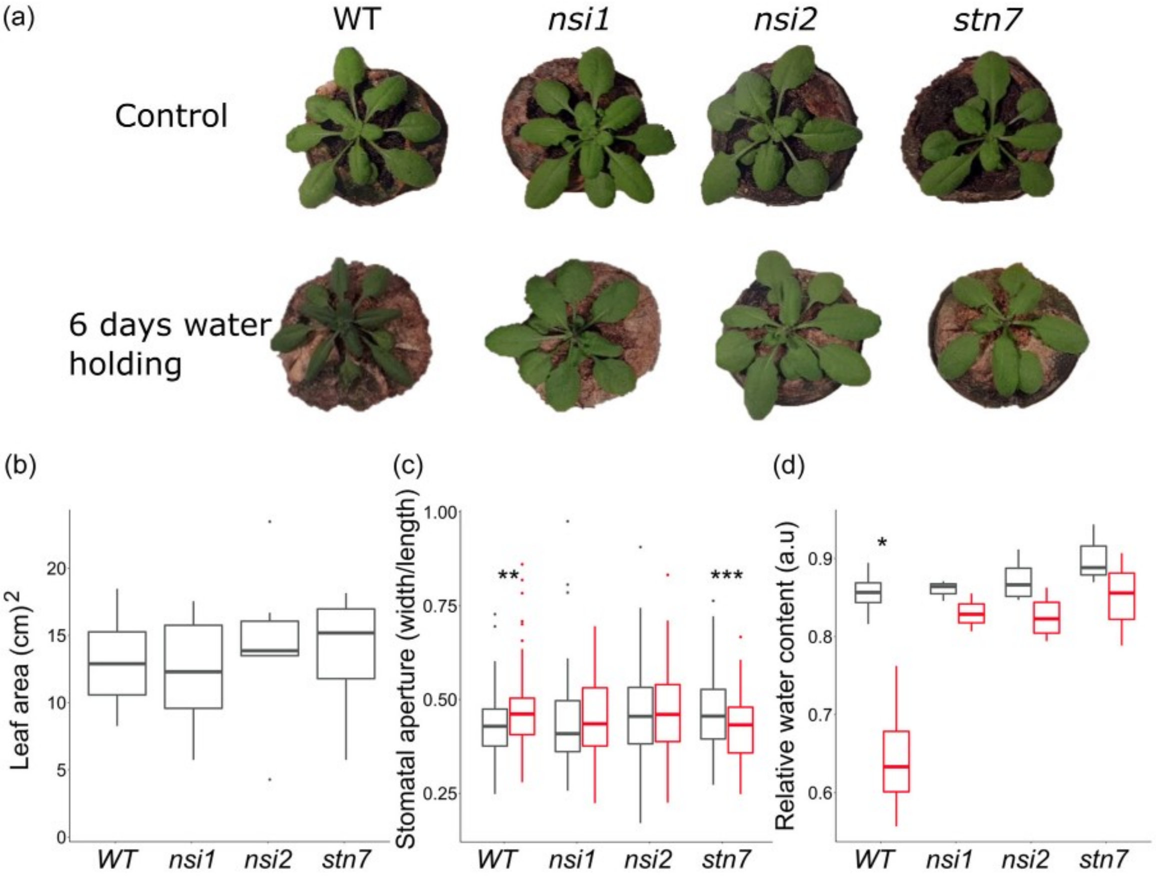

FIGURE 1 State transition mutants are more resistant to drought. (a) 4-week-old *A. thaliana* wild type and *nsi1*, *nsi2*, *stn7* plants well-watered and after 6 days without watering. (b) Rosette size ($n \geq 5$); plants from three different growth series. (c, d) Relative water content of total rosette in control conditions (grey) and after 4 days without watering (red). (d) Stomata aperture. Ratio width/length of stomata aperture in control conditions (black) and after 4 days without watering (red), counting about 100 stomata on at least three different leaves in each condition. Three replicates from four different independently grown sets of plants, $n = 12$, mean and *SD* are given. Stars indicate significant differences according to Student's *t* test (*$p < 0.05$, **$p < 0.01$, ***$p < 0.001$).

13653040, 2023, 12, Downloaded from https://onlinelibrary.wiley.com/doi/10.1111/pce.14695 by Portail BibCNRS INSU, Wiley Online Library on [23/11/2023]. See the Terms and Conditions (https://onlinelibrary.wiley.com/terms-and-conditions) on Wiley Online Library for rules of use; OA articles are governed by the applicable Creative Commons License

2.11 | Statistical analysis

Graphs and statistical tests were produced using the R software. For all boxplots, the various elements are defined as follows: upper whisker = largest observation less than or equal to upper hinge + 1.5 × interquartile range (IQR); lower whisker = smallest observation greater than or equal to lower hinge − 1.5 × IQR; centre line = median, 50% quantile; upper hinge = 75% quantile; lower hinge = 25% quantile; outliers are data beyond the end of the whiskers and represented by a dot; each dot in the box represents a single data point. Symbols represent the *p* value of Student test *: $p < 0.05$; **: $p < 0.01$; ***: $p < 0.001$; ****: $p < 0.0001$; no stars: $p > 0.05$.

3 | RESULTS

To investigate the drought stress tolerance of state transition mutants, we subjected wild type, *nsi1*, *nsi2*, and *stn7* to drought stress by withholding water for 6 days. The wild type leaves wilted while the state transition mutants were visibly much less affected (Figure 1a). The rosette sizes of the different genotypes were similar in well-watered plants (Figure 1b). For the following experiments water was withhold for 4 days to induce moderate drought stress. Under this condition, photosynthetic electron transport is not considered the primary damage site (Cornic & Fresneau, 2002; Kaiser, 1987). Upon moderate drought stress, the rosettes of the mutants showed a much higher water content (Figure 1c). Furthermore, stomata were significantly more closed in wild type upon moderate drought stress, while there was no change in stomata opening in the mutants (Figure 1d).

Since the mutants are affected in their ability to adapt the antenna size dependent on the light quality, intensity, and stress conditions, we investigated the effect of moderate drought on photosynthesis. No significant differences in chlorophyll and carotenoid compositions were observed between the genotypes with or without drought stress (SI Table 1). Upon drought, the content of β-carotene, lutein and neoxanthin increased in all genotypes. Analysis of chlorophyll fluorescence parameters showed that upon drought the effective quantum yield of photosystem II (YII) was significantly affected in wild type while there were no significant changes in the mutants (Figure 2a). For the statistical analysis, values measured at a light intensity of 100 µmol quanta $m^{-2} s^{-1}$ were chosen, an intensity close to the growth light intensity. When the light intensity exceeds the optimal intensity for assimilation, energy dissipation at the level of PSII sets in. According to Kramer et al. (2004), two types of quantum yields for energy dissipation can be defined, Y(NPQ) and Y(NO) which represent regulated and non-regulated energy dissipation, respectively. Dissipation of excess energy expressed as the yield of non-photochemical quenching, Y(NPQ), increased significantly in the wild type upon drought while it remained constant in the mutants

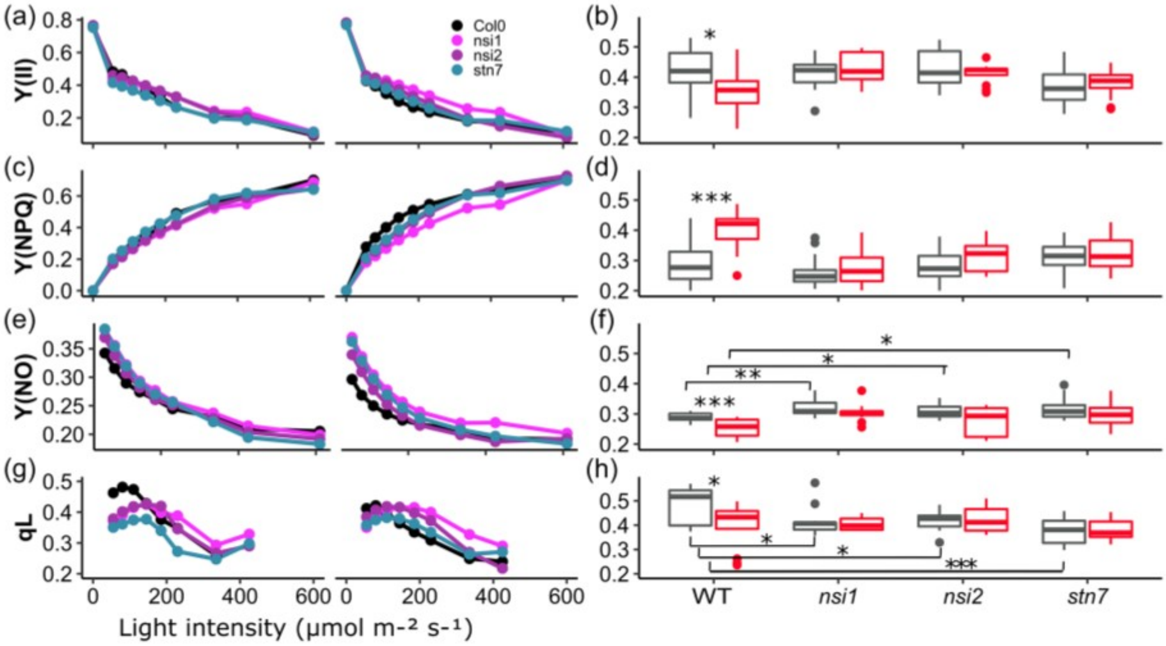

FIGURE 2 State transition mutants show no changes in the light dependency of chlorophyll fluorescence parameters upon moderate drought stress. Left: light response curves of fluorescence parameters in control conditions or after 4 days without watering (stress). (a, b) effective quantum yield PSII, Y(II), (c, d) controlled non-photochemical quenching, Y(NPQ), (e, f) Non-regulated non-photochemical quenching, Y(NO), and (g, h) fraction of open PSII centres, qL. The left panel shows variations of the fluorescence parameters as a function of the light intensity; the right panel shows boxplots of the fluorescence parameters for wild type and *nsi1*, *nsi2*, *stn7* at growth light intensity (100 µmol $m^{-2} s^{-1}$). Each light intensity was applied for 3 min before giving a saturating light flash. Three replicates from four different independently grown sets of plants, $n = 12$, mean and *SD* are given. Stars indicate significant differences according to Student's *t* test (*$p < 0.05$, **$p < 0.01$, ***$p < 0.001$).

13653040, 2023, 12, Downloaded from https://onlinelibrary.wiley.com/doi/10.1111/pce.14695 by Portail BibCNRS INSU, Wiley Online Library on [23/11/2023]. See the Terms and Conditions (https://onlinelibrary.wiley.com/terms-and-conditions) on Wiley Online Library for rules of use; OA articles are governed by the applicable Creative Commons License

(Figure 2b). Relevant here is that state transitions have only a minor contribution to chlorophyll fluorescence measurements of Y(NPQ), thus lack of change of Y(NPQ) in the mutants reflects lack of stress. This was the case of the regulated part of NPQ while the non-regulated quenching, Y(NO), decreased in the wild type upon stress (Figure 2c). When the genotypes were compared in control conditions, Y(NO) was significantly higher in the mutants, showing that state transitions influence chlorophyll fluorescence at growth light intensity. The larger amount of LHCII at PSII has the consequence that reaction centres of PSII were more closed in the mutants as indicated by significantly lower qL values in the control conditions, i.e., the primary quinone acceptor Q_A accumulated more in its reduced form in the mutants. In the case of qL, there was a significant decrease in the wild type upon drought, showing that more reaction centres were closed, while no significant differences were observed for the mutants (Figure 2h).

The results of the chlorophyll fluorescence parameters are in line with a lack of state transition in the mutants, however, they do not

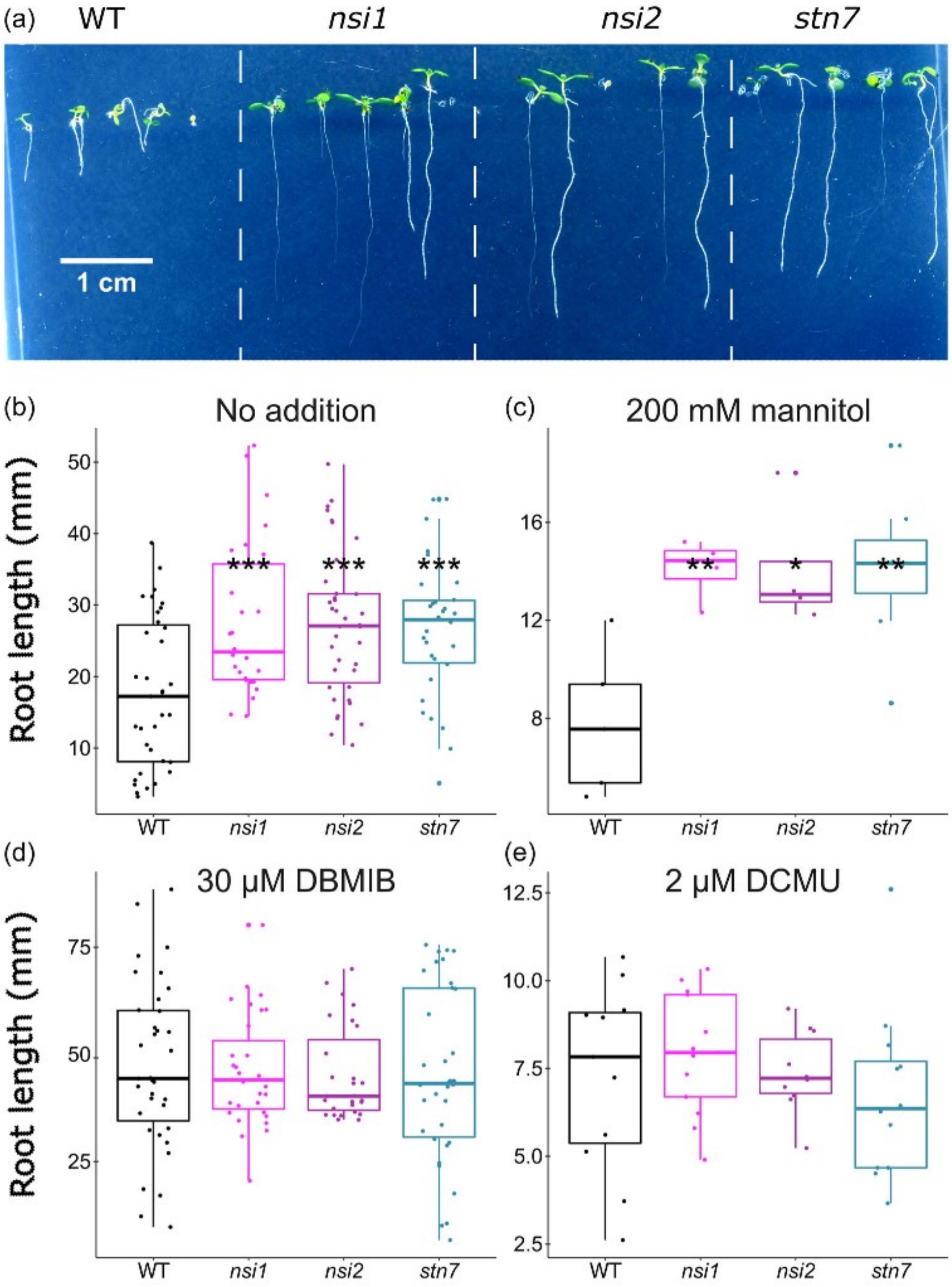

FIGURE 3 State transitions mutants show stimulation of growth root. (a) Photos of seedings of WT, *nsi1*, *nsi2*, and *stn7* after 7 days. (b) Length of the primary root of 7 days old in control conditions, $n \geq 21$. (c) Length of the primary root of 7 days old in the presence of 200 mM mannitol. (d, e) Length of the primary root of 7 days old in the presence of 30 µM DBMIB, $n \geq 10$, and 2 µM DCMU respectively, $n \geq 10$. Mean and *SD* are given. Stars indicate significant differences according to Student's *t* test (**p* < 0.05, ***p* < 0.01).

13653040, 2023, 12, Downloaded from https://onlinelibrary.wiley.com/doi/10.1111/pce.14695 by Portail BibCNRS INSU, Wiley Online Library on [23/11/2023]. See the Terms and Conditions (https://onlinelibrary.wiley.com/terms-and-conditions) on Wiley Online Library for rules of use; OA articles are governed by the applicable Creative Commons License

explain their improved drought tolerance. Since it has been described previously that N-acetylation of protein is important for germination and root development (Linster et al., 2015), we investigated the root growth of the seedlings. As shown in Figure 3a,b, the main root of the wild type was thinner and shorter compared with the mutants. In addition, lateral root development was strongly enhanced in the mutants. Differences in root architecture between the genotypes were not only observed in seedlings but also in 4-week-old plants grown in soil, with the wild type showing a slightly less well-developed root system (Figure S1). The difference between the lengths of the main root in seedlings of wild type and mutants was even higher when plants were grown under osmotic stress conditions (200 mM mannitol) (Figure 3c). However, when the photosynthetic electron transfer was blocked by DCMU, an inhibitor that blocks electron transport in PSII by binding to the Q_B-site of the D1 protein, or by DBMIB, an inhibitor of the cytochrome b_6f complex that binds to the Qo-binding site, differences between the genotypes were no longer observed. In the presence of DBMIB that leads to a more reduced PQ pool, growth of the main root was even stimulated in all genotypes compared to control conditions, while growth was retarded in the presence of DCMU that leads to an oxidised PQ pool. These results indicate that the reduction state of the PQ pool controls root growth.

In excess light conditions, more light is absorbed by the antenna than can be used for the reduction of $NADP^+$, and the PQ pool becomes more reduced. This is the case in the state transition mutants as seen by the lower qL compared to the wild type (Figure 2g,h). When Q_A is reduced, charge recombination reactions within PSII do occur between Q_A^- and the oxidised primary donor $P680^+$. This reaction leads to the generation of $^1O_2$, a highly oxidising reactive oxygen species. For visualising $^1O_2$ generation in leaves, we first used the fluorophore Singlet Oxygen Sensor Green, but, using this approach, we were not able to quantify differences between the four genotypes. Instead, we used an EPR spin probing assay with TEMPD as a probe to detect $^1O_2$ (Hideg et al., 2011). The assay cannot be performed with leaves or intact chloroplasts, and we used isolated thylakoid membranes instead. In thylakoids from wild-type plants, the L-LHCII is partly localised at PSI as is the case in leaves, while in the mutants all LHCII is localised at PSII as shown by 77K fluorescence (Figure 4a). As expected, when the PQ pool is more oxidised, less $^1O_2$ was generated in wild type compared with the mutants (Figure 4b,c).

To investigate whether there is a general increase in ROS generation in state transition mutants, we measured $O_2^{\bullet -}/H_2O_2$-derived hydroxyl radicals by a spin-trapping assay with 4-POBN/EtOH as a trap (Mubarakshina et al., 2010). Furthermore, the activity of a few antioxidant enzymes was measured. The amounts of $O_2^{\bullet -}/H_2O_2$ and the activities of the antioxidant enzymes superoxide dismutase, peroxidase, and catalase were slightly enhanced only in the wild type upon drought stress with only changes in peroxidase activity being statistically significant (Figure S2). In the mutants, the activities were unaltered or decreased upon drought in most cases. A statistically significant decrease of peroxidase activity was observed in *stn7*. However, an increase in catalase activity was observed in *nsi2*, although this increase was not significant. These data show that there was not a general increase in the level of oxidative stress in the mutants, but instead, a specific rise of $^1O_2$ levels. In the PSII reaction centre, $^1O_2$ can react with β-carotene, leading to oxidation products like β-cyclocitral and β-ionone. In addition, $^1O_2$ can react with lipids giving rise to additional RES. Figure 5 shows the most abundant RES detected in leaves from the wild type and the state transition

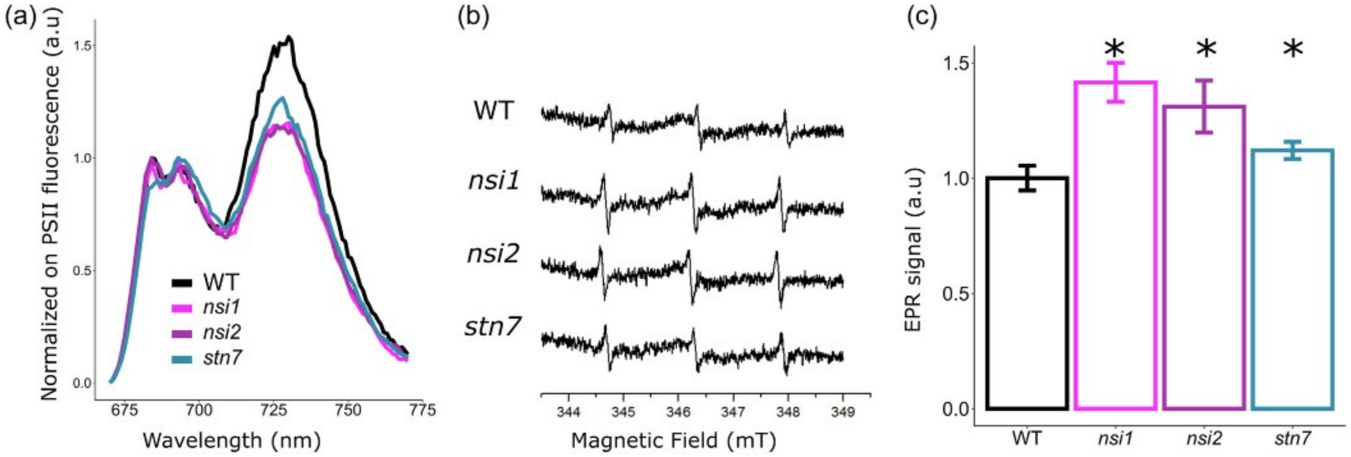

FIGURE 4 Thylakoid membranes of state transition mutants generate more singlet oxygen. (a) 77K chlorophyll fluorescence emission spectra of isolated thylakoid membranes. Signal normalised to PSII emission at 695 nm. Representative spectra are shown ($n = 3$). When chlorophyll *a* fluorescence emission spectra are measured at 77K, there are three emission maxima, two arising from PSII at 685 and 695 nm wavelength, and one arising from PSI around 733 nm wavelength. The lower emission from PSI in the mutants demonstrates that state transitions are not functional, and all LHCII are bound to PSII. (b) Detection of singlet oxygen by EPR using the spin probe TEMPD-HCl. Typical spectra are shown. (c) Quantification of the EPR signals ($n = 4$, 2 thylakoid preparations from set of plants grown at different times).
(c) Quantification of the EPR signals shown in (b). Mean and *SD* are given. Stars indicate significant differences according to Student's *t* test ($*p < 0.05$).

13653040, 2023, 12, Downloaded from https://onlinelibrary.wiley.com/doi/10.1111/pce.14695 by Portail BibCNRS INSU, Wiley Online Library on [23/11/2023]. See the Terms and Conditions (https://onlinelibrary.wiley.com/terms-and-conditions) on Wiley Online Library for rules of use; OA articles are governed by the applicable Creative Commons License

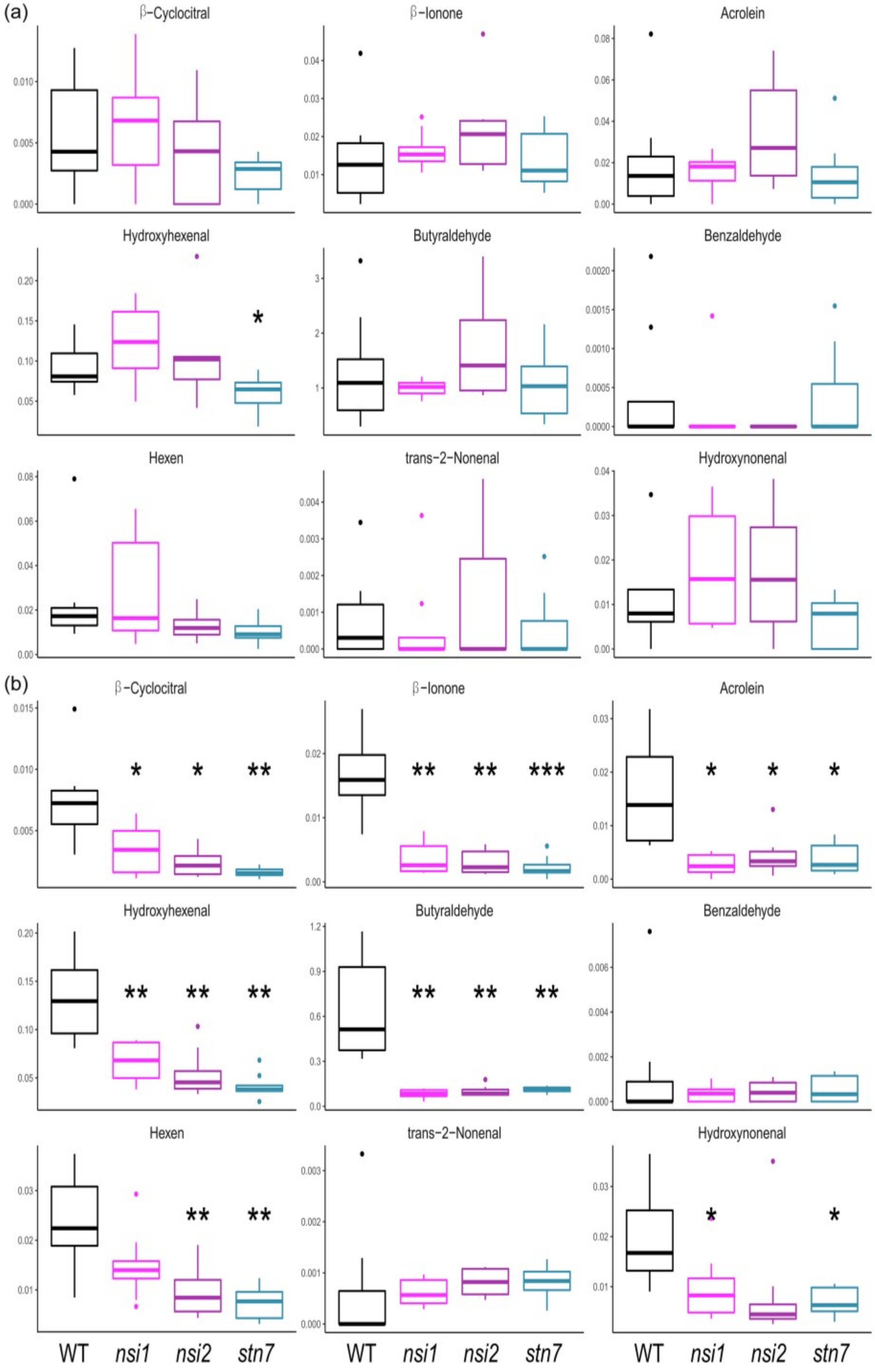

FIGURE 5 (See caption on next page).

13653040, 2023, 12, Downloaded from https://onlinelibrary.wiley.com/doi/10.1111/pce.14695 by Portail BibCNRS INSU, Wiley Online Library on [23/11/2023]. See the Terms and Conditions (https://onlinelibrary.wiley.com/terms-and-conditions) on Wiley Online Library for rules of use; OA articles are governed by the applicable Creative Commons License

mutants. In control conditions, there is no significant difference between the genotypes (Figure 5a), while upon moderate drought stress the wild type generated significantly more β-cyclocitral, β-ionone, acrolein, hydroxyhexanal, and butyraldehyde (Figure 5b). This is typical for a plant submitted to stress conditions. This shows that the wild-type plants are highly stressed, as already visible by the eye, while the state transition mutants cope with moderate drought stress without showing stress symptoms (Figure 1a).

4 | DISCUSSION

State transitions are controlled by the reduction state of the PQ pool via the activation of the STN7 kinase (Bellafiore et al., 2005; Depège et al., 2003). The results reported here raise the question of how the reduction state of the PQ pool affects root development. According to the data shown in Figure 3, the reduction state of the plastoquinone pool is crucial for primary root growth and lateral root development. In state transition mutants, the PQ pool is more reduced than in the wild type (Figure 2h). In all genotypes, when the PQ pool is reduced in the presence of DBMIB, root growth is stimulated (Figure 3d), whereas shorter roots are observed when the PQ pool is oxidised in the presence of DCMU (Figure 3e). Both, DCMU and DBMIB, inhibit photosynthetic electron transport, thereby showing that it is indeed the redox state of the PQ pool that exerts control of root growth and not differences in photosynthesis and sugar production. The inhibitory effect of DCMU on primary and lateral root growth has been observed previously and has been interpreted as photosynthesis promoting lateral root emergence partly through auxin biosynthesis (Duan et al., 2021). A yet unknown link between the redox state of the PQ pool and auxin signalling may be responsible for the observed differences in root architecture.

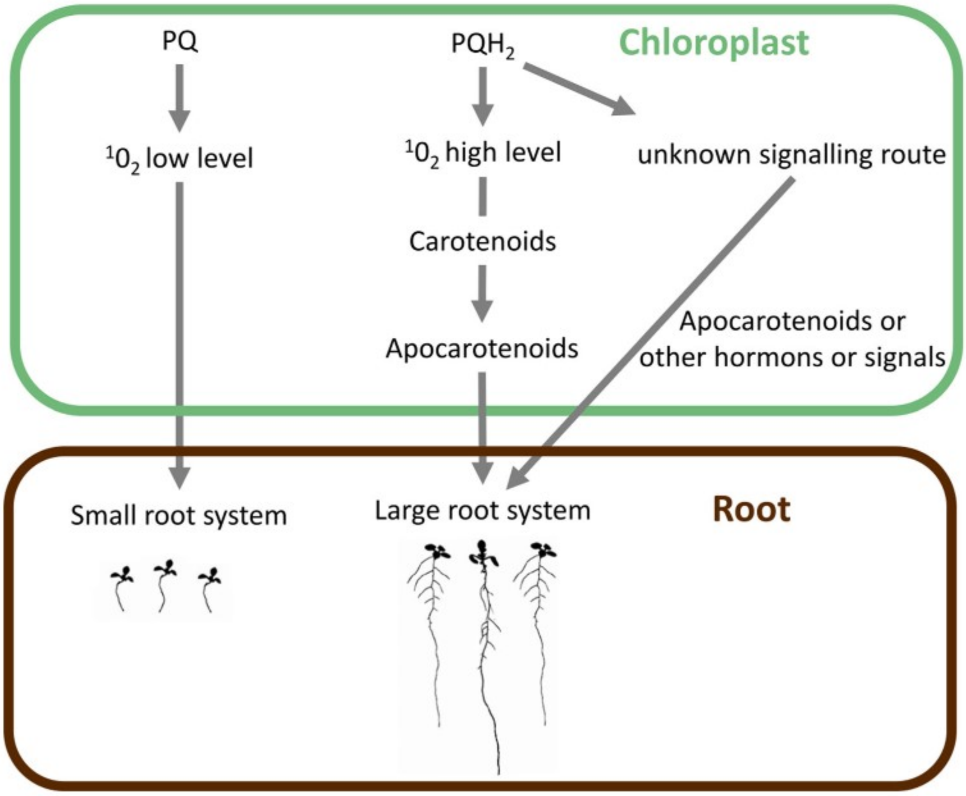

FIGURE 6 Connection between chloroplast redox state/$^1O_2$ generation and a long distance signalling pathway. When LHCII is blocked in state I (*stn7*, *nsi1*, *nsi2*), the plastoquinone pool is highly reduced in growth light in well-watered conditions. A highly reduced plastoquinone pool favours $^1O_2$ generation within PSII via charge recombination reactions between the primary donor P680 and the primary quinone acceptor Q_A^-. $^1O_2$ is supposed to react with β-carotene inside the reaction centre giving rise to the formation of apocarotenoids like β-cyclocitral. Its oxidation product, β-cyclocitric acid, is water soluble and could be transported from the shoot to the root, initiating signalling events far from the site of production. Other signalling events depending on the reduction state of the PQ pool are also imaginable.

FIGURE 5 Generation of reactive electrophile species is stimulated in wild type upon moderate drought stress. (a) Amounts of RES in leaves of 4-week-old WT, *nsi1*, *nsi2*, and *stn7* in control conditions. Shown are ion peak areas relative to the internal standard and normalised to the chlorophyll content of the extract. (b) Same as (a) after 4 days without watering ($n = 8$, independently grown sets of plants). Mean and *SD* are given. Stars indicate significant differences according to Student's *t* test (*$p < 0.05$, **$p < 0.01$, ***$p < 0.001$). WT, wild type.

13653040, 2023, 12, Downloaded from https://onlinelibrary.wiley.com/doi/10.1111/pce.14695 by Portail BibCNRS INSU, Wiley Online Library on [23/11/2023]. See the Terms and Conditions (https://onlinelibrary.wiley.com/terms-and-conditions) on Wiley Online Library for rules of use; OA articles are governed by the applicable Creative Commons License

As shown in Figure 4, state transition mutants generate slightly more $^1O_2$ than the wild type. $^1O_2$ may be the key to signalling events that promote root growth. Addition of DCMU inhibited root growth (Figure 3e), speaking at a first glance against the hypothesis that $^1O_2$ is responsible for the stimulation of root growth. However, although the addition of DCMU favours charge recombination in PSII, the yield of $^1O_2$ is low thanks to the modification of the midpoint potential of the redox couple Q_A/Q_A^- favoring charge recombination between $P680^+$ and Q_A^- via a direct route that does not yield ^{3}Chl (Fufezan et al., 2002; Krieger-Liszkay & Rutherford, 1998). The redox state of the PQ pool is known to be important for retrograde signalling (Dietz et al., 2016; Pfalz et al., 2012). In retrograde signalling, a signal travels from the chloroplast to the nucleus within the same cell. Here, a signal is required that travels over long distances. Figure 6 illustrates the hypothetical signal pathway. $^1O_2$ may produce signals such as apocarotenoids that are able to initiate signalling events far from the site of their production. β-Carotene oxidation products such as the volatile β-cyclocitral and its direct water-soluble oxidation product, β-cyclocitric acid, are known to regulate nuclear gene expression through several signalling pathways (D'Alessandro et al., 2019; Ramel et al., 2012; Shumbe et al., 2017). However, we were not able to detect an increase in β-cyclocitral or other RES in leaves of state transition mutants compared to wild type in plants under control conditions. This may be because the difference in $^1O_2$ production was, although significant, small. Even smaller differences are expected in the subsequently generated β-carotene oxidation products. We may technically not be able to detect such small differences in RES. Differences in levels of β-cyclocitral or other RES may also depend on the developmental stage of the plants. The RES measurements were performed with mature leaves while the root phenotype was observed in young seedlings. Besides $^1O_2$ and RES, the redox state of the PQ pool may activate other signalling pathways that involve microRNAs (Bertolotti et al., 2021) or changes in hormone levels like abscisic acid and strigolactones favoring root growth (Gomez-Roldan et al., 2008; Ruyter-Spira et al., 2011).

In conclusion, alterations in state transition appear to be a promising trait for improving plant growth and thereby crop productivity under harsh environmental conditions. The signalling pathway has to be elucidated in future work. It should be explored whether other photosynthetic mutants which exhibit an imbalance between PSII and PSI activity are also more drought resistant. Mutants affected not only in the antenna systems but also in the activity of the photosystems seem to be promising avenue for exploring drought tolerance. Especially mutants with slight defects in the turnover of the cytochrome b_6f complex or in photosystem I may be of interest since their PQ pool is in a more reduced state. Mutants lacking small subunits, for example PsaI (Schöttler et al., 2017), or expressing only one isoform of certain subunits, for example PsaE1 or PsaE2 (Hald et al., 2008; Krieger-Liszkay et al., 2020), which do not show a strong phenotype in control conditions seem to be ideal candidates to test their resistance to drought stress.

ACKNOWLEDGEMENTS

We would like to thank Sandrine Cot (I2BC) for technical assistance and Paula Mulo (University of Turku, Finland) for sending us the seeds of the state transition mutants. This work was supported by the Labex Saclay Plant Sciences-SPS (ANR-17-EUR-0007), the platform of Biophysics of the I2BC supported by the French Infrastructure for Integrated Structural Biology (FRISBI; grant number ANR-10-INSB-05), this work has benefited from the support of IJPB's Plant Observatory technological platforms and this work benefited from the French state aid managed by the ANR under the "Investissements d'avenir" programme with the reference ANR-16-CONV-0003 (CLand). L.L. is supported by a CLand and SPS PhD fellowship.

DATA AVAILABILITY STATEMENT

The data that support the findings of this study are available from the corresponding author upon reasonable request. Data will be made available on demand.

ORCID

Thomas Roach http://orcid.org/0000-0002-0259-0468
François Perreau http://orcid.org/0000-0001-7873-9866
Anja Krieger-Liszkay http://orcid.org/0000-0001-7141-4129

REFERENCES

Bellafiore, S., Barneche, F., Peltier, G. & Rochaix, J.-D. (2005) State transitions and light adaptation require chloroplast thylakoid protein kinase STN7. *Nature*, 433, 892–895.

Bertolotti, G., Scintu, D. & Dello Ioio, R. (2021) A small cog in a large wheel: crucial role of miRNAs in root apical meristem patterning. *Journal of Experimental Botany*, 72, 6755–6767.

Biswas, M.S., Fukaki, H., Mori, I.C., Nakahara, K. & Mano, J. (2019) Reactive oxygen species and reactive carbonyl species constitute a feed-forward loop in auxin signaling for lateral root formation. *The Plant Journal*, 100, 536–548.

Cornic, G. (2002) Photosynthetic carbon reduction and carbon oxidation cycles are the main electron sinks for photosystem II activity during a mild drought. *Annals of Botany*, 89, 887–894.

D'Alessandro, S., Mizokami, Y., Légeret, B. & Havaux, M. (2019) The apocarotenoid β-cyclocitric acid elicits drought tolerance in plants. *iScience*, 19, 461–473.

Depège, N., Bellafiore, S. & Rochaix, J.-D. (2003) Role of chloroplast protein kinase Stt7 in LHCII phosphorylation and state transition in Chlamydomonas. *Science*, 299, 1572–1575.

Dickinson, A.J., Lehner, K., Mi, J., Jia, K.P., Mijar, M., Dinneny, J. et al. (2019) β-Cyclocitral is a conserved root growth regulator. *Proceedings of the National Academy of Sciences*, 116, 10563–10567.

Dietz, K.J., Turkan, I. & Krieger-Liszkay, A. (2016) Redox- and reactive oxygen species-dependent signaling into and out of the photosynthesizing chloroplast. *Plant Physiology*, 171, 1541–1550.

Duan, L., Pérez-Ruiz, J.M., Cejudo, F.J. & Dinneny, J.R. (2021) Characterization of CYCLOPHILLIN38 shows that a photosynthesis-derived systemic signal controls lateral root emergence. *Plant Physiology*, 185, 503–518.

Fufezan, C., Rutherford, A.W. & Krieger-Liszkay, A. (2002) Singlet oxygen production in herbicide-treated photosystem II. *FEBS Letters*, 532, 407–410.

13653040, 2023, 12, Downloaded from https://onlinelibrary.wiley.com/doi/10.1111/pce.14695 by Portail BibCNRS INSU, Wiley Online Library on [23/11/2023]. See the Terms and Conditions (https://onlinelibrary.wiley.com/terms-and-conditions) on Wiley Online Library for rules of use; OA articles are governed by the applicable Creative Commons License

Gamborg, O.L., Miller, R.A., & Ojima, K. (1968) Nutrient requirements of suspension cultures of soybean root cells. *Experimental Cell Research*, 50, 151–158.

Gomez-Roldan, V., Fermas, S., Brewer, P.B., Puech-Pagès, V., Dun, E.A., Pillot, J.P. et al. (2008) Strigolactone inhibition of shoot branching. *Nature*, 455, 189–194.

Hald, S., Pribil, M., Leister, D., Gallois, P. & Johnson, G.N. (2008) Competition between linear and cyclic electron flow in plants deficient in photosystem I. *Biochimica et Biophysica Acta (BBA) - Bioenergetics*, 1777, 1173–1183.

Hideg, É., Deák, Z., Hakala-Yatkin, M., Karonen, M., Rutherford, A.W., Tyystjärvi, E. et al. (2011) Pure forms of the singlet oxygen sensors TEMP and TEMPD do not inhibit photosystem II. *Biochimica et Biophysica Acta (BBA) - Bioenergetics*, 1807, 1658–1661.

Kaiser, W.M. (1987) Effects of water deficit on photosynthetic capacity. *Physiologia Plantarum*, 71, 142–149.

Koskela, M.M., Brünje, A., Ivanauskaite, A., Grabsztunowicz, M., Lassowskat, I., Neumann, U. et al. (2018) Chloroplast acetyltransferase NSI is required for state transitions in *Arabidopsis thaliana*. *The Plant Cell*, 30, 1695–1709.

Kramer, D.M., Johnson, G., Kiirats, O. & Edwards, G.E. (2004) New fluorescence parameters for the determination of QA redox state and excitation energy fluxes. *Photosynthesis Research*, 79, 209–218.

Krieger-Liszkay, A. (2004) Singlet oxygen production in photosynthesis. *Journal of Experimental Botany*, 56, 337–346.

Krieger-Liszkay, A., & Rutherford, A.W. (1998) Influence of herbicide binding on the redox potential of the quinone acceptor in photosystem II: relevance to photodamage and phytotoxicity. *Biochemistry*, 37, 17339–17344.

Krieger-Liszkay, A., Shimakawa, G. & Sétif, P. (2020) Role of the two PsaE isoforms on O2 reduction at photosystem I in *Arabidopsis thaliana*. *Biochimica et Biophysica Acta (BBA) - Bioenergetics*, 1861, 148089.

Linster, E., Stephan, I., Bienvenut, W.V., Maple-Grødem, J., Myklebust, L.M., Huber, M. et al. (2015) Downregulation of N-terminal acetylation triggers ABA-mediated drought responses in arabidopsis. *Nature Communications*, 6, 7640.

Linster, E. & Wirtz, M. (2018) N-terminal acetylation: an essential protein modification emerges as an important regulator of stress responses. *Journal of Experimental Botany*, 69, 4555–4568.

Messant, M., Timm, S., Fantuzzi, A., Weckwerth, W., Bauwe, H., Rutherford, A.W. et al. (2018) Glycolate induces redox tuning of photosystem II in vivo: study of a photorespiration mutant. *Plant Physiology*, 177, 1277–1285.

Mubarakshina, M.M., Ivanov, B.N., Naydov, I.A., Hillier, W., Badger, M.R. & Krieger-Liszkay, A. (2010) Production and diffusion of chloroplastic H_2O_2 and its implication to signalling. *Journal of Experimental Botany*, 61, 3577–3587.

Van Norman, J.M., Zhang, J., Cazzonelli, C.I., Pogson, B.J., Harrison, P.J., Bugg, T.D.H. et al. (2014) Periodic root branching in arabidopsis requires synthesis of an uncharacterized carotenoid derivative. *Proceedings of the National Academy of Sciences*, 111, E1300–E1309.

Pfalz, J., Liebers, M., Hirth, M., Grübler, B., Holtzegel, U., Schröter, Y. et al. (2012) Environmental control of plant nuclear gene expression by chloroplast redox signals. *Frontiers in Plant Science*, 3, 257.

Porra, R.J., Thompson, W.A. & Kriedemann, P.E. (1989) Determination of accurate extinction coefficients and simultaneous equations for assaying chlorophylls a and b extracted with four different solvents: verification of the concentration of chlorophyll standards by atomic absorption spectroscopy. *Biochimica et Biophysica Acta (BBA) - Bioenergetics*, 975, 384–394.

Pribil, M., Pesaresi, P., Hertle, A., Barbato, R. & Leister, D. (2010) Role of plastid protein phosphatase TAP38 in LHCII dephosphorylation and thylakoid electron flow. *PLoS Biology*, 8, e1000288.

Ramel, F., Birtic, S., Ginies, C., Soubigou-Taconnat, L., Triantaphylides, C. & Havaux, M. (2012) Carotenoid oxidation products are stress signals that mediate gene responses to singlet oxygen in plants. *Proceedings National Academy of Sciences USA*, 109, 5535–5540.

Roach, T., Baur, T., Stöggl, W. & Krieger-Liszkay, A. (2017) *Chlamydomonas reinhardtii* responding to high light: a role for 2-propenal (acrolein). *Physiologia Plantarum*, 161, 75–87.

Rutherford, A.W. & Krieger-Liszkay, A. (2001) Herbicide-induced oxidative stress in photosystem II. *Trends in Biochemical Sciences*, 26, 648–653.

Ruyter-Spira, C., Kohlen, W., Charnikhova, T., van Zeijl, A., van Bezouwen, L., de Ruijter, N. et al. (2011) Physiological effects of the synthetic strigolactone analog GR24 on root system architecture in arabidopsis: another belowground role for strigolactones? *Plant Physiology*, 155, 721–734.

Schöttler, M.A., Thiele, W., Belkius, K., Bergner, S.V., Flügel, C., Wittenberg, G. et al. (2017) The plastid-encoded PsaI subunit stabilizes photosystem I during leaf senescence in tobacco. *Journal of Experimental Botany*, 68, 1137–1155.

Shapiguzov, A., Ingelsson, B., Samol, I., Andres, C., Kessler, F., Rochaix, J.-D. et al. (2010) The PPH1 phosphatase is specifically involved in LHCII dephosphorylation and state transitions in arabidopsis. *Proceedings of the National Academy of Sciences*, 107, 4782–4787.

Shumbe, L., D'Alessandro, S., Shao, N., Chevalier, A., Ksas, B., Bock, R. et al. (2017) METHYLENE BLUE SENSITIVITY 1 (MBS1) is required for acclimation of arabidopsis to singlet oxygen and acts downstream of β-cyclocitral. *Plant, Cell & Environment*, 40, 216–226.

Stone, J.M. & Walker, J.C. (1995) Plant protein kinase families and signal transduction. *Plant Physiology*, 108, 451–457.

SUPPORTING INFORMATION

Additional supporting information can be found online in the Supporting Information section at the end of this article.

How to cite this article: Leverne, L., Roach, T., Perreau, F., Maignan, F. & Krieger-Liszkay, A. (2023) Increased drought resistance in state transition mutants is linked to modified plastoquinone pool redox state. *Plant, Cell & Environment*, 46, 3737–3747. https://doi.org/10.1111/pce.14695

13653040, 2023, 12, Downloaded from https://onlinelibrary.wiley.com/doi/10.1111/pce.14695 by Portail BibCNRS INSU, Wiley Online Library on [23/11/2023]. See the Terms and Conditions (https://onlinelibrary.wiley.com/terms-and-conditions) on Wiley Online Library for rules of use; OA articles are governed by the applicable Creative Commons License

13.3 “Improving the SIF constraint on GPP for boreal evergreen needleleaf forests in a land surface model using a physiologically-based representation of non-photochemical quenching and data assimilation” (Leverne et al., submitted)

Improving the SIF constraint on GPP for boreal evergreen needleleaf forests in a land surface model using a physiologically-based representation of non-photochemical quenching and data assimilation

Lucas Leverne[1,2], Camille Abadie[1], Cédric Bacour[1], Yuan Zhang[1], Thomas Andrew Black[2], Vladislav Bastrikov[3], Nina Raoult[4], Philippe Peylin[1], Anja Krieger-Liszkay[5], and Fabienne Maignan[1,*]

[1]Laboratoire des Sciences du Climat et de l'Environnement, LSCE/IPSL, CEA-CNRS-UVSQ, Université Paris-Saclay, Gif-sur-Yvette, France

[2]Faculty of Land and Food Systems, University of British Columbia, Vancouver, BC, V6T1Z4, Canada

[3]Science Partners, 42 quai de Jemmapes, 75010 Paris, France

[4]College of Engineering, Mathematics and Physical Sciences, University of Exeter, Exeter, UK

[5]Université Paris-Saclay, Institute for Integrative Biology of the Cell (I2BC), CEA, CNRS, 91198 Gif-sur-Yvette Cedex, France

*Corresponding author: fabienne.maignan@lsce.ipsl.fr

Abstract

Boreal forests play an important role in the mitigation of climate change by capturing atmospheric CO_2 through photosynthesis. Their gross primary production (GPP) can be simulated using land surface models (LSMs). The associated uncertainty remains however quite large, mainly due to missing or incorrectly represented processes, as well as uncertain parameter values. Space-borne observations of solar-induced fluorescence (SIF) observations have previously been used in to improve LSMs' GPP simulations. However, accurately accounting for the third energy pathway that competes with fluorescence and photochemistry, that is to say non-photochemical quenching (NPQ), remains both a challenge and an imperative for reducing the prediction uncertainty. Here, we focused on improving the GPP simulated by the ORCHIDEE LSM over boreal evergreen needleleaf forests (BorENF), using a specific and more physiologically-based representation of NPQ mechanisms, plus a data assimilation approach with solar-induced fluorescence (SIF) data. First, we separated the modelling of the NPQ sustained part specific to this evergreen biome which does not photosynthesize under the cold winter temperatures, from the modelling of the NPQ reversible part common to all biomes, and we used active fluorescence measurements to calibrate the NPQ sustained and reversible models. Second, we assimilated recent SIF retrievals from the European Space Agency satellite TROPOspheric Monitoring Instrument (TROPOMI), as well as *in situ* GPP estimates from FLUXNET towers to optimise the GPP simulated by the ORCHIDEE LSM over BorENF. Compared to the prior simulations, the posterior ones show improved mean seasonal cycles for both GPP and SIF, in closer agreement to data-driven reference products FLUXSAT and FLUXCOM over the period 2001-2015 for GPP, and to the TROPOMI SIF retrievals for SIF. Steps towards improvement are identified in terms of both modelling and data assimilation.

Keywords

solar-induced fluorescence

gross primary production

land surface model

data assimilation

boreal evergreen needleleaf forests

non-photochemical quenching

1 Introduction

Land surfaces absorb about 30% of the CO_2 anthropogenic emissions, thus playing a key role in mitigating climate change (Friedlingstein et al., 2022). This contribution estimated using Land Surface

Models (LSMs) suffers however from remaining large uncertainties on the space-time distribution of both the gross fluxes simulated by LSMs, the Gross Primary Production (GPP), which is the quantity of carbon retrieved from the atmosphere through photosynthesis, as well as the total ecosystem respiration (Seiler et al., 2022). Regarding GPP, LSMs differ widely in their prediction and do not always compare well with data-driven GPP estimates (e.g., Anav et al., 2015; Slevin et al., 2017; Stocker et al., 2020; Seiler et al., 2022). Incorrect parameterizations, including missing processes and uncertain parameter values, mostly explain these large uncertainties in GPP simulations from regional to global scales.

It is even more challenging to improve GPP parameterisation of LSMs at large spatio-temporal scales because the corresponding key process, photosynthesis, can only be measured directly at the leaf scale. The growing networks of eddy-covariance (EC) flux towers provide ecosystem GPP estimates and have already led to large improvements of GPP modelling (Richardson et al., 2010; Groenendijk et al., 2011; Raoult et al., 2016). Nevertheless, the largest network (FLUXNET; Pastorello et al., 2020) does not sample the Earth vegetated surfaces in a representative manner. For example, large regions in Africa, South America and Boreal latitudes are not monitored (https://fluxnet.org/custom-map/cartographer.html, last access: 14 June 2023). The GPP products that are spatially extrapolated from this network are the reference values at the global scale (Jung et al., 2020; Joiner et al., 2018; Zeng et al., 2020b), but they still suffer from this sparsity of *in situ* observations. Land surface modellers are thus looking for large-scale proxies to better constrain the modelled GPP.

Over the last decade, Solar-Induced chlorophyll Fluorescence (SIF) has asserted its position as a prominent proxy for GPP. The first studies using satellite-derived fluorescence products evidenced a good correlation between SIF and GPP at large spatial and temporal scales (Frankenberg et al., 2011; Joiner et al., 2011). Following studies also showed a good correlation between SIF satellite observations and *in situ* GPP estimates (Joiner et al., 2014; Walther et al., 2016). Finally, the need for a better understanding of the underlying processes, at higher spatial and temporal resolutions, has pushed for the development of theoretical frameworks (Yang et al., 2020; Zeng et al., 2020a), and have encouraged the expansion of *in situ* measurements of fluorescence (e.g., Damm et al., 2015; Porcar-Castell et al., 2015; Parazoo et al., 2019). Several LSMs have implemented process-based representations of SIF, and used data assimilation techniques with some of the available SIF products to improve their simulated GPP (Norton et al., 2019; Bacour et al., 2019; Wang et al., 2021). Furthermore, the TROPOspheric Monitoring Instrument (TROPOMI) onboard the Copernicus Sentinel-5 Precursor platform has provided global scale retrievals of SIF since May 2018, with a pixel size of 3.5 km by 7.5 km before August 2019 and 3.5 km by 5.5 km since, and a daily coverage, thus offering a much larger number of observations than the former missions (Guanter et al., 2021; Köhler et al., 2018).

From a process perspective, SIF is radiation emitted by plants in the visible to near-infrared range, and triggered by incoming solar radiation. When light is absorbed by chlorophyll molecules of the photosystems (PS), the corresponding energy is primarily used for photochemistry. The excess of energy (compared to the capacity of carbon fixation in the Calvin cycle) is either dissipated as heat through different mechanisms of photoprotection grouped under the name of non-photochemical quenching (NPQ), or re-emitted as fluorescence (Baker, 2008). SIF is therefore a by-product of photosynthesis. However, several remaining challenges limit the interpretation and exploitation of SIF data, as recently listed in Porcar-Castell et al. (2021), in particular to constrain GPP in LSMs. Among those limitations, they identified a poor understanding of the energy partitioning in photosystem II (PSII) (between photochemistry, fluorescence, and NPQ processes), and of NPQ processes. Indeed, a correct attribution of SIF variations in terms of changes in GPP requires accurate representation of this third energy dissipation pathway. The three pathways using the energy of photons absorbed by chlorophyll pigments can be characterised by reaction rate constants (Kramer et al., 2004). These rate constants can be quantified based on active fluorescence measurements, using Pulse Amplitude Modulation (PAM) technology with a Light-Emitting Diode (LED) light. NPQ processes can be further split into a reversible component that is relaxed fast, and a sustainable one that is persistent over a longer period (Porcar-Castell, 2011). The reversible NPQ is mainly regulated by rapid changes in the thylakoid lumen pH as a response to light intensity fluctuations, enhancing conversions of xanthophyll cycle pigments (Jahns et al., 2009). The sustained NPQ results from an acclimation of evergreen needleleaf species to cold winter temperatures, and relies on a strong downregulation of PSII kinetics with a direct energy transfer from PSII to photosystem I, following reorganisation in the thylakoid membrane (Bag et al., 2020). A model for the total NPQ constant rate was formerly developed in Bacour et al. (2019) for the ORCHIDEE LSM, using *in situ* PAM measurements made on two boreal Scots pine (*Pinus sylvestris*) trees at the Hyytiälä forest in Finland (Porcar-Castell, 2011) and on Mediterranean species (Flexas et al., 2002). Raczka et al. (2019) used the same *in situ* PAM measurements performed at Hyytiälä to derive a model for the sustainable and reversible NPQ constant rates, implemented in the Community Land Model (CLM) version 4.5 LSM, and evaluated at Niwot Ridge (USA), another boreal evergreen needleleaf forest site.

Boreal forests represent a large carbon sink for the Northern Hemisphere, accounting for around 20% of the global forest sink, but the impacts of climate change on this biome and its feedback are highly uncertain (Luyssaert et al., 2007; Gauthier et al., 2015; Harris et al., 2021; Hayes et al., 2022). The low albedo of boreal forests enhances climate warming, while a rise in temperature could lead to an increase in net primary production (NPP) representing negative feedback on warming (Bonan et al., 2008). For boreal evergreen species, previous studies have evidenced a higher performance of SIF to monitor GPP seasonal variations compared to vegetation indices (VIs) (Joiner et al., 2014; Magney et al., 2019; Walther et al., 2016; Zuromski et al., 2018). Indeed, VIs track variations in vegetation greenness, meaning that VIs capture the potential photosynthetic rate but not the actual photosynthesis (Garbulsky et al., 2011). This limits the relevance of using VIs for cold-climate evergreen species that retain their foliage but for which photosynthesis is downregulated during winter. Therefore, sustainable NPQ is particularly important for boreal evergreen forests in winter when the absorbed energy is not used for photochemistry but needs to be dissipated as heat to avoid damage (Verhoeven, 2014; Bag et al., 2020). Since NPQ is the dominant pathway for energy usage in winter, a precise understanding and representation of NPQ dynamics is needed to investigate the link between SIF and GPP for such biomes.

In this study, our goal was to better represent the covariations of NPQ, SIF and GPP, simulated by the ORCHIDEE LSM over boreal evergreen needleleaf forests, taking advantage of the combination of the unique *in situ* PAM series at Hyytiälä, and of the dense spatial coverage of the TROPOMI SIF estimates. The study encompassed the following steps:

1. We implemented a more process-oriented model of the NPQ mechanisms, splitting between sustainable and reversible components, calibrated with the *in situ* PAM measurements at Hyytiälä.
2. We assimilated simultaneously SIF TROPOMI data and *in situ* GPP estimates from EC flux towers over an ensemble of sites in the boreal evergreen needleleaf forest (BorENF) vegetation type, to optimize the main photosynthesis, fluorescence and NPQ-related parameters of the ORCHIDEE LSM.
3. We evaluated the impact of the modifications over the entire BorENF vegetation type, with respect to SIF TROPOMI data and to independent data-driven GPP products.

2 Model, methodology, data

2.1 The ORCHIDEE model

2.1.1 Model description

ORCHIDEE is an LSM developed at the Institut Pierre Simon Laplace (IPSL). It is the land component of the IPSL Earth System Model (Boucher et al., 2020; Chéruy et al., 2020). ORCHIDEE computes the energy, carbon, and water exchanges at the interface between the land surfaces and the atmosphere

(Krinner et al., 2005). Fast processes such as the hydrological ones and photosynthesis are computed at a half-hourly time step, while other carbon-related processes such as allocation or turnover are computed at a daily time step. The sub-grid variability of vegetation properties and functioning is represented through fractions of Plant Functional Types (PFTs), where plants with the same photosynthetic pathway, and similar morphology, phenology, and climatic environment, are grouped together. PFT maps are derived from the European Space Agency (ESA) Climate Change Initiative (CCI) Land Cover (LC) products based on a cross-walking approach (Poulter et al., 2015). For hydrology, the soil texture is derived from the Zobler map (Zobler, 1986) and reduced to three types corresponding to the United States Department of Agriculture (USDA) classes of Sandy Loam, Medium Loam and Clay Loam (d'Orgeval et al., 2008). The CO_2 atmospheric concentration is considered as spatially constant, with a yearly varying global value provided by the TRENDY model intercomparison project (https://blogs.exeter.ac.uk/trendy/, last access: 14 June 2023; Sitch et al., 2015).

The Leaf Area Index (LAI) is calculated at a daily time step and is therefore a prognostic variable. The canopy is discretized from top to bottom over LAI layers of increasing thickness (from 0.1 to 1.8), with the last slab cut at the actual LAI value. The net assimilation of CO_2 through photosynthesis (A) is computed at leaf level following the scheme developed in Yin and Struik (2009), based on the Farquhar et al. (1980) model for C3 species and on the Collatz et al. (1992) model for C4 species. Important variables are the maximum carboxylation rate limited by Rubisco activity (V_{cmax}), and the maximum rate of electron transport (J_{max}), with the associated reference parameters at 25°C V_{cmax25} and J_{max25}, respectively. V_{cmax} varies with leaf age following Ishida et al. (1999), older leaves being photosynthetically less efficient, and the leaf life span is characterised by the $L_{agecrit}$ parameter. Carbon assimilation A is computed only when the growth temperature (moving average of the air temperature at 2 metres over 20 days) is larger than -4 °C (T_{min} parameter), otherwise it is simply set to 0. It is then upscaled at canopy level, by summing over all LAI layers. The temperature-dependency of the photosynthesis model variables is set following Medlyn et al. (2002), and Kattge and Knorr (2007) for the acclimation.

For the dedicated ORCHIDEE-SIF version used in this study, we adopted the updated light transmission model developed in Zhang et al. (2020), with a two-stream scheme describing direct and diffuse photosynthetically active radiation (PAR), and partitioning leaves between sunlit and shaded. Zhang et al. (2020) showed that the simulated GPP was improved when evaluated over 159 eddy covariance sites, as it could now reproduce the positive difference observed between cloudy and sunny conditions (for a given incident solar radiation level).

Based on this new scheme, we made additional modifications to improve both GPP and SIF modelling, which are briefly summarised here. The coefficients used to compute the light extinction through the canopy now depend on a clumping index (Nilson, 1999) and a leaf average angle (*ALA*; Campbell, 1990), both parameters being PFT-dependent. The leaf chlorophyll content is linearly related to V_{cmax} following Croft et al. (2017). The leaf-level photosynthetic yield of PSII is computed based on the assimilation and the absorption cross section for photosystem II, which is now set as a parameter, a_{PSII}, rather than a fixed constant, following Equation (4) in Bacour et al. (2019). The computation of the fluorescence yield for PSII is based on a lake model (Kramer et al., 2004), following Equation (3) in Bacour et al. (2019), and depends on the PSII photosynthetic yield and three rate constants: k_F for fluorescence, k_D for basal thermal energy dissipation, and k_{NPQ} for NPQ processes. We used the formalism developed for the FluorMODleaf model in Pedrós et al. (2010) to compute the leaf-level SIF emission. To upscale to the canopy level, we dropped the former parametric representation of the SCOPE model (Soil Canopy Observation, Photochemistry and Energy fluxes; van der Tol et al., 2009) adopted in Bacour et al. (2019), and summed the SIF fluxes escaping in the nadir direction over all LAI layers.

Regarding the NPQ rate constant, k_{NPQ}, Bacour et al. (2019) previously determined a generic parametric model that was calibrated against PAM data from both boreal species using the k_{NPQ}

estimated in Porcar-Castell (2011), and Mediterranean species using the estimates from Flexas et al. (2002). This k_{NPQ} model depends on air temperature, PAR, and the degree of photosynthetic saturation (χ) that varies linearly with the photosynthetic yield from 0 (maximum yield) to 1 (zero yield). The first objective here was to implement a more process-based model adapted to boreal evergreen species, which is presented in Section 3.1.

2.1.2 Model set-up and simulations

For the site and regional studies, we first performed a spin-up simulation to bring ecosystems to a hypothetical equilibrium state where all carbon stocks and fluxes are stable. To do so, we used a disturbance-free configuration, with a constant CO_2 atmospheric concentration (being the one of the first year of the considered forcing file), a fixed vegetation distribution and cycled over a few years of the forcing file. To accelerate this phase, we took advantage of the built-in pseudo-analytical spin-up procedure that iteratively converges towards the target carbon stocks, following Lardy et al. (2011).

Following the spin-up phase, we performed the site simulations using local micrometeorological fields over the available FLUXNET years (see Section 2.2.1). As the local forcing files usually stopped in 2014 (ending date of the FLUXNET2015 dataset) or earlier, and in order to allow simulation over the TROPOMI period (see Section 2.2.2), we extracted the corresponding meteorological fields from ECMWF fifth generation of atmospheric reanalysis (ERA5; Hersbach et al., 2020) encompassing the site location, as they are available at a 25 km spatial resolution and an hourly time step. Output variables were produced at a daily time step. We imposed a BorENF vegetation fraction of 1 for simulations that were intended to be used in a data assimilation experiment with FLUXNET GPP estimates, and the vegetation fractions extracted from the 0.1° PFT maps for simulations intended to be used in a data assimilation experiment with TROPOSIF estimates (see Section 2.2 and Table 1).

For evaluation purposes, we performed regional scale simulations over the 35°N-85°N latitudinal band using CRU (University of East Anglia Climate Research Unit; Harris et al., 2020) - JRA (Japanese Reanalysis; Kobayashi et al., 2015) forcing data, available at a 0.5° spatial resolution and a 6-hourly time step. Following the spin-up phase, we performed transient simulations from 1900 onwards, varying climate, yearly CO_2 atmospheric concentration and PFT map. Simulated SIF and GPP variables were generated at a monthly resolution over the recent period (2002-2021). For the analysis, we considered only grid cells with a BorENF PFT fraction greater than 50%; this corresponds to a surface of 1.9 million km^2, being 30% of the total surface covered by this PFT; the PFT fractions are shown in Figure S1.

2.2 Data

2.2.1 GPP

One of the main piece of information used for the model calibration are the GPP estimates from FLUXNET (La Thuile (Baldocchi et al., 2001) and FLUXNET2015 (Pastorello et al., 2020)) which are derived from the night-time method to partition net ecosystem exchange (NEE) measurements between respiration and GPP components (Reichstein et al., 2005). The FLUXNET data are available at a half-hourly timestep (https://fluxnet.org/data/, last access: 14 June 2023). A typical order of error for daily estimates is 0.5 $gC \cdot m^{-2} \cdot d^{-1}$ (Raj et al., 2016). We selected BorENF that are also homogeneous at the scale of TROPOMI footprint (about 20 km^2) in view of a SIF-GPP co-assimilation experiment (see Sections 2.2.2 and 2.3). To do so, we extracted the mean vegetation fractions (derived from the ESA CCI LC products, see Section 2.1.1) over 2001-2018 from the 0.1° grid cells encompassing the FLUXNET sites, keeping only those for which the BorENF PFT was dominant, with a fraction larger than 0.5 (except for Zotino to have at least one Eastern site, see Table 1 and Figure S1). Plus, we computed the RMSD (see Section 2.3.4) between the modelled GPP using *a priori* parameters and the observed FLUXNET GPP at a daily resolution, and further restricted the sites to those for which the normalised RMSD (the RMSD divided by the mean of the FLUXNET estimates) was higher than 25%. This threshold was used as a larger difference may indicate a missing or an incorrect process representation in this ORCHIDEE-SIF version (e.g., fires, clear-cuts, regrowth processes are not modelled), a problem which cannot be resolved with data assimilation. Finally, we only kept sites with at least three years of GPP estimates to get some interannual variability (three years being used for assimilation and an independent year for evaluation, as presented in Table 1). This process resulted in the selection of nine sites, listed in Table 1. All sites have a soil texture classified as Sandy Loam except for the northernmost site (Sodankylä, Finland) which has a Loam texture. The location of the sites is shown in Figure S1.

Table 1: Characteristics of the sites selected for data assimilation and evaluation. The BorENF PFT fraction at a 0.1° spatial resolution is provided, since these fractions and resolution are used when assimilating TROPOMI SIF estimates (over 2019-2020), and evaluating the simulated SIF (over 2021). The BorENF PFT fraction for GPP simulations is assumed to be 1 at the FLUXNET footprint. Data from FLUXNET2015 are indicated with ^{F} and the ones from la Thuile are indicated using $^{LT.}$

Site name and Reference	**Short name**	**Coordinates (latitude, longitude, °)**	**GPP Assimilation years**	**GPP Evaluation year**	**BorENF PFT fraction at 0.1° for SIF simulations**
Manitoba (Canada; Dunn et al., 2007)	CA-Man^{F}	55.8796, -98.4808	1998-2000	2001	0.61
Saskachewan (Canada; Amiro et al., 2006)	CA-Obs^{LT}	53.6289, -106.1978	2001-2003	2004	0.65
Saskachewan (Canada; Amiro et al., 2006)	CA-Ojp^{LT}	53.9163, -104.692	2001-2003	2004	0.61
Québec (Canada; Bergeron et al., 2007)	CA-Qfo^{F}	49.6925, -74.3421	2004-2006	2007	0.56
Hyytiälä (Finland; Suni et al., 2003)	FI-Hyy^{F}	61.8474, 24.2948	1997-1999	2000	0.69
Sodankylä (Finland; Thum et al., 2007)	FI-Sod^{F}	67.3624, 26.6386	2002-2004	2005	0.50
Zotino (Russia; Schulze et al., 1999)	RU-Zot^{LT}	60.8008, 89.3507	2002-2004	none	0.46

Flakaliden (Sweden; Lindroth et al., 2008)	SE-Fla^{LT}	64.1125, 19.45883	1997-1998, 2001	2002	0.69
Niwot Ridge Forest (United States; Knowles et al., 2015)	US-NR1^{F}	40.0329, -105.5464	2000-2002	2003	0.66

To evaluate the ORCHIDEE simulations at the regional scale, over the whole BorENF vegetation type, we used the FLUXCOM (Jung et al., 2020; http://fluxcom.org, last access: 14 June 2023) and FLUXSAT version 2.0 (Joiner et al., 2018; https://avdc.gsfc.nasa.gov, last access: 14 June 2023) GPP products. These products are obtained from machine learning methods using remote sensing data to upscale local GPP estimates from FLUXNET eddy covariance measurements. We used monthly GPP data at a 0.5° spatial resolution, over the period 2001-2015.

2.2.2 Fluorescence

Two different types of fluorescence data are considered in this study, each associated with a specific objective.

To improve the NPQ model, we used the active fluorescence measurements at the leaf scale performed at Hyytiälä (61.85°N, 24.29°W) using a Pulse Amplitude Modulation instrument positioned on the upper layer of the canopy, from 15 August 2008 to 15 August 2009, at a sub-hourly time step (Porcar-Castell, 2011). The fluorescence measurements allow estimating the rate constants and yields of NPQ and photochemistry (see Section 3.1).

For the data assimilation experiments and the regional scale assessment of the ORCHIDEE-SIF model, we used the ESA TROPOSIF products (Guanter et al., 2021). The SIF in the near infrared is retrieved over the 743-758 nm spectral fitting window. The associated retrieval error is typically 0.5 $W \cdot m^{-2} \cdot sr^{-1} \cdot m^{-2} \cdot \mu m^{-1}$, raising a relative uncertainty on the order of 30%. We used the daily average estimates, based on a daily correction factor following Frankenberg et al. (2011). We aggregated the daily estimates at a spatial resolution of 0.1° for the data assimilation study at site level (using 2019-

2020 for assimilation and 2021 for evaluation), and used monthly means at a 0.5° spatial resolution for evaluation at the regional scale. We screened out retrievals associated to view zenith angles (VZAs) larger than 50° and to cloud fraction larger than 0.4 in order to limit the impact of both directional effects and cloud contamination, while keeping a sufficient number of available observations.

2.3 Assimilation methodology

We relied on data assimilation (DA) to use information from observations in order to optimise a vector of selected ORCHIDEE parameters (the corresponding data and parameters are described in Section 2.2 and Section 3.2, respectively).

2.3.1 Data assimilation framework

The approach we used is formulated within a Bayesian framework, which states that, assuming that errors in the model, observations and parameters have Gaussian probability density functions, the optimal vector minimises the cost function defined as (Tarantola, 1987):

$$J(\boldsymbol{x}) = \frac{1}{2}[(H(\boldsymbol{x}) - \boldsymbol{y})^T \mathbf{R}^{-1}(H(\boldsymbol{x}) - \boldsymbol{y}) + (\boldsymbol{x} - \boldsymbol{x_b})^T \mathbf{B}^{-1}(\boldsymbol{x} - \boldsymbol{x_b})] \tag{1}$$

with $\boldsymbol{x}$ the vector of parameters to be optimised, $H(\boldsymbol{x})$ the model output, y the observations, $\mathbf{R}$ the matrix of model and observations errors, $\boldsymbol{x_b}$ the vector of prior values of the parameters and $\mathbf{B}$ the matrix of *a priori* parameters errors. The minimization of this cost function implies a reduction of the first term, which quantifies the deviation of the model from the observations, while ensuring at the same time that the vector of optimised parameters cannot depart too much from their prior values (which contain our initial knowledge), thanks to the second term. Given the larger number of data assimilated compared to the number of the parameters to be optimised, the reduction of the first term is preponderant. We consider, as a simplification, that uncertainties are uncorrelated and hence the $\mathbf{R}$ and $\mathbf{B}$ matrices are diagonal (Kuppel et al., 2012). As in previous studies, the model-data errors in $\mathbf{R}$ are defined as the mean squared difference between the observations and the prior simulation (Kuppel et al., 2012; Bacour et al., 2015), and the prior uncertainty in $\mathbf{B}$ is set to 15% of the parameter range of variation following Bacour et al. (2023). To perform the DA, we used the ORCHIDAS tool, specifically developed around the ORCHIDEE LSM (https://orchidas.lsce.ipsl.fr/, last access: 14 June 2023; see a recent review of related scientific studies in MacBean et al., 2022). Among the available minimization methods, we selected the Genetic Algorithm (GA; Goldberg, 1989; Haupt and Haupt, 2004), which has increased performances in finding the global minimum of $J(\boldsymbol{x})$, unlike gradient-descent approaches that can become stuck in local minima (Santaren et al., 2014; Bastrikov et al., 2018). We ran the algorithm for 25 iterations to ensure the convergence of the optimization algorithm (other settings related to the GA such as population size, mutation and crossover rates are detailed in Bastrikov et al., 2018).

2.3.2 Sensitivity analysis-based selection of the parameters to be optimised

One important first step for data assimilation is the choice of the parameters to be optimised. The list cannot be too long because data assimilation is computationally expensive and more parameters means a longer optimization phase. Plus, we want to avoid overfitting as much as possible, and we don’t want to change parameters with little to no sensitivity which may degrade other parts of the model. An objective way to select the most influential parameters for a given variable is to perform a sensitivity analysis (SA). We selected here the Morris (1991) approach, which simply provides a ranking of the considered parameters, but is less costly than more quantitative alternative methods (Iooss and Lemaître, 2015; Dantec-Nédélec et al., 2017). For a list of *p* parameters, each associated with a variation range, within which *n* random values are sampled, the Morris SA performs *n(p+1)* simulations to establish the parameter ranking. In this study, we used a pool of *p*=126 parameters related to fluorescence, photosynthesis, vegetation structure, respiration, turnover, and hydrology processes, and a number of random samples *n*=10. Regarding the variation range, we generally used ± 25% of the prior value set in the model (e.g., for $V_{cmax,25}$, a_{PSII} and $L_{agecrit}$), except for a few parameters for which we lacked observations to correctly constrain them, such as for the parameters of the new NPQ model where we took a larger range (see Section 3.1). The same ranges were applied for the selected most influential parameters during the data assimilation phase (see Table 3 in the Results section).

2.3.3 Data assimilation experiments

Bacour et al. (2019) assimilated SIF data from OCO-2 observations, and demonstrated a general improvement of the simulated SIF and GPP at regional and global scales, in spite of a degradation of the modelled GPP for a few PFTs. We decided to perform here three DA experiments: one assimilating only SIF data, one only GPP data and one assimilating both SIF and GPP data, in order to assess the impact of each assimilated data-stream on the model parameter values and modelled predictions. Multi-sites DA experiments were performed in order to obtain generic parameter values over the whole BorENF PFT, as was done in Kuppel et al. (2012). For GPP, we used *in situ* estimates from EC flux towers, and, for SIF, as there is not yet an equivalent network of standardised *in situ* measurements, we used co-located TROPOMI SIF data (Guanter et al., 2021) albeit at a coarser space-time resolution. For GPP, we systematically used three years for data assimilation, and another year, if available, for an independent evaluation (see Table 1). For SIF, we used two years (2019-2020) for data assimilation, and one year (2021) for the evaluation. Given the respective data uncertainties, we assimilated daily means of GPP and weekly means of SIF. Negative means were considered outliers (as negative quantities cannot be represented by the model) and therefore discarded. When assimilating simultaneously both datasets, we applied coefficients in the cost function to equilibrate the respective weights of GPP and SIF observations, the former being 10 times more numerous.

2.3.4 Evaluation metrics

To quantify the fit between modelled or observed variables $\mathbf{y_1}$ and $\mathbf{y_2}$ over N samples, we mainly used the Root Mean Square Difference:

$$RMSD = \sqrt{\frac{\sum_{n=1}^{N}\left(\mathbf{y_1}(n) - \mathbf{y_2}(n)\right)^2}{N}} \tag{2}$$

To specifically compare the scores of various parametric models in Section 3.1, we used the Akaike Information Criterion (AIC; Ding et al., 2018). The AIC provides a quantitative measure of the trade-off between goodness of fit and model complexity, penalising models incorporating more parameters to fit the data. It is computed as the sum of the negative log-likelihood of the model and twice the number of parameters used. Models with lower AIC values are considered preferable as they strike a better balance between accuracy and parsimony. In the case of least squares model fitting, AIC expresses as (Burnham and Anderson, 2002):

$$AIC = n\log(\hat{\sigma}^2) + 2K \tag{3}$$

with n the number of observations, $\hat{\sigma}^2$the mean of the estimated squared residuals, and K the number of estimated regression parameters.

To evaluate how well each parameter is constrained after optimization, we computed the reduction in posterior parameter uncertainty. The posterior parameter error covariance matrix, $\mathbf{B}'$**,** can be approximated using the Jacobian matrix of the model (which is computed using a finite difference approach) at the minimum of the cost function J, $\mathbf{H}_\infty$, following Tarantola (1987):

$$\mathbf{B}' = [\mathbf{H}_\infty^{\mathrm{T}}\mathbf{R}^{-1}\mathbf{H}_\infty + \mathbf{B}^{-1}]^{-1} \tag{4}$$

The error reduction on model parameters is computed as $1 - \sigma_{post}/\sigma_{prior}$, with σ_{post} and σ_{post} the error standard deviation derived from the posterior ($\mathbf{B}'$) and prior ($\mathbf{B}$) covariance matrices, respectively.

3 Results

3.1 NPQ modelling

In the initial model version described in Bacour et al. (2019), the calculation of the rate constants (k_P, k_{NPQ}), yields (for photosynthesis, NPQ and fluorescence) and SIF were generic over all model PFTs, and were computed alongside GPP. Thus, they were not estimated under too cold conditions, when the growth temperature is lower than T_{min} (-4°C). In order to improve the representation of SIF temporal dynamics, in particular for boreal ecosystems, we then extended the computation of these variables to all temperature conditions. In conditions too cold for photosynthesis to occur, the photosynthetic yield is now set to the minimum value observed in the Hyytiälä PAM measurements, namely 0.049, obtained at a temperature of -11.2°C in January 2009.

Bacour et al. (2019) previously determined a single parametric model for the total NPQ rate constant, k_{NPQ}. Raczka et al. (2019) proposed a modelling of k_{NPQ} in two sub-models, one dealing with the seasonal and long-lasting variations of NPQ (related to the cold temperatures experienced by the BorENF vegetation type), and the other one dealing with the diurnal and reversible variations of the NPQ (related to solar radiation). The active fluorescence measurements made at Hyytiälä allow for a separate computation of the sustained (k_S) and reversible (k_R) parts of the k_{NPQ} rate constant. Note that we used here unitless relative rate constants (i.e., absolute rate constants (in s^{-1}) normalised by the sum of the absolute rate constants for fluorescence and for basal thermal energy dissipation), which are more commonly used (Porcar-Castell, 2011). We thus also modelled the two components separately, and calibrated their parameters using the Python Model from the lmfit library (Newville et al., 2016).

We modelled the k_S component according to Raczka et al. (2019):

$$k_{NPQ} = k_S + k_R \tag{5}$$

$$k_S = \frac{k_{S,max}}{1 + e^{b(S-T_S)}} \tag{6}$$

where $k_{S,max}$ (unitless) represents the maximum sustained NPQ rate constant, and S represents the temperature acclimation (°C) and is defined as a moving average of the air temperature at 2m T (°C) over a period τ (day) following Mäkelä et al. (2004):

$$\frac{dS}{dT} = \frac{T - S}{\tau} \tag{7}$$

We calibrated the parameters $k_{S,max}$, b, T_S, and τ at a daily time step, using the k_S estimates derived in by Porcar-Castell (2011) (Table 2, Figure S2), resulting in a RMSD of 0.69 and a R^2 of 0.97, comparable to the scores obtained by Raczka et al. (2019) with their model (RMSD=0.62, R^2=0.93).

k_R is usually empirically modelled as a function of the degree of photosynthetic saturation, χ, using either two (Lee et al., 2015) or three parameters (van der Tol et al., 2014; Raczka et al., 2019). To select the best model, we calibrated these functions, as well as a few new others (see Table S1 for the whole list), at a half-hourly time step using the Hyytiälä PAM dataset, and filtering for k_S < 1 and PAR > 1 $\mu mol \cdot m^{-2} \cdot s^{-1}$ to exclude wintertime with a dominating sustained NPQ and night-time observations. All tested models leading to the same RMSD (0.28), we kept the one giving the best (lowest) Akaike Information Criterion, with a new formulation:

$$k_R = p1_{NPQr} \cdot \chi + p2_{NPQr} \cdot \chi^3 \tag{8}$$

The optimised parameter values are provided in Table 2, and Figure S3 shows the dependency of k_R on x, for the data and the selected k_R model. These parameters may be further selected during the sensitivity analysis, and optimised again against GPP and SIF estimates.

Table 2: Parameters of the k_{NPQ} model optimised from active fluorescence measurements at the Hyytiälä site.

Parameter	$k_{S,\ max}$	b	T_S	τ	$p1_{NPQr}$	$p2_{NPQr}$
Unit	1	$°C^{-1}$	°C	day	1	1
Calibrated value	7.919	0.390	-0.214	19	0.94	5.15

3.2 Sensitivity analysis and parameter selection

We performed Morris' sensitivity analyses for the SIF and GPP variables over the nine selected sites. We selected for each variable separately the most influential parameters, with a limited number (nine) to avoid overfitting, over the nine sites (Figure S4) based on a rank product approach (Koziol, 2010). These parameters were kept for the subsequent SIF and GPP DA experiments, and are presented in Table 3.

Table 3: Parameters selected for the DA experiments (exp.) following sensitivity analyses. A dash (-) in the last three columns listing the posterior parameter values indicates that the parameter was not selected for the corresponding DA experiment. Parameters are grouped per broad categories.

Parameter symbol or code name	**Description**	**Unit**	**Prior value**	**Range**	**SIF-only exp.**	**GPP-only exp.**	**SIF-GPP exp.**
SIF and GPP models							
ALA	Average leaf angle (Campbell, 1990)	°	75	[56, 90]	80	-	79
k_F	Fluorescence relative rate constant	1	0.05	[0.04, 0.11]	0.07	-	0.07
a_{PSII}	Absorption cross section for photosystem II	1	0.5	[0.375, 0.625]	0.380	0.416	0.376
k_R *model*							
$p1_{NPQr}$	First parameter of the reversible NPQ model (Eq. (8))	1	0.94	[0.71, 1.18]	1.08	-	1.08
$p2_{NPQr}$	Second parameter of the reversible NPQ model (Eq. (8))	1	5.15	[3.87, 6.44]	6.16	-	6.14
Carboxylation							
$V_{cmax,25}$	Maximum carboxylation rate limited by Rubisco activity at 25°C	$\mu mol \cdot m^{-2} \cdot s^{-1}$	45	[34, 56]	37	36	47

$L_{agecrit}$	Critical leaf age, used for computing the age-dependence of the maximum carboxylation rate limited by Rubisco activity, and for leaf turnover (Krinner et al., 2005)	day	910	[683, 1138]	698	1108	762
KMC25	Michaelis–Menten constant of Rubisco for CO_2 at 25°C (Medlyn et al., 2002)	$\mu mol \cdot mol^{-1}$	404.9	[204.9, 604.9]	-	470.2	435.1
Temperature-related							
$a_{S,J}$	Offset of the linear temperature acclimation relationship for the entropy parameter of the J_{max} temperature-dependence function, following Kattge and Knorr (2007)	$J \cdot K^{-1} \cdot mol^{-1}$	660	[495, 825]	-	704	785
$a_{S,V}$	Offset of the linear temperature acclimation relationship for the entropy parameter of the V_{cmax} temperature-	$J \cdot K^{-1} \cdot mol^{-1}$	668	[501, 835]	740	517	564

	dependence function, following Kattge and Knorr (2007)						
$a_{R,JV}$	Offset of the linear temperature acclimation relationship for the ratio J_{max}/V_{cmax}, following Kattge and Knorr (2007)	μmol e$^-$·m^{-2}·s^{-1} / μmol CO$_2$·m^{-2}·s^{-1}	2.59	[1.55, 3.63]	-	2.08	1.74
T_{min}	Minimum growth temperature to compute photosynthesis	°C	-4	[-6, -2]	-	-2.7	-4.0
Biomass							
SLA	Specific leaf area	m^2·gC^{-1}	0.00926	[0.00695, 0.01158]	0.007039	0.007611	0.007160

For SIF, we note the major importance of the average leaf angle (ALA) parameter, characterising the leaf angle distribution (LAD) in ORCHIDEE. This structural parameter has already been identified as one of the most important factors, along with leaf chlorophyll content and LAI, for Top of Canopy (TOC) SIF in the sensitivity analysis led with the SCOPE model in Verrelst et al. (2015). Boreal forests have been reported to have an erectophile LAD adapted to the low solar zenith angles (Huemmerich et al., 2013). Zhu et al. (2018) estimated LAD for coniferous trees in Germany based on laser measurements, and showed they were erectophile with most ALA between the normal and the zenith in the [50°-80°] range. Using DART (Discrete Anisotropic Radiative Transfer)-FLUSPECT simulations, Liu et al. (2019) showed a 60% decrease of the TOC SIF between planophile and erectophile LAD. The fluorescence rate constant (k_F), as well as the absorption cross section for PSII (a_{PSII}), also have predominant roles. The modelled fluorescence flux of PSII is indeed directly proportional to these two parameters. The prior value of k_F is fixed at 0.05 in accordance with van der Tol et al. (2014), albeit a value of 0.1 is used in Porcar-Castell et al. (2014). a_{PSII} is also selected for GPP, it represents the fraction of the radiation that is absorbed by PSII, complementary to the fraction absorbed by PSI. For SIF, the $p1_{NPQr}$ and $p2_{NPQr}$ parameters of the NPQ reversible model are selected, while no parameters from the sustained model were retained, having a moderate importance for SIF, which shows low values in the wintertime.

As expected, $V_{cmax,25}$ is identified as a crucial parameter for both GPP and SIF, as it directly impacts the photosynthetic yield and thus the fluorescence yield. It is complemented by the critical leaf age ($L_{agecrit}$) parameter, as leaf age modulates the photosynthetic efficiency (Ishida et al., 1999). For GPP, the Michaelis–Menten constant of Rubisco for CO_2 at 25°C (*KMC25*) is also selected, whose value varies among plants (Galmés et al., 2016).

Several ranked parameters stress the importance of the temperature for this cold biome: both SIF and GPP are sensitive to the offset of the linear temperature acclimation relationship for the entropy term of the V_{cmax} temperature-dependence function (Kattge and Knorr, 2007), $a_{S,V}$. Additionally, the offsets

$a_{S,J}$ and $a_{R,JV}$ of the linear temperature acclimation relationships for the entropy term of J_{max} and for the ratio J_{cmax}/V_{cmax}, following (Kattge and Knorr, 2007), have a strong impact on GPP, while the temperature threshold below which we consider there is no GPP (T_{min} parameter) shows a less important one.

Finally, the specific leaf area parameter (*SLA*), linking the leaf biomass to LAI, is identified as a parameter of medium importance for both SIF and GPP.

3.3 Data Assimilation

After implementing the new NPQ models relative to k_R and k_S in ORCHIDEE-SIF, we performed three DA experiments: one in which only SIF data are assimilated with nine parameters to be optimised, one GPP-only assimilation also with nine parameters, and one in which GPP and SIF are assimilated simultaneously (with weighted terms in the cost function, see Section 2.3.3) accounting for a total of thirteen parameters (five common to the two variables, plus eight specific ones, see Table 3). We further compared this last optimization experiment with a similar optimization assimilating both GPP and SIF data, but using the former formulation of total NPQ from Bacour et al. (2019) to evaluate the impact of distinguishing between reversible and sustained NPQ in ORCHIDEE-SIF.

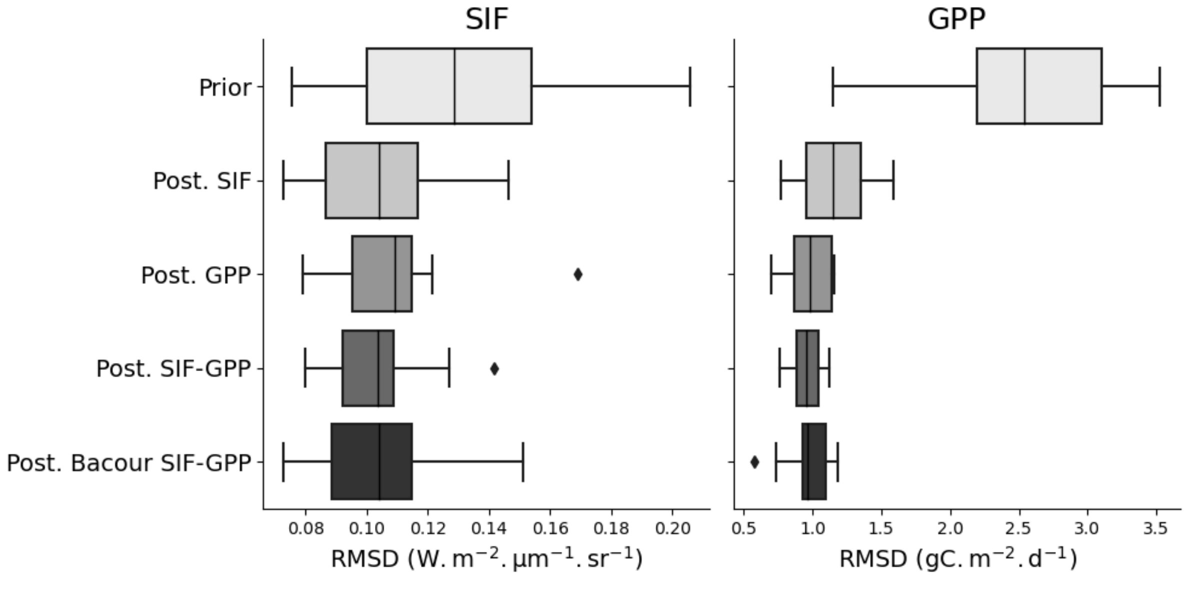

Figure 1: Boxplots of Root Mean Square Difference (RMSD) between simulated and observed values for SIF (left) and GPP (right) of the selected sites, for the prior simulations (top row), the posterior simulations obtained for the SIF-only DA experiment (second row), the GPP-only DA experiment (third row), the joint assimilation of GPP and SIF (fourth row), and the joint assimilation of GPP and SIF using the initial total NPQ model described in Bacour et al. (2019) (last **r**ow). The evaluation against observed data is done for periods not considered in the DA experiments (year 2021 for SIF (see Section 2.2.2), and the year following the 3 years used in the DA experiments for GPP (see Table 1)). The left and right sides of each box represent the first *(Q1)* and third *(Q3)* quartiles, the intermediate segment is the mean value, and the whiskers evidence the range of observed values between Q1 minus 1.5 times the interquartile range (IQ=Q3-Q1) and Q3 plus 1.5 times IQ. Outlier values outside of the whiskers range are represented with diamond markers.

Figure 1 shows the distribution of the RMSD over the evaluation sites (8 sites for GPP – all sites but Zotino – and 9 sites for SIF, see section 2.2.2 and Table 1) for the prior and posterior simulations, using independent evaluation data corresponding to one year that was not included in the DA experiments. The RMSD mean values and the RMSD reductions (in %) of posterior simulations as compared to the prior ones are given in Table 4. All DA experiments improve the model-data agreement, as quantified by the RMSD reduction, even when the variable (SIF or GPP) is not included in the assimilation, thus demonstrating the close connection between the SIF and GPP models within ORCHIDEE, consistent with the observations. Regarding SIF, the SIF-only and joint SIF-GPP DA experiments yield the same posterior RMSD score (0.104 $W \cdot m^{-2} \cdot \mu m^{-1} \cdot sr^{-1}$), corresponding to a RMSD reduction of 19%, performing better than the GPP-only assimilation with a 15% RMSD reduction, as expected. Regarding GPP, all DA experiments show very large RMSD reductions, from 55% for the SIF-only DA experiment, to 62% for the joint SIF-GPP DA experiment. These large reductions could also be linked to the fact that the prior parameter values are issued from the ORCHIDEE CMIP6 version, and have up until now not been calibrated with the new two-stream radiative transfer scheme. Note also that the larger RMSD reduction obtained with the joint assimilation experiment for both SIF and GPP is partly explained by the larger number of optimised parameters.

When co-assimilating SIF and GPP data, the new representation of NPQ with a distinction between its reversible and sustained components yields a performance similar to that of the optimization experiment based on the formulation of total NPQ from Bacour et al. (2019). Note that it however benefits from the optimization of the two parameters of the k_R model, whereas the parameters of the k_{NPQ} model of Bacour et al. (2019) were not optimised. Given the two NPQ models perform similarly for the same number of parameters (6), we prefer to stick to the one developed in this study in the next sections, favouring its more processed-based justification.

Table 4: Mean RMSD for SIF and GPP related to the prior and posterior simulations, for the selected sites over the evaluation years. RMSD reductions are computed for the posterior simulations as compared to the prior simulations of the ORCHIDEE-SIF version.

	Prior	**Posterior SIF-only**	**Posterior GPP-only**	**Posterior GPP and SIF**	**Posterior Bacour GPP and SIF**
RMSD SIF ($W \cdot m^{-2} \cdot \mu m^{-1} \cdot sr^{-1}$)	0.119	0.104	0.109	0.104	0.104
RMSD SIF reduction (%)	-	19	15	19	19
RMSD GPP ($gC \cdot m^{-2} \cdot d^{-1}$)	2.54	1.15	0.98	0.96	0.97
RMSD GPP reduction (%)	-	55	61	62	62

Figure S5 (S6 respectively) compares the seasonal cycles of SIF (GPP respectively) weekly averages of the observations with the prior and posterior simulations, computed over the year chosen for evaluation (year 2021 for SIF (see section 2.2.2), and the year following the three years used in the DA experiments for GPP (see Table 1)), at the selected sites.

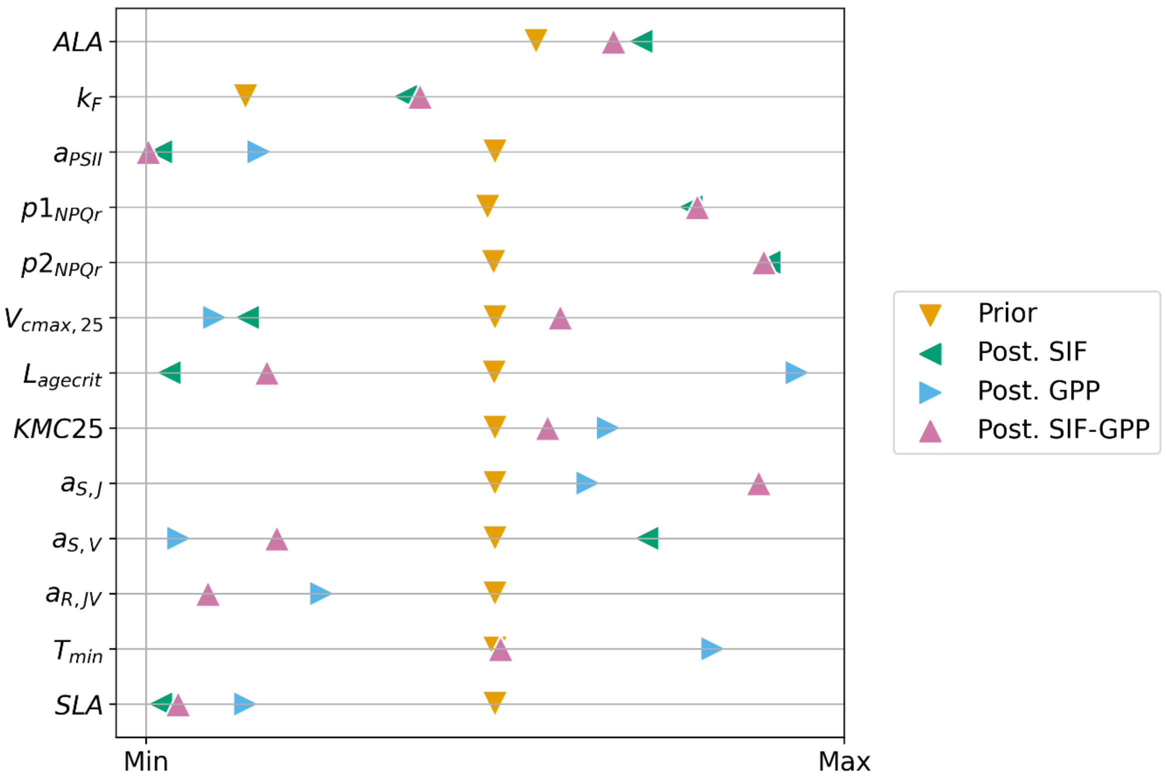

Figure 2: Prior (down-pointing triangles) and posterior (blue left-pointing triangles for the SIF-only DA experiment, green right-pointing triangles for the GPP-only DA experiment, and pink up-pointing triangles for the SIF-GPP DA experiment) values of the 13 parameters, normalized with respect to their authorised variation range.

Table 3 gives the optimised posterior parameter values after the three DA experiments, and Figure 2 shows their relative change within the imposed minimum and maximum bounds. Most parameters show a coherent variation among the three DA experiments: seven parameters have a posterior value higher than the prior one (*ALA*, k_F, $p1_{NPQr}$, $p2_{NPQr}$, *KMC25*, $a_{S,J}$, T_{min}) and three parameters have a lower one (a_{PSII}, $a_{R,JV}$, *SLA*). Three parameters show opposite change depending on the DA experiment ($V_{cmax,25}$, $L_{agecrit}$, $a_{S,V}$).

3.4 Regional scale impacts

In this section, we compare regional simulations to observation-derived products TROPOSIF for SIF, and FLUXSAT and FLUXCOM for GPP, hereafter called reference products. In all figures and tables, we only consider grid cells with a BorENF fraction larger than 50%. The monthly negative values observed in grid cells of the TROPOSIF products (with a mean value of -0.032 $W \cdot m^{-2} \cdot \mu m^{-1} \cdot sr^{-1}$) have been set to zero for this evaluation. The study period is May 2018-December 2020 for SIF, and 2001-2015 for GPP.

We first focus on maps of SIF and GPP temporal means, computed over each respective whole study period. We consider here only on one hand the simulation based on parameters estimated following the SIF-GPP DA experiment, – as those calibrated parameters yielded the best performance at site scale (Figure 1 and Table 4) and as the SIF and GPP spatial distributions are very similar between all posterior simulations (not shown; correlation coefficients varying between 0.91 and 0.99) – and on the other hand the FLUXSAT GPP product, to which our former posterior GPP was closer than to FLUXCOM (Bacour et al., 2019). Figure 3 shows the maps (Figure 3.a, 3.b, 3.c, 3.d), as well as the difference with TROPOSIF and FLUXSAT data (Figure 3.e and 3.f, respectively). For comparison, Figure S7 shows similar maps based on the prior simulations. The mean bias between the two maps of Figure 3.a and Figure 3.c is 0.006 $W \cdot m^{-2} \cdot \mu m^{-1} \cdot sr^{-1}$, with a standard deviation of the difference normalised by the mean TROPOSIF of 35%. The mean GPP bias between the two maps of Figure 3.b and Figure 3.d is 0.16 $gC \cdot m^{-2} \cdot d^{-1}$ with a standard deviation of the difference normalised by the mean FLUXSAT GPP of 21%. Both the simulated SIF and GPP show an overestimation over the Canadian Northwest Territories (Figure 3.e and 3.f). This region has lots of lakes (Pienitz et al., 1997), and the continental fraction of the ORCHIDEE model may not accurately take them into account, introducing some uncertainty in the simulated fluxes. This is likely to also impact the SIF and data-driven GPP reference products; Cheng et al. (2022) indeed reported that the high heterogeneity of the land cover in the Arctic-Boreal region, with mixed pixels of vegetation and surface waters, may represent a challenge for the GPP reference products such as FLUXCOM. There also appears to be much overestimation of both SIF and GPP through much of British Columbia. The simulated SIF and GPP show opposite behaviours over Scandinavia, where ORCHIDEE rather tends to underestimate SIF, while overestimating GPP. The model also exhibits a strong underestimation of SIF over a region in Northwest USA, corresponding to forests of the Idaho and Montana states in the Rocky Mountains. Then, while the simulated GPP is able to reproduce the range of the spatial variability found in the FLUXSAT reference product over the selected grid cells (with a correlation coefficient between the two maps R=0.70), the simulated SIF shows a lower spatial variability compared to TROPOSIF (R=0.62). Note that the simulation using model parameters optimized using the SIF-GPP DA experiment gives a slightly better correlation with both SIF and GPP evaluation datasets, than the simulations using parameters optimised with the SIF-only and GPP-only DA experiments.

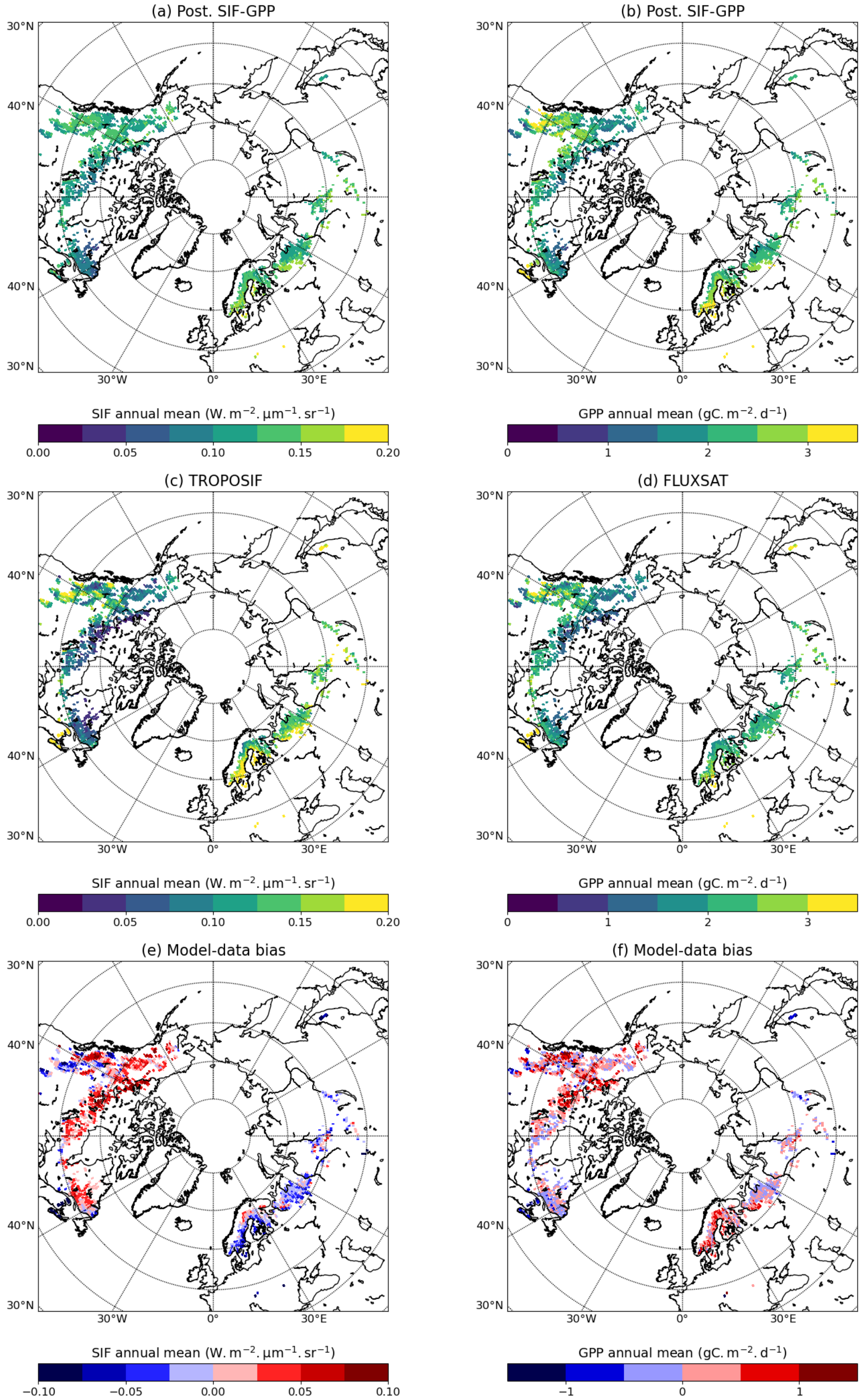
(a) Post. SIF-GPP
(b) Post. SIF-GPP
30°N
40°N
40°N
30°N
30°W
0°
30°E
SIF annual mean (W. m^{-2}. µm^{-1}. sr^{-1})
0.00
0.05
0.10
0.15
0.20
GPP annual mean (gC. m^{-2}. d^{-1})
0
1
2
3
(c) TROPOSIF
(d) FLUXSAT
SIF annual mean (W. m^{-2}. µm^{-1}. sr^{-1})
GPP annual mean (gC. m^{-2}. d^{-1})
(e) Model-data bias
(f) Model-data bias
SIF annual mean (W. m^{-2}. µm^{-1}. sr^{-1})
−0.10
−0.05
0.00
0.05
0.10
GPP annual mean (gC. m^{-2}. d^{-1})
−1
0
1

Figure 3: Maps of temporal means for SIF (left column) and GPP (right column), based on the parameters estimated with the joint SIF-GPP DA experiment (a and b), the associated reference product, TROPOSIF for SIF (c) and FLUXSAT for GPP (d); and differences between simulated variables and the corresponding reference product (e and f). All means are computed over grid cells with a BorENF fraction larger than 50%, over the period May 2018-December 2020 for SIF, and over the period 2001-2015 for GPP.

Regarding latitudinal profiles, they are correctly simulated for GPP after assimilation in all DA experiments as seen in Figure 4a (top plot). The weighted differences (RMDs taking into account the number of valid grid cells, represented in the bottom plots) normalised by the weighted mean of FLUXSAT GPP are 11% for the simulations based on the SIF-only and GPP-only DA experiments, and 12% for the simulation based on the SIF-GPP DA experiment. On another hand, all SIF simulations fail to correctly reproduce the latitudinal profile of the TROPOSIF product as seen in Figure 4b (top plot), with notably a poor agreement of the posterior versions around the TROPOSIF peak region, between 46°N and 49°N, corresponding to the above identified region in the Rocky Mountains. This could partly be explained by the absence of assimilation sites between 41°N (above US-NR1) and 49°N (below CA-Qfo), where another one or two sites would have been helpful. Note however that there is also a limited number of valid grid cells in this region. Above 50°N, where the bulk of valid grid cells is located, the agreement between the posterior versions and the TROPOSIF product is better. Still, the latitudinal variability of the simulated SIF is lower than that of TROPOSIF. The weighted RMSDs normalised by the weighted mean of TROPOSIF are 19% for the SIF-GPP DA experiment, and 22% for the SIF-only and GPP-only DA experiments.

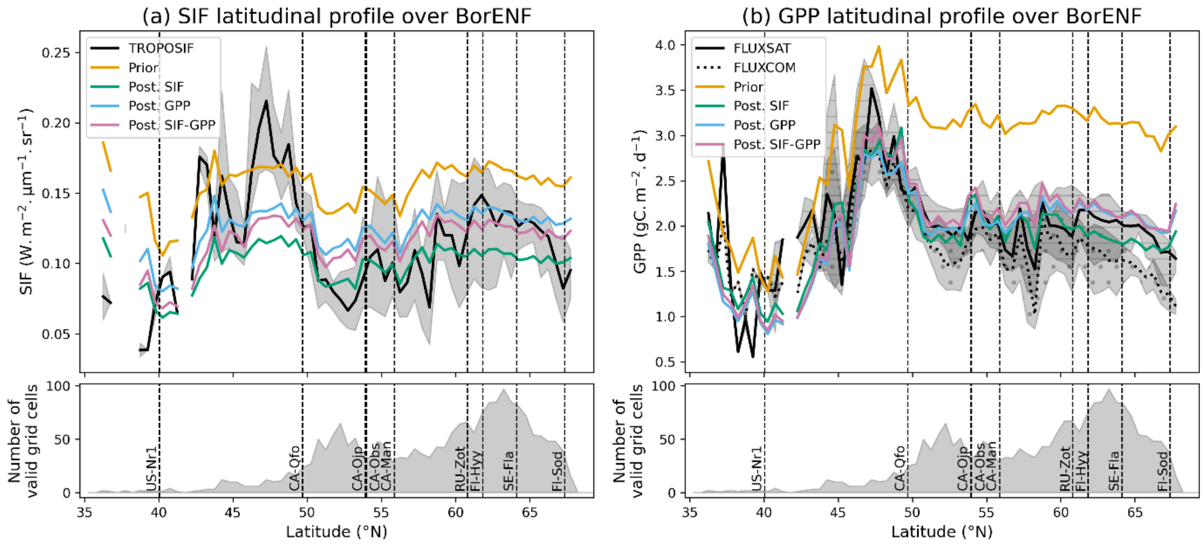

Figure 4: Latitudinal profiles of SIF (a top) and GPP (b top) computed over 0.5° grid cells with a BorENF fraction larger than 50%, and latitudinal profile of the number of valid grid cells (i.e., with a BorENF fraction larger than 50%, bottom plots). In the top plots, the curve for the prior simulation is in orange, the curve for the posterior simulation related to the SIF-only DA experiment is in green, the curve for the posterior simulation related to the GPP-only DA experiment is in blue, and the curve for the posterior simulation related to the SIF-GPP DA experiment is in pink. For SIF, the TROPOSIF curve is in black, the shaded grey area represents the interquartile range (IQR) of the TROPOSIF estimates over all selected grid cells, all means are computed over the period May 2018-December 2020. For GPP, the FLUXSAT curve is the solid black line, while the FLUXCOM curve is the dotted black line, FLUXSAT IQR is figured by the hatched grey shaded area, and FLUXCOM IQR by the dotted grey shaded area, all means are computed over the period 2001-2015. Vertical dashed lines represent the latitudes of the nine sites where data have been assimilated, with the short name of each site (Table 1) written near the bottom of the corresponding line.

Figure 5 compares the mean seasonal cycles of monthly SIF and GPP for the prior and optimised simulations following the three DA experiments, with the respective reference products. Related statistics (amplitude, bias, RMSD) are reported in Table 5. For SIF, the mean seasonal cycle of the prior simulation overestimates TROPOSIF estimates, by 0.06 $W{\cdot}m^{-2}{\cdot}\mu m^{-1}{\cdot}sr^{-1}$ at the peak of the growing season in July and yields a large RMSD of 0.042 $W{\cdot}m^{-2}{\cdot}\mu m^{-1}{\cdot}sr^{-1}$. All posterior simulations show a reduced amplitude, and a shorter growing season, closer to the TROPOSIF mean seasonal cycle. The

SIF-only and GPP-only simulations lead to similar RMSDs of 0.017 and 0.016 W·m^{-2}·µm^{-1}·sr^{-1}, more than twice lower than for the prior simulation, respectively, with an underestimation in the SIF-only case (falling at -0.05 W·m^{-2}·µm^{-1}·sr^{-1} in July), and an overestimation in the GPP-only case (peaking at 0.04 W·m^{-2}·µm^{-1}·sr^{-1} in June). The simulation based on the SIF-GPP DA experiment yields the lowest RMSD, and the lowest bias (Table 5). Regarding GPP, the two reference products show similar mean seasonal cycles, however the FLUXSAT cycle has a larger amplitude (6.2 gC·m^{-2}·d^{-1}) than that of FLUXCOM (5.5 gC·m^{-2}·d^{-1}), with a RMSD between the two products of 0.41 gC·m^{-2}·d^{-1}. As is the case for SIF, the prior simulation correctly identifies the production peak in July, but the amplitude (8.8 gC·m^{-2}·d^{-1}) is too large compared to that of the reference products, and the growing season length is too long (earlier onset combined to a later ending). The simulation based on the SIF-only DA experiment, with an amplitude of 5.8 gC·m^{-2}·d^{-1}, leads to the lowest bias with both FLUXSAT and FLUXCOM, whereas the simulations based on the GPP-only and SIF-GPP DA experiments evidence larger positive biases. However, the simulation based on the GPP-only DA experiment leads to the highest improvement when compared to FLUXSAT (RMSD=0.26 gC·m^{-2}·d^{-1}, a RMSD reduction of 84%), while the simulation based on the SIF-only DA experiment shows the best agreement with FLUXCOM (RMSD=0.38 gC·m^{-2}·d^{-1}, a RMSD reduction of 80%).

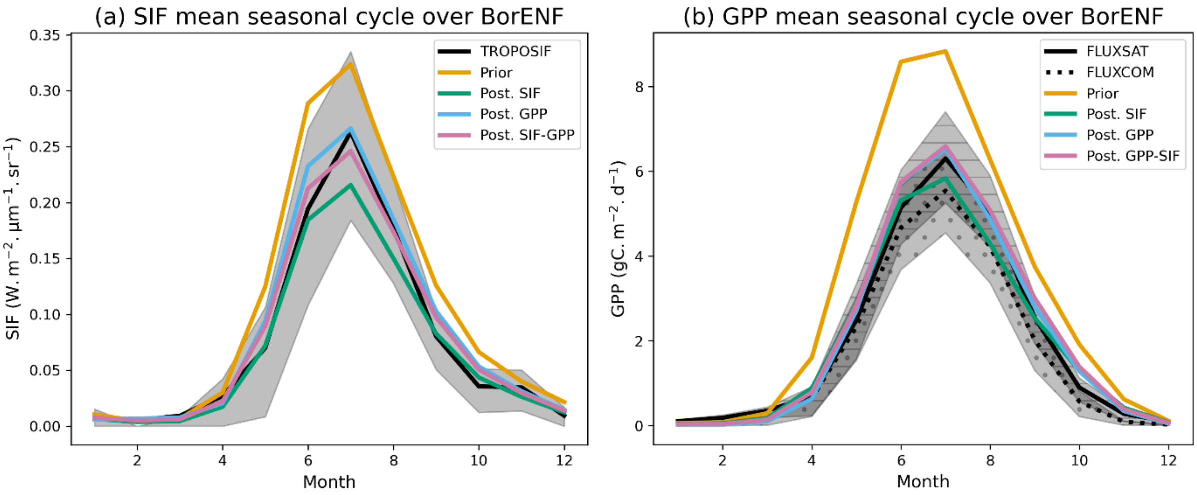

Figure 5: Mean monthly seasonal variations of SIF (a) and GPP (b) for the reference products, and for the prior and posterior simulations, computed over all 0.5° grid cells with a BorENF fraction larger than 50%, between latitudes of 35°N to 85°N. The same legends and colours as in Figure 4 are used.

Table 5: Statistics related to the mean seasonal cycles of SIF and GPP represented in Figure 5: amplitude (computed as the difference between maximum and minimum monthly averages of the seasonal cycle), bias and RMSD (computed versus the reference product named in the corresponding column).

	Amplitude	**Bias**		**RMSD**	
SIF ($W \cdot m^{-2} \cdot \mu m^{-1} \cdot sr^{-1}$)					
		with TROPOSIF		**with TROPOSIF**	
TROPOSIF	0.26	-		-	
Prior	0.32	0.029		0.042	
Posterior SIF-only	0.21	-0.008		0.017	
Posterior GPP-only	0.26	0.009		0.016	
Posterior GPP and SIF	0.24	0.003		0.012	
GPP ($gC \cdot m^{-2} \cdot d^{-1}$)					
		with FLUXSAT	**with FLUXCOM**	**with FLUXSAT**	**with FLUXCOM**
FLUXSAT	6.2	-	0.32	-	0.41
FLUXCOM	5.5	-0.32	-	0.41	-
Prior	8.8	1.11	1.43	1.61	1.94
Posterior SIF-only	5.8	-0.03	0.29	0.32	0.38
Posterior GPP-only	6.5	0.08	0.40	0.26	0.57
Posterior GPP and SIF	6.6	0.16	0.49	0.31	0.65

Table 6 compares the mean annual GPP of the prior and optimised simulations based on the three DA experiments with the ones of the FLUXSAT and FLUXCOM GPP reference products. Similar to what was already observed for the mean GPP seasonal cycles in Figure 5.b, the mean annual GPP for the prior simulation is quite larger than the ones of both evaluation products, by 45% for FLUXSAT and 71% for FLUXCOM. The simulations based on parameters optimised during the three DA experiments result in a decreased GPP, in closer agreement to that of FLUXSAT (2.41 GtC y^{-1}) and FLUXCOM (2.04 GtC y^{-1}). Note that the mean annual GPP of the three posterior simulations do not differ from that of FLUXSAT by more than 8%, while they overestimate the one of FLUXCOM by 16% (SIF-only DA experiment) to 27% (GPP-only DA experiment), as the FLUXCOM mean annual GPP is also 15% lower than the one of FLUXSAT.

Table 6: Mean annual total GPP ($GtC \cdot y^{-1}$) computed between 2001-2015 over grid cells with a BorENF fraction of at least 50% (representing a surface of 1.9 million km^2), for the simulations (Prior, Posterior SIF-only, Posterior GPP-only, Posterior SIF-GPP) and the two GPP reference products (FLUXSAT, FLUXCOM).

	Prior	Posterior SIF-only	Posterior GPP-only	Posterior SIF-GPP	FLUXSAT	FLUXCOM
GPP ($GtC \cdot y^{-1}$)	3.71	2.37	2.59	2.48	2.41	2.04

Figure 6 presents the interannual variations of the total GPP for the simulations and the two reference products. As expected from the mean annual total GPP values (Table 6), the SIF-only GPP estimates are closer to that of FLUXSAT (RMSD=0.07 $GtC \cdot y^{-1}$), with larger estimates for the SIF-GPP posterior simulation, and even larger ones for the GPP-only posterior simulation. The GPP trends for these four products are increasing from 0.012 $GtC \cdot y^{-2}$ (FLUXSAT) to 0.031 $GtC \cdot y^{-2}$ (GPP-only posterior simulation). On the contrary, the FLUXCOM reference product does not show any trend in GPP, with a regression slope of -0.002 $GtC \cdot y^{-2}$, as it does not represent the fertilisation effect of the increasing CO_2 atmospheric concentrations. Compared to the FLUXSAT reference product, including SIF data in the assimilation reduces the slope overestimation found in the GPP-only assimilation.

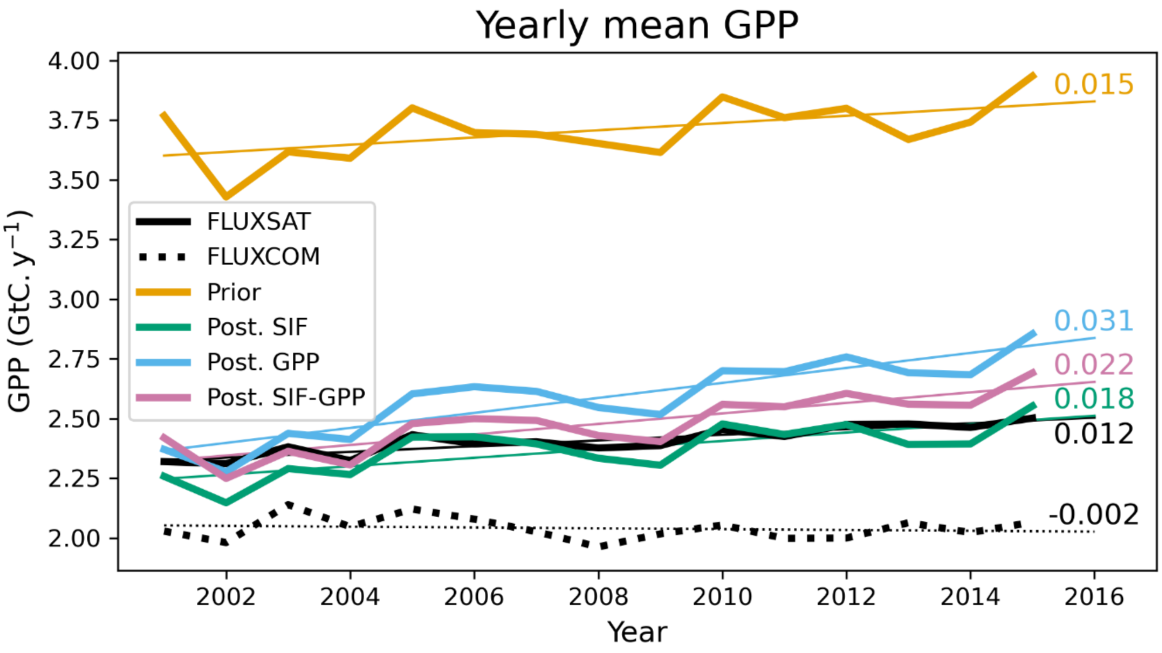

Figure 6: Interannual variations of the total GPP between 2001 and 2015 for the simulations and the two GPP reference products (FLUXSAT, FLUXCOM), computed over grid cells with a BorENF fraction larger than 50%. The same colours and line styles as in Figure 4 are used. The thin straight lines represent the linear regression of each curve in the corresponding colour and line style, and the trend (in GtC·y^{-2}) is marked on the right side.

4 Discussion

4.1 Advantages of a process-based SIF model

The main advantage of using a process-based SIF model as done in this study, compared to relying on a simple SIF-GPP linear relationship (Parazoo et al., 2014; MacBean et al., 2018) is that a process-based model enables differences in SIF and GPP temporal dynamics to be accounted for (Bacour et al., 2019). This is related to different sensitivities of GPP and SIF to their environmental drivers, and thus to model parameters as illustrated by the sensitivity analyses (Figure S4). For example, Pierrat et al. (2022) explored GPP and SIF drivers in a Canadian boreal forest using random forest models. They found that when considering only two predictors in their random forest, daily-SIF was found to be best predicted using air temperature and PAR while soil and air temperature were the best predictors of daily-GPP. Pierrat et al. (2022) also showed that while the SIF-GPP relationship is almost linear close to the winter months, it becomes less linear during summer. This nonlinearity between SIF and GPP over summer was attributed to light saturation of GPP, also stressing the interest of correctly representing NPQ processes.

Moreover, relying on process-based models is critical as divergences in SIF and GPP variations at small spatiotemporal scales or during stress conditions can lead to a decoupling between the two variables (Magney et al., 2020). Indeed, Wohlfahrt et al. (2018) observed a decoupling between SIF and GPP variations during an intense heat wave in a Mediterranean Pine forest, with SIF explaining less than 35% of GPP variability. However, the relationship between SIF and GPP during drought events requires further research (Song et al., 2021) with studies highlighting SIF potential to monitor drought (Sun et al., 2015) and others reporting nonlinearities between SIF and GPP under stress conditions (Wohlfahrt et al., 2018).

Finally, it should be noted that opposite changes in SIF and GPP have been found for some biomes after parameter optimisation using a process-based SIF model (Bacour et al., 2019; Norton et al., 2019), which would not be possible using a positive linear relationship to link GPP and SIF. In this study, both the seasonal amplitudes of GPP and SIF for BorENF decrease after optimisation (Figure 5). This is in line with Bacour et al. (2019) where a reduction in the simulated SIF and GPP was also found for this PFT after assimilating OCO-2 SIF data using a previous version of the SIF model implemented in ORCHIDEE. In contrast, opposite changes for SIF and GPP were observed in Norton et al. (2019) for evergreen coniferous trees after assimilating OCO-2 SIF data to optimise biophysical parameters in the BETHY-SCOPE model using a process-based representation of SIF.

4.2 Additional constraint of assimilating SIF

Assimilating GPP and SIF simultaneously enables to improve both variables even slightly better than the corresponding variable-only DA experiments at the site level (Figure 1), possibly reducing some overfitting by finding a compromise between the two data streams during the optimization (Bacour et al., 2023). In our DA experiments, some parameters, such as a_{PSII} and ALA, play a role in the representation of both the simulated SIF and GPP. These parameters could thus be used as adjustment parameters to fit the measurements during the DA phase, and hence move away from their physical significance if the authorised range of variation is too large. Therefore, we can have a greater confidence in the joint assimilation posterior values for these parameters.

Moreover, because of common drivers between GPP and SIF, such as the absorbed PAR that controls the light-dependent part of photosynthesis, SIF can provide an additional constraint on the parameters involved in this process. In particular, the a_{PSII} parameter, which determines the electron transport rate and photosynthetic yield, impacts both GPP and SIF (Table 3). The strongest reductions in a_{PSII} after optimisation are obtained for the two DA experiments assimilating SIF data, with lower values than the prior value of 0.5, equilibrating the absorption cross-section between the two photosystems. This decrease involves having a sustained NPQ where more energy is diverted to photosystem I; Bag et al. (2020) show that this is possible thanks to a reorganisation of the thylakoid membrane that brings PSII and PSI complexes closer. Note that the joint assimilation of SIF and GPP also provides a greater number of data to constrain this parameter to which both SIF and GPP are sensitive, leading to a stronger reduction in parameter uncertainty (74% for the joint assimilation against 56% and 19% for the GPP-only and SIF-only DA experiment, respectively, see Figure S8). Nevertheless, the model is presently hampered by having a static a_{PSII} value. It should eventually be made variable over time, the transfer of light-harvesting complexes from PSII to PSI being one of the NPQ mechanisms allowing the energy absorbed between the two photosystems to be balanced (Ruban and Johnson, 2009).

In addition, SIF sensitivity to canopy structure can provide information on the related parameters that are not well constrained by the GPP-only DA experiment. Canopy structure is critical as it determines the radiative transfer of incoming radiation impacting SIF and GPP, but also the emission, scattering, and reabsorption of SIF (van der Tol et al., 2009). Structural factors such as leaf angle distribution, leaf clumping, or leaf age and area, play a key role in modelling the diversity and complexity of canopy structure for different biomes (Sun et al., 2023). In this study, the most important parameter for simulating SIF in ORCHIDEE was found to be *ALA* following the sensitivity analysis, whereas it does not appear in the top ten parameters to which GPP is sensitive (Figure S4); Migliavacca et al. (2017) also noted this different sensitivity to the leaf angle distribution, which explains that the SIF-GPP relationship is mainly controlled by changes in canopy structure in a Mediterranean grassland. The optimised values of the average leaf angle *ALA* are 80° for the SIF-only DA experiment and 79° for the SIF-GPP one, and tend toward erectophile leaves. These values are at the upper bound of the *ALA* estimates from Zhu et al. (2018) for coniferous trees (between 50° and 80°). The large reduction in *ALA* posterior uncertainty after assimilating SIF (56% for the SIF-only DA experiment and 62% for the SIF-GPP DA experiment, see Figure S8) stresses its value to better constrain parameters determining canopy structure. Bacour et al. (2019) considered a lower prior value for *ALA* in the former ORCHIDEE version using a parametric simplification of the radiative transfer of the SCOPE model (57.4° for a spherical distribution), but also increased its value after assimilation of OCO-2 SIF data (65°). Note that *ALA* varies between plant species within the same biome (Barclay et al., 2001; Pisek et al., 2013, 2020), which cannot be accounted for in ORCHIDEE where vegetation types are grouped into PFTs. Moreover, several studies have also observed, for different species including conifers, that the leaf angle distribution varies vertically within the canopy, which enables optimising light interception and carbon assimilation at the canopy level (Utsugi et al., 2006; Niinemets, 2010).

All DA experiments also consistently decrease *SLA* by around 25% (Table 3), evolving in the same direction as in Bacour et al. (2019) where a 10% reduction was found. A lower *SLA* value decreases the simulated leaf biomass in ORCHIDEE and changes leaf absorption. As for *ALA*, the description of *SLA* could be refined to account for its vertical distribution within the canopy. Indeed, Rajewicz et al. (2023) collected *SLA* estimates from needle samples of Pine and Spruce and found lower *SLA* values in the upper canopy compared to needles in the lower canopy, with stronger differences for Spruce compared to Pine. The optimised *SLA* values in ORCHIDEE (between 0.007039 and 0.007611 $m^2 \cdot gC^{-1}$) are in the middle of their *SLA* estimates, which range from 0.004 to 0.011 $m^2 \cdot gC^{-1}$ for the two species.

In addition, they highlighted a decreasing trend in *SLA* over the season for both species; considering temporal variations of a parameter value is not yet possible in the ORCHIDEE model.

It is interesting to note that the main parameters related only to SIF variations according to the sensitivity analysis (*ALA*, k_F, $p1_{NPQr}$, $p2_{NPQr}$) have similar optimised values between the SIF-only and the SIF and GPP DA experiments, confirming that assimilating GPP data did not alter these parameters in the joint assimilation. Also note that the consistent optimised values of k_F and *ALA* between these two DA experiments are found despite the strong positive error correlation between these parameters (Figure S9). Concerning k_F, the two DA experiments in which SIF data are assimilated increase its value from 0.05 to 0.07 (Table 3). This prior value of 0.05 has been commonly used in the literature following van der Tol et al. (2014) (Bacour et al., 2019; Raczka et al., 2019). However, Porcar-Castell et al. (2014) used a higher value of 0.1, and Liu et al. (2022) recently estimated the same value for $k_F$from leaf chamber measurements of fluorescence flux performed on winter wheat under different air temperature and CO_2 concentration treatments.

4.3 Limited constraint on carboxylation related parameters and associated foreseen model improvements

One limitation that can be highlighted when performing data assimilation is model equifinality, corresponding to several combinations of parameters that lead to similar reductions of the cost function, with respect to the prescribed errors on observations and parameters (Medlyn et al., 2005; Williams et al., 2009). In this study, the DA experiments disagree on the optimised values of three common parameters ($V_{cmax,25}$, $L_{agecrit}$, and $a_{S,V}$), all of them having an impact on the simulated temporal dynamics of the V_{cmax} variable. The fact that the parameters evolve from their prior value in divergent directions between the DA experiments can be related to equifinality of the solution and error correlation between parameters, which can lead to different GPP estimates when upscaled to the boreal region. Indeed, the highest model-data agreement with respect to *in situ* GPP data is obtained for the two DA experiments that use those data as observational constraint (Figure 1 and Table 4). However, at the regional scale, while the GPP-only DA experiment also yields the lowest RMSD compared to FLUXSAT, the joint assimilation leads to a higher RMSD, similar to the one obtained with the SIF-only DA experiment, and to the strongest bias against this evaluation product (Figure 5 and Table 5).

Regarding $V_{cmax,25}$, the SIF-only and GPP-only DA experiments both agree on decreasing it by about 20%, but the SIF-GPP DA experiment slightly increases it, as compared to its prior value (Table 3 and Figure 2). This reduction in $V_{cmax,25}$ is in line with Bacour et al. (2019) who also found a decrease in this parameter value after assimilating SIF data only (from 45 µmol·m^{-2}·s^{-1} to 42 µmol·m^{-2}·s^{-1}), but to a smaller extent compared to the SIF-only DA experiment in this study.

In the two DA experiments that assimilate SIF data, the decrease in $L_{agecrit}$ agrees with the one in Bacour et al. (2019) for BorENF, who found a reduction from 910 to 855 days. However, the diverging change in the value of $L_{agecrit}$ compared to the optimization assimilating only GPP data could highlight an incorrect representation of leaf life span in ORCHIDEE, that fails to reproduce several observational constraints, and therefore indicates a need for improvement. Indeed, it has been reported that the leaf life span of boreal forest needles varies in fact with latitude, being longer in the north due to colder temperatures. Thus, a temperature-dependent leaf life span should be implemented in LSMs (Reich et al., 2014). The longer leaf life span is also associated with a lower nitrogen content, and this relationship could also be implemented in the ORCHIDEE version integrating an explicit nitrogen cycle (Vuichard et al., 2019).

Finally, assimilating only SIF data brings no constraint on the temperature acclimation parameters in ORCHIDEE. Indeed, $a_{S,V}$ increases in the SIF-only DA experiment (from 668 J•K^{-1}•mol^{-1} for the prior to 740 J•K^{-1}•mol^{-1}), while it decreases in both DA experiments using GPP (517 J•K^{-1}•mol^{-1} for the GPP-only DA experiment and 564 J•K^{-1}•mol^{-1} for the joint DA experiment) (Table 3 and Figure 2). In the SIF-only DA experiment, $a_{S,V}$ is also the less constrained parameter with a reduction in parameter uncertainty of less than 1% (Figure S8). Two other parameters related to the temperature acclimation functions, $a_{S,J}$ and $a_{R,JV}$, have consistent changes of their optimised values after the two DA experiments that assimilate GPP data (they are not considered in the SIF-only one). However, note that in the GPP-only DA experiment, their posterior errors are strongly positively correlated, and the posterior error of $a_{R,JV}$ is negatively correlated with that of $a_{S,V}$ (Figure S9). These error correlations highlight limits in the confidence we can have in these optimised parameter values. Kumarathunge et al. (2019) recently updated the values of these acclimation parameters for growth temperature between 3°C and 30°C, which agree with the ones derived by Kattge and Knorr (2007) between 11°C and 35°C and used in ORCHIDEE. Although the temperature acclimation function in ORCHIDEE is derived from growth temperature measurements between 11°C and 35°C (Kattge and Knorr, 2007), hence likely not adapted to boreal vegetation, a recent update of the parameter values based on an enlarged database with growth temperatures ranging from 3°C and 30°C (Kumarathunge et al., 2019) did not change much the derived values for $a_{S,J}$, $a_{S,V}$, and $a_{R,JV}$. However, for the ratio $\frac{J_{cmax}}{V_{cmax}}$, they mentioned that they had a much lower value for the Finland Scots pine dataset, this is in line with the lower $a_{R,JV}$ found in this study (2.08 μmol $e^{-}\cdot m^{-2}\cdot s^{-1}$ / μmol $CO_2\cdot m^{-2}\cdot s^{-1}$ for the GPP-only DA experiment, and 1.74 for the joint DA experiment). At last, note that the SIF-only DA experiment cannot help to better constrain the last temperature-related parameter T_{min} as SIF was not found to be sensitive to this parameter (Figure S4), while assimilating GPP data enables to reduce the posterior uncertainty of T_{min} by 98% (Figure S8).

4.4 Challenges of modelling NPQ

Specifically accounting for the sustained component of NPQ in addition to the reversible part is required for needleleaf evergreen biomes to represent the excess energy dissipation during wintertime in the absence of photosynthetic activity. Raczka et al. (2019) found that distinguishing between sustained and reversible NPQ in CLM Version 4.5 improved the seasonality of the simulated

SIF compared to the GOME-2 satellite SIF product at the Niwot Ridge site (see Table 1). Similarly, in this study, accounting for the sustained and reversible NPQ components impacts the dynamics of the simulated SIF compared to the total NPQ model of Bacour et al. (2019) after calibration against both SIF and GPP data (Figure S5). Indeed, notwithstanding similar overall performances at site level once optimised (RMSDs in Table 4), the two component NPQ modelling scheme results in lower SIF flux during wintertime (typically from January to May) together with higher SIF levels during the growing season and senescence (Figure S5).

Despite the key roles of NPQ to in preventing damage of the photosynthetic machinery, theoretical gaps remain for improving NPQ understanding and modelling. Representing NPQ temporal dynamics is associated with a high level of complexity due to its multiple mechanisms and response timescales from seconds to seasonal variations. This complexity is illustrated by the different representations that have been developed to quantify the NPQ reversible and sustained components. Zaks et al. (2012) proposed a mathematical model capable of simulating reversible NPQ kinetics under different light intensities. However, this model consists of 26 nonlinear differential equations and 78 parameters in total. Due to its complexity and the uncertainty of an increasing number of parameters, such a model could not be implemented in LSMs. For greater simplicity, empirical models have also been developed. Serôdio and Lavaud (2011) represented the NPQ dynamics as a sigmoidal response to the irradiance level that is able to account for photoacclimation, based on an adaptation of the Hill equation. Then, Raczka et al. (2019) defined k_r as a function of light saturation in CLM 4.5. The k_r formulations in Serôdio and Lavaud (2011) and Raczka et al. (2019) rely on 3 parameters that can be calibrated with PAM measurements; we recall that the k_R model developed in this study (Eq. (8)) uses 2 parameters ($p1_{NPQr}$ and $p2_{NPQr}$).

Therefore, the implementation of empirical models of reversible and sustained NPQ in LSMs depends on the availability of PAM data to validate the models and calibrate their parameters. However, few PAM data are available and do not cover the diversity of biomes or environmental conditions represented in LSMs, with only one full-year PAM measurement campaign conducted at Hyytiälä on Scots pines for BorENF. Also note that the Hyytiälä PAM measurements were performed on needles from the top canopy, which does not allow to consider potential NPQ vertical variations inside the canopy in the k_R and k_S formulations. The new model for k_r developed in this study and the formulation of k_S from Raczka et al. (2019) would need to be tested against PAM data from other vegetation species, climatic conditions, and light conditions within the canopy. For example, PAM data from other cold climate biomes might not support a k_S model that only depends on air temperature. However, for cold climate evergreen species, similar heat dissipation occurring through sustained NPQ have been found in winter (Öquist and Huner, 2003), which has been related in Scots pines to structural rearrangements of the thylakoid membrane with a disorganisation of photosystems chlorophyll antenna leading to heat dissipation (Bag et al., 2020).

Optical remote sensing data could also provide new constraints on NPQ at larger scales than what is obtained from PAM measurements. Gamon et al. (1992) proposed the photochemical reflectance index (PRI) as an indicator of reversible NPQ. PRI is defined based on two reflectance bands, one at 531 nm that is associated with the de-epoxidation of the xanthophyll pigments indicating short term decrease in photosynthetic efficiency, and a reference band at 570 nm (Gamon et al., 1992). This indexwas found to correlate with an increase in heat dissipation, such as under excess light or water stress conditions. Recently, Wang et al. (2020) estimated PRI using MODIS reflectance bands 11 and 12 and showed that it could be used as a proxy of NPQ to better characterise the relationship between SIF and GPP for several biomes, including evergreen needleleaf forests. A complementary optical remote sensing index that has been related to sustained NPQ is the chlorophyll/carotenoid index (CCI) (Gamon et al., 2016; Pierrat et al., 2022). CCI tracks the seasonal variations in GPP through changes in carotenoid pigments, informing on sustained photoprotection mechanisms in winter for cold evergreen species. Then, remote sensing-based PRI and CCI could be used to evaluate and better constrain the reversible and sustained NPQ simulated in LSMs. However, the potential of these indices has been primarily established at the leaf and canopy scales (Gamon et al., 1992; Springer et al., 2017; Wong and Gamon, 2015), and their application at larger scales is also limited by errors associated with satellite measurements. Finally, colour-based vegetation indices obtained from digital camera imagery, such as PhenoCam, also have the potential to provide new insights on chlorophyll fluorescence and PRI seasonal variations by tracking changes in canopy colours (Seyednasrollah et al., 2021).

4.5 Limitations to improving GPP constraint using data assimilation

The ability of DA (here with *in situ* GPP estimates combined with space-borne SIF retrievals) to improve simulated GPP is affected by the representativity of the data used for parameter calibration. In this study focusing on BorENF, it is essential to consider a diverse and sufficiently large number of sites representative of this biome to prevent overfitting to the individual specificities of different sites when optimising the model parameters. Although we selected several sites having a large gradient of climate conditions and locations, with latitudes ranging from 40° to 67°N (Table 1), the use of *in situ* GPP data as observational constraint is intrinsically limited by the number of FLUXNET sites (all the more since we imposed selection criteria relative to the length of the available GPP time series, as well as the coverage of the BorENF PFT over the footprint of TROPOMI observations). This limited availability of *in situ* data could lead to a representativeness issue for BorENF when scaling the optimised parameters from the site scale to the regional scale. Indeed, in addition to the potential equifinality issue previously mentioned (see section 4.3), this could also explain why the two DA experiments assimilating GPP data give the best improvement in simulated GPP when evaluated against *in situ* GPP (Figure 1 and Table 4), but not necessarily at the regional scale (Figure 5 and Table 5).

Although satellite SIF products offer a global spatial coverage and therefore a large number of pixels available for data assimilation, we have limited our analysis to grid cells around the FLUXNET sites as we aimed at comparing the assimilation of GPP and SIF data with similar constraints in terms of spatial sampling. However, an increased constraint could be reached by using a greater number of SIF grid cells; not limiting the selection to the vicinity of the FLUXNET sites would also allow considering more homogeneous grid cellswith respect to the considered PFT.

In addition to the issue of spatial sampling, there is also a limitation due to the temporal sampling considered here for data assimilation. The observations of GPP and SIF are available during two distinct periods: the assimilated FLUXNET GPP estimates span three consecutive years between 1998 and 2006 depending on site (Table 1), while the assimilated TROPOSIF estimates cover the period 2019-2020 (section 2.2.2). The GPP interannual variations presented in Figure 6 shows that the simulation related to the GPP-only DA experiment better matches FLUXSAT GPP at the beginning of the evaluation period, while the agreement obtained for the simulation relying on the SIF-only DA experiment is higher towards the end of the evaluation period. Here, co-assimilating SIF and GPP data enabled the simulation of a mean annual GPP that is closer to the FLUXSAT reference product over the whole period, with an RMSD of 0.09 GtC·y^{-1} compared to 0.21 and 0.14 GtC·y^{-1} for the GPP-only and SIF-only DA, respectively. However, it is difficult to identify which parameters are responsible for this improvement as they could be related to temperature acclimation or the representation of the CO_2 fertilisation effect for example. The joint assimilation of SIF with GPP over a longer and more recent period should allow for an in-depth study of the impact of the temporal sampling on the estimation of the long--term trend of GPP; this could be achieved for instance with the *in situ* GPP dataset from Warm Winter 2020 Team, & ICOS Ecosystem Thematic Centre (2022).

The estimation error associated with the GPP and SIF data used for assimilation and evaluation is another major limitation. The GPP data considered here for parameter optimisation are FLUXNET estimates derived from eddy-covariance measurements of NEE, which are affected by the chosen partitioning method, with its underlying assumptions and uncertainties (Tramontana et al., 2020). This is illustrated by the recent paper of Kohonen et al. (2022) who compared the standard GPP estimates based on NEE measurements to GPP estimates based on the 5-year (2013-2017) time-series of carbonyl sulfide (COS) ecosystem fluxes they acquired at the Hyytiälä site. At the daily scale, their two COS-based GPP estimates were 23% and 7% higher, respectively, than the CO_2-based estimates. On the other hand, Lee et al. (2020) found that the CO_2-based GPP estimates from the night-time partitioning method were 19% higher than GPP estimates using a stable-C-isotope-based partitioning approach in a Douglas fir stand in Canada. Then, the uncertainty on the global GPP evaluation products is illustrated by the 15% difference between FLUXCOM and FLUXSAT mean annual GPP over the grid cells covered with at least 50% of BorENF. While these two evaluation products highlight a strong overestimation of the prior GPP in ORCHIDEE, the discrepancy between FLUXCOM and FLUXSAT hinders the evaluation of the optimised mean annual GPP for the different DA experiments. The TROPOSIF retrievals also have their own error, estimated at 0.5 $W \cdot m^{-2} \cdot sr^{-1} \cdot m^{-2} \cdot \mu m^{-1}$ for the considered spectral window (743-758 nm), with a low mean bias of -0.008 $W \cdot m^{-2} \cdot sr^{-1} \cdot m^{-2} \cdot \mu m^{-1}$ (Guanter et al., 2021). The quality of these retrievals also depends on cloud fraction filtering and viewing angle. Although the 743-758 nm spectral window has been found to be less impacted by atmospheric effects than the 735-758 nm retrievals that are also available from the ESA product, the choice of a cloud fraction threshold still affects SIF estimates (Guanter et al., 2021). Here, filtering for cloud fractions above 40% enables a constraint on the simulated SIF and GPP for more illumination conditions than considering only cloud fractions lower than 20%. Then, considering TROPOSIF retrievals with VZA lower than 50° in this study agrees with the recommendations of Guanter et al. (2021) as a VZA higher than 60° leads to lower quality SIF estimates. Note however that in this data assimilation framework, the observation error covariance matrix $\mathbf{R}$ is defined based on the RMSD between the observations and the prior model (Section 2.3.1); in doing so, the error in the model likely dominates the error budget related to the GPP and SIF data (Kuppel et al., 2013; Bacour et al., 2015).

Finally, the accuracy of data assimilation is limited by the existence of model structural errors related to the implementation of the processes in ORCHIDEE as these errors will be aliased onto parameter optimised values (MacBean et al., 2016; Bacour et al., 2023). For example, the inability of the simulated SIF to reproduce the latitudinal variations of the TROPOSIF product after data assimilation can point to structural errors in the current SIF model (Figure 4). More generally, systematic structural errors can be due to incorrect representations or missing processes in the ORCHIDEE version used in this study, such as accounting for carbon and nitrogen interactions or disturbances like clearcutting or fires (Vuichard et al., 2019; Zheng et al., 2023). Curasi et al. (2023) also recommend to implement a representation of boreal disturbances, but also of peatlands and permafrost soils in the Canadian Land Surface Scheme Including Biogeochemical Cycles (CLASSIC) model to improve the model performances. In addition, they found that refining the vegetation cover map by increasing the number of PFTs to represent Canada's ecosystems improves CLASSIC ability to simulate the carbon cycle. On the other hand, Peaucelle et al. (2019) highlighted the need to use more plant functional trait based-approaches in LSMs to better represent the relationship between traits and climate, instead of relying on optimising constant parameter values defined per PFT and specific to the LSM.

5 Conclusion and outlook

By using a physiologically-based NPQ model and assimilating *in situ* GPP FLUXNET estimates as well as ESA TROPOSIF retrievals within the ORCHIDEE LSM, we improved the co-variations of SIF and GPP simulated over boreal evergreen needleleaf forests. The structural code modifications, as well as the observation-based information now embedded in the optimised parameter values, have reduced the uncertainty of the simulated SIF and GPP. In spite of the limitations discussed above, this study advocates using TROPOMI SIF estimates in conjunction with *in situ* GPP estimates, to improve the SIF and GPP simulated by LSMs. Co-assimilating SIF and GPP helps to mitigate overfitting to each individual flux, and SIF provides useful additional information to reduce the uncertainty on model parameters that are not well constrained by GPP alone, especially parameters related to canopy structure. Regarding the future of NPQ modelling, Johnson and Berry (2021) and Johnson et al. (2021) proposed a new promising approach, with a process-based model of the linear electron transport, and a direct activation of NPQ under photosynthetic control. This model can easily be implemented in LSMs. Another next step would be to improve the NPQ model in stress conditions, especially droughts as boreal forests are predicted to experience more frequent and intense droughts in the future (Seidl et al., 2017), so that models are able to simulate the decoupling observed between SIF and GPP in such conditions.

Acknowledgements

This work benefited from the French state aid managed by the ANR under the “Investissements d'avenir” programme with the reference ANR-16-CONV-0003 (CLand), and by the LabEx Saclay Plant Sciences-SPS (grant number ANR-17-EUR-0007). It was also supported by the CNES-TOSCA FORGE project.

We are very grateful to Professor Albert Porcar-Castell (University of Helsinki) who provided the unique *in situ* PAM time series measured at the Hyytiälä forest site.

This work used eddy covariance data acquired by the FLUXNET community and in particular by the following networks: AmeriFlux (U.S. Department of Energy, Biological and Environmental Research, Terrestrial Carbon Program (DE-FG02-04ER63917 and DE-FG02-04ER63911)), AfriFlux, AsiaFlux, CarboAfrica, CarboEuropeIP, CarboItaly, CarboMont, ChinaFlux, Fluxnet-Canada (supported by CFCAS, NSERC, BIOCAP, Environ-ment Canada, and NRCan), Green-Grass, KoFlux, LBA, NECC, OzFlux, TCOS-Siberia, USCCC. We acknowledge the financial support to the eddy covariance data harmonization provided by CarboEuropeIP, FAO-GTOS-TCO, iLEAPS, Max Planck Institute for Biogeochemistry, National Science Foundation, University of Tuscia, Université Laval and Environment Canada and US Department of Energy and the database development and technical support from Berkeley Water Center, Lawrence Berkeley National Laboratory, Microsoft Research eScience, Oak Ridge National Laboratory, University of California - Berkeley, University of Virginia.

Special thanks to the Helmholtz Centre for Environmental Research - UFZ (and Dr Corinna Rebmann) for providing the RU-Zot data, and to Lund University (and Professor Anders Lindroth) for providing the SE-Fla data.

We thank Nicolas Vuichard for providing the ERA5 forcing files formatted for the ORCHIDEE LSM, and Xiaoni Wang-Faivre for processing the spatio-temporal averages of the FLUXCOM GPP products.

Data availability statement

The FLUXNET *in situ* data are freely available at https://fluxnet.org following the Creative Commons (CC-BY 4.0) licence (Pastorello et al., 2020). The FLUXCOM GPP product can be downloaded from the Max Planck Institute for Biogeochemistry data portal at http://fluxcom.org. The FLUXSAT GPP product is available from the NASA Goddard Space Flight Center at https://avdc.gsfc.nasa.gov. The operational production of ESA TROPOSIF data files is ensured by the ESA S5P-PAL (Product Algorithm Laboratory) system, with products available from May 2018 onwards and a daily update, see at https://data-portal.s5p-pal.com/browser.

All figures were created using Python programming language version 3 (van Rossum and Drake, 2009).

References

Amiro, B.D., Barr, A.G., Black, T.A., Iwashita, H., Kljun, N., McCaughey, J.H., Morgenstern, K., Murayama, S., Nesic, Z., Orchansky, A.L., Saigusa, N., 2006. Carbon, energy and water fluxes at mature and disturbed forest sites, Saskatchewan, Canada. Agric. For. Meteorol. 136, 237–251. https://doi.org/10.1016/J.AGRFORMET.2004.11.012

Anav, A., Friedlingstein, P., Beer, C., Ciais, P., Harper, A., Jones, C., Murray-Tortarolo, G., Papale, D., Parazoo, N.C., Peylin, P., Piao, S., Sitch, S., Viovy, N., Wiltshire, A., Zhao, M., 2015. Spatiotemporal patterns of terrestrial gross primary production: A review. Rev. Geophys. https://doi.org/10.1002/2015RG000483

Bacour, C., MacBean, N., Chevallier, F., Léonard, S., Koffi, E.N., Peylin, P., 2023. Assimilation of multiple datasets results in large differences in regional- to global-scale NEE and GPP budgets simulated by a terrestrial biosphere model. Biogeosciences 20, 1089–1111. https://doi.org/10.5194/BG-20-1089-2023

Bacour, C., Maignan, F., MacBean, N., Porcar-Castell, A., Flexas, J., Frankenberg, C., Peylin, P., Chevallier, F., Vuichard, N., Bastrikov, V., 2019. Improving Estimates of Gross Primary Productivity by Assimilating Solar-Induced Fluorescence Satellite Retrievals in a Terrestrial Biosphere Model Using a Process-Based SIF Model. J. Geophys. Res. Biogeosciences 124, 3281–3306. https://doi.org/10.1029/2019JG005040

Bacour, C., Peylin, P., MacBean, N., Rayner, P.J., Delage, F., Chevallier, F., Weiss, M., Demarty, J., Santaren, D., Baret, F., Berveiller, D., Dufrêne, E., Prunet, P., 2015. Joint assimilation of eddy covariance flux measurements and FAPAR products over temperate forests within a process-oriented biosphere model. J. Geophys. Res. Biogeosciences 120, 1839–1857. https://doi.org/10.1002/2015JG002966

Bag, P., Chukhutsina, V., Zhang, Z., Paul, S., Ivanov, A.G., Shutova, T., Croce, R., Holzwarth, A.R., Jansson, S., 2020. Direct energy transfer from photosystem II to photosystem I confers winter sustainability in Scots Pine. Nat. Commun. 2020 111 11, 1–13. https://doi.org/10.1038/s41467-020-20137-9

Baker, N.R., 2008. Chlorophyll Fluorescence: A Probe of Photosynthesis In Vivo. Annu. Rev. Plant Biol 59, 89–113. https://doi.org/10.1146/annurev.arplant.59.032607.092759

Baldocchi, D., Falge, E., Gu, L., Olson, R., Hollinger, D., Running, S., Anthoni, P., Bernhofer, C., Davis, K., Evans, R., Fuentes, J., Goldstein, A., Katul, G., Law, B., Lee, X., Malhi, Y., Meyers, T., Munger, W., Oechel, W., Paw, U.K.T., Pilegaard, K., Schmid, H.P., Valentini, R., Verma, S., Vesala, T., Wilson, K., Wofsy, S., 2001. FLUXNET: A New Tool to Study the Temporal and Spatial Variability of Ecosystem-Scale Carbon Dioxide, Water Vapor, and Energy Flux Densities. Bull. Am. Meteorol. Soc. 82, 2415–2434. https://doi.org/10.1175/1520-0477(2001)082<2415:FANTTS>2.3.CO;2

Barclay, H.J., 2011. Distribution of leaf orientations in six conifer species. https://doi.org/10.1139/b01-014 79, 389–397. https://doi.org/10.1139/B01-014

Bastrikov, V., Macbean, N., Bacour, C., Santaren, D., Kuppel, S., Peylin, P., 2018. Land surface model parameter optimisation using in situ flux data: Comparison of gradient-based versus random search algorithms (a case study using ORCHIDEE v1.9.5.2). Geosci. Model Dev. 11, 4739–4754. https://doi.org/10.5194/gmd-11-4739-2018

Bergeron, O., Margolis, H.A., Black, T.A., Coursolle, C., Dunn, A.L., Barr, A.G., Wofsy, S.C., 2007. Comparison of carbon dioxide fluxes over three boreal black spruce forests in Canada. Glob. Chang. Biol. 13, 89–107. https://doi.org/10.1111/J.1365-2486.2006.01281.X

Bonan, G.B., 2008. Forests and climate change: Forcings, feedbacks, and the climate benefits of forests. Science (80-.). https://doi.org/10.1126/science.1155121

Boucher, O., Servonnat, J., Albright, A.L., Aumont, O., Balkanski, Y., Bastrikov, V., Bekki, S., Bonnet, R., Bony, S., Bopp, L., Braconnot, P., Brockmann, P., Cadule, P., Caubel, A., Cheruy, F., Codron, F., Cozic, A., Cugnet, D., D'Andrea, F., Davini, P., de Lavergne, C., Denvil, S., Deshayes, J., Devilliers, M., Ducharne, A., Dufresne, J.L., Dupont, E., Éthé, C., Fairhead, L., Falletti, L., Flavoni, S., Foujols, M.A., Gardoll, S., Gastineau, G., Ghattas, J., Grandpeix, J.Y., Guenet, B., Guez, L.E., Guilyardi, E., Guimberteau, M., Hauglustaine, D., Hourdin, F., Idelkadi, A., Joussaume, S., Kageyama, M., Khodri, M., Krinner, G., Lebas, N., Levavasseur, G., Lévy, C., Li, L., Lott, F., Lurton, T., Luyssaert, S., Madec, G., Madeleine, J.B., Maignan, F., Marchand, M., Marti, O., Mellul, L., Meurdesoif, Y., Mignot, J., Musat, I., Ottlé, C., Peylin, P., Planton, Y., Polcher, J., Rio, C., Rochetin, N., Rousset, C., Sepulchre, P., Sima, A., Swingedouw, D., Thiéblemont, R., Traore, A.K., Vancoppenolle, M., Vial, J., Vialard, J., Viovy, N., Vuichard, N., 2020. Presentation and Evaluation of the IPSL-CM6A-LR Climate Model. J. Adv. Model. Earth Syst. 12, e2019MS002010. https://doi.org/10.1029/2019MS002010

Burnham, K.P. and Anderson, D.R, 2002. Model selection and multimodel inference: a practical information-theoretic approach, 2nd edn. Springer, New York

Campbell, G.S., 1990. Derivation of an angle density function for canopies with ellipsoidal leaf angle distributions. Agric. For. Meteorol. 49, 173–176. https://doi.org/10.1016/0168-1923(90)90030-A

Chen, J.M., Menges, C.H., Leblanc, S.G., 2005. Global mapping of foliage clumping index using multi-angular satellite data. Remote Sens. Environ. 97, 447–457. https://doi.org/10.1016/j.rse.2005.05.003

Cheng, R., Magney, T.S., Orcutt, E.L., Pierrat, Z., Köhler, P., Bowling, D.R., Bret-Harte, M.S., Euskirchen, E.S., Jung, M., Kobayashi, H., Rocha, A. V., Sonnentag, O., Stutz, J., Walther, S., Zona, D., Frankenberg, C., 2022. Evaluating photosynthetic activity across Arctic-Boreal land cover types using solar-induced fluorescence. Environ. Res. Lett. 17, 115009. https://doi.org/10.1088/1748-9326/AC9DAE

Chéruy, F., Ducharne, A., Hourdin, F., Musat, I., Vignon, É., Gastineau, G., Bastrikov, V., Vuichard, N., Diallo, B., Dufresne, J.-L., Ghattas, J., Grandpeix, J.-Y., Idelkadi, A., Mellul, L., Maignan, F., Ménégoz, M., Ottlé, C., Peylin, P., Servonnat, J., Wang, F., Zhao, Y., 2020. Improved Near-Surface Continental Climate in IPSL-CM6A-LR by Combined Evolutions of Atmospheric and Land Surface Physics. J. Adv. Model. Earth Syst. 12. https://doi.org/10.1029/2019MS002005

Collatz, G., Ribas-Carbo, M., Berry, J., 1992. Coupled Photosynthesis-Stomatal Conductance Model for Leaves of C4 Plants. Funct. Plant Biol. 19, 519. https://doi.org/10.1071/pp9920519

Croft, H., Chen, J.M., Luo, X., Bartlett, P., Chen, B., Staebler, R.M., 2017. Leaf chlorophyll content as a proxy for leaf photosynthetic capacity. Glob. Chang. Biol. 23, 3513–3524. https://doi.org/10.1111/gcb.13599

Curasi, S.R., Melton, J.R., Humphreys, E.R., Wang, L., Seiler, C., Cannon, A.J., Chan, E., Qu, B., 2023. Evaluating the Performance of the Canadian Land Surface Scheme Including Biogeochemical Cycles (CLASSIC) Tailored to the Pan-Canadian Domain. J. Adv. Model. Earth Syst. 15, e2022MS003480. https://doi.org/10.1029/2022MS003480

Damm, A., Guanter, L., Paul-Limoges, E., van der Tol, C., Hueni, A., Buchmann, N., Eugster, W., Ammann, C., Schaepman, M.E., 2015. Far-red sun-induced chlorophyll fluorescence shows ecosystem-specific relationships to gross primary production: An assessment based on observational and modeling approaches. Remote Sens. Environ. 166, 91–105. https://doi.org/10.1016/j.rse.2015.06.004

Dantec-Nédélec, S., Ottlé, C., Wang, T., Guglielmo, F., Maignan, F., Delbart, N., Valdayskikh, V., Radchenko, T., Nekrasova, O., Zakharov, V., Jouzel, J., 2017. Testing the capability of ORCHIDEE land surface model to simulate Arctic ecosystems: Sensitivity analysis and site-level model calibration. J. Adv. Model. Earth Syst. 9, 1212–1230. https://doi.org/10.1002/2016MS000860

Ding, J., Tarokh, V., Yang, Y., 2018. Model Selection Techniques: An Overview. IEEE Signal Process. Mag. 35, 16–34. https://doi.org/10.1109/MSP.2018.2867638

D’Orgeval, T., Polcher, J., De Rosnay, P., 2008. Sensitivity of the West African hydrological cycle in ORCHIDEE to infiltration processes. Hydrol. Earth Syst. Sci. 12, 1387–1401. https://doi.org/10.5194/hess-12-1387-2008

Dunn, A.L., Barford, C.C., Wofsy, S.C., Goulden, M.L., Daube, B.C., 2007. A long-term record of carbon exchange in a boreal black spruce forest: means, responses to interannual variability, and decadal trends. Glob. Chang. Biol. 13, 577–590. https://doi.org/10.1111/J.1365-2486.2006.01221.X

Farquhar, G.D., von Caemmerer, S., Berry, J.A., 1980. A biochemical model of photosynthetic CO2 assimilation in leaves of C3 species. Planta 149, 78–90. https://doi.org/10.1007/BF00386231

Flexas, J., Escalona, J.M., Evain, S., Gulías, J., Moya, I., Osmond, C.B., Medrano, H., 2002. Steady-state chlorophyll fluorescence (Fs) measurements as a tool to follow variations of net CO 2 assimilation and stomatal conductance during water-stress in C 3 plants. Physiol. Plant. 114, 231–240. https://doi.org/10.1034/j.1399-3054.2002.1140209.x

Frankenberg, C., Fisher, J.B., Worden, J., Badgley, G., Saatchi, S.S., Lee, J.E., Toon, G.C., Butz, A., Jung, M., Kuze, A., Yokota, T., 2011. New global observations of the terrestrial carbon cycle from GOSAT: Patterns of plant fluorescence with gross primary productivity. Geophys. Res. Lett. 38, 1–6. https://doi.org/10.1029/2011GL048738

Friedlingstein, P., Jones, M.W., O'Sullivan, M., Andrew, R.M., Bakker, D.C.E., Hauck, J., Le Quéré, C., Peters, G.P., Peters, W., Pongratz, J., Sitch, S., Canadell, J.G., Ciais, P., Jackson, R.B., Alin, S.R., Anthoni, P., Bates, N.R., Becker, M., Bellouin, N., Bopp, L., Chau, T.T.T., Chevallier, F., Chini, L.P., Cronin, M., Currie, K.I., Decharme, B., Djeutchouang, L.M., Dou, X., Evans, W., Feely, R.A., Feng, L., Gasser, T., Gilfillan, D., Gkritzalis, T., Grassi, G., Gregor, L., Gruber, N., Gürses, Ö., Harris, I., Houghton, R.A., Hurtt, G.C., Iida, Y., Ilyina, T., Luijkx, I.T., Jain, A., Jones, S.D., Kato, E., Kennedy, D., Klein Goldewijk, K., Knauer, J., Korsbakken, J.I., Körtzinger, A., Landschützer, P., Lauvset, S.K., Lefèvre, N., Lienert, S., Liu, J., Marland, G., McGuire, P.C., Melton, J.R., Munro, D.R., Nabel, J.E.M.S., Nakaoka, S.-I., Niwa, Y., Ono, T., Pierrot, D., Poulter, B., Rehder, G., Resplandy, L., Robertson, E., Rödenbeck, C., Rosan, T.M., Schwinger, J., Schwingshackl, C., Séférian, R., Sutton, A.J., Sweeney, C., Tanhua, T., Tans, P.P., Tian, H., Tilbrook, B., Tubiello, F., van der Werf, G.R., Vuichard, N., Wada, C., Wanninkhof, R., Watson, A.J., Willis, D., Wiltshire, A.J., Yuan, W., Yue, C., Yue, X., Zaehle, S., Zeng, J., 2022. Global Carbon Budget 2021. Earth Syst. Sci. Data 14, 1917–2005. https://doi.org/10.5194/essd-14-1917-2022

Galmés, J., Hermida-Carrera, C., Laanisto, L., Niinemets, Ü., 2016. A compendium of temperature responses of Rubisco kinetic traits: variability among and within photosynthetic groups and impacts on photosynthesis modeling. J. Exp. Bot. 67, 5067–5091. https://doi.org/10.1093/jxb/erw267

Gamon, J.A., Huemmrich, K.F., Wong, C.Y.S., Ensminger, I., Garrity, S., Hollinger, D.Y., Noormets, A., Peñuelas, J., 2016. A remotely sensed pigment index reveals photosynthetic phenology in evergreen conifers. Proc. Natl. Acad. Sci. https://doi.org/10.1073/pnas.1606162113

Gamon, J.A., Peñuelas, J., Field, C.B., 1992. A narrow-waveband spectral index that tracks diurnal changes in photosynthetic efficiency. Remote Sens. Environ. 41, 35–44. https://doi.org/10.1016/0034-4257(92)90059-S

Garbulsky, M.F., Peñuelas, J., Gamon, J., Inoue, Y., Filella, I., 2011. The photochemical reflectance index (PRI) and the remote sensing of leaf, canopy and ecosystem radiation use efficiencies. A review and meta-analysis. Remote Sens. Environ. https://doi.org/10.1016/j.rse.2010.08.023

Gauthier, S., Bernier, P., Kuuluvainen, T., Shvidenko, A.Z., Schepaschenko, D.G., 2015. Boreal forest health and global change. Science (80-.). 349, 819–822. https://doi.org/10.1126/SCIENCE.AAA9092/SUPPL_FILE/GAUTHIER.SM.PDF

Goldberg, D.E., 1989. Genetic algorithms in search, optimization, and machine learning. Addison-Wesley Longman Publishing Co., Inc., MA, United States.

Groenendijk, M., Dolman, A.J., van der Molen, M.K., Leuning, R., Arneth, A., Delpierre, N., Gash, J.H.C., Lindroth, A., Richardson, A.D., Verbeeck, H., Wohlfahrt, G., 2011. Assessing parameter variability in a photosynthesis model within and between plant functional types using global Fluxnet eddy covariance data. Agric. For. Meteorol. 151, 22–38. https://doi.org/10.1016/j.agrformet.2010.08.013

Guanter, L., Bacour, C., Schneider, A., Aben, I., Van Kempen, T.A., Maignan, F., Retscher, C., Köhler, P., Frankenberg, C., Joiner, J., Zhang, Y., 2021. The TROPOSIF global sun-induced fluorescence dataset from the Sentinel-5P TROPOMI mission. Earth Syst. Sci. Data 13, 5423–5440. https://doi.org/10.5194/essd-13-5423-2021

Harris, N.L., Gibbs, D.A., Baccini, A., Birdsey, R.A., de Bruin, S., Farina, M., Fatoyinbo, L., Hansen, M.C., Herold, M., Houghton, R.A., Potapov, P. V., Suarez, D.R., Roman-Cuesta, R.M., Saatchi, S.S., Slay, C.M., Turubanova, S.A., Tyukavina, A., 2021. Global maps of twenty-first century forest carbon fluxes. Nat. Clim. Chang. 2021 113 11, 234–240. https://doi.org/10.1038/S41558-020-00976-6

Harris, I., Osborn, T.J., Jones, P., Lister, D., 2020. Version 4 of the CRU TS monthly high-resolution gridded multivariate climate dataset. Sci. Data 7, 1–18. https://doi.org/10.1038/s41597-020-0453-3

Haupt, R.L., Haupt, S.E., 2004. Practical Genetic Algorithms, Practical Genetic Algorithms. John Wiley & Sons. https://doi.org/10.1002/0471671746

Hayes, D.J., Butman, D.E., Domke, G.M., Fisher, J.B., Neigh, C.S.R., Welp, L.R., 2022. Boreal forests. Balanc. Greenh. Gas Budgets Account. Nat. Anthropog. Flows CO2 other Trace Gases 203–236. https://doi.org/10.1016/B978-0-12-814952-2.00025-3

Hersbach, H., Bell, B., Berrisford, P., Hirahara, S., Horányi, A., Muñoz-Sabater, J., Nicolas, J., Peubey, C., Radu, R., Schepers, D., Simmons, A., Soci, C., Abdalla, S., Abellan, X., Balsamo, G., Bechtold, P., Biavati, G., Bidlot, J., Bonavita, M., Chiara, G., Dahlgren, P., Dee, D., Diamantakis, M., Dragani, R., Flemming, J., Forbes, R., Fuentes, M., Geer, A., Haimberger, L., Healy, S., Hogan, R.J., Hólm, E., Janisková, M., Keeley, S., Laloyaux, P., Lopez, P., Lupu, C., Radnoti, G., Rosnay, P., Rozum, I., Vamborg, F., Villaume, S., Thépaut, J., 2020. The ERA5 global reanalysis. Q. J. R. Meteorol. Soc. 146, 1999–2049. https://doi.org/10.1002/qj.3803

Huemmrich, K.F., 2013. Simulations of Seasonal and Latitudinal Variations in Leaf Inclination Angle Distribution: Implications for Remote Sensing. Adv. Remote Sens. 2, 93–101. https://doi.org/10.4236/ARS.2013.22013

Iooss, B., Lemaître, P., 2015. A review on global sensitivity analysis methods. Oper. Res. Comput. Sci. Interfaces Ser. 59, 101–122. https://doi.org/10.1007/978-1-4899-7547-8_5/COVER

Ishida, A., Uemura, A., Koike, N., Matsumoto, Y., Hoe, A.L., 1999. Interactive effects of leaf age and self-shading on leaf structure, photosynthetic capacity and chlorophyll fluorescence in the rain forest tree, Dryobalanops aromatica. Tree Physiol. 19, 741–747. https://doi.org/10.1093/treephys/19.11.741

Jahns, P., Latowski, D., Strzalka, K., 2009. Mechanism and regulation of the violaxanthin cycle: The role of antenna proteins and membrane lipids. Biochim. Biophys. Acta - Bioenerg. 1787, 3–14. https://doi.org/10.1016/J.BBABIO.2008.09.013

Johnson, J.E., Berry, J.A., 2021. The role of Cytochrome b 6f in the control of steady-state photosynthesis: a conceptual and quantitative model. Photosynth. Res. 148, 101–136. https://doi.org/10.1007/s11120-021-00840-4

Johnson, J.E., Field, C.B., Berry, J.A., 2021. The limiting factors and regulatory processes that control the environmental responses of C3, C3–C4 intermediate, and C4 photosynthesis. Oecologia. https://doi.org/10.1007/s00442-021-05062-y

Joiner, J., Yoshida, Y., Vasilkov, A.P., Schaefer, K., Jung, M., Guanter, L., Zhang, Y., Garrity, S., Middleton, E.M., Huemmrich, K.F., Gu, L., Belelli Marchesini, L., 2014. The seasonal cycle of satellite chlorophyll fluorescence observations and its relationship to vegetation phenology and ecosystem atmosphere carbon exchange. Remote Sens. Environ. 152, 375–391. https://doi.org/10.1016/j.rse.2014.06.022

Joiner, J., Yoshida, Y., Vasilkov, A.P., Yoshida, Y., Corp, L.A., Middleton, E.M., 2011. First observations of global and seasonal terrestrial chlorophyll fluorescence from space. Biogeosciences 8, 637–651. https://doi.org/10.5194/bg-8-637-2011

Joiner, J., Yoshida, Y., Zhang, Y., Duveiller, G., Jung, M., Lyapustin, A., Wang, Y., Tucker, C., 2018. Estimation of Terrestrial Global Gross Primary Production (GPP) with Satellite Data-Driven Models and Eddy Covariance Flux Data. Remote Sens. 10, 1346. https://doi.org/10.3390/rs10091346

Jung, M., Schwalm, C., Migliavacca, M., Walther, S., Camps-Valls, G., Koirala, S., Anthoni, P., Besnard, S., Bodesheim, P., Carvalhais, N., Chevallier, F., Gans, F., Goll, D.S., Haverd, V., Köhler, P., Ichii, K., Jain, A.K., Liu, J., Lombardozzi, D., Nabel, J.E.M.S., Nelson, J.A., O'Sullivan, M., Pallandt, M., Papale, D., Peters, W., Pongratz, J., Rödenbeck, C., Sitch, S., Tramontana, G., Walker, A., Weber, U., Reichstein, M., 2020. Scaling carbon fluxes from eddy covariance sites to globe: synthesis and evaluation of the FLUXCOM approach. Biogeosciences 17, 1343–1365. https://doi.org/10.5194/bg-17-1343-2020

Kattge, J., Knorr, W., 2007. Temperature acclimation in a biochemical model of photosynthesis: A reanalysis of data from 36 species. Plant, Cell Environ. 30, 1176–1190. https://doi.org/10.1111/j.1365-3040.2007.01690.x

Knowles, J.F., Burns, S.P., Blanken, P.D., Monson, R.K., 2015. Fluxes of energy, water, and carbon dioxide from mountain ecosystems at Niwot Ridge, Colorado. https://doi.org/10.1080/17550874.2014.904950. https://doi.org/10.1080/17550874.2014.904950

Kobayashi, S., Ota, Y., Harada, Y., Ebita, A., Moriya, M., Onoda, H., Onogi, K., Kamahori, H., Kobayashi, C., Endo, H., Miyaoka, K., Takahashi, K., 2015. The JRA-55 Reanalysis: General Specifications and Basic Characteristics. J. Meteorol. Soc. Japan. Ser. II 93, 5–48. https://doi.org/10.2151/jmsj.2015-001

Köhler, P., Frankenberg, C., Magney, T.S., Guanter, L., Joiner, J., Landgraf, J., 2018. Global Retrievals of Solar-Induced Chlorophyll Fluorescence With TROPOMI: First Results and Intersensor Comparison to OCO-2. Geophys. Res. Lett. 45, 10,456-10,463. https://doi.org/10.1029/2018GL079031

Kohonen, K.M., Dewar, R., Tramontana, G., Mauranen, A., Kolari, P., Kooijmans, L.M.J., Papale, D., Vesala, T., Mammarella, I., 2022. Intercomparison of methods to estimate gross primary production based on CO2 and COS flux measurements. Biogeosciences 19, 4067–4088. https://doi.org/10.5194/BG-19-4067-2022

Koziol, J.A., 2010. Comments on the rank product method for analyzing replicated experiments. FEBS Lett. 584, 941–944. https://doi.org/10.1016/j.febslet.2010.01.031

Kramer, D.M., Johnson, G., Kiirats, O., Edwards, G.E., 2004. New fluorescence parameters for the determination of QA redox state and excitation energy fluxes. Photosynth. Res. 79, 209–218. https://doi.org/10.1023/B:PRES.0000015391.99477.0d

Krinner, G., Viovy, N., de Noblet-Ducoudré, N., Ogée, J., Polcher, J., Friedlingstein, P., Ciais, P., Sitch, S., Prentice, I.C., 2005. A dynamic global vegetation model for studies of the coupled atmosphere-biosphere system. Global Biogeochem. Cycles. https://doi.org/10.1029/2003GB002199

Kumarathunge, D.P., Medlyn, B.E., Drake, J.E., Tjoelker, M.G., Aspinwall, M.J., Battaglia, M., Cano, F.J., Carter, K.R., Cavaleri, M.A., Cernusak, L.A., Chambers, J.Q., Crous, K.Y., De Kauwe, M.G., Dillaway, D.N., Dreyer, E., Ellsworth, D.S., Ghannoum, O., Han, Q., Hikosaka, K., Jensen, A.M., Kelly, J.W.G., Kruger, E.L., Mercado, L.M., Onoda, Y., Reich, P.B., Rogers, A., Slot, M., Smith, N.G., Tarvainen, L., Tissue, D.T., Togashi, H.F., Tribuzy, E.S., Uddling, J., Vårhammar, A., Wallin, G., Warren, J.M., Way, D.A., 2019. Acclimation and adaptation components of the temperature dependence of plant photosynthesis at the global scale. New Phytol. 222, 768–784. https://doi.org/10.1111/nph.15668

Kuppel, S., Chevallier, F., Peylin, P., 2013. Quantifying the model structural error in carbon cycle data assimilation systems. Geosci. Model Dev. 6, 45–55. https://doi.org/10.5194/GMD-6-45-2013

Kuppel, S., Peylin, P., Chevallier, F., Bacour, C., Maignan, F., Richardson, A.D., 2012. Constraining a global ecosystem model with multi-site eddy-covariance data. Biogeosciences 9, 3757–3776. https://doi.org/10.5194/bg-9-3757-2012

Lardy, R., Bellocchi, G., Soussana, J.F., 2011. A new method to determine soil organic carbon equilibrium. Environ. Model. Softw. 26, 1759–1763. https://doi.org/10.1016/j.envsoft.2011.05.016

Lee, J.-E., Berry, J. a., van der Tol, C., Yang, X., Guanter, L., Damm, A., Baker, I., Frankenberg, C., 2015. Simulations of chlorophyll fluorescence incorporated into the Community Land Model version 4. Glob. Chang. Biol. 21, 3469–3477. https://doi.org/10.1111/gcb.12948

Lee, S.C., Christen, A., Black, T.A., Jassal, R.S., Ketler, R., Nesic, Z., 2020. Partitioning of net ecosystem exchange into photosynthesis and respiration using continuous stable isotope measurements in a Pacific Northwest Douglas-fir forest ecosystem. Agric. For. Meteorol. 292–293, 108109. https://doi.org/10.1016/J.AGRFORMET.2020.108109

Lindroth, A., Klemedtsson, L., Grelle, A., Weslien, P., Langvall, O., 2008. Measurement of net ecosystem exchange, productivity and respiration in three spruce forests in Sweden shows unexpectedly large soil carbon losses. Biogeochemistry 89, 43–60. https://doi.org/10.1007/S10533-007-9137-8

Liu, W., Atherton, J., Mõttus, M., Gastellu-Etchegorry, J.P., Malenovský, Z., Raumonen, P., Åkerblom, M., Mäkipää, R., Porcar-Castell, A., 2019. Simulating solar-induced chlorophyll fluorescence in a boreal forest stand reconstructed from terrestrial laser scanning measurements. Remote Sens. Environ. 232, 111274. https://doi.org/10.1016/J.RSE.2019.111274

Liu, Z., Zhao, F., Liu, X., Yu, Q., Wang, Y., Peng, X., Cai, H., Lu, X., 2022. Direct estimation of photosynthetic CO2 assimilation from solar-induced chlorophyll fluorescence (SIF). Remote Sens. Environ. 271, 112893. https://doi.org/10.1016/J.RSE.2022.112893

Luyssaert, S., Inglima, I., Jung, M., Richardson, A.D., Reichstein, M., Papale, D., Piao, S.L., Schulze, E.D., Wingate, L., Matteucci, G., Aragao, L., Aubinet, M., Beer, C., Bernhofer, C., Black, K.G., Bonal, D., Bonnefond, J.M., Chambers, J., Ciais, P., Cook, B., Davis, K.J., Dolman, A.J., Gielen, B., Goulden, M., Grace, J., Granier, A., Grelle, A., Griffis, T., Grünwald, T., Guidolotti, G., Hanson, P.J., Harding, R., Hollinger, D.Y., Hutyra, L.R., Kolari, P., Kruijt, B., Kutsch, W., Lagergren, F., Laurila, T., Law, B.E., Le Maire, G., Lindroth, A., Loustau, D., Malhi, Y., Mateus, J., Migliavacca, M., Misson, L., Montagnani, L., Moncrieff, J., Moors, E., Munger, J.W., Nikinmaa, E., Ollinger, S. V., Pita, G., Rebmann, C., Roupsard, O., Saigusa, N., Sanz, M.J., Seufert, G., Sierra, C., Smith, M.L., Tang, J., Valentini, R., Vesala, T., Janssens, I.A., 2007. CO2 balance of boreal, temperate, and tropical forests derived from a global database. Glob. Chang. Biol. 13, 2509–2537. https://doi.org/10.1111/J.1365-2486.2007.01439.X

MacBean, N., Bacour, C., Raoult, N., Bastrikov, V., Koffi, E.N., Kuppel, S., Maignan, F., Ottlé, C., Peaucelle, M., Santaren, D., Peylin, P., 2022. Quantifying and Reducing Uncertainty in Global Carbon Cycle Predictions: Lessons and Perspectives From 15 Years of Data Assimilation Studies With the ORCHIDEE Terrestrial Biosphere Model. Global Biogeochem. Cycles. https://doi.org/10.1029/2021GB007177

MacBean, N., Maignan, F., Bacour, C., Lewis, P., Peylin, P., Guanter, L., Köhler, P., Gómez-Dans, J., Disney, M., 2018. Strong constraint on modelled global carbon uptake using solar-induced chlorophyll fluorescence data. Sci. Rep. 8, 1–12. https://doi.org/10.1038/s41598-018-20024-w

MacBean, N., Peylin, P., Chevallier, F., Scholze, M., Schürmann, G., 2016. Consistent assimilation of multiple data streams in a carbon cycle data assimilation system. Geosci. Model Dev. 9, 3569–3588. https://doi.org/10.5194/GMD-9-3569-2016

Magney, T.S., Barnes, M.L., Yang, X., 2020. On the Covariation of Chlorophyll Fluorescence and Photosynthesis Across Scales. Geophys. Res. Lett. 47, e2020GL091098. https://doi.org/10.1029/2020GL091098

Magney, T.S., Bowling, D.R., Logan, B.A., Grossmann, K., Stutz, J., Blanken, P.D., Burns, S.P., Cheng, R., Garcia, M.A., Köhler, P., Lopez, S., Parazoo, N.C., Raczka, B., Schimel, D., Frankenberg, C., 2019. Mechanistic evidence for tracking the seasonality of photosynthesis with solar-induced fluorescence. Proc. Natl. Acad. Sci. U. S. A. 116, 11640–11645. https://doi.org/10.1073/pnas.1900278116

Mäkelä, A., Hari, P., Berninger, F., Hänninen, H., Nikinmaa, E., 2004. Acclimation of photosynthetic capacity in Scots pine to the annual cycle of temperature. Tree Physiol. 24, 369–376. https://doi.org/10.1093/treephys/24.4.369

Medlyn, B.E., Dreyer, E., Ellsworth, D., Forstreuter, M., Harley, P.C., Kirschbaum, M.U.F., Le Roux, X., Montpied, P., Strassemeyer, J., Walcroft, A., Wang, K., Loustau, D., 2002. Temperature response of parameters of a biochemically based model of photosynthesis. II. A review of experimental data. Plant, Cell Environ. 25, 1167–1179. https://doi.org/10.1046/j.1365-3040.2002.00891.x

Medlyn, B.E., Robinson, A.P., Clement, R., McMurtrie, R.E., 2005. On the validation of models of forest CO2 exchange using eddy covariance data: some perils and pitfalls. Tree Physiol. 25, 839–857. https://doi.org/10.1093/TREEPHYS/25.7.839

Migliavacca, M., Perez-Priego, O., Rossini, M., El-Madany, T.S., Moreno, G., van der Tol, C., Rascher, U., Berninger, A., Bessenbacher, V., Burkart, A., Carrara, A., Fava, F., Guan, J.H., Hammer, T.W., Henkel, K., Juarez-Alcalde, E., Julitta, T., Kolle, O., Martín, M.P., Musavi, T., Pacheco-Labrador, J., Pérez-Burgueño, A., Wutzler, T., Zaehle, S., Reichstein, M., 2017. Plant functional traits and canopy structure control the relationship between photosynthetic CO2 uptake and far-red sun-induced fluorescence in a Mediterranean grassland under different nutrient availability. New Phytol. 214, 1078–1091. https://doi.org/10.1111/NPH.14437

Morris, M.D., 1991. Factorial sampling plans for preliminary computational experiments. Technometrics 33, 161–174. https://doi.org/10.1080/00401706.1991.10484804

Newville, M., Stensitzki, T., Allen, D.B., Rawlik, M., Ingargiola, A., Nelson, A., Newville, M., Stensitzki, T., Allen, D.B., Rawlik, M., Ingargiola, A., Nelson, A., 2016. Lmfit: Non-Linear Least-Square Minimization and Curve-Fitting for Python. ascl ascl:1606.014.

Niinemets, Ü., 2010. A review of light interception in plant stands from leaf to canopy in different plant functional types and in species with varying shade tolerance. Ecol. Res. 25, 693–714. https://doi.org/10.1007/S11284-010-0712-4/TABLES/1

Nilson, T., 1999. Inversion of gap frequency data in forest stands. Agric. For. Meteorol. 98–99, 437–448. https://doi.org/10.1016/S0168-1923(99)00114-8

Norton, A.J., Rayner, P.J., Koffi, E.N., Scholze, M., Silver, J.D., Wang, Y.-P., 2019. Estimating global gross primary productivity using chlorophyll fluorescence and a data assimilation system with the BETHY-SCOPE model. Biogeosciences 16, 3069–3093. https://doi.org/10.5194/bg-16-3069-2019

Öquist, G., Huner, N.P.A., 2003. Photosynthesis of Overwintering Evergreen Plants. https://doi.org/10.1146/annurev.arplant.54.072402.115741 54, 329–355. https://doi.org/10.1146/ANNUREV.ARPLANT.54.072402.115741

Parazoo, N.C., Bowman, K., Fisher, J.B., Frankenberg, C., Jones, D.B.A., Cescatti, A., Pérez-Priego, Ó., Wohlfahrt, G., Montagnani, L., 2014. Terrestrial gross primary production inferred from satellite fluorescence and vegetation models. Glob. Chang. Biol. 20, 3103–3121. https://doi.org/10.1111/gcb.12652

Parazoo, N.C., Frankenberg, C., Köhler, P., Joiner, J., Yoshida, Y., Magney, T., Sun, Y., Yadav, V., 2019. Towards a Harmonized Long-Term Spaceborne Record of Far-Red Solar-Induced Fluorescence. J. Geophys. Res. Biogeosciences 124, 2518–2539. https://doi.org/10.1029/2019jg005289

Pastorello, G., Trotta, C., Canfora, E., Chu, H., Christianson, D., Cheah, Y.W., Poindexter, C., Chen, J., Elbashandy, A., Humphrey, M., Isaac, P., Polidori, D., Ribeca, A., van Ingen, C., Zhang, L., Amiro, B., Ammann, C., Arain, M.A., Ardö, J., Arkebauer, T., Arndt, S.K., Arriga, N., Aubinet, M., Aurela, M., Baldocchi, D., Barr, A., Beamesderfer, E., Marchesini, L.B., Bergeron, O., Beringer, J., Bernhofer, C., Berveiller, D., Billesbach, D., Black, T.A., Blanken, P.D., Bohrer, G., Boike, J., Bolstad, P. V., Bonal, D., Bonnefond, J.M., Bowling, D.R., Bracho, R., Brodeur, J., Brümmer, C., Buchmann, N., Burban, B., Burns, S.P., Buysse, P., Cale, P., Cavagna, M., Cellier, P., Chen, S., Chini, I., Christensen, T.R., Cleverly, J., Collalti, A., Consalvo, C., Cook, B.D., Cook, D., Coursolle, C., Cremonese, E., Curtis, P.S., D'Andrea, E., da Rocha, H., Dai, X., Davis, K.J., De Cinti, B., de Grandcourt, A., De Ligne, A., De Oliveira, R.C., Delpierre, N., Desai, A.R., Di Bella, C.M., di Tommasi, P., Dolman, H., Domingo, F., Dong, G., Dore, S., Duce, P., Dufrêne, E., Dunn, A., Dušek, J., Eamus, D., Eichelmann, U., ElKhidir, H.A.M., Eugster, W., Ewenz, C.M., Ewers, B., Famulari, D., Fares, S., Feigenwinter, I., Feitz, A., Fensholt, R., Filippa, G., Fischer, M., Frank, J., Galvagno, M., Gharun, M., Gianelle, D., Gielen, B., Gioli, B., Gitelson, A., Goded, I., Goeckede, M., Goldstein, A.H., Gough, C.M., Goulden, M.L., Graf, A., Griebel, A., Gruening, C., Grünwald, T., Hammerle, A., Han, S., Han, X., Hansen, B.U., Hanson, C., Hatakka, J., He, Y., Hehn, M., Heinesch, B., Hinko-Najera, N., Hörtnagl, L., Hutley, L., Ibrom, A., Ikawa, H., Jackowicz-Korczynski, M., Janouš, D., Jans, W., Jassal, R., Jiang, S., Kato, T., Khomik, M., Klatt, J., Knohl, A., Knox, S., Kobayashi, H., Koerber, G., Kolle, O., Kosugi, Y., Kotani, A., Kowalski, A., Kruijt, B., Kurbatova, J., Kutsch, W.L., Kwon, H., Launiainen, S., Laurila, T., Law, B., Leuning, R., Li, Yingnian, Liddell, M., Limousin, J.M., Lion, M., Liska, A.J., Lohila, A., López-Ballesteros, A., López-Blanco, E., Loubet, B., Loustau, D., Lucas-Moffat, A., Lüers, J., Ma, S., Macfarlane, C., Magliulo, V., Maier, R., Mammarella, I., Manca, G., Marcolla, B., Margolis, H.A., Marras, S., Massman, W., Mastepanov, M., Matamala, R., Matthes, J.H., Mazzenga, F., McCaughey, H., McHugh, I., McMillan, A.M.S., Merbold, L., Meyer, W., Meyers, T., Miller, S.D., Minerbi, S., Moderow, U., Monson, R.K., Montagnani, L., Moore, C.E., Moors, E., Moreaux, V., Moureaux, C., Munger, J.W., Nakai, T., Neirynck, J., Nesic, Z., Nicolini, G., Noormets, A., Northwood, M., Nosetto, M., Nouvellon, Y., Novick, K., Oechel, W., Olesen, J.E., Ourcival, J.M., Papuga, S.A., Parmentier, F.J., Paul-Limoges, E., Pavelka, M., Peichl, M., Pendall, E., Phillips, R.P., Pilegaard, K., Pirk, N., Posse, G., Powell, T., Prasse, H., Prober, S.M., Rambal, S., Rannik, Ü., Raz-Yaseef, N., Reed, D., de Dios, V.R., Restrepo-Coupe, N., Reverter, B.R., Roland, M., Sabbatini, S., Sachs, T., Saleska, S.R., Sánchez-Cañete, E.P., Sanchez-Mejia, Z.M., Schmid, H.P., Schmidt, M., Schneider, K., Schrader, F., Schroder, I., Scott, R.L., Sedlák, P., Serrano-Ortíz, P., Shao, C., Shi, P., Shironya, I., Siebicke, L., Šigut, L., Silberstein, R., Sirca, C., Spano, D., Steinbrecher, R., Stevens, R.M., Sturtevant, C., Suyker, A., Tagesson, T., Takanashi, S., Tang, Y., Tapper, N., Thom, J., Tiedemann, F., Tomassucci, M., Tuovinen, J.P., Urbanski, S., Valentini, R., van der Molen, M., van Gorsel, E., van Huissteden, K., Varlagin, A., Verfaillie, J., Vesala, T., Vincke, C., Vitale, D., Vygodskaya, N., Walker, J.P., Walter-Shea, E., Wang, H., Weber, R., Westermann, S., Wille, C., Wofsy, S., Wohlfahrt, G., Wolf, S., Woodgate, W., Li, Yuelin, Zampedri, R., Zhang, J., Zhou, G., Zona, D., Agarwal, D., Biraud, S., Torn, M., Papale, D., 2020. The FLUXNET2015 dataset and the ONEFlux processing pipeline for eddy covariance data. Sci. data 7, 225. https://doi.org/10.1038/s41597-020-0534-3

Peaucelle, M., Ciais, P., Maignan, F., Nicolas, M., Cecchini, S., Viovy, N., 2019. Representing explicit budburst and senescence processes for evergreen conifers in global models. Agric. For. Meteorol. 266–267, 97–108. https://doi.org/10.1016/j.agrformet.2018.12.008

Pedrós, R., Goulas, Y., Jacquemoud, S., Louis, J., Moya, I., 2010. FluorMODleaf: A new leaf fluorescence emission model based on the PROSPECT model. Remote Sens. Environ. 114, 155–167. https://doi.org/10.1016/j.rse.2009.08.019

Pienitz, R., Smol, J.P., Lean, D.R.S., 1997. Physical and chemical limnology of 59 lakes located between the southern Yukon and the Tuktoyaktuk Peninsula, Northwest Territories (Canada). Can. J. Fish. Aquat. Sci. 54, 330–346. https://doi.org/10.1139/F96-274/ASSET/F96-274.FP.PNG_V03

Pierrat, Z., Magney, T., Parazoo, N.C., Grossmann, K., Bowling, D.R., Seibt, U., Johnson, B., Helgason, W., Barr, A., Bortnik, J., Norton, A., Maguire, A., Frankenberg, C., Stutz, J., 2022. Diurnal and Seasonal Dynamics of Solar-Induced Chlorophyll Fluorescence, Vegetation Indices, and Gross Primary Productivity in the

Boreal Forest. J. Geophys. Res. Biogeosciences 127, e2021JG006588. https://doi.org/10.1029/2021JG006588

Pisek, J., Adamson, K., 2020. Dataset of leaf inclination angles for 71 different Eucalyptus species. Data Br. 33, 106391. https://doi.org/10.1016/J.DIB.2020.106391

Pisek, J., Sonnentag, O., Richardson, A.D., Mõttus, M., 2013. Is the spherical leaf inclination angle distribution a valid assumption for temperate and boreal broadleaf tree species? Agric. For. Meteorol. 169, 186–194. https://doi.org/10.1016/J.AGRFORMET.2012.10.011

Porcar-Castell, A., 2011. A high-resolution portrait of the annual dynamics of photochemical and non-photochemical quenching in needles of Pinus sylvestris. Physiol. Plant. 143, 139–153. https://doi.org/10.1111/j.1399-3054.2011.01488.x

Porcar-Castell, A., Mac Arthur, A., Rossini, M., Eklundh, L., Pacheco-Labrador, J., Anderson, K., Balzarolo, M., Martín, M.P., Jin, H., Tomelleri, E., Cerasoli, S., Sakowska, K., Hueni, A., Julitta, T., Nichol, C.J., Vescovo, L., 2015. EUROSPEC: At the interface between remote-sensing and ecosystem CO2 flux measurements in Europe. Biogeosciences 12, 6103–6124. https://doi.org/10.5194/bg-12-6103-2015

Porcar-Castell, A., Malenovský, Z., Magney, T., Van Wittenberghe, S., Fernández-Marín, B., Maignan, F., Zhang, Y., Maseyk, K., Atherton, J., Albert, L.P., Robson, T.M., Zhao, F., Garcia-Plazaola, J.I., Ensminger, I., Rajewicz, P.A., Grebe, S., Tikkanen, M., Kellner, J.R., Ihalainen, J.A., Rascher, U., Logan, B., 2021. Chlorophyll a fluorescence illuminates a path connecting plant molecular biology to Earth-system science. Nat. Plants. https://doi.org/10.1038/s41477-021-00980-4

Porcar-Castell, A., Tyystjärvi, E., Atherton, J., Van Der Tol, C., Flexas, J., Pfündel, E.E., Moreno, J., Frankenberg, C., Berry, J.A., 2014. Linking chlorophyll a fluorescence to photosynthesis for remote sensing applications: Mechanisms and challenges. J. Exp. Bot. 65, 4065–4095. https://doi.org/10.1093/jxb/eru191

Poulter, B., MacBean, N., Hartley, A., Khlystova, I., Arino, O., Betts, R., Bontemps, S., Boettcher, M., Brockmann, C., Defourny, P., Hagemann, S., Herold, M., Kirches, G., Lamarche, C., Lederer, D., Ottlé, C., Peters, M., Peylin, P., 2015. Plant functional type classification for earth system models: Results from the European Space Agency's Land Cover Climate Change Initiative. Geosci. Model Dev. 8, 2315–2328. https://doi.org/10.5194/gmd-8-2315-2015

Raczka, B., Porcar-Castell, A., Magney, T., Lee, J.E., Köhler, P., Frankenberg, C., Grossmann, K., Logan, B.A., Stutz, J., Blanken, P.D., Burns, S.P., Duarte, H., Yang, X., Lin, J.C., Bowling, D.R., 2019. Sustained Nonphotochemical Quenching Shapes the Seasonal Pattern of Solar-Induced Fluorescence at a High-Elevation Evergreen Forest. J. Geophys. Res. Biogeosciences 124, 2005–2020. https://doi.org/10.1029/2018JG004883

Raj, R., Alexander Samuel Hamm, N., Van Der Tol, C., Stein, A., 2016. Uncertainty analysis of gross primary production partitioned from net ecosystem exchange measurements. Biogeosciences 13, 1409–1422. https://doi.org/10.5194/BG-13-1409-2016

Rajewicz, P.A., Zhang, C., Atherton, J., Van Wittenberghe, S., Riikonen, A., Magney, T., Fernandez-Marin, B., Plazaola, J.I.G., Porcar-Castell, A., 2023. The photosynthetic response of spectral chlorophyll fluorescence differs across species and light environments in a boreal forest ecosystem. Agric. For. Meteorol. 334, 109434. https://doi.org/10.1016/J.AGRFORMET.2023.109434

Raoult, N.M., Jupp, T.E., Cox, P.M., Luke, C.M., 2016. Land-surface parameter optimisation using data assimilation techniques: the adJULES system V1.0. Geosci. Model Dev. 9, 2833–2852. https://doi.org/10.5194/gmd-9-2833-2016

Reich, P.B., Rich, R.L., Lu, X., Wang, Y.P., Oleksyn, J., 2014. Biogeographic variation in evergreen conifer needle longevity and impacts on boreal forest carbon cycle projections. Proc. Natl. Acad. Sci. U. S. A. 111, 13703–13708. https://doi.org/10.1073/PNAS.1216054110

Reichstein, M., Falge, E., Baldocchi, D., Papale, D., Aubinet, M., Berbigier, P., Bernhofer, C., Buchmann, N., Gilmanov, T., Granier, A., Grünwald, T., Havránková, K., Ilvesniemi, H., Janous, D., Knohl, A., Laurila, T., Lohila, A., Loustau, D., Matteucci, G., Meyers, T., Miglietta, F., Ourcival, J.M., Pumpanen, J., Rambal, S., Rotenberg, E., Sanz, M., Tenhunen, J., Seufert, G., Vaccari, F., Vesala, T., Yakir, D., Valentini, R., 2005. On the separation of net ecosystem exchange into assimilation and ecosystem respiration: Review and improved algorithm. Glob. Chang. Biol. 11, 1424–1439. https://doi.org/10.1111/j.1365-2486.2005.001002.x

Richardson, A.D., Williams, M., Hollinger, D.Y., Moore, D.J.P., Dail, D.B., Davidson, E.A., Scott, N.A., Evans, R.S., Hughes, H., Lee, J.T., Rodrigues, C., Savage, K., 2010. Estimating parameters of a forest ecosystem C model with measurements of stocks and fluxes as joint constraints. Oecologia 164, 25–40. https://doi.org/10.1007/s00442-010-1628-y

Ruban, A. V., Johnson, M.P., 2009. Dynamics of higher plant photosystem cross-section associated with state transitions. Photosynth. Res. 99, 173–183. https://doi.org/10.1007/s11120-008-9387-x

Santaren, D., Peylin, P., Bacour, C., Ciais, P., Longdoz, B., 2014. Ecosystem model optimization using in situ flux observations: Benefit of Monte Carlo versus variational schemes and analyses of the year-to-year model performances. Biogeosciences 11, 7137–7158. https://doi.org/10.5194/BG-11-7137-2014

Schulze, E.D., Lloyd, J., Kelliher, F.M., Wirth, C., Rebmann, C., Luhker, B., Mund, M., Knohl, A., Milyukova, I.M., Schulze, W., Ziegler, W., Varlagin, A.B., Sogachev, A.F., Valentini, R., Dore, S., Grigoriev, S., Kolle, O., Panfyorov, M.I., Tchebakova, N., Vygodskaya, N.N., 1999. Productivity of forests in the Eurosiberian boreal region and their potential to act as a carbon sink –- a synthesis. Glob. Chang. Biol. 5, 703–722. https://doi.org/10.1046/J.1365-2486.1999.00266.X

Seidl, R., Thom, D., Kautz, M., Martin-Benito, D., Peltoniemi, M., Vacchiano, G., Wild, J., Ascoli, D., Petr, M., Honkaniemi, J., Lexer, M.J., Trotsiuk, V., Mairota, P., Svoboda, M., Fabrika, M., Nagel, T.A., Reyer, C.P.O., 2017. Forest disturbances under climate change. Nat. Clim. Chang. 2017 76 7, 395–402. https://doi.org/10.1038/NCLIMATE3303

Seiler, C., Melton, J.R., Arora, V.K., Sitch, S., Friedlingstein, P., Anthoni, P., Goll, D., Jain, A.K., Joetzjer, E., Lienert, S., Lombardozzi, D., Luyssaert, S., Nabel, J.E.M.S., Tian, H., Vuichard, N., Walker, A.P., Yuan, W., Zaehle, S., 2022. Are Terrestrial Biosphere Models Fit for Simulating the Global Land Carbon Sink? J. Adv. Model. Earth Syst. 14. https://doi.org/10.1029/2021MS002946

Serôdio, J., Lavaud, J., 2011. A model for describing the light response of the nonphotochemical quenching of chlorophyll fluorescence. Photosynth. Res. 108, 61–76. https://doi.org/10.1007/S11120-011-9654-0/FIGURES/6

Seyednasrollah, B., Bowling, D.R., Cheng, R., Logan, B.A., Magney, T.S., Frankenberg, C., Yang, J.C., Young, A.M., Hufkens, K., Arain, M.A., Black, T.A., Blanken, P.D., Bracho, R., Jassal, R., Hollinger, D.Y., Law, B.E., Nesic, Z., Richardson, A.D., 2021. Seasonal variation in the canopy color of temperate evergreen conifer forests. New Phytol. 229, 2586–2600. https://doi.org/10.1111/NPH.17046

Sitch, S., Friedlingstein, P., Gruber, N., Jones, S.D., Murray-Tortarolo, G., Ahlström, A., Doney, S.C., Graven, H., Heinze, C., Huntingford, C., Levis, S., Levy, P.E., Lomas, M., Poulter, B., Viovy, N., Zaehle, S., Zeng, N., Arneth, A., Bonan, G., Bopp, L., Canadell, J.G., Chevallier, F., Ciais, P., Ellis, R., Gloor, M., Peylin, P., Piao, S.L., Le Quéré, C., Smith, B., Zhu, Z., Myneni, R., 2015. Recent trends and drivers of regional sources and sinks of carbon dioxide. Biogeosciences 12, 653–679. https://doi.org/10.5194/bg-12-653-2015

Slevin, D., Tett, S.F.B., Exbrayat, J.F., Bloom, A.A., Williams, M., 2017. Global evaluation of gross primary productivity in the JULES land surface model v3.4.1. Geosci. Model Dev. 10, 2651–2670. https://doi.org/10.5194/GMD-10-2651-2017

Song, Y., Wang, L., Wang, J., 2021. Improved understanding of the spatially-heterogeneous relationship between satellite solar-induced chlorophyll fluorescence and ecosystem productivity. Ecol. Indic. 129, 107949. https://doi.org/10.1016/J.ECOLIND.2021.107949

Springer, K.R., Wang, R., Gamon, J.A., 2017. Parallel Seasonal Patterns of Photosynthesis, Fluorescence, and Reflectance Indices in Boreal Trees. Remote Sens. 2017, Vol. 9, Page 691 9, 691. https://doi.org/10.3390/RS9070691

Stocker, B.D., Wang, H., Smith, N.G., Harrison, S.P., Keenan, T.F., Sandoval, D., Davis, T., Prentice, I.C., 2020. P-model v1.0: An optimality-based light use efficiency model for simulating ecosystem gross primary production. Geosci. Model Dev. 13, 1545–1581. https://doi.org/10.5194/GMD-13-1545-2020

Sun, Y., Frankenberg, C., Jung, M., Joiner, J., Guanter, L., Köhler, P., Magney, T., 2018. Overview of Solar-Induced chlorophyll Fluorescence (SIF) from the Orbiting Carbon Observatory-2: Retrieval, cross-mission comparison, and global monitoring for GPP. Remote Sens. Environ. 209, 808–823. https://doi.org/10.1016/j.rse.2018.02.016

Sun, Y., Gu, L., Wen, J., Tol, C. van der, Porcar-Castell, A., Joiner, J., Chang, C.Y., Magney, T., Wang, L., Hu, L., Rascher, U., Zarco-Tejada, P., Barrett, C.B., Lai, J., Han, J., Luo, Z., 2023. From remotely sensed solar-induced chlorophyll fluorescence to ecosystem structure, function, and service: Part I—Harnessing theory. Glob. Chang. Biol. 29, 2926–2952. https://doi.org/10.1111/GCB.16634

Suni, T., Rinne, J., Reissell, A., Altimir, N., Keronen, P., Rannik, Ü., Dal Maso, M., Kulmala, M., Vesala, T., 2003. Long-term measurements of surface fluxes above a Scots pine forest in Hyytiälä, southern Finland, 1996–2001. Boreal Env. Res 8, 287–301.

Tarantola, A., 1987. Inverse Problem Theory and Methods for Model Parameter Estimation, Inverse Problem Theory and Methods for Model Parameter Estimation. Elsevier, Amsterdam, The Netherlands.

Thum, T., Aalto, T., Laurila, T., Aurela, M., Kolari, P., Hari, P., 2007. Parametrization of two photosynthesis models at the canopy scale in a northern boreal Scots pine forest. Tellus, Ser. B Chem. Phys. Meteorol. 59, 874–890. https://doi.org/10.1111/J.1600-0889.2007.00305.X

Tramontana, G., Migliavacca, M., Jung, M., Reichstein, M., Keenan, T.F., Camps-Valls, G., Ogee, J., Verrelst, J., Papale, D., 2020. Partitioning net carbon dioxide fluxes into photosynthesis and respiration using neural networks. Glob. Chang. Biol. 26, 5235–5253. https://doi.org/10.1111/GCB.15203

Utsugi, H., Araki, M., Kawasaki, T., Ishizuka, M., 2006. Vertical distributions of leaf area and inclination angle, and their relationship in a 46-year-old Chamaecyparis obtusa stand. For. Ecol. Manage. 225, 104–112. https://doi.org/10.1016/J.FORECO.2005.12.028

van der Tol, C., Berry, J.A., Campbell, P.K.E.E., Rascher, U., 2014. Models of fluorescence and photosynthesis for interpreting measurements of solar-induced chlorophyll fluorescence. J. Geophys. Res. G Biogeosciences 119, 2312–2327. https://doi.org/10.1002/2014JG002713

van der Tol, C., Verhoef, W., Timmermans, J., Verhoef, a., Su, Z., 2009. An integrated model of soil-canopy spectral radiances, photosynthesis, fluorescence, temperature and energy balance. Biogeosciences 6, 3109–3129. https://doi.org/10.5194/bg-6-3109-2009

Van Rossum, G., Drake, F.L., 2009. Python 3 Reference Manual, CreateSpace Scotts Valley, CA.

Verhoeven, A., 2014. Sustained energy dissipation in winter evergreens. New Phytol. 201, 57–65. https://doi.org/10.1111/nph.12466

Verrelst, J., Rivera, J.P., van der Tol, C., Magnani, F., Mohammed, G., Moreno, J., 2015. Global sensitivity analysis of the SCOPE model: What drives simulated canopy-leaving sun-induced fluorescence? Remote Sens. Environ. 166, 8–21. https://doi.org/10.1016/j.rse.2015.06.002

Vuichard, N., Messina, P., Luyssaert, S., Guenet, B., Zaehle, S., Ghattas, J., Bastrikov, V., Peylin, P., 2019. Accounting for carbon and nitrogen interactions in the global terrestrial ecosystem model ORCHIDEE (trunk version, rev 4999): multi-scale evaluation of gross primary production. Geosci. Model Dev. 12, 4751–4779. https://doi.org/10.5194/gmd-12-4751-2019

Walther, S., Voigt, M., Thum, T., Gonsamo, A., Zhang, Y., K??hler, P., Jung, M., Varlagin, A., Guanter, L., Köhler, P., Jung, M., Varlagin, A., Guanter, L., 2016. Satellite chlorophyll fluorescence measurements reveal large-scale decoupling of photosynthesis and greenness dynamics in boreal evergreen forests. Glob. Chang. Biol. 22, 2979–2996. https://doi.org/10.1111/gcb.13200

Wang, X., Chen, J.M., Ju, W., 2020. Photochemical reflectance index (PRI) can be used to improve the relationship between gross primary productivity (GPP) and sun-induced chlorophyll fluorescence (SIF). Remote Sens. Environ. 246, 111888. https://doi.org/10.1016/J.RSE.2020.111888

Wang, J., Jiang, F., Wang, H., Qiu, B., Wu, M., He, W., Ju, W., Zhang, Y., Chen, J.M., Zhou, Y., 2021. Constraining global terrestrial gross primary productivity in a global carbon assimilation system with OCO-2 chlorophyll fluorescence data. Agric. For. Meteorol. 304–305, 108424. https://doi.org/10.1016/j.agrformet.2021.108424

Warm Winter 2020 Team, & ICOS Ecosystem Thematic Centre, 2022. Warm Winter 2020 ecosystem eddy covariance flux product for 73 stations in FLUXNET-Archive format—release 2022-1 (Version 1.0), ICOS Carbon Portal. https://doi.org/10.18160/2G60-ZHAK

Williams, M., Richardson, A.D., Reichstein, M., Stoy, P.C., Peylin, P., Verbeeck, H., Carvalhais, N., Jung, M., Hollinger, D.Y., Kattge, J., Leuning, R., Luo, Y., Tomelleri, E., Trudinger, C.M., Wang, Y.P., 2009. Improving land surface models with FLUXNET data. Biogeosciences 6, 1341–1359. https://doi.org/10.5194/BG-6-1341-2009

Wong, C.Y.S., Gamon, J.A., 2015. The photochemical reflectance index provides an optical indicator of spring photosynthetic activation in evergreen conifers. New Phytol. 206, 196–208. https://doi.org/10.1111/NPH.13251

Yang, P., van der Tol, C., Campbell, P.K.E., Middleton, E.M., 2020. Fluorescence Correction Vegetation Index (FCVI): A physically based reflectance index to separate physiological and non-physiological information in far-red sun-induced chlorophyll fluorescence. Remote Sens. Environ. 240, 111676. https://doi.org/10.1016/j.rse.2020.111676

Yin, X., Struik, P.C., 2009. C3 and C4 photosynthesis models: An overview from the perspective of crop modelling. NJAS - Wageningen J. Life Sci. 57, 27–38. https://doi.org/10.1016/j.njas.2009.07.001

Zaks, J., Amarnath, K., Kramer, D.M., Niyogi, K.K., Fleming, G.R., 2012. A kinetic model of rapidly reversible nonphotochemical quenching. Proc. Natl. Acad. Sci. 109, 15757–15762. https://doi.org/10.1073/pnas.1211017109

Zeng, Y., Badgley, G., Chen, M., Li, J., Anderegg, L.D.L., Kornfeld, A., Liu, Q., Xu, B., Yang, B., Yan, K., Berry, J.A., 2020. A radiative transfer model for solar induced fluorescence using spectral invariants theory. Remote Sens. Environ. 240, 111678. https://doi.org/10.1016/j.rse.2020.111678

Zeng, J., Matsunaga, T., Tan, Z.H., Saigusa, N., Shirai, T., Tang, Y., Peng, S., Fukuda, Y., 2020. Global terrestrial carbon fluxes of 1999–2019 estimated by upscaling eddy covariance data with a random forest. Sci. Data 7, 1–11. https://doi.org/10.1038/s41597-020-00653-5

Zhang, Y., Bastos, A., Maignan, F., Goll, D., Boucher, O., Li, L., Cescatti, A., Vuichard, N., Chen, X., Ammann, C., Arain, A., Black, T.A., Chojnicki, B., Kato, T., Mammarella, I., Montagnani, L., Roupsard, O., Sanz, M., Siebicke, L., Urbaniak, M., Vaccari, F.P., Wohlfahrt, G., Woodgate, W., Ciais, P., 2020. Modeling the impacts of diffuse light fraction on photosynthesis in ORCHIDEE (v5453) land surface model. Geosci. Model Dev. Discuss. 1–35. https://doi.org/10.5194/gmd-2020-96

Zheng, B., Ciais, P., Chevallier, F., Yang, H., Canadell, J.G., Chen, Y., van der Velde, I.R., Aben, I., Chuvieco, E., Davis, S.J., Deeter, M., Hong, C., Kong, Y., Li, Haiyan, Li, Hui, Lin, X., He, K., Zhang, Q., 2023. Record-high CO2 emissions from boreal fires in 2021. Science (80-.). 379, 912–917. https://doi.org/10.1126/SCIENCE.ADE0805/SUPPL_FILE/SCIENCE.ADE0805_SM.PDF

Zhu, X., Skidmore, A.K., Wang, T., Liu, J., Darvishzadeh, R., Shi, Y., Premier, J., Heurich, M., 2018. Improving leaf area index (LAI) estimation by correcting for clumping and woody effects using terrestrial laser scanning. Agric. For. Meteorol. 263, 276–286. https://doi.org/10.1016/J.AGRFORMET.2018.08.026

Zobler, L., 1986. A World Soil File for Global Climate Modelling. NASA Technical Memorandum 87802, NASA Goddard Institute for Space Studies, New York, USA

Zuromski, L.M., Bowling, D.R., Köhler, P., Frankenberg, C., Goulden, M.L., Blanken, P.D., Lin, J.C., 2018. Solar-Induced Fluorescence Detects Interannual Variation in Gross Primary Production of Coniferous Forests in the Western United States. Geophys. Res. Lett. 45, 7184–7193. https://doi.org/10.1029/2018GL077906

Supplementary Material

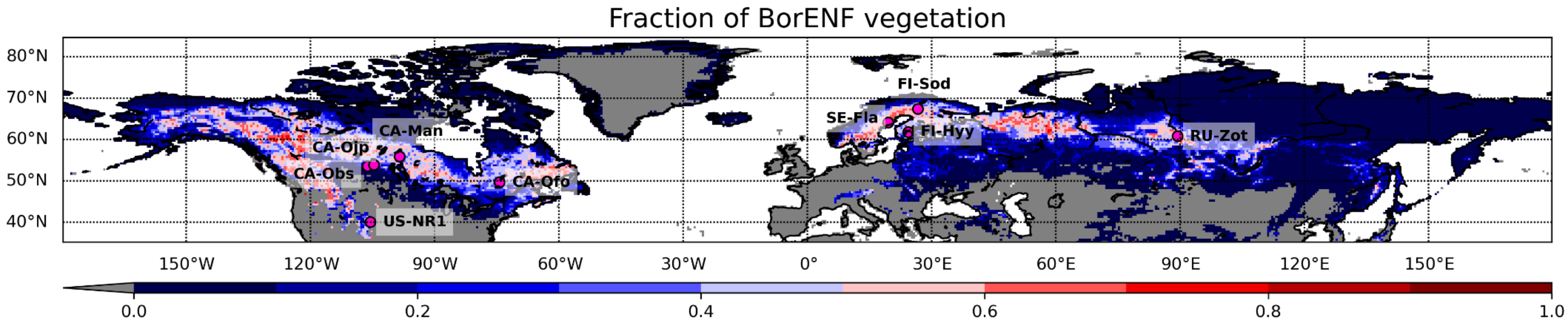

Figure S1: Mean distribution of the BorENF PFT over the period 2001-2015 (data source: https://orchidas.lsce.ipsl.fr/dev/lccci/orchidee_pfts.php, last access: 12 July 2023). Grid cells (0.5°) with a null fraction are shown in grey. The location of the selected FLUXNET sites is represented with magenta circles.

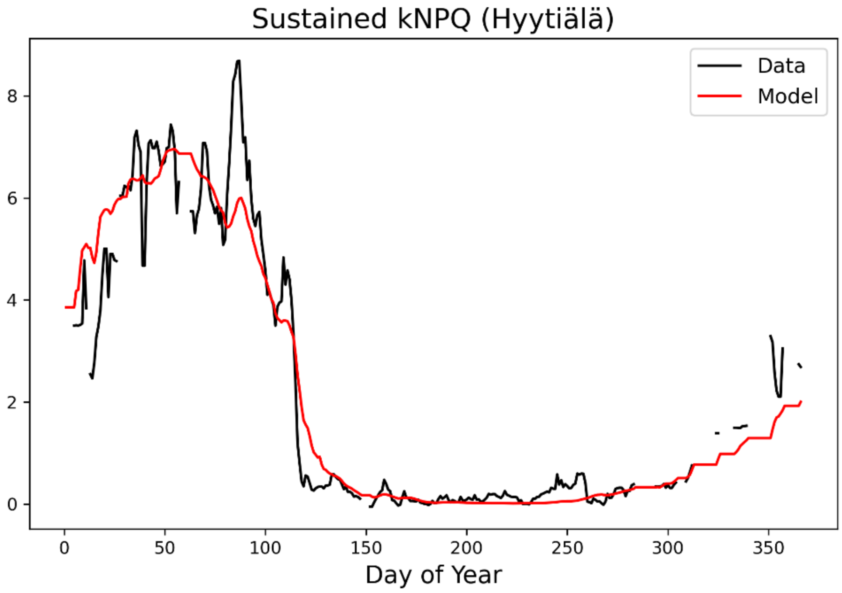

Figure S2: Seasonal cycles of the sustained NPQ relative rate constant k_S of an upper canopy layer at the Hyytiälä site. The PAM daily data for the period from August 15, 2008 to August 14, 2009 are shown in black, the 2009 data (January-August) preceding those of 2008 (August-December) to show a complete growing season from January to December. The fitted k_S model is represented by the red line.

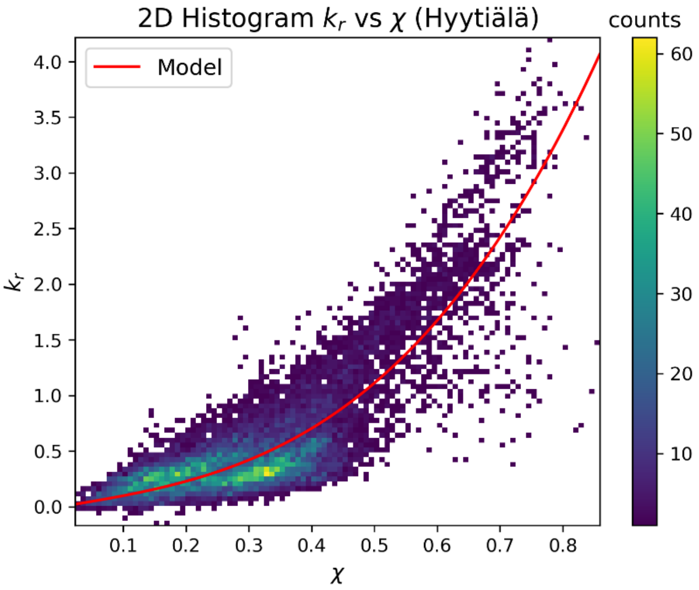

Figure S3: Bidimensional histogram of the reversible NPQ relative rate constant k_R against the relative light saturation of photosynthesis χ, for an upper canopy layer at the Hyytiälä site, using half-hourly data. The fitted k_R model is represented by the red line.

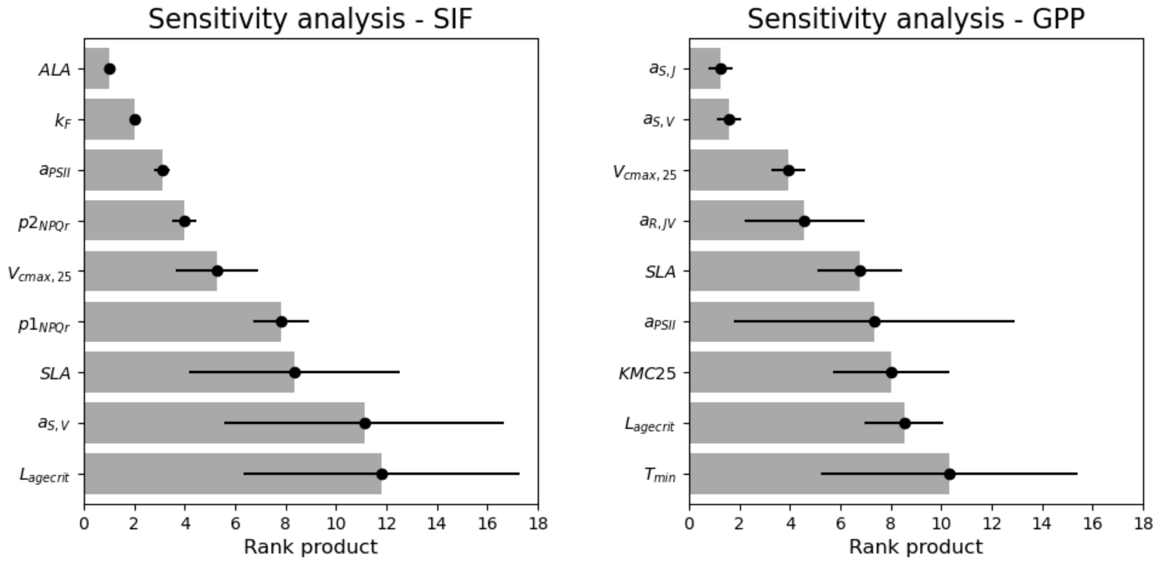

Figure S4: Ranking of the impact of the parameters on the simulated SIF (left) and GPP (right), identified by a sensitivity analysis according to Morris (1991). The nine most important parameters for each variable (detailed in Table 3) are represented according to the rank product over the nine selected sites (the lower the rank, the larger the influence). The error bars represent the standard-deviation of the ranking among the nine sites.

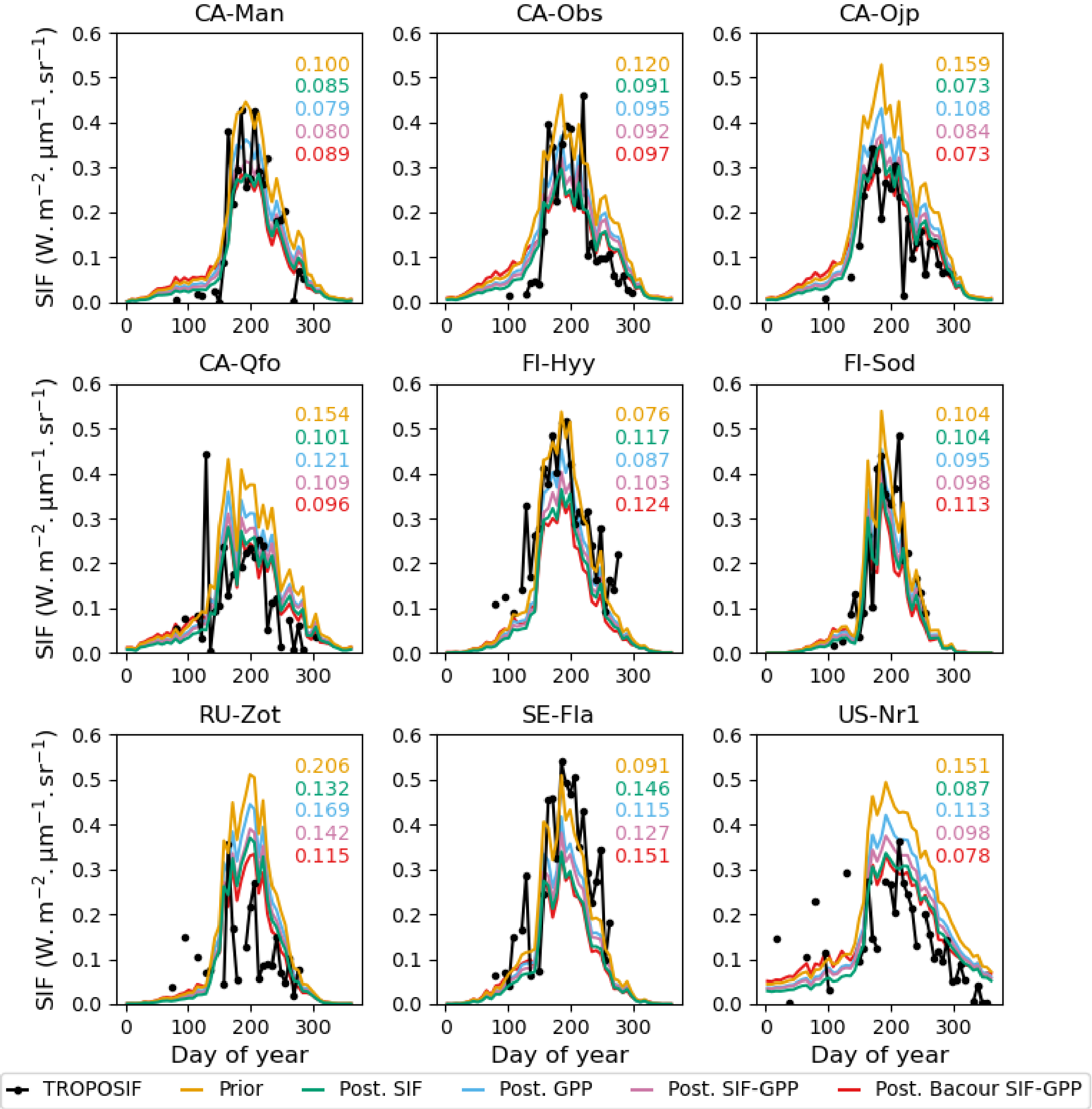

Figure S5: Seasonal cycle of SIF weekly averages over the evaluation year 2021. TROPOSIF estimates are in black, the prior simulation in orange, the posterior simulation related to the SIF-only DA experiment in green, the posterior simulation related to the GPP-only DA experiment in blue, the posterior simulation related to the SIF-GPP DA experiment in pink, and the posterior simulation related to the Bacour SIF-GPP DA experiment in red. The values in each subplot give the RMSD between the simulated SIF and TROPOSIF estimates in W·m^{-2}·µm^{-1}·sr^{-1}, using the same colour code.

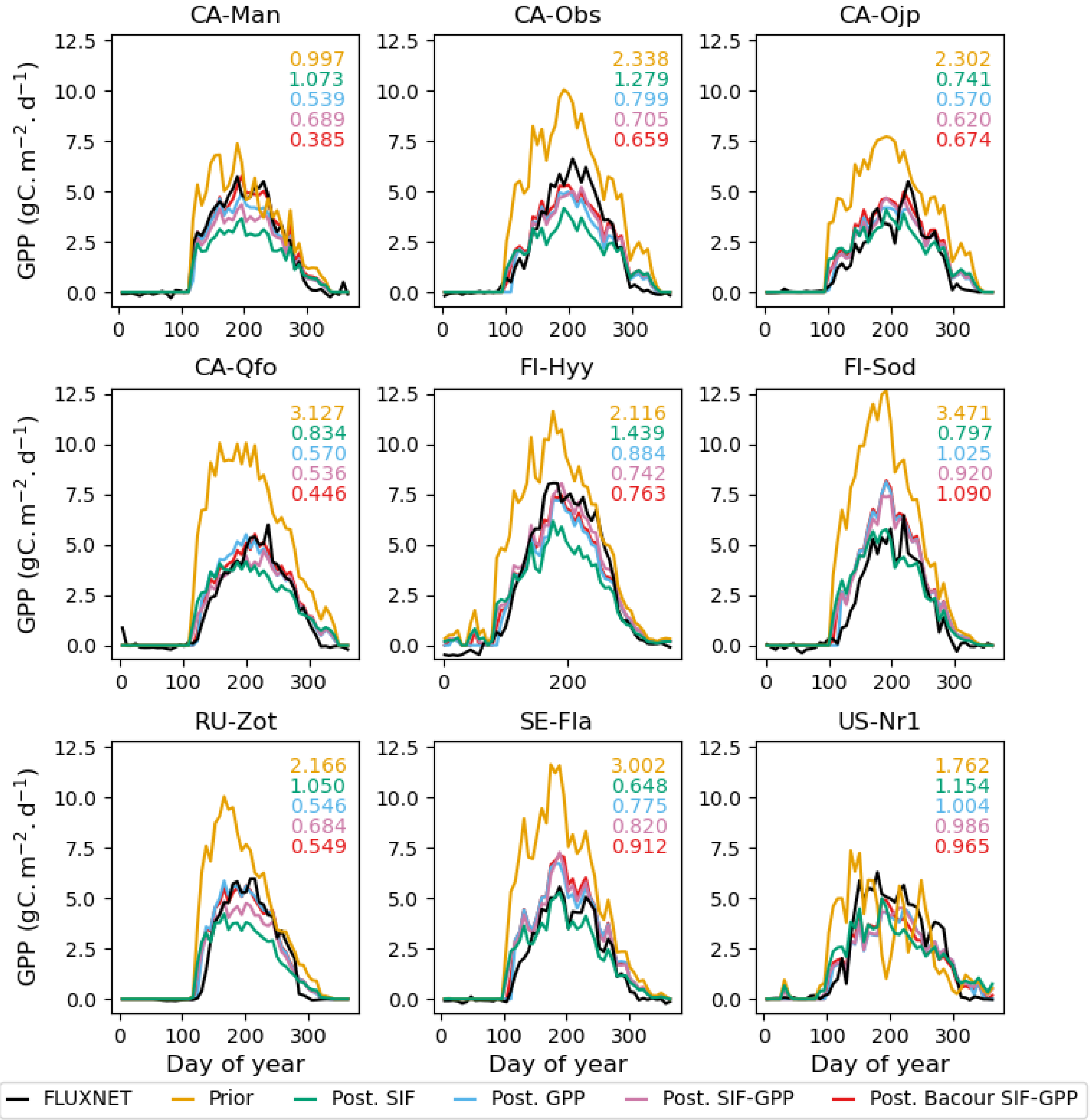

Figure S6: Seasonal cycle of GPP weekly averages for each site's dedicated evaluation year (see Table 1). FLUXNET GPP estimates are in black, the prior simulation in orange, the posterior simulation related to the SIF-only DA experiment in green, the posterior simulation related to the GPP-only DA experiment in blue, the posterior simulated related to the SIF-GPP DA experiment in pink, and the posterior simulation related to the Bacour SIF-GPP DA experiment in red. The values in each subplot give the RMSD between the simulated GPP and FLUXSAT estimates in gC·m^{-2}·d^{-1}, using the same colour code. Due to the absence of an evaluation year for RU-Zot, we have used the average seasonal cycles over the assimilation years in the corresponding subplot.

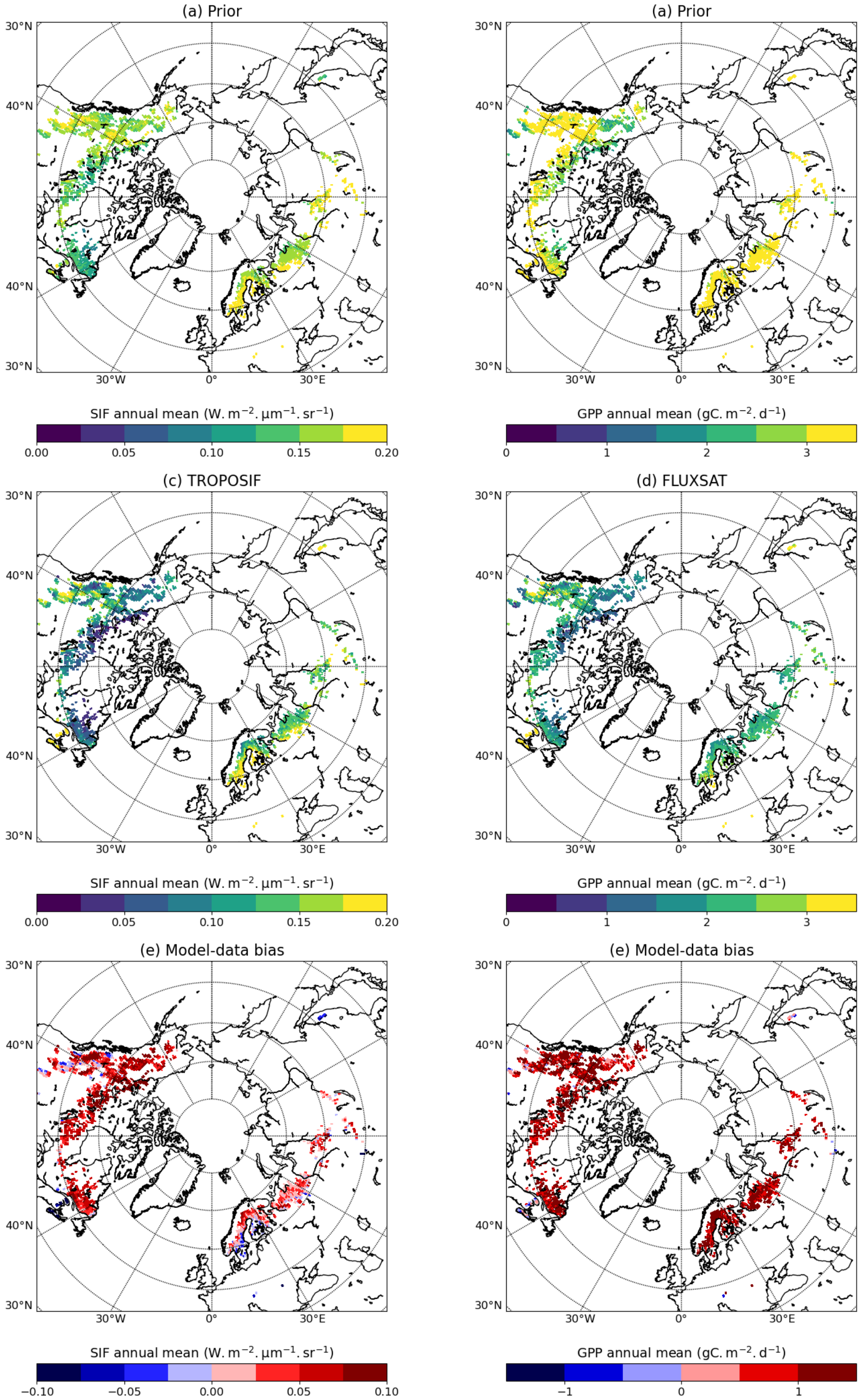
(a) Prior
(a) Prior
(c) TROPOSIF
(d) FLUXSAT
(e) Model-data bias
(e) Model-data bias
30°N
40°N
30°W
0°
30°E
SIF annual mean (W. m⁻². µm⁻¹. sr⁻¹)
0.00
0.05
0.10
0.15
0.20
GPP annual mean (gC. m⁻². d⁻¹)
0
1
2
3
−0.10
−0.05
0.00
0.05
0.10
−1
0
1

Figure S7: Maps of temporal means for SIF (left column) and GPP (right column), based on the prior simulations (a and b), the associated reference product, TROPOSIF for SIF (c) and FLUXSAT for GPP (d); and differences between simulated variables and the corresponding reference product (e and f). All means are computed over grid cells with a BorENF fraction larger than 50%, over the period May 2018-December 2020 for SIF, and over the period 2001-2015 for GPP.

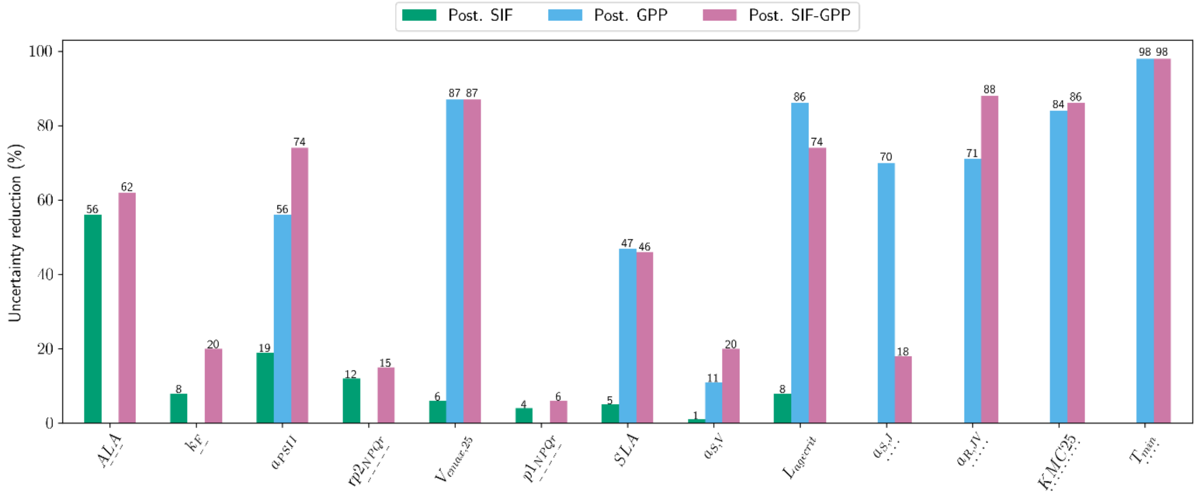

Figure S8: Reduction in parameter uncertainty (%) for the posterior SIF-only DA experiment in green, the posterior GPP-only DA experiment in blue, and the posterior SIF-GPP DA experiment in pink. SIF-only parameters are underlined with a dashed style, GPP-only parameters are underlined with a dotted style, all other parameters are common to both variables.

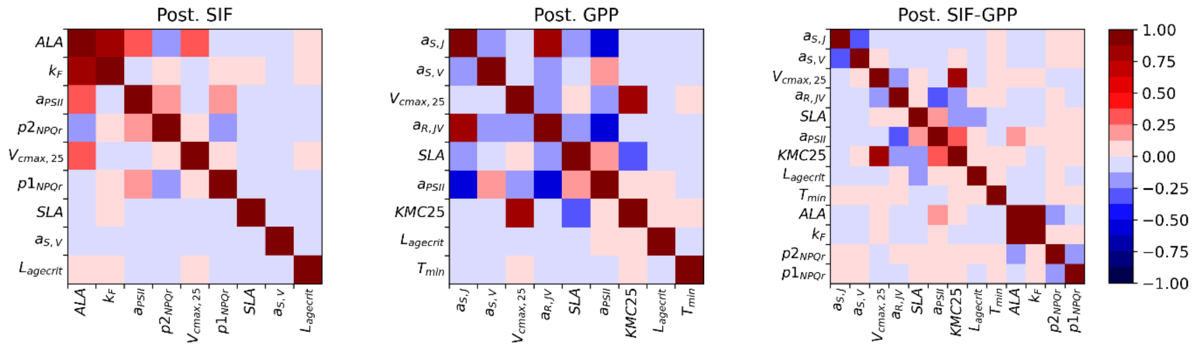

Figure S9: Posterior parameter error correlation matrices for the SIF-only (left), the GPP-only (middle), and the SIF-GPP (right) DA experiments.

Table S1: Akaike Information Criterion (AIC) for various k_R parametric models fitted with active fluorescence measurements at the Hyytiälä site. All RMSDs equal 0.28.

References	**k_R model**	**AIC**
van der Tol et al. (2014); Raczka et al. (2019)	$p_1(1+p_3)\frac{e^{p_2 \ln x}}{p_{3+}e^{p_2 \ln x}}$	-33472
Lee et al. (2015)	$(p_1x-p_2)x$	-33405
Other tested parametric models		
This study	$p_1x^{p_2}$	-33474
This study	$e^{p_1x^{p_2}}-1$	-33680
This study	$p_1x+p_2x^3$	-34012